Stony Brook University

A Multi-Scale Study on the Role of Trace Metals on Physiological and Pathological Mineralization

A Dissertation Presented

by

Derek Rammelkamp

to

The Graduate School

in Partial Fulfillment of the

Requirements

for the Degree of

Doctor of Philosophy

in

Materials Science and Engineering

Stony Brook University

May 2017

Stony Brook University

The Graduate School

Derek Rammelkamp

We, the dissertation committee for the above candidate for the

Doctor of Philosophy degree, hereby recommend

acceptance of this dissertation.

Yizhi Meng – Dissertation Advisor
Assistant Professor, Materials Science and Engineering

T.A. Venkatesh - Chairperson of Defense
Associate Professor and Graduate Program Director, Materials Science and Engineering

Tae Jin Kim – Committee Member
Assistant Professor, Materials Science and Engineering

Wei Yin – Committee Member
Associate Professor, Biomedical Engineering

This dissertation is accepted by the Graduate School

Charles Taber
Dean of the Graduate School

Abstract of the Dissertation

A Multi-Scale Study on the Role of Trace Metals on Pathological Mineralization

by

Derek Ramelkamp

Doctor of Philosophy

in

Materials Science and Engineering

Stony Brook University

2017

Physiological mineralization is necessary for the formation of healthy skeletal tissues and their appropriate functions. However, pathological mineralization seen in breast cancers have been linked to malignancy and lower survival rates. Recent findings suggest many mechanisms involved in skeletal mineralization may be similar in regulating pathological mineralization in breast cancer. This work demonstrates multi-scale contributions towards understanding the effects of trace metals on the pathological mineralization process relating to both the development of healthy bone tissue, the diseased state of osteoporosis, and microcalcifications which develop in breast cancers. A protein level study was performed on ECM protein fibronectin, which plays a role in cell adhesion. The protein studies showed zinc interactions with fibronectin and its fragment, anastellin, to influence protein structure. Zinc is also shown to decrease cell migration in vitro, which may be influenced by changes in fibronectin ECM structure. The effects of osteoporosis on micronutrient composition in vivo were examined using the technique of x-ray fluorescence (XRF) in an ovariectomized rat model. Compared to healthy bone, subtle difference are observed in zinc and iron in osteoporotic rat bones, showing micronutrients may play an important role in healthy bone regulation. Micronutrient zinc may also play an important role in pathological mineralization of breast cancer microcalcifications.

In this work, exogenous zinc is used to inhibit microcalcification formation, and metastatic potential of breast cancer cells in vitro in both a 2D and 3D spheroid environment. A novel in vitro self-assembled three dimensional multi-cellular tumor spheroid (MCTS) model for the study of breast cancer microcalcifications was developed for this experiment. A MCTS model for studying breast cancer microcalcifications has potential to be used in drug discovery, or for basic research applications studying mechanisms of microcalcification formation, which are still not fully understood. Taken together this study uses a multi-scale approach to gain a better understanding of micronutrients involved in pathological mineralization.

Dedication Page

I dedicate the work of this dissertation to all of my friends and family who have supported me throughout my life. I would not be the person I am today without the love and support from my parents who raised me to work hard and pursue my education. I would like to thank everyone in my life who helped and supported me in completing my doctorate degree.

A special thanks to my advisor, Dr. Yizhi Meng. Without your support and guidance, I would not have completed this work or learned the skills necessary to help me in the next chapter of my life. Also, I would like to thank all of my labmates, both graduate and undergraduate, who have helped with the many experiments in this thesis. I have had a lot of help from many people at Stony Brook University throughout the work of this thesis and I would like to thank you all for your contributions.

Table of Contents

List of Figures

List of Abbreviations

AR – Alizarin red

ALP – alkaline phosphatase

Ca - calcium

CAII – carbonic anhydrase II

ECM – extracellular matrix

EXAFS – extended x-ray absorption fine structure

DLS – dynamic light scattering

GBD – gelatin binding domain

Fe – iron

FN - fibronectin

HA - hydroxyapatite

HUVEC – human umbilical vein endothelial cell

MCTS – multi-cellular tumor spheroid

MMP – matrix metalloproteinase

MSF – migration stimulation factor

OC – osteogenic cocktail

OVX – ovariectomized

PBS – phosphate buffered saline

ROS – reactive oxygen species

SEM – scanning electron microscopy

TGFβ – transforming growth factor β

VK – von Kossa

XRF – X-ray fluorescence

Zn - zinc

Acknowledgments

I would like to acknowledge my advisor, Yizhi Meng, for all of her hard work and guidance throughout my graduate career. Her hard work and sacrifices have helped me tremendously become the person I am today both inside and outside of the laboratory. I am very thankful to have been her graduate student, as her knowledge and guidance will surely help take the next step in my career path.

Many thanks to my peers who have assisted me in numerous projects including my lab group members Wei Li and Giulia Surarato. I would also like to thank Tatiana Zaliznyak for her great help in collecting Raman spectroscopy data at the SoMAS's Nano-Raman Molecular Imaging Laboratory. Finally, I would like to give thanks to the numerous undergraduate students who have helped with the many projects in this work.

Raman data were acquired in SoMAS' NAno-Raman Molecular Imaging Laboratory (NARMIL), a community facility dedicated to environmental sciences' applications and founded with NSF-MRI grant OCE-1336724.

Research carried out in part at the Center for Functional Nanomaterials, Brookhaven National Laboratory, which is supported by the U.S. Department of Energy, Office of Basic Energy Sciences, under Contract No. DE-AC02-98CH10886

Research was carried out in part at the National Synchrotron Light Source (NSLS) and the Center for Functional Nanomaterials of Brookhaven National Laboratory, which is supported by the U.S. Department of Energy, Office of Science, Office of Basic Energy Sciences under Contract No. DE-AC02-98CH10886.

Publications

This is a list of peer-reviewed publications, book chapters, and conference proceedings that were produced during the course of this dissertation.

PEER REVIEWED JOURNAL PUBLICATIONS

Rammelkamp, D.; Li, W.; Meng, Y., Intracellular Delivery of Fluorescently Labeled Polysaccharide Nanoparticles to Cultured Breast Cancer Cells. Methods Mol Biol 2016, 1406, 289-302.

Dorst, K.; **Rammelkamp, D**.; Hadjiargyrou, M.; Meng, Y., The Effect of Exogenous Zinc Concentration on the Responsiveness of MC3T3-E1 Pre-Osteoblasts to Surface Microtopography: Part II (Differentiation). Materials 2014, 7, 1097-1112.

Dorst, K.; **Rammelkamp, D**.; Hadjiargyrou, M.; Meng, Y., The Effect of Exogenous Zinc Concentration on the Responsiveness of MC3T3-E1 Pre-Osteoblasts to Surface Microtopography: Part I (Migration). Materials 2013, 6, 5517-5532.

CONFERENCE PRESENTATIONS

Rammelkamp, D; Lin, J.; Meng, Y.; (2016, October) Establishment of a 3D Tumor Spheroid Model for Investigating Breast Cancer Microcalcifications. Poster session. New Frontiers in 3D Cell-culture Based Screening Technologies., Johns Hopkins University, Baltimore, MD.

Rammelkamp, D; Dorst, K.; Farquhar, E.; Chance, M.; Meng, Y. (2014, October) The Effect of Exogenous Zinc Concentration on the Migration of Osteoblast-like and Osteosarcoma Cells. Poster session at Annual Biomedical Engineering Society Conference, San Antonio, TX.

Rammelkamp, D.; Farquhar, E.; Chance, M.; Meng, Y. (2013, May) Investigating the Role of Zinc in the Cryptic Activity of Fibronectin Using Time-Resolved EXAFS. Poster session at the Annual NSLS & CFN User' Meeting, Brookhaven National Laboratory, Upton, NY.

Chapter 1 : Introduction

1.1 Background

1.1.1 Bone Biology

The structure of bone will ultimately determine its properties, function, and overall health. Bone is a composite material that is made up of an organic collagen protein and an inorganic mineral phase called hydroxyapatite. Collagen comprises about 20% of the weight of bone. Each collagen fibril is made up of several individual collagen units called tropocollagen. A single tropocollagen unit is composed of three polypeptide chains, each having about 1000 amino acids. The amino acid content varies from chain to chain, but the most common amino acids in collagen are glycine, proline, and hydroxyproline. The polypeptide chains are intertwined into a triple helix, creating a cylindrical shape that is about 300nm in length and 1.5nm in diameter, as shown in **Figure 1.1**. When aligned in a fibril, tropocollagen units are parallel to each other, but are separated by gaps that are about 35nm in length. There is an overlap region of 68nm, where neighboring tropocollagen units are staggered. The gap regions become very important to the overall structure of bone because it is where hydroxyapatite mineralizes and resides.[1,2]

Hydroxyapatite (HA) is the inorganic crystalline component of bone which has the following chemical formula: $Ca_{10}(PO_4)_6(OH)_2$. HA mineralizes the collagen fibrils, specifically between the gaps of tropocollagen units, as seen in **Figure 1.1**. The crystals will form plate-shaped structures with approximate length, width, and thickness of 50nm, 25nm, and 2-6nm respectively. The crystals have hexagonal symmetry. HA makes up about 60% of bone by weight. The percentage varies because there is a different degree of mineralization depending on the structure and function of bone. The nanoscale structure of bone, including degree of mineralization will affect its macroscopic properties. As bone becomes more and more mineralized, it will increase in strength and decrease in elasticity. For example, unmineralized tendon, which is comprised of collagen, is very elastic because it lacks the rigidity and support caused by HA.[1,2] Conversely, the highly mineralized ossicles found in the human ear are very inelastic due to its function of converting sound waves to the inner ear. From the nanoscale, HA along with collagen will organize into several hierarchical levels to form what we see on the macroscale as bone tissue.[3]

The smallest of the hierarchical levels is of the mineralized tropocollagen units within a collagen fibril. The next level is the mineralized collagen fibril. Mineralized collagen fibrils align together in patterns to form tissue fibers. The fiber patterns can be oriented in different directions depending on the bone. Bone fibers can be parallel, woven, radial, or in a plywood-like structure. The most common fibril array is the plywood-like structure which is found in lamellar bone. In lamellar bone, collagen fibrils are aligned into parallel sheets, which exhibit a high degree of mechanical strength. A woven fibril array has a random orientation of collagen fibrils. It is seen when bone is produced rapidly after fractures before it can be remodeled into stronger, lamellar bone. Parallel fibril arrays are often found in tendons, and radial fibril arrays are found in dentin, the main component in teeth. After the array of fibrils the next hierarchical level of bone structure is the osteon. An osteon is a repeating cylindrical unit of bone which contains a small channel for the flow of fluid, ions, and bone serum. An osteon unit is about 100 micrometers in diameter. Blood vessels flow through the channels to bring nutrients to the bone. Within the osteon structure, there are also small canals where the bone cells reside. Several osteons form a network, usually in parallel with the long axis of bone to form either cortical or cancellous bone. Cortical bone is the hard, dense outer layer of bone, whereas cancellous, or trabecular, bone is the porous, spongy interior of bone. Together, these two layers make up the organ known as bone.[2] A model of the structural hierarchy of bone ranging from the macroscale to the molecular level can be seen in **Figure 1.1**.[4]

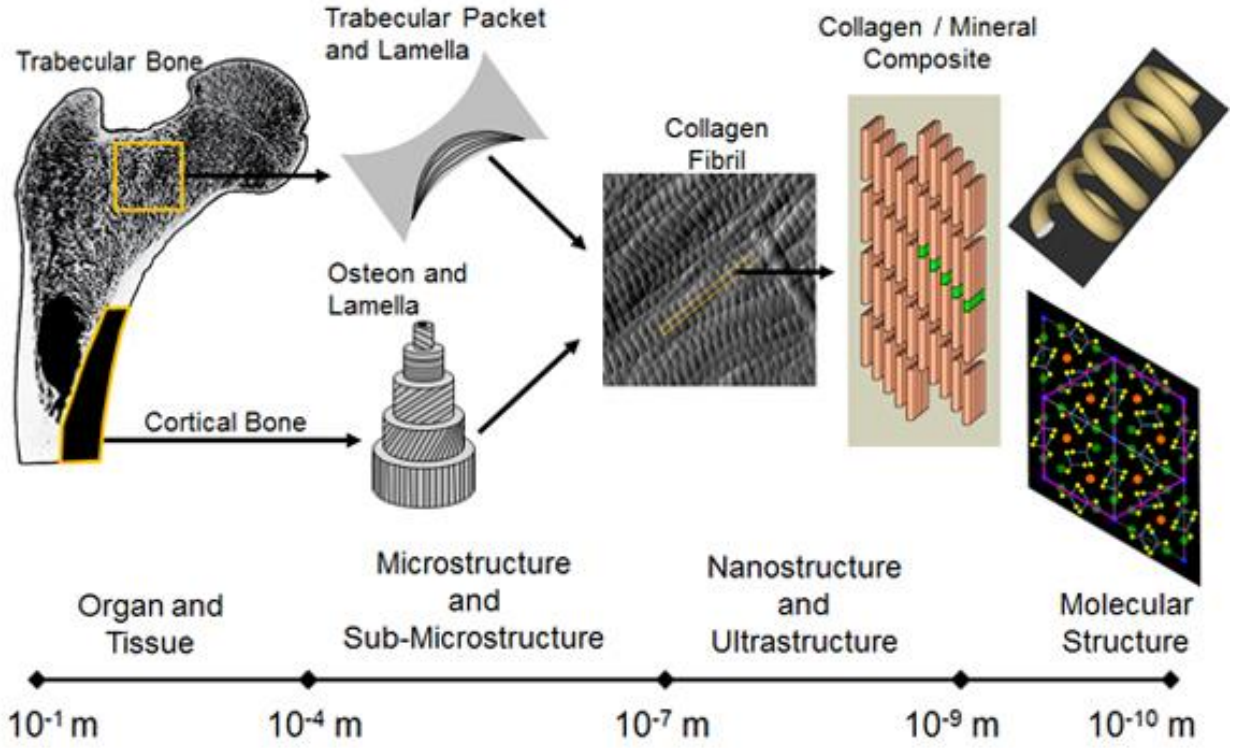

Figure 1.1. Hierarchical structure of bone ranging from the macrostructure to the molecular structure. Figure taken from Bone Biology and Mechanics Laboratory, Indiana University – Purdure University at Indianapolis.[4]

The microstructure of bone is constantly changing in a process known as the bone remodeling cycle. In a properly balanced bone remodeling cycle, old or damaged bone is removed and new bone is formed in its place. Osteoclast cells are responsible for the resorption of old bone and osteoblasts are responsible for building the new bone tissue. Immobile osteocyte cells send signals to osteoblasts and osteoclasts in order to activate the bone remodeling pathway. Osteocyte signaling is caused by several factors including mechanical stimulus. The mechanical stimulus is reproduced into an electrical, and ultimately a chemical response in the process known as mechanotransduction. The bone remodeling cycle can explain Wolff's Law, which postulates that the strength and shape of bone changes in response to mechanical loads. A mechanical load will be interpreted by the osteocytes cell, which will send a signal to the osteoblasts and osteoclasts to remodel and strengthen bone tissue.

Bone remodeling is a three step process, which is shown in **Figure 1.2.**[5] Firstly, osteoclasts resorb the old bone tissue, breaking down the ECM. Next, mononuclear cells, such as macrophages are recruited to the bone surface in a phase known as reversal. As part of the body's immune response, macrophages are recruited to the site of resorption to complete the resorption process and initiate signals for the osteoblasts to begin formation of the new ECM. Finally, osteoblasts are recruited to build and mineralize the ECM.[5–7] In healthy adults, the rate of bone resorption is about equal to the rate of new bone formation. Therefore, there is no net loss in bone tissue. However, the remodeling equilibrium changes in the diseased state of osteoporosis. When more bone is being resorbed than new bone is being formed, there is a net loss of bone tissue, resulting in a decrease in mechanical strength and a greater risk of fracture. In most animals, as well as in humans, bone becomes more brittle and stiffer with age, which is the result of a dysfunction in the bone remodeling cycle. The net loss of bone with age causes morphological changes to the microstructure of bone making it more susceptible to fracture. The morphological changes are caused by genetics, mechanical loading of the bone, and the cellular activities.[1]

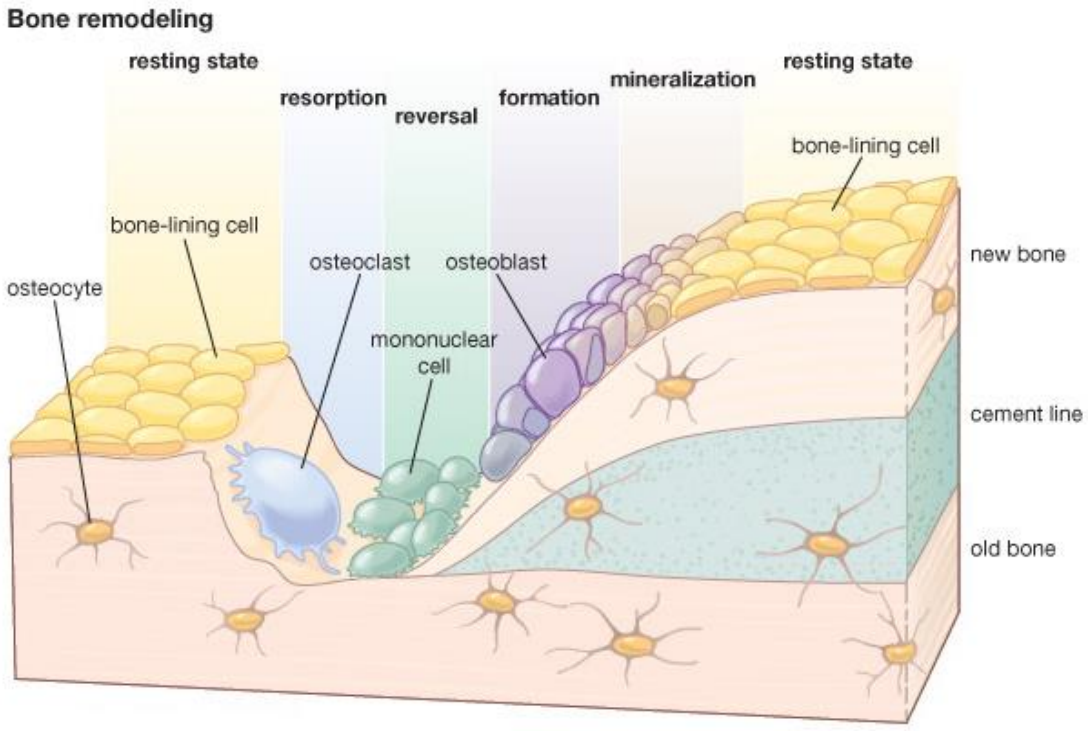

Figure 1.2. A representation of the bone remodeling cycle. The cycle can be broken down into 3 phases: (1) resorption of bone tissue by osteoclasts, (2) reversal phase by mononuclear cells, and (3) new bone formation and mineralization by osteoblasts.[5]

1.1.2 MMP-2

MMP-2 is a gelatinase protein produced by osteoblasts which are involved in the remodeling of bone ECM through the cleavage of collagen at the C-terminus. MMPs are produced by cells involved in the remodeling process shown in **Figure 1.2**. MMP-2 is produced by osteoblast cells during the first stages of new bone formation.[11] Expression of MMP-2 has been used as a marker for bone remodeling around the site of implants.[11,12] MMP-2 is expressed as an inactive pro-enzyme where the catalytic domain is essentially shielded by a pro-peptide which must be removed to become active, seen in the top of **Figure 1.3**.. Inactive 72-kDa MMP-2 becomes 64k-Da active MMP-2 upon pro-peptide removal, through an interaction with tissue inhibitor metalloproteinase 2 (TIMP2). TIMP2 activates MMP-2 at low concentrations but inhibits the activation at high concentrations.[13] The catalytic domain contains a zinc ion coordinated between three histadine residues. MMP-2 structure and mechanism of activation are seen in **Figure 1.3**.[14] The catalytic zinc binding domain must be available for the enzyme to be activated. This can be achieved through proteolytic activation or through post translational modification. Proteolytic activation by TIMP2 cleaves off the propeptide, exposing the catalytic zinc binding domain. Post translational modification requires the presence of a reactive oxygen species (ROS), specifically peroxynitrile. Glutathione binds to the sulfur atom of the cystine residue in the pro-peptide domain, disrupting the bond to zinc, and exposing the catalytic binding domain of MMP-2.[14] The activity of the catalytic domain of MMP-2 is dependent on the coordination to a zinc atom. [15,16] Activation of MMPs are thought to be multi-factorial, dependent on zinc and calcium ion concentration, and other factors.

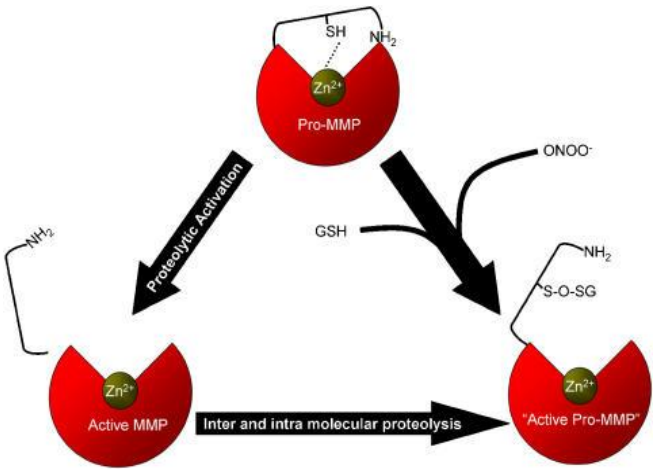

Figure 1.3. Activation of full length MMP-2 can occur from two mechanisms: (1) removal of pro-peptide domain by protoytic activation of TIMP2 (left), and (2) post translational modification of the cystine residue at catalytic site on the pro-peptide from the addition of glutathione (GSH) activated by peroxynitrile (ONOO-) (right).[14]

1.1.3 Migration Stimulation Factor

A shortened isoform of the ECM protein fibronectin, known as migration stimulation factor (MSF) has also been shown to display gelatinase activity similar to MMP-2.[17] MSF has been shown to be secreted by fibroblasts and breast cancer cells, and has been shown to stimulate cell migration, likely through its gelatinase activity. MSF is obtained from the alternative splicing of fibronectin mRNA. MSF is a 77-kDa protein which corresponds to the N-terminal fragment of fibronectin mRNA. Expression of MSF in healthy human cells is uncommon, with the exceptions being acute wound healing and cancers. Over-expression of MSF is common in many cancers, which often is linked to cancer metastasis.[18]

1.1.4 Gelatin Binding Domain

The collagen binding site on fibronectin is the 45-kDa GBD region, which borders the heparin or fibrin region, which is the closest region to the N-terminus of fibronectin. In **Figure 2.4**, GBD is labeled as 'collagen.' Fibronectin plays a crucial role in collagen production, which is apparent in that anti-GBD antibodies were shown to inhibit collagen fiber formation in fibroblast, which are cells in the connective tissues that produce ECM and collagen.[19] GBD binding to collagen has been shown to be similar to MMP-2; both in structure and in the fact that there is strong evidence for the involvement of zinc.[9]

Unlike the MSF, GBD is found to be expressed in full length fibronectin. Since the motogenic activities of the GBD fragment of fibronectin and MSF are indistinguishable, cells have two ways to acquire migrational bioactivity. Cells can either degrade the ECM to utilize the GBD of fibronectin or they can genetically control MSF during gene transcription. Since MSF and GBD have similar bioactivities it is suggested by Schor et al. that MSF is generated in the absence of some fibronectin fragments such as GBD.[20]

1.1.5 Involvement of Trace Metals in ECM Regulation

Trace elements copper and zinc are tightly regulated in the body and are essential for living organisms to participate in a variety of cellular metabolic processes including the function of cellular enzymes and proteins. Metal binding is necessary for the proper function of certain cellular proteins. For example, zinc binding to MMP-2 is necessary for the function of its catalytic domain.[13] Although metal ions are necessary for protein function, excessive accumulation can become toxic. High copper accumulation is seen as toxic due to its effect in

the production of oxidative stress. Conversely, zinc has a protective effect against damage induced by oxidative stress which is potentially a result of metallothionein (MT) induction.[21] MT is a low molecular weight metal binding protein which binds to both copper and zinc and is used to prevent intercellular metal toxicity.[22]

1.1.6 Micronutrient Copper

Copper is a trace element in the body that found in even lower quantities than zinc. The average human body contains about 80mg copper, with the liver having the highest relative copper content. Almost all copper found in the body is bound to proteins.[23] Copper uptake occurs in the intestines, where absorption is dependent upon intake. Humans given a high copper diet of 7.5mg/day were found to uptake 12% of that copper, whereas humans given a low copper diet of 0.78mg/day were found to uptake 56% of the copper. The normal copper adequate diet of 1.68mg/day saw patients absorb of 36% of their copper intake.[24] Copper absorption is dependent upon dietary copper intake. The body responds to low dietary copper by absorbing more and responds to high dietary copper by absorbing less in order to maintain a healthy level. Once copper is absorbed, specific copper transporter proteins transport copper throughout the body through the serum, with the liver being the primary site of copper storage.[24] An imbalance of copper levels in the body, as seen in patients with Wilson's Disease, is caused by a genetic order in how copper is excreted from the body. Copper is not removed efficiently from the body (in the bile fluid), and therefore accumulates heavily in the liver and brain. Wilson's Disease is one case where copper is mis-regulated in the body due to a genetic disorder.[25]

Copper is highly regulated and involved in the activity of numerous enzymes including superoxide dismutase (SOD). SOD is an enzyme which functions to scavenge intracellular free radicals to prevent damage caused by oxidative stress. Interestingly, unbound copper produces free radicals through the Haber-Weiss and Fenton reactions shown in **equation 2.1**.

(2.1) $Cu^{2+} + O_2 + H_2O \rightarrow Cu^{+} + H_2O_2 \rightarrow Cu^{2+} + OH\cdot$

The amount of copper in the body is highly regulated through the absorption in the intestines, a process that is not strongly understood. Free copper ions are found in extremely small amounts. The cellular copper transport pathway is a complex mechanism mammalian cells

use to regulate the amounts of cellular copper. Essentially all copper that crosses the cell membrane is bound to proteins. It is understood that copper is transported across cell membranes through transporter protein CTR1. Copper is bound to chaperone proteins which transport extracellular copper to copper binding proteins in the cytosol through an unknown mechanism. [26]

At high concentrations, copper induces apoptosis through the activation of the p53 pathway. Tumor protein 53 (p53) is a tumor suppressor protein which regulates the cell cycle to prevent cancer cell growth. Intracellular production of reactive oxygen species (ROS) through the reduction of copper(II) to copper(I) activates the p53 pathway through regulation of genes that encode for ROS production. Cells have a preventative mechanism against ROS induced cytotoxicity. Cells can produce a family of low molecular weight metal binding proteins know as metallothionein (MT). MT is a cystine-rich protein with the capacity to bind to heavy metals such as zinc, copper, and selenium. MTs are heavily localized in the Golgi apparatus of the cell.[22] Copper also binds to an extracellular protein known as lysyl oxidase. Lysyl oxidase is a copper containing enzyme that covalently cross-links fibrillar collagen, which is the final step in the fabrication of mature collagen fibers.[27]

1.1.7 Copper and Cancer

Copper is also being mis-regulated in cancer patients. Copper is found in high levels in the serum and tumor sites of cancer patients, and is thought to be a promoter of tumor angiogenesis.[25] Since copper is being found in such high levels in cancer patients, is it now being targeted by copper chelator drugs in order to help regulate copper levels, prevent tumor angiogenesis, and cancer metastasis.[25] Copper deficiency in mice was shown to suppress tumor growth and angiogenesis using an in vitro copper chelating agent. Mice administered the copper chelator developed smaller, avascular tumors and had a lower serum copper levels then their untreated counterparts.[25]

Copper's mis-regulated role in cancer is not only present in serum, but also the tumor microenvironment. High levels of copper containing lysyl oxidase were found in the tumor microenvironment of lung adenocarcinoma patients.[28] Increased levels of lysyl oxidase are proposed to be a marker for cancer migration and metastasis.[27,28] Interestingly, lysyl oxidase was found to bind to cellular fibronectin with a similar affinity to that of collagen. Fibronectin-lysyl

oxidase interactions were found to regulate the activity of lysyl oxidase, in that binding was found to inhibit lysyl oxidase induced cross-linking of collagen. [27]

1.1.8 Copper and Zinc Interdependence

An in vitro experiment by Reeves et al. showed the increase in zinc into culture medium of Caco-2 intestinal adenocarcinoma cells affected the uptake of copper transport. In this study, cells exposed to 50μM zinc in the culture medium for a period of 7 days transported significantly less copper across the cell monolayer compared to cells that were cultured in 6μM zinc. Interestingly, cells exposed to 200μM zinc transported significantly more copper than those cells grown in 6μM zinc. In this experiment copper concentration was held constant at 0.7μM. Caco-2 cells also expressed significantly higher cellular MT with zinc concentrations over 50μM . This study demonstrates the effects of zinc concentration on copper uptake. It appears the uptake of trace elements copper and zinc is correlated to cellular MT and is dependent upon each other.[29]

The role of copper and other trace elements in cancer and cancer metastasis is being increasingly investigated. The serum of cancer patients shows an increase in the Cu:Zn ratio that is marked by an increase in copper concentration and decrease in zinc concentration compared to healthy individuals.[30,31] This difference was less significant in patients with benign breast tumors, and greater in patients with metastatic breast cancer. [30] In fact, serum trace element ratios have been suggested as use for differential diagnosis for certain cancers.[30]

1.1.9 Micronutrient Zinc

Even though the average human body only contains 2 to 3 grams of zinc, it is an essential nutrient that the body needs to maintain homeostasis. Zinc is a trace element necessary for important cellular functions including DNA synthesis, wound healing, and immune system function. Zinc is involved in the catalytic activity of over 100 cellular enzymes. Unlike calcium, the body has no specialized storage system for zinc. Therefore, daily intake of zinc is necessary from an individual's diet.[32] In the developed world, zinc deficiency, known as hypozincemia, is rarely seen due to the high bioavailability by dietary means. Symptoms of hypozincemia include loss of appetite, impaired growth, impaired immune function, hair loss, skin lesions, and impaired bone growth.[33]

Zinc plays an important role in regulating bone metabolism on many different levels in the body. Hormonal, cellular, and enzymatic functions have all been shown to be affected by levels of zinc.[34–36] Hormonally, bone growth is controlled in the body by the thyroid and parathyroid glands. Homeostatic levels of calcium in the blood are between 9 and 11mg per 100mL. When this level becomes imbalanced due to rising calcium levels, the thyroid gland secrets calcitonin, a hormone which stimulates production of calcium deposits from osteoblasts. Inversely, when calcium levels fall, the parathyroid gland secretes parathyroid hormone (PTH) which activates osteoclast activity to degrade bone matrix. The net result is a maintained balance of calcium in the blood. Zinc levels in the body have been shown to affect the hormonal activities of PTH and calcitonin. For example, zinc deficiency in rats has been shown to significantly reduce the amount of calcitonin, while increasing the amounts of PTH in the serum of rats.[36]

1.1.10 Zinc and Bone Remodeling

On the cellular level, zinc deficiency has been shown to decrease the cellular activity of osteoblasts, which build and mineralize bone, while increasing the activity of osteoclasts, which resorb old bone tissue. A net bone loss is seen with an imbalance between osteoblast and osteoclast activity, leading to a decreased bone mineral density and higher risk of fracture. In vivo, a rat model was used to study the effects of dietary zinc on both osteoclast resorption markers, and osteoblast differentiation and mineralization makers. An increase in dietary zinc was shown to decrease osteoclast resorption potential, shown by a decrease in levels of matrix metalloproteinases (MMP-2 and MMP-9) and decreased levels of carbonic anhydrase-2 (CAII). MMP-2 and MMP-9 are enzymes produced by osteoclasts responsible of degrading ECM collagen. CAII is an enzyme produced by osteoclasts which aids in dissolving bone ECM, specifically through catalyzing the reaction between the production of protons from CO_2 and H_2O. The protons act as an acid to dissolve hydroxyapatite crystal out of mineralized bone matrix. Increased levels of CAII and MMPs indicate an increase in osteoclast activity.[34]

In contrast to osteoclast resorption makers, osteoblast marker alkaline phosphatase (ALP) was shown to increase with increasing dietary zinc intake in rats.[34] ALP is an enzyme produced by post-proliferating mature osteoblasts which regulates the ECM. An increase in ALP activity

indicates increased biosynthetic activity of osteoblasts. Increased trabecular bone mass and density is also seen with an increase in dietary zinc intake.[34,37]

At the enzymatic level, the effects of zinc on bone formation are still being explored. A great deal of focus is being driven towards the role of zinc in MMP activity. An increase zinc concentration in vitro was shown to decrease the amount of C-telopeptide pyridinoline crosslinks of type I collagen (ICTP).[38] ICTP is a product of MMP degradation of collagen which results in the cleavage of type I collagen at the C-terminal side of the peptide chain. A decrease in ICTP is the result of decreased MMP activity, resulting from a higher zinc concentration in cell culture. Another focal point of zinc deficiency's effect on bone growth has been Runx2, or Runt-related transcription factor 2. Runx2 manages the transcription of bone marker genes by binding to the DNA sequence that encodes for collagen, ostoecalcin, and osteopontin. An under-expression of Runx2 has been shown to decrease mineralization of MC3T3-E1 cells in vitro.[35] A zinc deficiency induced a decrease in the quantity of Runx2 transcriptional factors, leading to a lower production of proteins such as collagen necessary to assemble the ECM of bone. Zinc deficiency has been shown to down-regulate the expression of Runx2, leading to decreased protein synthesis necessary for ECM assembly.[35,39] The mechanism of zinc regulation on Runx2 is still being investigated.

The IIICs segment of fibronectin is another region that has been shown to interact with zinc. IIICS functions in a specific role in the adhesion of leukocytes, melanoma cells, and peripheral neurons.[17,40] Askari et al. has recently shown that the IIICS region of fibronectin contains a divalent cation binding site.[10] The binding site is coordinated by four histadine residues located in two of the sub-domains of the IIICS subunit. Copper, nickel and zinc were all found to bind competitively to fibronectin in the IIICS region, but the physiological metal ion that was detected through metal ion affinity chromatography was the zinc cation. The specific stoichiometry of zinc binding was variable, and therefore, unable to be confirmed, but it is important to note that zinc is binding to subunits of fibronectin and could play a role in maintaining its structural integrity.[10] The four histadine residues that zinc coordinates to are structurally reminiscent of the zinc binding domains in MMP-2. The structure of the IIICS region has not been solved yet. However, high affinity chelation to metallic ions has been shown to only occur in the context of an α-helix.[41] Fibronectin fragments must be further analyzed to

determine the effect of metal binding on its overall structure.[10] The IIICS region is not the only region that has been shown to bind to zinc.[9,20]

1.1.11 Mis-differentiated bone

A disruption in the differentiation of bone cells can lead to diseased conditions characterized by the cellular malfunctions. Bone mis-differentation has recently been examined in the cases of osteoporosis and osteosarcoma.[42,43] Cell differentiation is thought to be influenced by cellular microenvironment. Therefore, changes to ECM microenvironment may influence differentiation markers which lead to the progression of osteoporosis and osteosarcoma.

1.1.12 Osteoporosis

As mentioned previously, bone loses its strength over time and becomes more susceptible to fracture; of which, the underlying mechanisms are still unknown. Osteoporotic-like bone conditions are characterized by a loss in total bone volume that can be attributed to both cortical and trabecular bone. In **Figure 1.4**, a comparison between healthy and osteoporotic bone is shown. A common treatment for conditions like osteoporosis is the restoration of bone mineral density (BMD) through dietary supplements, which only partially replenish the inorganic component while leaving patients with many unwanted side effects. As such, the increase in bone fragility cannot be explained by mere loss of inorganic hydroxyapatite. Elderly individuals may have a ten-fold increase in risk of bone fracture compared to younger individuals with the same BMD.[44] Therefore, changes in the organic component of bone are now being increasingly investigated as suspects to age related increase in fracture risk.

Mis-differentiation of bone cells has been proposed for its role in osteoporosis. A malfunction in the mesenchymal stromal cell (MSC) differentiation pathway has been proposed as a possible link to osteoporotic conditions.[43] It is suggested that a disruption between MSCs differentiation into the osteoblast lineage results in is a cause of osteoporotic-like conditions. Either age or local cellular environment could play a role in disrupting MSC differentiation into osteoblasts.[43]

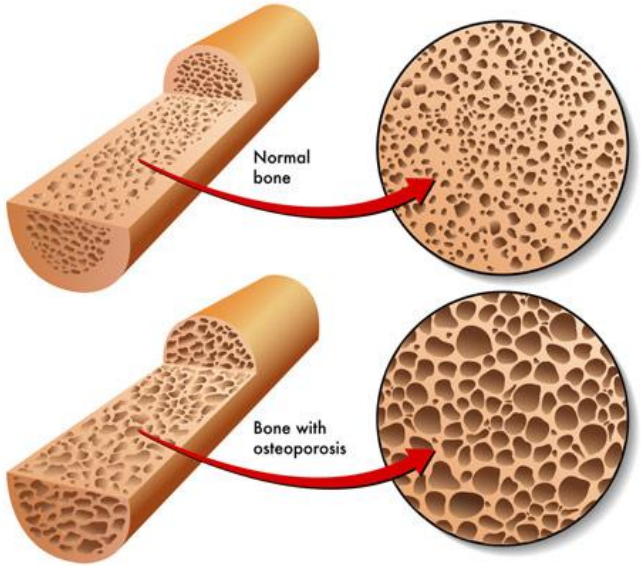

Figure 1.4. A comparison of healthy bone and osteoporotic bone. Notice a thinner cortical layer and increased porosity in osteoporotic bone.

1.1.13 MMPs and Metastasis

Cancer metastasis at the cellular level cannot occur without interactions between the cell and the ECM. MMPs, such as MMP-2 are highly expressed in metastatic cancer cells, where the ECM is being degraded to allow for cancer cells to migrate.[45] MMPs are also highly expressed in tumors undergoing angiogenesis, or the building of blood vessels. The role of zinc in cancer metastasis was studied by Huang et. al using a zinc chelator and exogenous $ZnCl_2$. Chelation of zinc significantly lowered MMP-2 activity related angiogenesis of human umbilical vein endothelial cells (HUVEC) in vitro, in a dose dependent manner. Addition of a zinc chelator significantly lowered migration of HVUE cells in vitro, and addition of zinc back into culture medium returned migration to near control speeds.[45] MMPs are important secreted ECM proteins which regulate cancer metastasis.

Metastatic potential of tumor cells is highly dependent on proteins in the micro-tumor environment. In particular, two zinc active proteins, ZEB-1 and MMP-2, play roles in the multi-factorial process. ZEB-1 binds to SMAD receptors which regulate the EMT. MMP-2 is helps break down the ECM of the tumor microenvironment, making cell migration possible. Both ZEB-1 and MMP-2 are shown to be over expressed in cancer cells and their inhibition has been shown to reduce the metastatic potential of cancer cells.[45,46]

1.1.14 MSF and Metastasis

MSF clearly has a regulatory role in tumor metastasis, which is influenced by ECM proteins such as fibronectin and MMP-2. The interactions between cancer cells and ECM proteins must be studied to understand the mechanism of cancer metastasis. For metastasis to occur there must be a change in the cell-ECM attachment, and a subsequent ECM degradation by a proteolytic gelatinase enzyme. According to experiments by Das et al., the presence of fibronectin upregulates the activity of MMP-2 and MMP-9 in human breast cancer cells.[13] Fibronectin may generate a signaling cascade to cancer cells which activates MMP production, leading to an increase in cancer metastasis. An important integrin, the $\alpha_5\beta_1$ integrin, was found to possibly be involved in the cellular signaling of MMP-2 activation. When $\alpha_5\beta_1$ was blocked using a monoclonal antibody, MMP activation decreased measurably. This indicates that the $\alpha_5\beta_1$ integrins are involved in the fibronectin induced MMP activation. Several other integrins were shown to be involved in MMP regulation through interactions with ECM proteins such as fibronectin.[47]

Similar to MMP-2, MSF has been shown to display zinc dependent gelatinase activity. The specificity of zinc binding was shown by Houard et al., through a loss of activity upon mutating the zinc binding motif.[17] MSF uses its gelatinase activity as the primary mechanism for promoting migration. MSF is heavily expressed in cancer cells, suggesting the gelatinase activity of the enzyme is partially responsible for cancer migration. MSF was also inhibited by several MMP-2 inhibitors, suggesting that the active site has a similar structure. The migratory activity of MSF seems to be dependent upon its gelatinase activity, but may also be related to a GBD in MSF itself. MSF contains GBD in the Fibrin-I domain of its 77-kDa structure. MSF uses the GBD to bind to the ECM protein collagen, when performing its gelatinase degradation activity. Hourad et al. suggests that the sequence of the amino acids in the primary structure of GBD resembles that of an integrins binding sequence which is recognized by cells initiating a signal transduction pathway that correlates to the migratory activity of MSF.[17] A mutation in the amino acid sequence of GBD was shown to completely inhibit the migratory activity of MSF.[13] GBD has been shown to be structurally zinc dependent.[13] Therefore, MSF could be regulated by cellular zinc concentrations in the body, which control how GBD binds to collagen, and ultimately its migration activity.

MSF is highly expressed in wound healing and cancer cells but rarely in healthy cells. Although zinc plays an important role in some of the binding domains involved in MSF, the regulation of MSF production has not been addressed. Transforming growth factor β_1 (TGFβ) may be involved in the regulation of MSF. TGFβ is a protein secreted by many cells which is involved in cellular signaling for certain functions, including cell growth, proliferation, and differentiation. Cell migration of adult skin fibroblasts was tested by Schor et al. in a 2012 study where migration dependence on TGFβ was tested.[48] TGFβ was found to act as a bistable switch which controls MSF production in fibroblasts cells on both healthy ECM and denatured ECM. Surprisingly, TGFβ shows that it could not only activate MSF production of cells on a partially denatured ECM, but it could also deactivate MSF production of those cells once attached to a healthy ECM. Subsequent exposure of TGFβ to cells that are producing MSF on a healthy ECM prevented further MSF activation. Exposure of TGFβ to fibroblasts cells increased MSF activation in as little as a 2 hour period. When cultured under standard in vitro conditions, initial TGFβ exposure resulted in a permanent on switch of MSF production for the entire lifespan of the cells. Cell migration on both healthy and denatured ECM were shown to be dependent upon

TGFβ, which regulates MSF activation. Clearly, the pathway that regulates MSF activation through TGFβ is an important function of healthy cellular and cancer cell migration, which needs to be further analyzed to fully understand the mechanism.[49]

1.2 Techniques

1.2.1 Dynamic Light Scattering

DLS is a technique which uses monochromatic scattered light to determine the size distribution of small particles in a suspension. Light from a laser will hit small particles in suspension and scatter light in all directions according to Raleigh Scattering. Based on the time dependent fluctuations of scattering intensity, the particle size can be calculated using the diffusion coefficient. DLS is a reliable technique for measuring particle size of proteins, polymers, and nanoparticles as long as the particle size is small compared to the wavelength of light.

Malvern Zetasizer Nano ZS Dynamic Light Scattering and Zeta Potential analyzer was used to measure the diameter of fibronectin protein in solution. Non-invasive backscattering optics were used for greater accuracy when determining particle size.

Light that enters a sample containing particles in solution will scatter from the random movement of particles known as Brownian motion. A fast photon counter detects time dependent fluctuations in scattered light caused by Brownian motion. Fluctuations are related to the rate of diffusion of the particle or protein in the solvent, which in turn is related to the hydrodynamic radius. Based on the intensity of light and the scattering angle, the radius, and diameter of a particle can be calculated using the Diffusion equation and Stokes-Einstein equation. Using the first order function of single exponential decay, the decay rate can be converted to solve for the diffusion constant using **equation 1.1**:

$$(1.1) \quad D = \frac{\Gamma}{q2}$$

where D is the diffusion constant, Γ is the decay rate, and q is the magnitude of the scattering vector of light given by **equation 1.2**

$$(1.2) \quad q = \frac{4\pi n}{\lambda} \sin(\theta/2)$$

where n is the index of refraction of light, λ is the wavelength of light, and θ is the scattering angle). Finally, the hydrodynamic radius (r_h) is calculated using **equation 1.3**

(1.3) $$r_h=\frac{kT}{6\pi\eta D}$$

(where k is Boltzmann's constant, T is the temperature, η is the solvent viscosity, and D is the diffusion constant).[50]

Detecting changes in radius or diameter of proteins could correlate to structural changes in the secondary or tertiary structure. A protein which has a larger hydrodynamic radius, compared to the same protein with a smaller radius, will have more of its structural binding sites exposed. For example, a metal binding protein may become coiled up due to interactions with the solvent, concealing a binding site to either a metal, or another protein. Interactions with a solvent may also expose binding sites that were previously concealed, leading to an increase in protein functional activity. Potential applications in using DLS include confirming changes in protein structure due to solvent interactions or thermal denaturation.

DLS is a technique which uses monochromatic scattered light to determine the size distribution of small particles in a suspension. Light from a laser will hit small particles in suspension and scatter light in all directions according to Raleigh Scattering. Based on the time dependent fluctuations of scattering intensity, the particle size can be calculated using the diffusion coefficient. DLS is a reliable technique for measuring particle size of proteins, polymers, and nanoparticles as long as the particle size is small compared to the wavelength of light.

Malvern Zetasizer Nano ZS Dynamic Light Scattering and Zeta Potential analyzer was used to measure the diameter of ECM protein fibronectin of choice in solution. Non-invasive backscattering optics is used for greater accuracy when determining particle size.

1.2.2 Extended X-ray Absorption Fine Structure

EXAFS is a technique used to measure coordination number, number of neighboring atoms, and the atomic distance between central and neighboring atoms. EXAFS works on the principle of x-ray absorption. When x-ray energy hitting an atom is above the ionization threshold, electrons will be knocked off of the atom and scattered. The interaction of scattered

electrons with the scattered waves from surrounding, or neighboring atoms, will cause oscillations. Constructive and destructive interference between scattered electrons and backscattered waves from neighboring atoms cause local maxima and local minima in the absorption spectra, respectively.[51]

The probability of x-ray absorption occurring as it passes through a material is given by the linear absorption coefficient (μ) in the **equation 1.4**

(1.4) $I=I_o e^{-\mu t}$

In this equation, I is the intensity of the transmitted beam, I_o is the original intensity of the monochromatic x-ray, and t is the thickness of the sample. The linear absorption coefficient is heavily dependent on atomic number and incoming x-ray energy, as shown in the **equation 1.5**

(1.5) $\mu \sim \rho Z^4/AE^3$

This relationship is used to derive the EXAFS fine structure function χ(E), given by **equation 1.6**

(1.6) $\chi(E)=[\mu(E)-\mu_o(E)]/\Delta\mu_o(E)$

Here, $\mu_o(E)$ is the background absorption coefficient, and $\Delta\mu_o(E)$ is the jump in absorption at the threshold energy level. Ultimately, the EXAFS fine structure equation is used to derive a function relating atomic distance to energy. The Fourier transformation is a mathematical operation used to interpret the frequency signals, caused by energy oscillations, into different constituent frequencies. Fourier transform creates a radial structure function, of which higher magnitudes indicate atomic bonding radius.[51]

EXAFS was run on ECM protein fibronectin to interpret changes in the coordination distance with zinc caused by pH. The experiment was performed at Brookhaven National Laboratory at the National Synchrotron Light Source on Beamline X3A.

1.2.3 X-ray Fluorescence

The principle of X-ray fluorescence (XRF) relies on ionization of a principle atom when exposed to x-ray radiation. X-ray radiation must have enough energy to eject one of the electrons. This energy is known as ionization energy. The removal of the ejected electron leaves

the atom in an unstable state. Electrons from the higher orbitals fall to lower orbitals to fill in the hole left behind from the ejected electron. In falling to the lower energy state, energy is released in the form of a photon which has equivalent energy of the energy difference between the two orbitals. Therefore, the atom is releasing radiation in the form of radiation, known as x-ray fluorescence. The radiation emitted is characteristic for each element. Thus, elemental composition can be detected based on the energy of the radiation emitted.[52]

Radiation is detected on the principle that an incoming photon will ionize a large number of detector atoms with a proportional amount of charge to the energy of the photon. Thus, energy difference in photons are converted to charge differences, which allows us to distinguish between elements. The charges are collected and the process repeats until the next photon ionizes the detector atoms.[52]

Synchrotron Radiation X-Ray Fluorescence (XRF) experiments were conducted at Beamline X26A, located at the National Synchrotron Light Source (NSLS), Brookhaven National Laboratory (Upton, NY). The x-ray microprobe was operated in monochromatic mapping mode under 9-11 keV tuned by a Si (111) channel cut monochromator, which is non-destructive to the sample. Samples were mounted on the stage 45° toward the incident photon beam).[53] The energy dispersive 9 element Ge detector was at 90° to the beam to eliminate backgrounds from Compton scattering.

1.2.4 Raman Spectroscopy

Raman spectroscopy is a fingerprinting technique which relies on vibrational modes between covalent bonds. It is commonly used in chemistry to identify molecules based on observed functional groups. The principle of Raman spectroscopy relies on monochromatic light from a laser source which, when exposed to a sample, will interact with molecular vibrations in covalent bonds and cause the energy of the laser photons to be shifted either up or down. The shift in energy will give information about the vibrational modes of the system.

In short, a sample is exposed to monochromatic laser light, and radiation from the illuminated spot is collected through a lens and monochromator. Raleigh scattered radiation (which is elastic, having the same energy as the laser light) is filtered out and the remaining light is sent to a detector. The inelastic radiation collected is caused by Raman scattering, which

means these photons have a differing energy from the incident photon. Only a small fraction (1 in 10 million) of the photons which are scattered are inelastic, making Raman scattering a very weak signal. The use of photomultiplier tubes in detectors are used to amplify the weak signals. The intensity of the Raman signal is proportional to the electric-dipole polarizability of the atoms. In short, this is dependent upon the dipole present in the molecules. Each covalent bond has a unique dipole which corresponds to a unique Raman intensity. Therefore, non-symmetric functional groups can be identified by their intensities using Raman spectroscopy.

Chapter 2 : Effects of Micronutrient Zinc on Extracellular Matrix at the Protein Level

Abstract

The potential effects of micronutrients zinc and copper on ECM protein fibronectin were investigated using a series of characterization techniques including dynamic light scattering (DLS), hydrophobic fluorescence probes, and extended x-ray absorption fine structure (EXAFS). Subsequent effects on cell morphologies and migration of osteoblasts and osteosarcoma cells were tested. Size of full length fibronectin in solution was found to be influenced by both pH and interaction with Cu and Zn. More specifically, the fibronectin fragment known as anastellin, which is responsible for fibril formation, was found to potentially interact with Zn according to our EXAFS study. Also, interaction with Zn was found to influence exposure to hydrophobic core of anastellin in solution. Theses interactions of fibronectin with zinc show potential to influence ECM formation, affecting quality of bone matrix. Zinc was also found to influence morphology and decrease migration in osteoblasts and osteosarcoma. Migration is another part of bone matrix formation which was potentially affects ECM and bone quality.[54,55] More experiments on structural interactions of fibronectin are necessary to determine the full effect of zinc interactions with fibronectin. Fibronectin conformational changes caused by zinc together may play a role in motility, healthy bone and ECM formation, and cancer metastasis.

2.1 Introduction

2.1.1 ECM Synthesis, Assembly, and Mineralization

The organic component of bone is comprised of mostly collagen, which is produced by osteoblast cells as part of their extracellular matrix (ECM). The structure of collagen fibrils and mineralized collagen are shown in **Figure 1.1**. The ECM is a connective network that provides structural support for the cells. In particular, the ECM of osteoblast cells has a significant impact on the health and integrity of bone tissue. Important ECM proteins produced by osteoblast control cellular functions such as mineralization, motility, and cell adhesion. Besides collagen, two other important proteins involved in ECM synthesis and assembly are matrix metalloproteinase II (MMP-2), and fibronectin.

1.1.3 Fibronectin

The primary component of bone ECM is collagen. The ECM provides a supportive microenvironment for cells to adhere. Cells adhere to collagen through integrins, which are

membrane bound proteins which bind indirectly to collagen. A non-collagenous protein produced by cells known as fibronectin is responsible for linking integrins to a binding site on collagen. Fibronectin is responsible for multiple cell behaviors including adhesion, migration, gene expression, and maintenance of cell morphology. The structure of fibronectin becomes very important when discussing the binding affinity to other ECM macromolecules such as collagen.[8] Fibronectin exists as a 440kDa glycoprotein containing two similar, but not identical polypeptide chains linked together by a disulfide bond at the C terminal. Each monomer is between 220 and 250-kDa in size.[9]

Fibronectin plays an important role in tissue repair, and homeostatic wound healing. There is a distinct difference between soluble fibronectin found in bodily fluids, and fibronectin found attached to extracellular matrices. Soluble fibronectin is known as plasma fibronectin, and is found in blood plasma and produced by liver cells. Insoluble, cellular fibronectin is a major component of the ECM, secreted by numerous cells throughout the body. Plasma fibronectin has a coiled structure, hiding many of the binding domains that cells use to attach. Cellular fibronectin is partially uncoiled, leaving the binding domains exposed for the cells to utilize.[9]

Bone cells attach to the ECM through transmembrane receptors called integrins. A diagram of cell adhesion to collagen via fibronectin-integrin adhesion is seen in **Figure 2.1**.

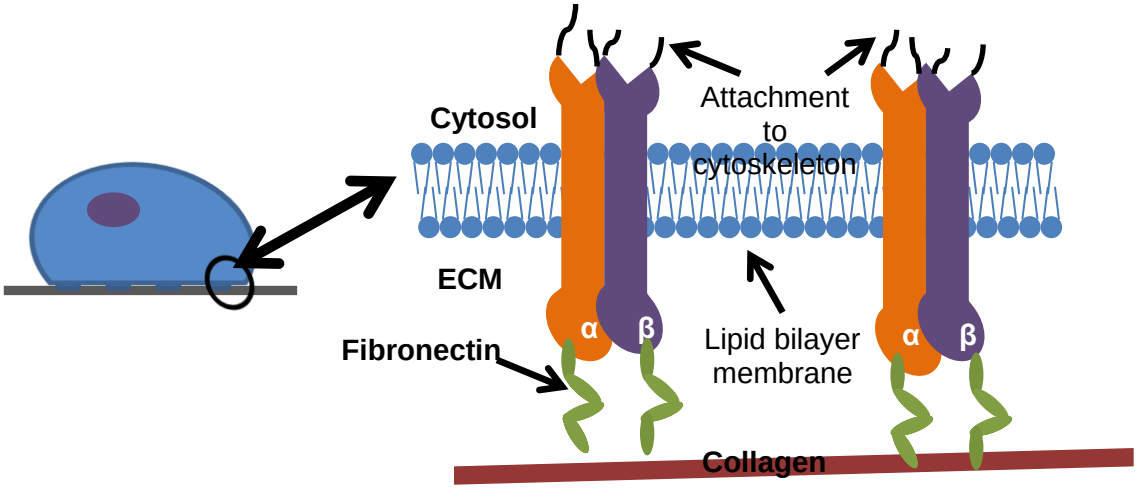

Figure 2.1. Cell adhesion to collagen is illustrated via fibronectin binding domains.

Although the structure of fibronectin consists of two subunits, it is also composed of a series of independently folding type I, II and III subunits. There are multiples of the type I, II, and III subunits throughout the complex structure of fibronectin. A series of subunits forms functional domains; of which, each is specialized to bind to specific matrix proteins, cell membrane receptors, or integrins.[3] For example, the type III connecting segment (IIICS) of fibronectin is the major binding site for the $\alpha_4\beta_1$ and $\alpha_4\beta_7$ integrins. In **Figure 2.2** below, the structure of a single polypeptide chain from fibronectin is depicted from N-terminus to C-terminus. The disulfide bond bonding the two chains is located at the C-terminus. In this figure, subunits I, II, and III are represented by circles, hexagons, and squares, respectively.[10]

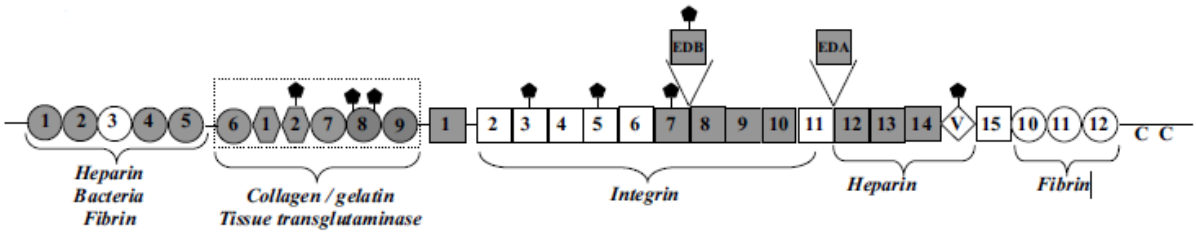

Figure 2.2. Structure of cellular fibronectin taken from Graille et al. Gray regions represent fragments with solved structures. Diamonds depict glycosalation sites. Interaction sites are listed below the schematic.[9]

2.1.1 Osteosarcoma

Osteosarcoma is the most common primary bone malignancy. Unlike other tumors, osteosarcoma is usually found in the extremities of children and adolescents.[56] Osteosarcoma is characterized by aggressive growth and a high propensity to form metastases. At the time of diagnosis approximately 10-20% of patients will have metastatic lesions, with the most common sites being bone and lung. With traditional treatment methods, patients with localized osteosarcoma of the extremity have a survival rate of approximately 70%. However, this rate drastically decreases with patients who have metastatic osteosarcoma.[57] Therefore, morbidity is dependent on the existence of metastatic lesions, not the primary tumor.

Recently osteosarcoma has been proposed as a differentiation disorder. A recent study by Thomas et al. shows that terminal osteoblast differentiation is disrupted in the case of osteosarcoma. Interestingly, one of the mediators of terminal differentiation in osteoblasts is the runx2 transcription factor, which was previously mentioned to be influenced by zinc concentrations.[42]

Understanding the mechanism of metastasis is important for developing an effective therapy for combating the spread of cancers. Metastasis is the last step malignant tumors take in the process of tumorogenesis. The metastatic process occurs in four distinct steps beginning with a primary tumor and ending with metastatic tumors populating distant organs or bodily tissues. Initially, the cell will detach from the primary tumor, via the epithelial mesenchymal transition (EMT). Next, the cell or cells will migrate through the neighboring stroma tissue to the circulatory system. From there, the cell will pass through the bloodstream and finally attach to some distant organ or tissue and begin to grow cancerous tissue. In the case of metastatic osteosarcoma, malignancies are often seen in the lungs and bone.

1.1.13 Zinc and Fibronectin

Recently, the 45-kDa GBD of fibronectin was analyzed and tested for structural reorganization upon interactions with zinc.[9] Since fibronectin and integrins receptors play a crucial role in the formation and adhesion to the ECM, studying how fibronectin interacts with collagen is essential for knowing the mechanism of cell-ECM attachments. Graille, et al. performed a study on the effects zinc has on the structure of GBD and its subsequent affinity for collagen.[9] Experiments confirmed that zinc induces a structural adjustment in the GBD of

fibronectin. Similar to other zinc containing metallic proteins, the GBD was found to contain multiple zinc binding sites. Zinc was found to drastically influence the quaternary, tertiary, and secondary organization of the GBD. However, this experiment used zinc concentrations that were much higher than physiological, cellular concentration levels. Zinc concentrations in the millimolar range were used to study the structure of the GBD. Physiological zinc concentrations in the cells range from 15 to 50 micromolar. Structural effects of zinc on the GBD fragment of fibronectin must be studied at physiologically relevant concentration in order to fully understand the mechanism of a zinc induced structural change.[9]

Zinc binding was shown to change the structure of the GBD of fibronectin but also change the fragment's affinity for collagen. Graille et al. studied GBD affinity to collagen while varying zinc concentration using fluorescence anisotropy titrations.[9] The results showed that zinc dissociates collagen from GBD. As zinc concentration increased up to about 300μM, GBD and collagen dissociation increased. This experiment did use physiological relevant concentrations of zinc, as concentrations under 50μM were examined. Graille et al. suggests that structural rearrangements induced by zinc binding inhibit the binding of collagen to GBD.[7] Clearly zinc has a structural effect on GBD and zinc deficiency will lead to dissociation between collagen and fibronectin.[9]

2.2 Objective

The goal of this study was to gain a better understanding of the roles of Cu and Zn in their interactions with ECM protein fibronectin and its potential roles in cell motility, healthy ECM and bone formation, and cancer metastasis. This was to be achieved by using techniques to study FN protein size and conformation in the presence of Cu and Zn. Also, morphological characteristics and cell speed were to be analyzed to study the effects of Zn on cell migration. The aim of this study was to support evidence of the interaction of Zn and FN, and to show its potential effects of ECM formation and cell migration. Work performed by Dorst et al. showed zinc as a trace metal which impacts osteoblast migration and differentiation, inhibiting the ability to form calcifications and migrate.[54,55] In this project, we scaled the results of osteoblast interaction with zinc down to the protein level and examined potential effects of zinc on ECM protein fibronectin. Also, effects of zinc on cell migration were repeated with osteoblasts and then applied to an in vitro osteosarcoma model. Studying trace metal interactions with ECM

proteins involved in the mineralization process can help understand differences in healthy mineralized tissue and cancerous osteosarcoma. Metastasis is an important part of the development of cancer. Therefore, understanding how ECM proteins interact migration will help better understand the metastasis process. This work aimed to investigate the effects of trace metals Zn and Cu on bone formation, specifically, with regards to the interaction of FN with trace metals.

2.3 Materials and Methods

2.3.1 Fibronectin Particle Size

Commercially available lyophilized fibronectin (FN) powder from bovine plasma were used to test the effects of pH and zinc concentration on protein particle size using dynamic light scattering (DLS). Malvern Zetasizer Nano ZS Dynamic Light Scattering and Zeta Potential analyzer was used to measure the diameter of FN in solution. Non-invasive backscattering optics is used for greater accuracy when determining particle size. All particle size measurements were performed at the standard room temperature setting of 25^{o}C, so that denaturation of the protein was not an issue. Increasing concentrations of $ZnCl_2$ or $CuCl_2$ were added into FN solutions, keeping protein concentration constant while analyzing particle size.

The protein concentration of fibronectin (440kDa) used to measure particle size was 0.04mg/mL. Fibronectin samples were analyzed for particle size in both HPLC water in MES buffer at pH5.5, MES buffer at pH6.5 and HEPES buffer at pH7.4, and in a buffered tris glycine solution at pH7.4. Fibronectin:Zn^{2+} ratios of 1:8 and 1:25 were analyzed for particle size and compared to the control sample of no $ZnCl_2$ added. The protein concentration of FN (440kDa) used to measure particle size was 0.04mg/mL. Initial measurements were performed with no ions in buffered HPLC water with 10mM HEPES buffer at pH7.4, 10mM MES buffer at pH6.5, or 10mM MES buffer at pH5.5. Next, two zinc concentrations were added to FN at 1:1 and 1:20 molar ratios to determine the effects of Zn and pH on FN particle size.

Next, fibronectin samples were analyzed for particle size a buffered tris glycine solution. Tris glycine buffer at pH7.4 is used in protein electrophoresis, and is thought to produce a stable protein conformation. Fibronectin:Zn^{2+} ratios of 1:8 and 1:25 were analyzed for particle size and compared to the control sample containing no $ZnCl_2$ added.

2.3.2 ANS Fluorescence of Anastellin

In order to specifically study fibronectin interactions with divalent cations Zn and Cu, we chose a fragment of fibronectin known as anastellin or FN-III-1C. Since fibronectin is such a large protein, anastellin fragment was chosen because it is responsible for polymerization of fibronectin into fibrils. Anastellin is the carboxy-terminal fragment of the first FN3 domain in fibronectin. This fragment has been shown to bind to whole length fibronectin to help unravel its structure and form ECM fibrils.[58] Since a previous study by Graille et al. on a different fragment of fibronectin, the gelatin binding domain, have shown interaction with zinc to cause conformational changes to the protein structure, we sought to examine any potential changes in structure of anastellin with its interaction with zinc or copper.[9] If Zn or Cu influence anastellin structurally, they may ultimately be influencing fibronectin fibril structure, affecting ECM quality.

8-Anilinonaphthalene-1-sulfonate (ANS) is an extrinsic fluorescent probe which has been extensively used to monitor protein conformation. ANS binds non-covalently to proteins and produces and dramatic enhancement in fluorescence and shift in emission maximum to shorter wavelengths when in a non-polar environment. The effects of twisted intramolecular charge transfer and solvent relaxation are responsible for the low fluorescence signal when ANS is in hydrophilic environments. When ANS enters a non-polar environment, like that of a hydrophobic protein core, the charge transfer and relaxation effects are diminished and the fluorescence signal is increased. The maximum excitation wavelength for ANS is 375nm and its emission maximum wavelength is about 495nm when in a hydrophobic environment. The maximum emission wavelength is shifted to around 525nm when in a hydrophilic polar solvent.

50µM anastellin and 50µM ANS were used in accordance to the experiments performed by Gee et al.[59] Triplicate 200µL samples in 10mM buffer were prepared in 96 well plates with no trace metals, with 100µM $ZnCl_2$, and with 100µM $CuCl_2$. Samples were prepared at pH5.5 in MES buffer, pH6.5 in MES buffer, and pH7.4 HEPES buffer. A set of control samples containing 50µM ANS in buffer only were prepared to determine background ANS fluorescence. After 15 min incubation time at room temperature, samples were read in a Tecan Infinite M200 plate reader. Excitation wavelength was set to 375nm and emission wavelength was read at hydrophobic maximum of 495nm. Average fluorescence at 495nm maximum emission

wavelength is corrected by subtracting the background fluorescence emission of ANS in buffer with no protein. Finally, fluorescence is normalize to neutral pH 7.4 with no addition of trace metals.

2.3.3 EXAFS of Anastellin Zinc and Copper Interactions

Samples of anastellin (Fn-III-1C) were prepared for EXAFS in aqueous solution at 250µM in 20mM MES or HEPES buffer with either 500µM CuCl2 or 500µM ZnCl2 with 20% glycerol. Anastellin, $ZnCl_2$, and $CuCl_2$ stock solutions were prepared and diluted into buffer of appropriate pH. Finally glycerol was added to each sample prior to freezing at -80oC. A total of 6 samples containing Anastellin were made: MES pH5.5 with Zn, MES pH6.5 with Zn, HEPES pH7.4 with Zn, MES pH5.5 with Cu, MES pH6.5 with Cu, HEPES pH7.4 with Cu. Equivalent samples without protein were synthesized and tested.

X-ray absorption spectroscopy data was collected at beamline X3B of National Synchrotron Light Source (NSLS) at Brookhaven National Laboratory. Zn K-edge XAS (X-ray absorption spectroscopy) data were collected over an energy range of 9458 to 10421 eV. Cu K-edge XAS was collected over an energy range of 8779 to 9741 eV. Both Zn and Cu data were collected using a 31 element Ge detector. A photo graph of the experimental setup is shown in **Figure 2.3**. Samples remained under vacuum at temperatures of 20K. Prior to running an EXAFS scan, the samples were transferred to titanium sample holders backed with Kapton tape and frozen in liquid nitrogen. For each sample 3-6 scans were collected. Data analysis were performed with Athena and peak fitting were performed with Artemis software.

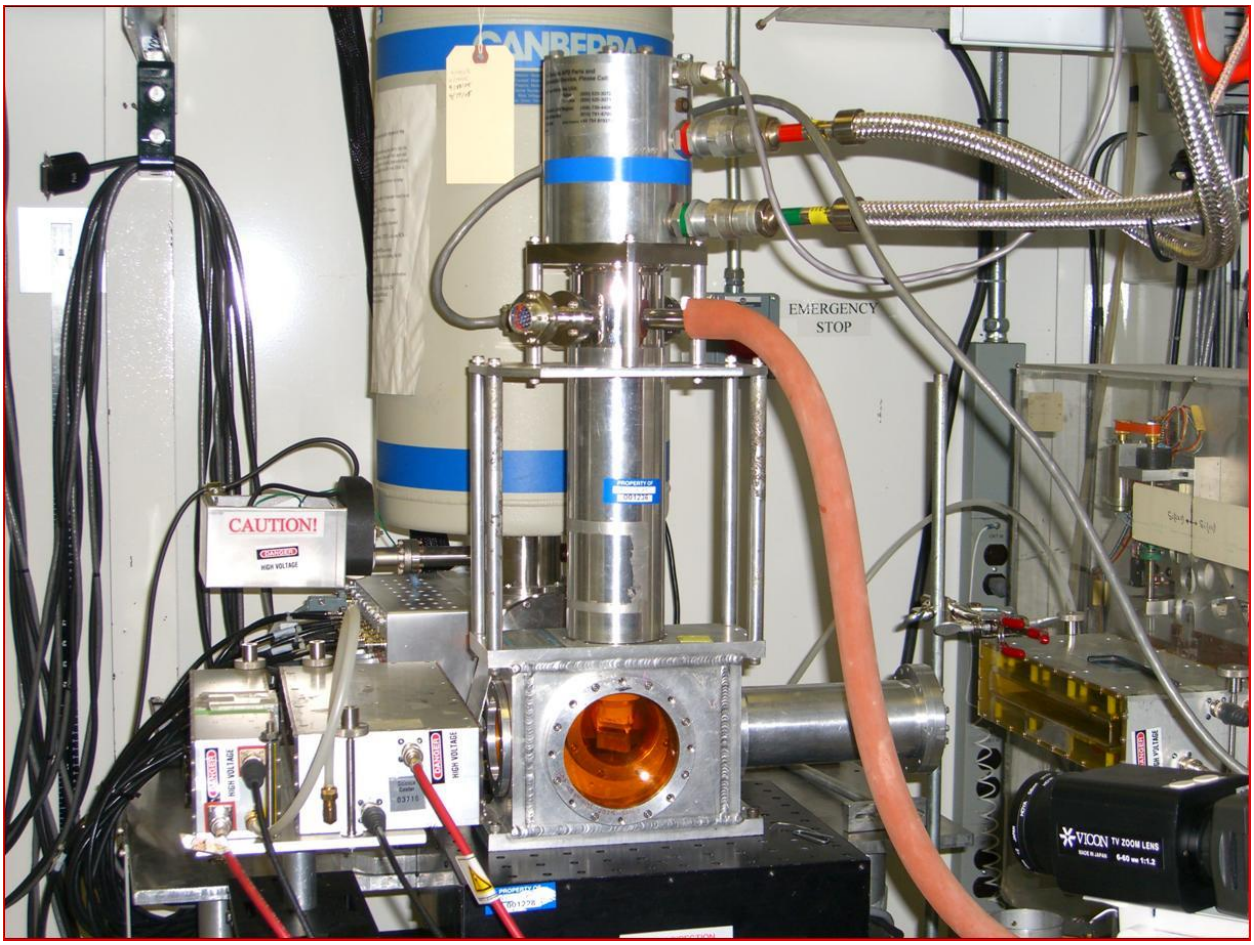

Figure 2.3 Photograph showing experimental EXAFS setup at X3B beamline located at Brookhaven National Laboratory's NSLS. Protein samples are frozen on Kapton tape sample holders and placed inside low temperature chamber where they are exposed to synchrotron x-ray radiation. X-ray absorption is detected through the 31 element Ge detector located behind the chamber. Photograph taken from X3B website (http://csb.case.edu/x3b-photos.html)

2.3.4 Immunofluorescence staining of Fibronectin

Immunofluorescent staining was performed on MC3T3-E1 subclone 4 and 24 using standard culture medium. Anti-fibronectin, anti-EDA, and anti-β1 integrin primary antibodies were used along with a fluorescent secondary antibody. Figure 20 shows fibronectin stained images of MC3T3-E1 subclone 4 and 24 cells 24 hours after plating at 20x magnification. Figure 21 shows staining specific for the EDA segment of fibronectin on MC3T3-E1 subclone 4 and 24 cells on day 7. In Figure 22, immunofluorescent images of MC3T3-E1 subclone 4 and 24 cells, stained for β1 integrins, 7 days after induction of mineralization are shown. Standard culture medium, without varying zinc or copper concentrations were used to culture cells.

Immunofluorescent staining was performed on MC3T3-E1 osteoblast-like cells on fibronectin, the specific EDA region of fibronectin, and β1 integrin. The EDA region of fibronectin was targeted in this experiment because it is only present in cellular fibronectin, and absent in plasma fibronectin.[60] The presence of EDA region of fibronectin was shown to enhance integrin binding compared to fibronectin peptides lacking the EDA region.[61] Two subclones of MC3T3-E1 cells were stained to compare any differences between the strongly mineralizing subclone 4 and weakly mineralizing subclone 24. Primary antibodies specific for the protein, or integrin of selection were used in conjunction with fluorescent secondary antibodies. MC3T3-E1 cells were cultured in MEM alpha supplemented with 10% fetal bovine serum (FBS) and 1% Penicillin-streptomycin solution. Cells were plated at low density, 5,000 cell/cm^2 and imaged 24 hours after plating for fibronectin staining. Cells were plated at high density 50,000 cells/cm^2 and imaged after 7 days for EDA and β1 integrin staining. After cells were plated, fixed, and incubated with the antibodies, they were visualized under the Olympus IX51 inverted fluorescent microscope to collect images and observe any differences.

2.3.5 Cell Morphology

Cell morphology characteristics in vitro were quantified through immunofluorescence staining. MC3T3-E1 murine preosteoblasts and MG-63 human osteosarcoma cells were plated at a density of 5,000 cells/cm^2 on tissue culture polystyrene in culture medium for time periods of 4, or 24 hours. MC3T3-E1 cells are grown in growth medium containing MEM alpha with 10% fetal bovine serum (FBS) and 1% Penicillin-streptomycin solution. MG-63 cells were grown in growth medium containing high glucose DMEM (4.5g/L glucose) with 10% FBS, and 1% Penicillin-streptomycin solution. Culture medium containing GM with no added Zn, GM +15μM $ZnCl_2$, or GM +50μM $ZnCl_2$ representing adequate zinc, moderate zinc, and high physiological zinc levels were used for both cell types. After cells were fully attached to the surface and growing in the culture medium, they were fixed by gently removing the culture medium and treating cells with a solution of 4% formaldehyde for 15 minutes. The cell membranes were then permeabilized through treatment with 0.4% Triton X-100 for 7 minutes. Finally cells were fluorescently labeled using Alexa Fluor 488 Phalloidin, a fluorescent label which selectively stains the filamentous actin in the cell. Filamentous actin are microfilament proteins in the cells which provide structural support to the cell and are used in important cellular functions such as motility and cell division. Since actin fibers provide skeletal-like support to the cell, it is a useful parameter for measuring cell area. Alexa Fluor 488 Phalloidin provides a green fluorescence signal with excitation and emission signals at 495nm and 518nm, respectively. Cells were also stained with 4',6-diamidino-2-phenylindole (DAPI), a blue fluorescence nuclear dye which strongly binds to adenine and thymine rich regions of DNA. DAPI has excitation and emission signals at 358nm and 461nm, respectively.

Parameters such as cell spreading area, circularity, and roundness were analyzed in ImageJ through the fluorescent images captured of the cells using the Olympus LX51 inverted microscope using filters for both green and blue fluorescence. Compiled color images of both fluorescence signals were analyzed. Spreading area was analyzed by converting fluorescent images to binary form then calculating the area of a singular cell's green fluorescence signal in ImageJ and converting the area from $pixels^2$ to $micrometers^2$. The area of cellular networks (multiple cells touching) was not considered. Circularity and roundness of each cell was then calculated by analyzing the binary images in ImageJ. Circularity and roundness of a cell attached to a surface are discrete ways of observing a cell's locomotion. When cells are motile,

they will be more polarized in the direction of movement. Cells that are less motile will be inherently more circular and rounder compared to highly motile cells. Circularity is a mathematical ratio given by **equation 2.2**

(2.2) $\text{Circularity} = 4\pi(\text{area}/\text{perimeter}^2)$

A perfect circle has circularity equal to 1, and the circularity of an object as it approaches the morphology of a straight line approaches 0. Roundness is a mathematically similar parameter to circularity which is shown in **equation 2.3**

(2.3) $\text{Roundness} = 4(\text{area})/[\pi*(\text{major axis})^2]$

A circle is perfectly round with roundness equal to 1. As an object gets less and less round, the major axis length increases and its roundness approaches zero.

2.3.6 Two-Dimensional Migration Tracking

Next, migration of MC3T3-E1 murine preosteoblast cells, MG-63 human osteosarcoma, and 4T1 murine breast cancer cells were tested using a two-dimensional manual tracking assay. MC3T3-E cells were grown in growth medium containing MEM alpha supplemented with 10% fetal bovine serum (FBS), and 1% Penicillin-streptomycin solution. MG-63 cells were grown in growth medium containing high glucose DMEM (4.5g/L glucose) with 10% FBS, and 1% Penicillin-streptomycin solution. 4T1 cells grown in growth medium containing low glucose DMEM (1g/L glucose) supplemented with 10% fetal bovine serum (FBS), and 1% Penicillin-streptomycin solution were cultured on tissue culture polystyrene dishes. A confluent plate was detached through incubation with 0.05% trypsin for 5 minutes, counted, and plated at a concentration of 7,500 cells/cm^2 in 35mm tissue culture treated polystyrene dishes. After attachment for 18 hours overnight, culture medium was replaced with a CO_2 dependent culture medium (CIM) with no added Zn, 50 µM added Zn, or 100 µM Zn added Zn. Using a migration chamber set to 37 °C, phase contrast images of 4T1 cells were captured every 2 minutes for 2 hours. Images were analyzed using the Manual Tracking plugin in ImageJ. Each individual cell is tracked by hand, a total of between 30-40 cells per field of view are tracked. A total of 3 experiments were performed for each Zn condition. Average cell speed is reported in µm/min for each condition.

2.4 Results

2.4.1 Fibronectin Particle Size

Particle size of FN was first examined in HPLC water containing 10mM HEPES at pH7.4, 10mM MES at pH6.5, and 10mM MES at pH5.5 to capture the effects of pH on FN size. As increasing concentrations of Zn were added to the solution, the effects of Zn interaction on particle size were captured at the 3 different pHs. This was accomplished by addition of 1:1 and 1:20 molar ratios of FN:Zn. An average of 3 different particle size measurements were taken for each experimental condition. Average particle size measurements are reported in **Figure 2.4**. At pH 7.4, particle size in solution of FN, FN:Zn 1:1, and FN:Zn 1:20 molar ratios were 42.7, 40.2, and 38.8 nm, respectively. Overall, this shows little change in with addition of Zn at neutral pH. However, when pH is decreased to 6.5, particle size of FN, FN:Zn 1:1, and FN:Zn 1:20 molar ratios were 44.6, 67.7, and 31.5 nm, respectively. At pH 5.5, particle size of FN, FN:Zn 1:1, and FN:Zn 1:20 molar ratios were 49.0, 52.1, and 74.1 nm, respectively. Compared to the low range, and stable particle size measurements at pH 7.4, when pH is lowered into the acidic range of 6.5 and 5.5, addition of Zn has effects of changing particle size, either lower or higher. With no addition of Zn, particle size at pH 7.4, 6.5, and 5.5 is 42.7, 44.6, and 49.0, respectively. This indicates an increase in size with increasing acidity. When Zn is added at pH 7.4, there is little decrease in size, which does not affect it significantly. However, when Zn is added at acidic pH 5.5, there is a large increase in size from 49.0 to 74.1 nm at 1:20 molar ratios. Overall, the data indicates a conformational change in FN at lower pH which may be further affected by protein interactions with Zn.

Particle size distributions of fibronectin related to zinc concentration in glycine buffer at pH 7.4 are shown in **Figure 2.5**. Concentrations of 0.04mg/mL fibronectin (~440kDa) were optimized for instrumental conditions. Relative molar concentrations were 0.091μM FN. FN particle size was measured in 10mM glycine buffer at pH 7.4 using a concentration of 40μg/mL FN. The effect of zinc on particle size was investigated by testing particle size with no added zinc, 1:8 ratio FN:Zn, and 1:25 ratio FN:Zn. Particle size in relation to zinc concentrations are reported in **Table 2.1.** According to the results, FN size in solution decreases from 19.5nm, 16.3nm, and 15.9nm as 0, 8, and 25 molar equivalents of zinc are added to solution. As zinc increases, FN particle size in solution is decreasing. Also, the distribution range is decreasing with added zinc in solution, as apparent by the narrowing histogram peak. Together, this would suggest an interaction between zinc and FN protein molecules.

Compared to the interaction with Zn, the interaction of FN with Cu is noticeably different, especially at pH5.5. According to the data shown n **Figure 2.6**, interaction with Cu at pH 7.4, and pH 6.5 show little effect on size. At pH 7.4 particle size of FN, FN:Cu 1:1, and FN Cu 1:20 are 42.7, 36.8, and 36.8 nm, respectively. Compared to pH 6.5, the sizes of FN, FN:Cu 1:1 and FN:Cu 1:20 are 44.6, 39.1, and 32.3 nm, respectively. At neutral pH of 7.4 and at slightly acidic pH of 6.5, there is a trend of Cu decreasing size of FN in solution. However, at the more acidic pH 5.5, Cu tends to increase FN size. Sizes at pH 5.5 of FN, FN:Cu 1:1, and FN:Cu 1:20 are 49.0, 335.8, and 160.7 nm, respectively.

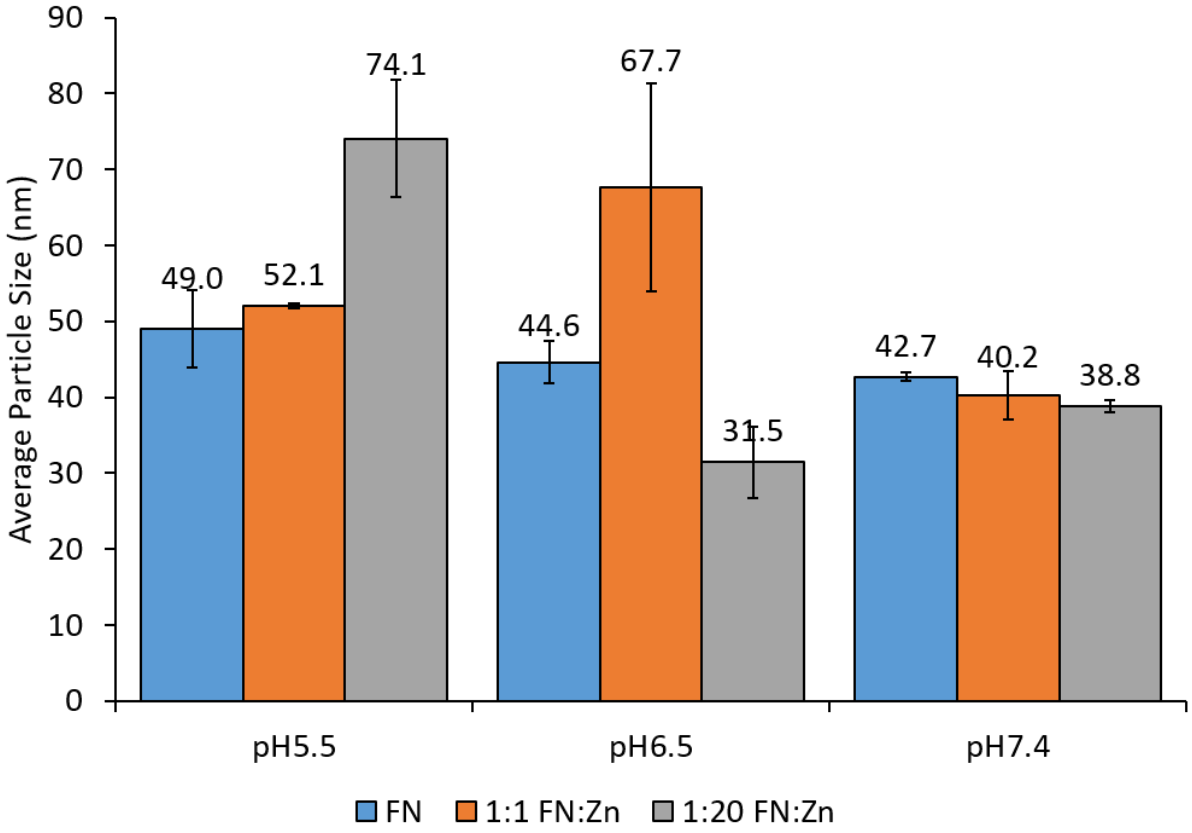

Figure 2.4. Particle size measurements of FN, measuring interaction with Zn at pH 7.4, pH 6.5, and pH 5.5. Average particle size measured from 3-5 independent experiments per condition.

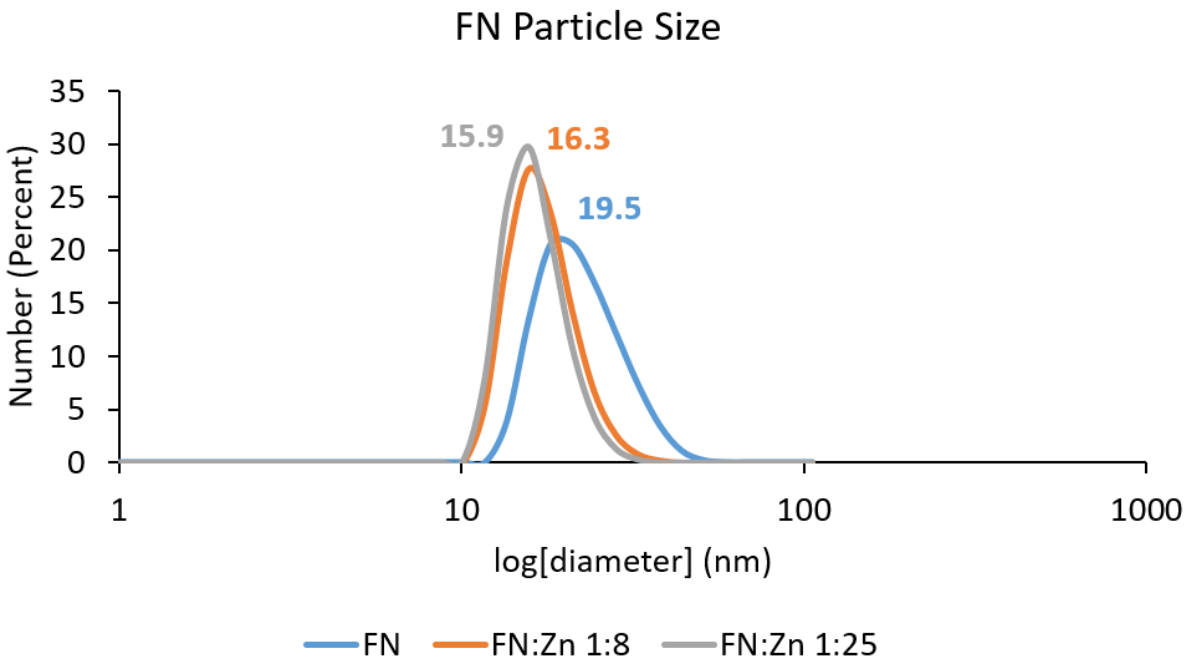

Figure 2.5. FN particle size measured in glycine buffer at concentration of 40 µg/mL with increasing amounts of Zn added to solution. Size of FN, FN:Zn 1:8, and FN:Zn 1:25 are 19.5, 16.3, and 15.9 nm, respectively. Representative particle size histogram taken from 3 independent experiments.

Sample	Peak (size nm)
FN in glycine buffer	19.5
FN:Zn 1:8	16.3
FN:Zn 1:25	15.9

Table 2.1. Particle size of FN in a solution of 10mM glycine buffer with increasing zinc concentrations.

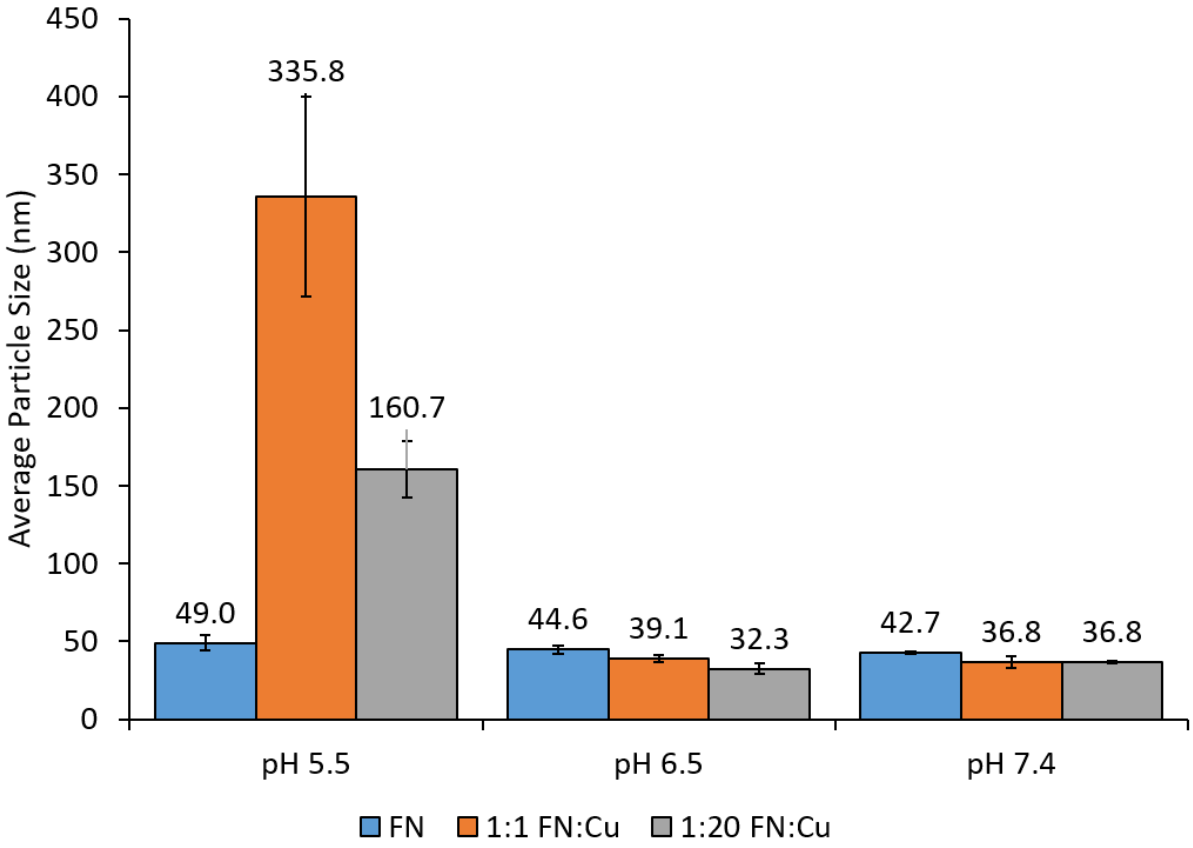

Figure 2.6. Particle size measurements of FN, measuring interaction with Cu at pH 7.4, pH 6.5, and pH 5.5. Average particle size measured from 3-5 independent experiments per condition.

2.4.2 ANS Fluorescence of Anastellin

ANS fluorescence results were first successfully tested against pH without any trace metals in the protein-buffer mixture. Fluorescence intensity was first measured using only ANS and buffer with the recommended excitation wavelength of 375nm. Next, ANS fluorescence with anastellin were tested using the same concentrations found in the experiment performed by Gee et al.[59] ANS Fluorescence of 50 µM anastellin in pH 7.4 HEPES buffer, pH6.5 MES buffer, and pH5.5 MES buffer with and without the addition of 100 µM $ZnCl_2$. Results normalized to anastellin at pH 7.4 HEPES buffer. As seen in **Figure 2.7** there is a clear trend of increasing fluorescence with decreasing pH. The acidic environment allows for increased binding of ANS to the hydrophobic protein cores resulting in an increase in fluorescence signal. This trend is similar to that seen in Qadeer et al. where an increase in fluorescence signal of ANS is seen with a decrease in pH and attributed to a loss in secondary structure of the protein.[62] Compared to the fluorescence signal of protein free samples, the signal in samples containing anastellin is 3 to 4 times greater (data not shown). Average ANS fluorescence of the interaction with anastellin at pH 6.5 and pH 5.5 are 110% and 143% of anastellin at pH 7.4, respectively. The increase in fluorescence intensity at pH 5.5 compared to pH 7.4 is considered statistically significant ($p<0.01$).

Next, to study the effects of trace metal zinc on the protein structure, similar samples of anastellin and ANS were prepared using $ZnCl_2$ in 2:1 metal:protein ratio. Protein samples were prepared with 100µM Zn or Cu. Emission spectra were taken for triplicate samples, of those a representative spectrum from each group is shown in **Figure 2.7**. There is minimal change in fluorescence intensity with the addition of zinc. Compared to the fluorescence intensity at pH 7.4 with no zinc, the addition of zinc at pH 7.4, pH 6.5, and pH 5.5 resulted in a normalized fluorescence intensity of 104%, 115%, and 144%, respectively. There is no statistical significance resulting from the addition of zinc compared to anastellin protein alone. However, the addition of Cu resulted in lower ANS fluorescence for pH 7.4, pH 6.5, and pH 5.5. Addition of Cu resulted in ANS fluorescence at pH 7.4, pH 6.5, and pH 5.5 of 81%, 87%, and 94%, respectively. Compared to protein alone, these values are all lower. However, compared to each other, we see a statistical significant increase between pH 7.4 and pH 5.5, showing a large increase as pH decreases ($p<0.01$).

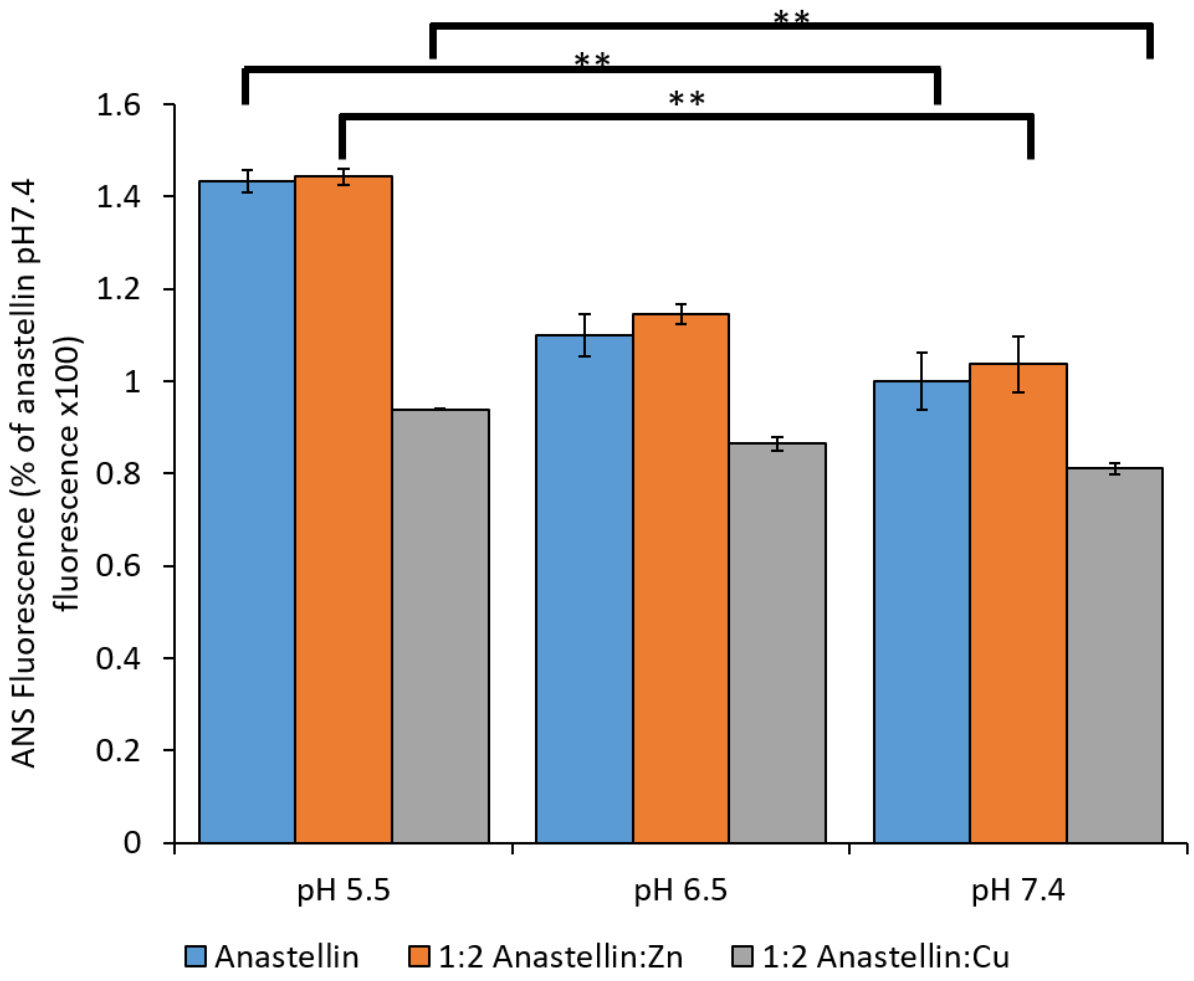

*Figure 2.7. ANS Fluorescence of 50 µM anastellin in pH 7.4 HEPES buffer, pH6.5 MES buffer, and pH5.5 MES buffer with the addition of 100 µM $ZnCl_2$ and the addition of 100µM $CuCl_2$. Results normalized to anastellin at pH7.4 HEPES buffer. (**p<0.01) Average ANS fluorescence intensity taken from three independent experiments.*

2.4.3 EXAFS of Anastellin Zinc and Copper Interactions

EXAFS absorption of zinc was first measured in pH 7.4, pH 6.5 and pH 5.5 in HEPES, MES, and MES buffer to determine the background interaction coordination distance with water. Next, EXAFS absorption of zinc interaction with anastellin was measured in pH 7.4, pH 6.5 and pH 5.5 to determine the interaction coordination distance with the protein. **Figure 2.8** shows the Zn absorption energy plot and corresponding Fourier transform plot to determine coordination distance with Zn in buffer. Coordination distances of Zn in pH 7.4, pH 6.5 and pH 5.5 were determined to be 1.93, 1.93 and 1.94 Å, respectively. Next, Zn coordination with anastellin was examined at pH 7.4, pH 6.5, and pH 5.5. **Figure 2.9** shows the Zn absorption energy plot and corresponding Fourier transform plot to determine coordination distance of Zn and anastellin at the three examined pHs. The most prevalent peaks appear at 1.88, 1.91, and 1.93 Å at pH 7.4, 6.5 and 5.5, respectively. Overall, this shows changes in peak distance at higher pH compared to the Zn buffer interaction. At pH 5.5, there is little difference between coordination distance in Zn-buffer and Zn-anastellin interactions, as both are observed at 1.93 Å. However, at pH 6.5 and pH 7.4 there is a shortening of coordination distance observed from 1.93 to 1.91 Å, and from 1.92 to 1.88 Å, respectively.

Next, EXAFS absorption was measured to determine any anastellin interaction with copper. Similar to Zn, absorption and coordination distance of Cu in pH 7.4 HEPES, pH 6.5 MES, and pH 5.5 MES buffer was determined to measure background interaction with the buffer. **Figure 2.10** shows the Cu absorption energy plot and corresponding Fourier transform plot to determine coordination distance with Cu in buffer. Coordination distances of Cu in pH 7.4, pH 6.5 and pH 5.5 were determined to be 1.81, 1.81 and 1.82 Å, respectively. Next, Cu coordination with anastellin was examined at pH 7.4, pH 6.5, and pH 5.5. **Figure 2.11** shows the Cu absorption energy plot and corresponding Fourier transform plot to determine coordination distance of Cu and anastellin at pH 7.4, 6.5, and 5.5. The most prevalent peaks appear at 1.81, 1.81, and 1.82 Å, at pH 7.4, 6.5, and 5.5, respectively. Overall, this shows little difference between Cu interaction with buffer and Cu interaction with anastellin in buffer. Coordination distances of the major peaks with copper did not change, and unlike Zn, this indicates Cu-anastellin interactions are minimal and not enough to alter average bond distances of Cu.

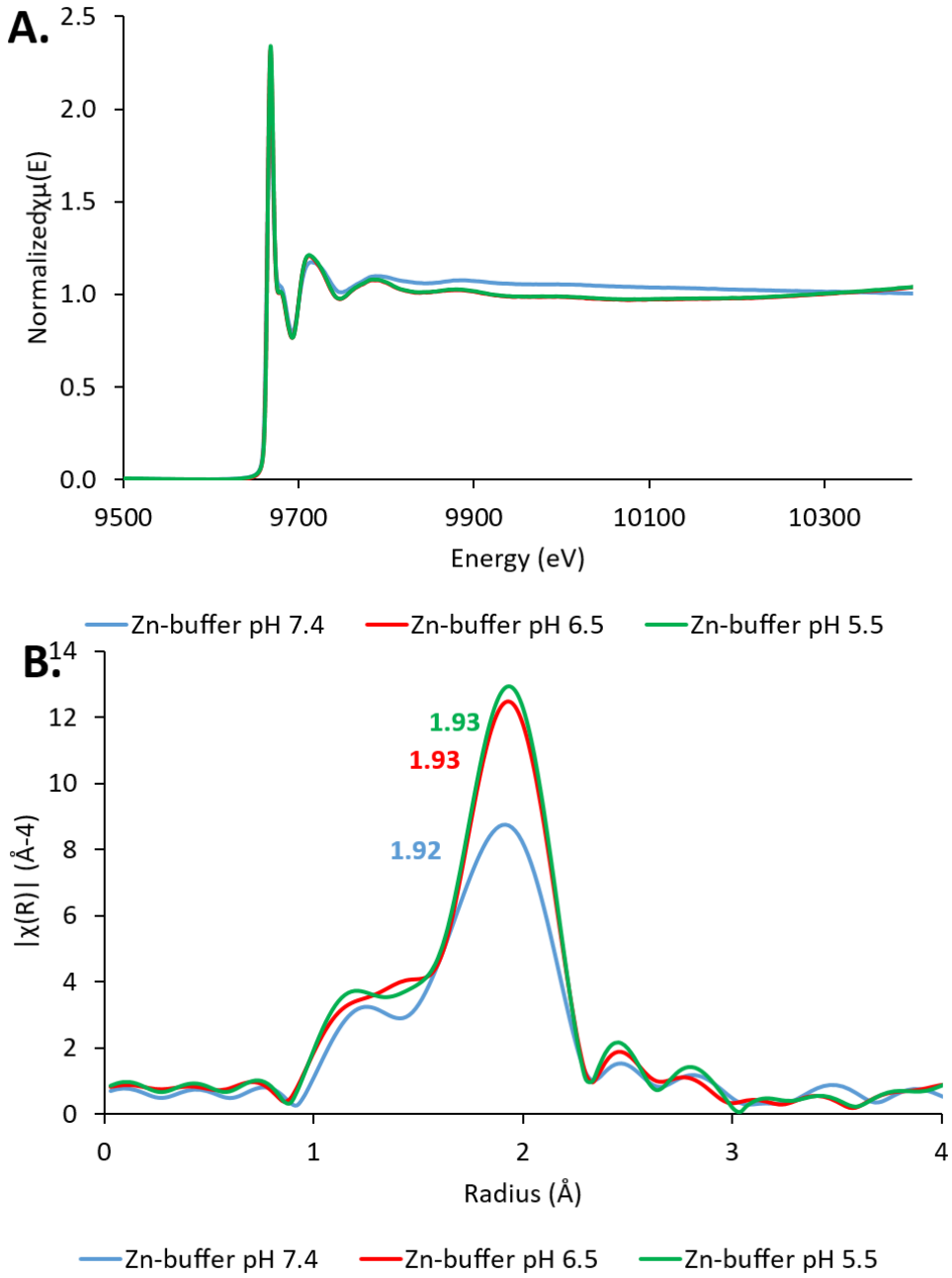

Figure 2.8. X-ray absorption of Zn-buffer showing (A) Zn-absorption energy plot and (B) Fourier-Transform plotted in R-space showing coordination distance. Coordination distance of Zn in buffer at pH 7.4, 6.5, and 5.5 are 1.92, 1.93, and 1.93 Å.

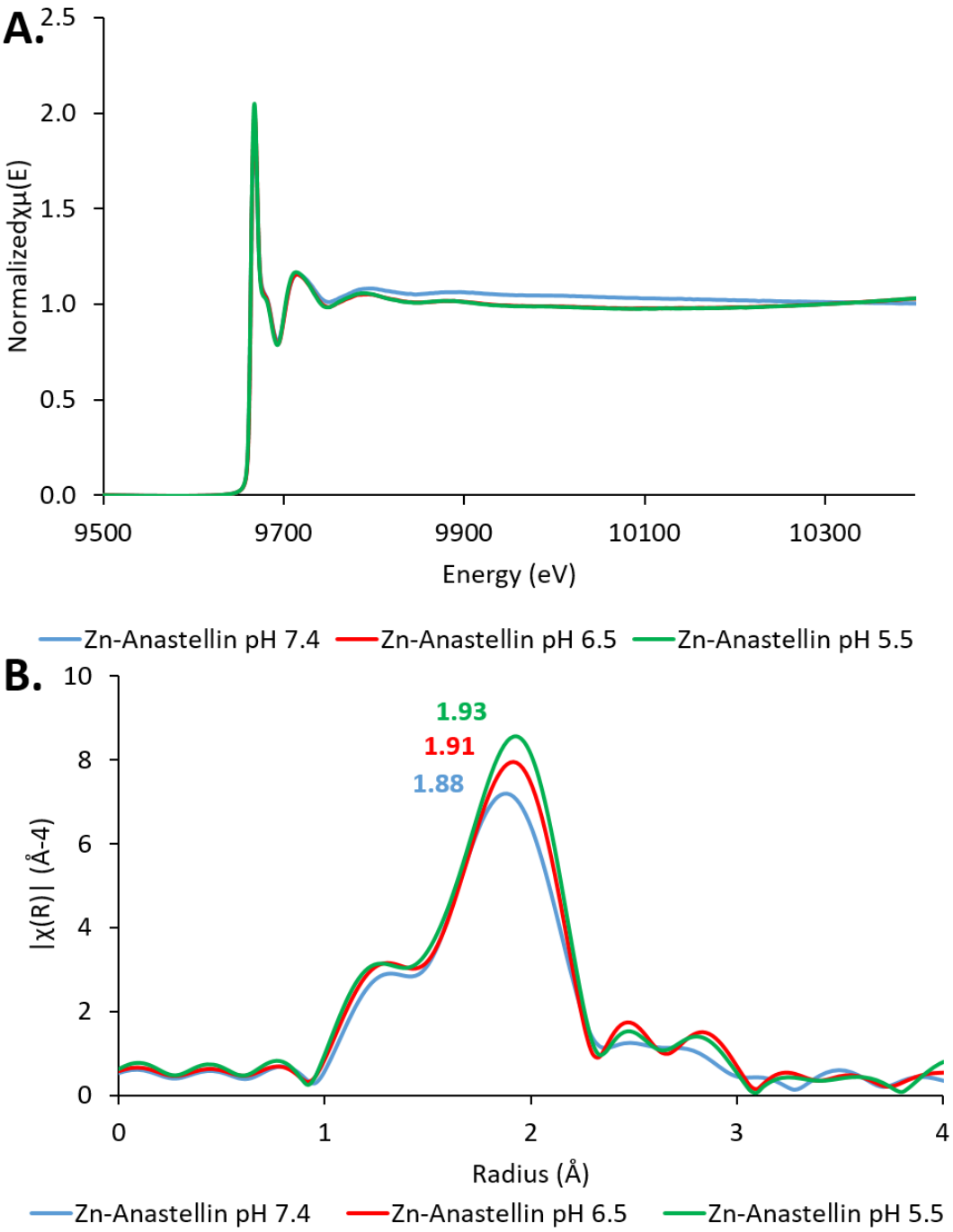

Figure 2.9. X-ray absorption of Zn-anastellin in buffer showing (A) Zn-absorption energy plot and (B) Fourier-transform plotted in R-space showing coordination distance. Coordination distance of Zn-anastellin in buffer at pH 7.4, 6.5, and 5.5 are 1.93, 1.91, and 1.88 Å.

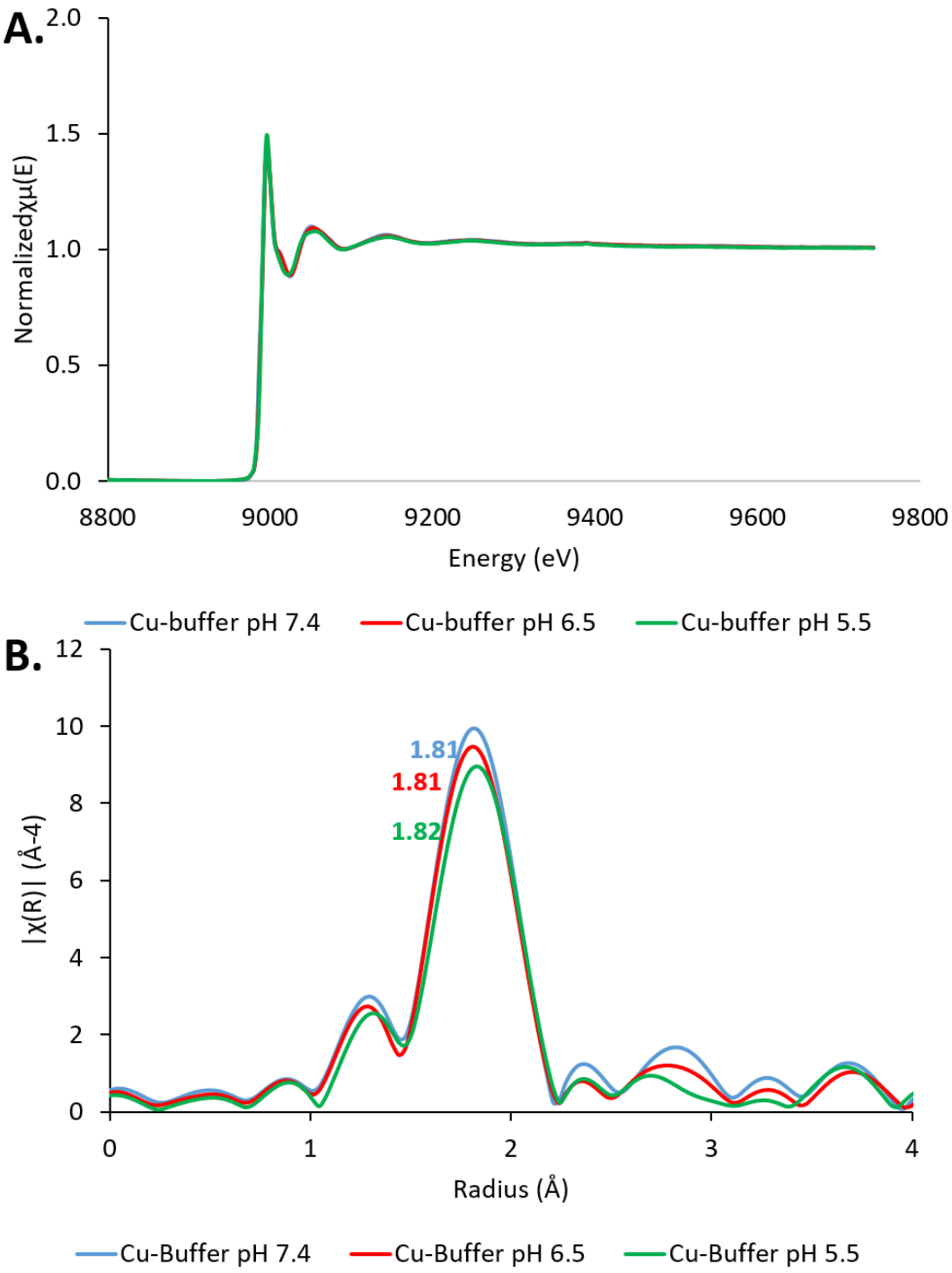

Figure 2.10. X-ray absorption of Cu-buffer showing (A) Cu-absorption energy plot and (B) Fourier-Transform plotted in R-space showing coordination distance. Coordination distance of Cu in buffer at pH 7.4, 6.5, and 5.5 are 1.81, 1.81, and 1.82 Å.

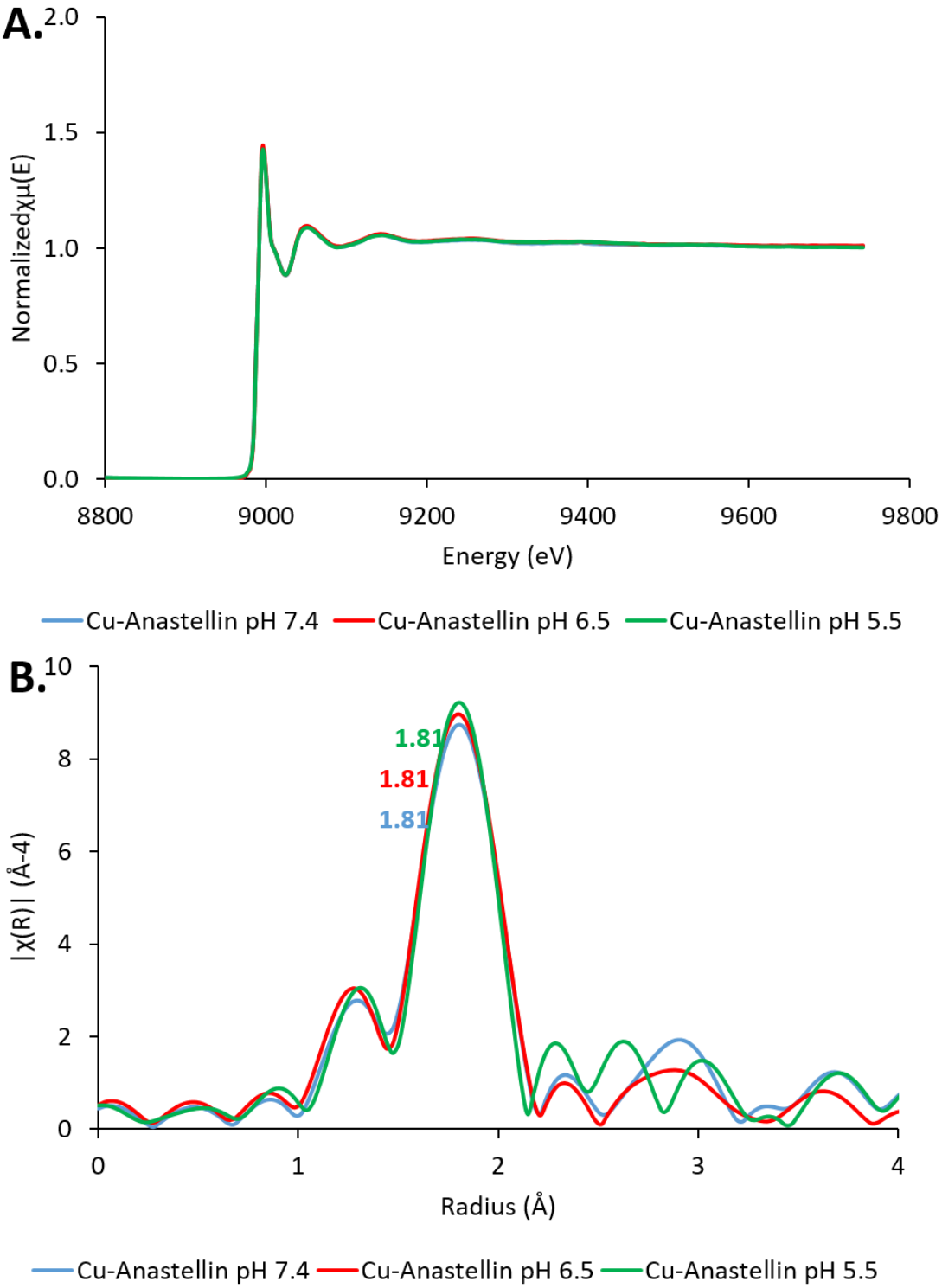

Figure 2.11. X-ray absorption of Cu-anastellin in buffer showing (A) Cu-absorption energy plot and (B) Fourier-transform plotted in R-space showing coordination distance. Coordination distance of Cu-anastellin in buffer at pH 7.4, 6.5, and 5.5 are 1.81, 1.81, and 1.82 Å.

2.4.4 Immunofluorescence Staining

MC3T3-E1 cells stained with immunofluorescence for FN to determine any differences in cellular FN produced by the strongly mineralizing subclone 4 and weakly mineralizing subclone 24. Images of cells plated at low density after 24 hours and high density after 7 days in culture are shown in **Figure 2.12**. After 24 hours it is difficult to observe any differences between the two subclones, but after 7 days there may be small differences. The mineralizing subclone 4, appears to be a more ordered structure as FN patterns assemble the ECM. Subclone 24, which is weakly mineralizing has a more disordered FN ECM pattern.

Also, using immunofluorescence, a specific segment of FN known as EDA was tested to observe potential differences, as well. **Figure 2.13** shows representative immunofluorescence stained EDA MC3T3-E1 subclone 4 and 24 cells after 7 days in culture. The strongly mineralizing subclone 4 cells have a more ordered, well defined ECM structure, when compared to the subclone 24 cells. Subclone 24 cells have a more disorganized EDA staining, as it is faintly stained everywhere. Immunofluorescence staining was also performed on β1 integrins, a cellular integrin involved in binding to FN, specifically the type III subunit which contains the EDA domain.[10] **Figure 2.14** shows representative immunofluorescence stained β1 integrins of MC3T3-E1 subclone 4 and 24 cells after 7 days in culture. Similar to the EDA staining, it appears that subclone 4 cells have a slightly more ordered structure.

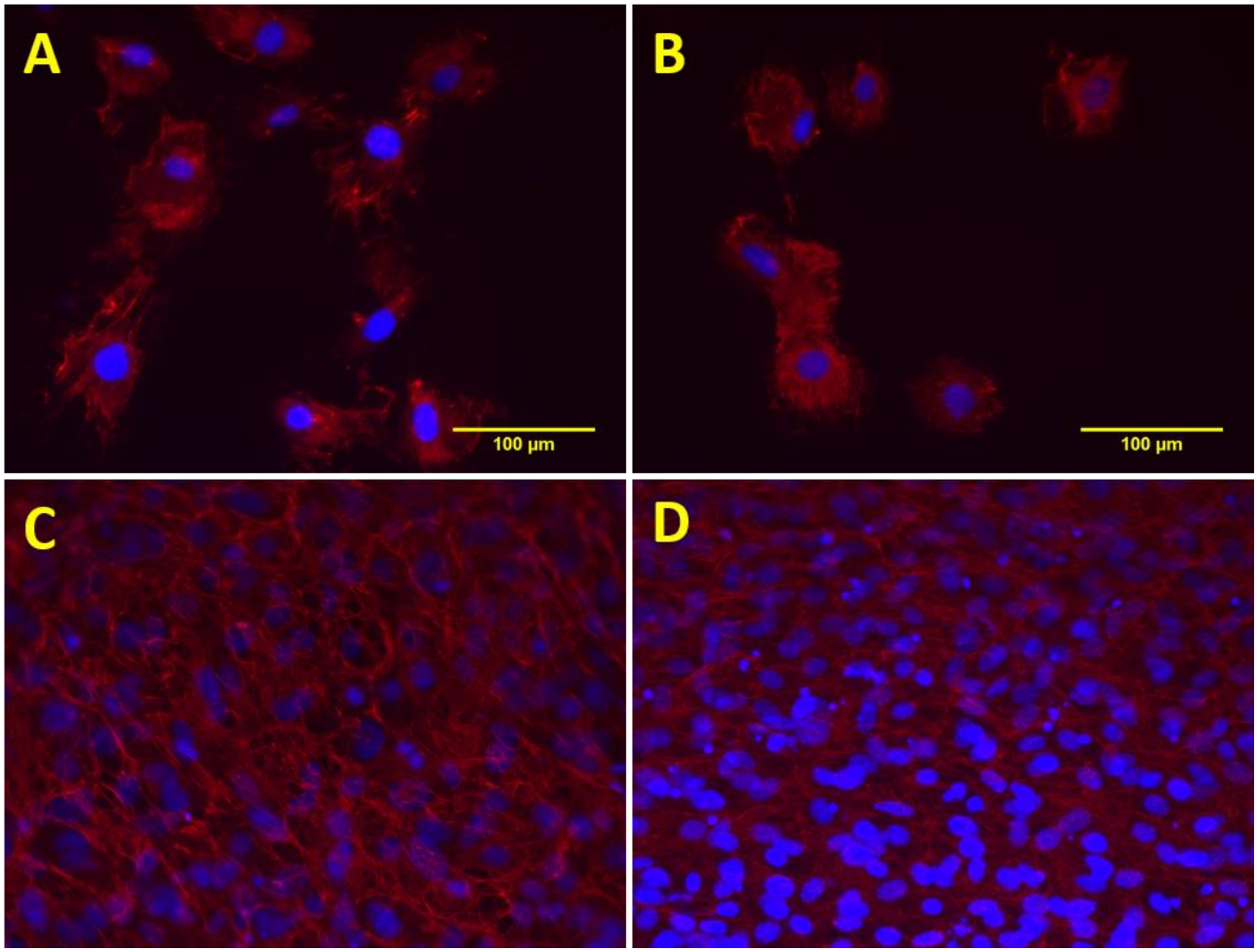

Figure 2.12. Representative fibronectin immunofluorescence staining of MC3T3-E1 subclone 4(A,C) and subclone 24 (B,D) stained at 24 hours (A,B) and 7 days (C,D) after plating. Anti-FN is stained with red secondary antibody and the nuclei are stained with DAPI (blue). (Scale = 100 µm) Images representative of 3 micrographs per experiment taken in 2 independent experiments.

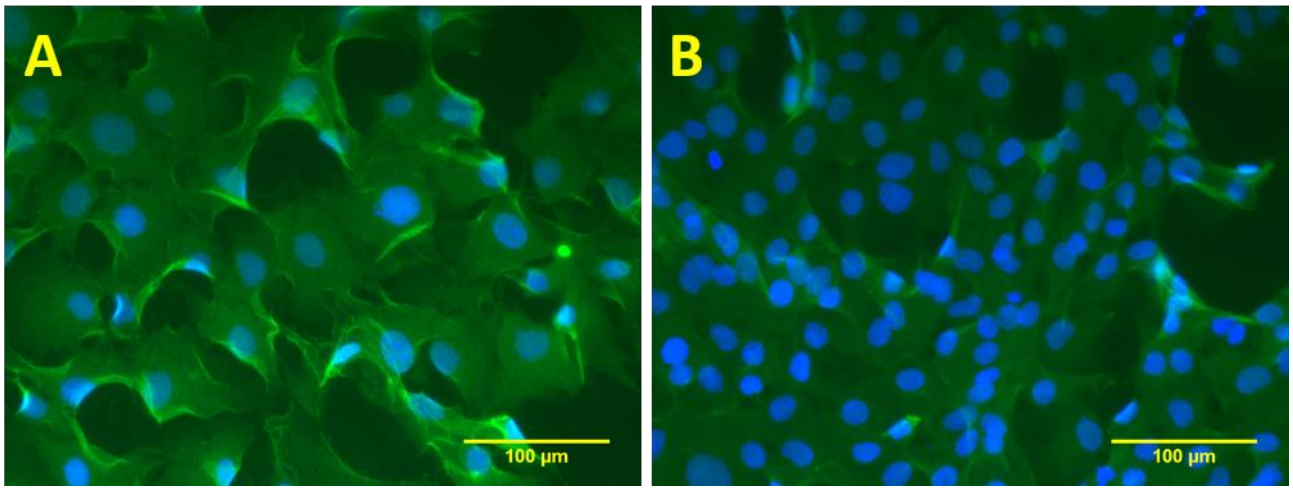

Figure 2.13. Representative FN-EDA staining performed on MC3T3-E1 (A) subclone 4, and (B) subclone 24 cells after 7 days in culture. Images representative of 3 micrographs taken per experiment in 2 independent experiments.

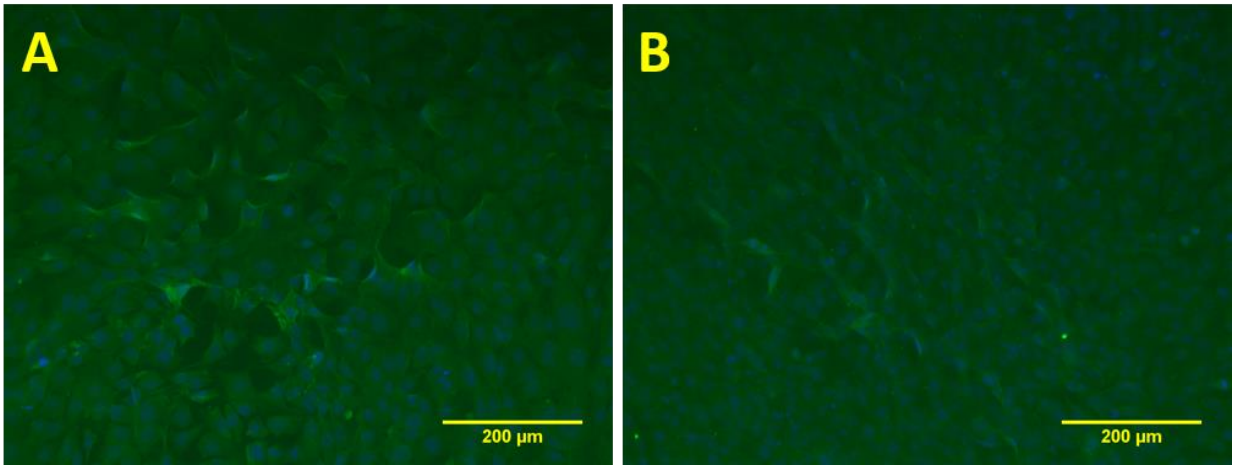

Figure 2.14. Representative β1 integrin staining performed on MC3T3-E1 (A) subclone 4, and (B) subclone 24 cells after 7 days in culture. Images representative of 3 micrographs per experiment taken in 2 independent experiments.

2.4.5 Cell Morphology

Cell area, circularity, and roundness of fluorescently labeled MC3T3-E1 and MG-63 cells were analyzed through ImageJ software. Representative fluorescently stained images of MC3T3-E1 and MG-63 cells grown in GM for 24 hours are shown in **Figure 2.15**. These images were analyzed in ImageJ to determine the effects of Zn on cell morphology. MC3T3-E1 and MG-63 cells area results after 24 hours attachment to tissue culture polystyrene in GM, GM + 15 µM Zn, and GM + 50 µM Zn are shown below in **Figure 2.16**. High zinc concentrations in the culture medium of MC3T3-E1 cells had little effect on the cell area compared to no added Zn or moderate zinc levels concentrations. Cell area of MC3T3-E1 cells grown in GM, GM + 15 µM Zn, and GM + 50 µM Zn are 5102, 5292, and 5020 μm^2, respectively. However, MG-63 cells saw a noticeable increase in cell area at 15µM and 50µM zinc compared to serum level zinc. Cell are of MG-63 cells after 24 hours grown in GM, GM + 15 µM Zn, and GM + 50 µM Zn were 1911, 2142, and 2037 μm^2 , respectively. The increase in cell area from GM to GM + 15 µM Zn is statistically significant according to the students T-test ($p<0.05$). MG-63 osteosarcoma cells are much smaller in size, when attached to tissue culture polystyrene, compared to MC3T3-E1 preosteoblast cells. MG-63 cell area spreading is affected by increased exogenous zinc concentrations, showing increased cell area with higher zinc concentrations in culture medium.

Circularity of MC3T3-E1 and MG-63 cells are reported in **Figure 2.17**. Average circularity of MC3T3-E1 cells grown in in GM, GM + 15 µM Zn, and GM + 50 µM Zn are 0.43, 0.50, and 0.53, respectively. The differences between MC3T3-E1 cells treated with GM and both Zn treated groups are considered statistically significant ($p<0.001$). Average circularity of MG-63 cells grown in GM, GM + 15 µM Zn, and GM + 50 µM Zn are 0.27. 0.31, and 0.34, respectively. The difference between GM and GM + 50 µM Zn are considered statistically significant ($p<0.05$). In both cell lines, the increase in exogenous zinc concentration results in an increase in circularity. An increase in circularity means cell morphology is becoming closer to a perfect circle, which has a circularity of 1.0. An increase in circularity indicates cell motility is decreasing. As cells migrate, their shape becomes less circular as the cell moves in a directionally.

Roundness is another measure of morphology, similar to circularity, which can be used to determine polarity of cells attached to a surface. Roundness of MC3T3-E1 and MG-63 cells are

reported in **Figure 2.18**. Average roundness of MC3T3-E1 cells grown in in GM, GM + 15 µM Zn, and GM + 50 µM Zn are 0.79, 0.75, and 0.76, respectively. Theses difference are not considered statistically significant. Similar to circularity, MG-63 cell roundness was much lower compared to MC3T3-E1 cells. Average roundness of MG-63 cells grown in in GM, GM + 15 µM Zn, and GM + 50 µM Zn are 0.27, 0.34, and 0.40, respectively. The increase seen with addition of 50 µM Zn, compared to MG-63 cells treated with GM is statistically significant ($p<0.01$). No differences are observed in MC3T3-E1 cell roundness, but MG-63 osteosarcoma cells increase in roundness with an increase in zinc concentration, similar to cell circularity.

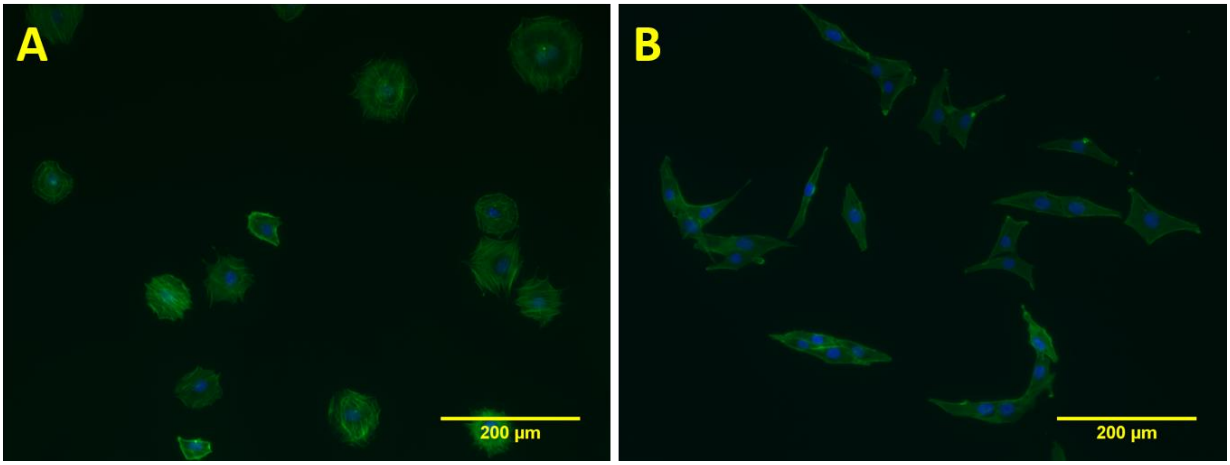

Figure 2.15. Representative images of (A) MC3T3-E1 and (B) MG-63 cells after 24 hours in growth medium stained with Alexa Fluor 488 phallodalin (green) for actin fibers and DAPI (blue) for nuclei. Images representative of about 8-10 images per experiment in 3 independent experiments.

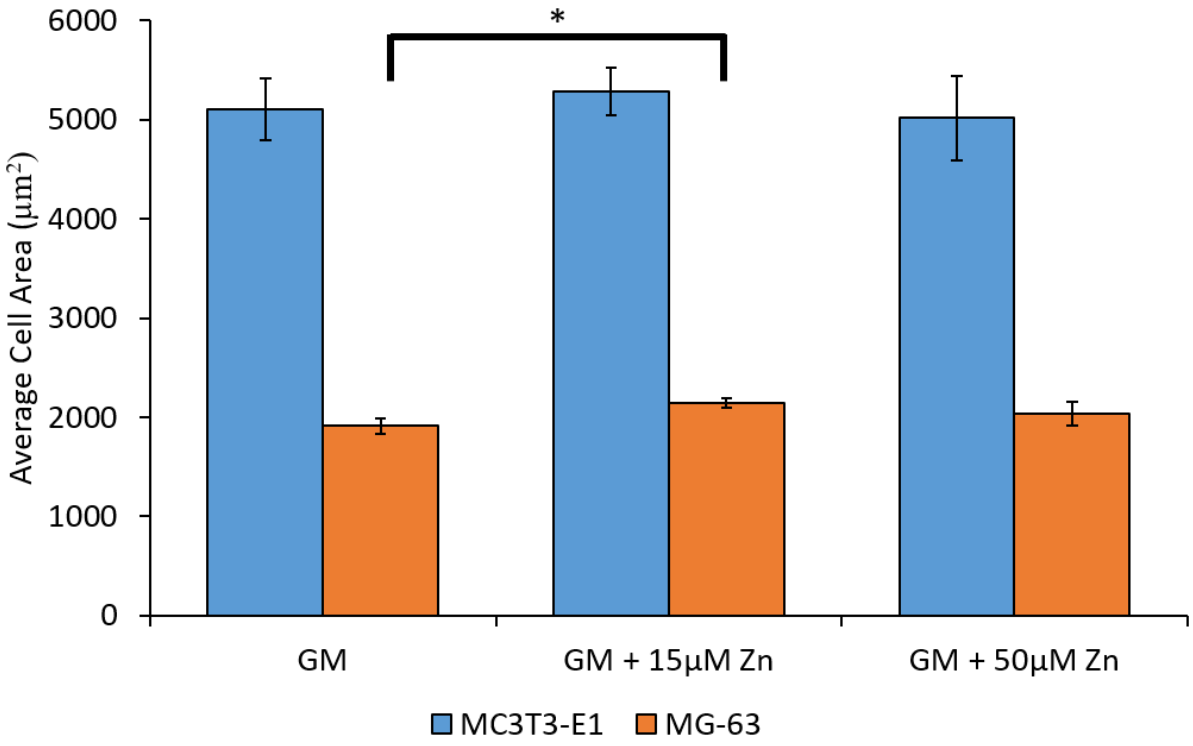

Figure 2.16. Average cell area of MC3T3-E1 and MG-63 after 24 hours in GM, GM + 15 µM Zn, and GM + 50 µM Zn.

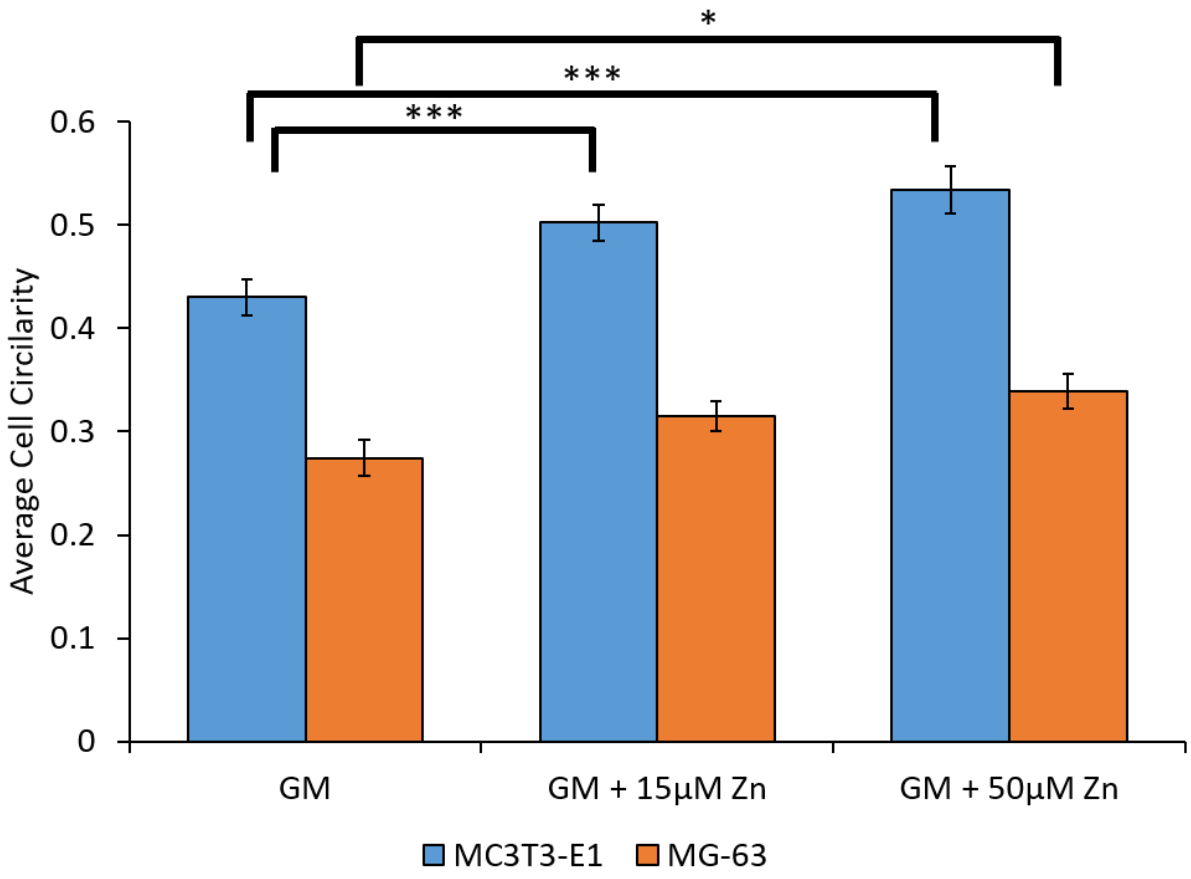

*Figure 2.17. Average cell circularity of MC3T3-E1 and MG-63 cells after 24 hours in GM, GM + 15 µM Zn, and GM + 50 µM Zn. (*p,0.05, ***p<0.001) Average circularity calculated from about 20 cells per experiment in 3 independent experiments.*

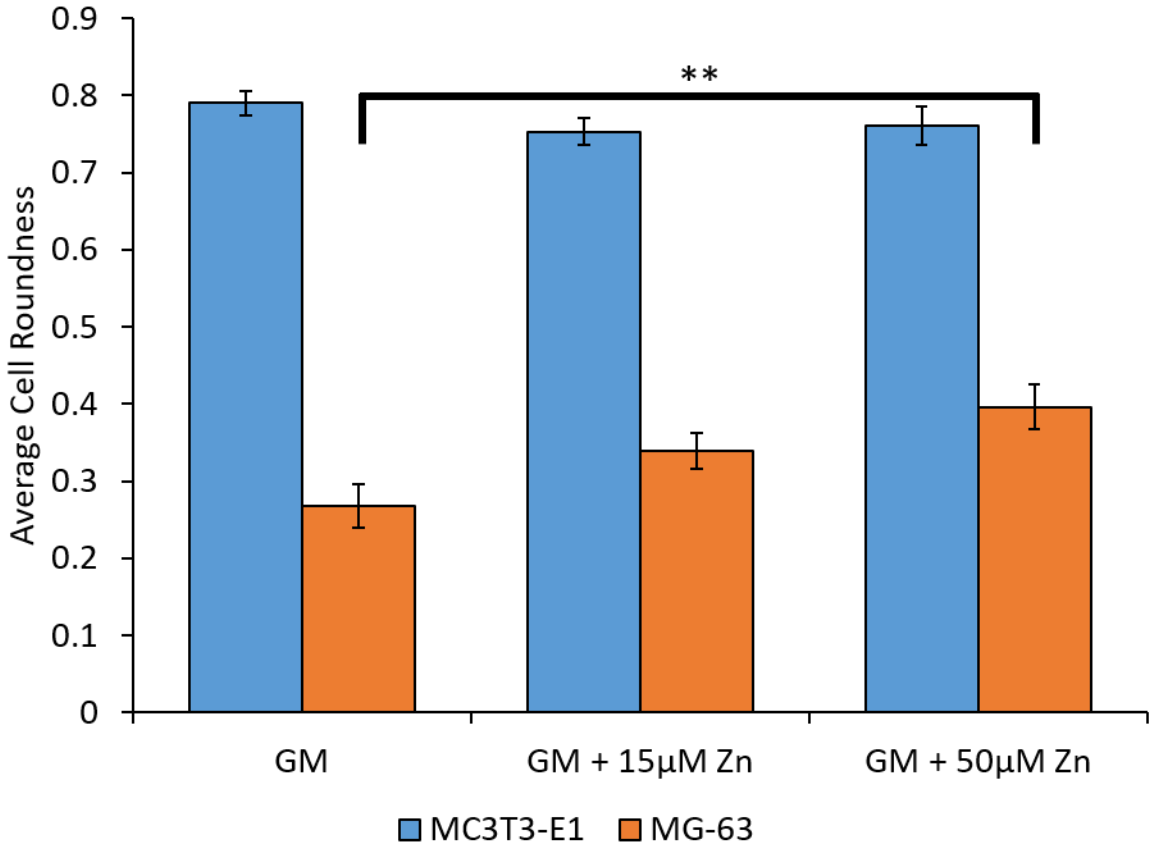

*Figure 2.18. Roundness of MC3T3-E1 and MG-63 cells grown in GM, GM + 15 µM Zn, and GM + 50 µM Zn.(**p<0.01) Average roundness calculated from about 20 cells per experiment in 3 independent experiments.*

2.4.6 Two-Dimensional Migration Tracking

Average cell speed of MC3T3-E1 and MG-63 cells manually tracked are reported in **Figure 2.19**. Cells are tracked by tracing nuclei of each successive picture taken 2 minutes apart. Cell speed is determined by calculating number of pixels traveled and converting to a distance over the 2 hour time period. The average cell speed of MC3T3 cells in cells in CO_2 independent medium (CIM), CIM + 50 µM Zn, and CIM + 100 µM Zn are 9.3, 8.4, and 7.6 µm/hour, respectively. The decrease in cell speed with increasing zinc concentration is not considered statistically significant across the three concentrations. The average cell speed of MG-63 cells in cells in CO_2 independent medium (CIM), CIM + 50 µM Zn, and CIM + 100 µM Zn are 14.7, 13.0, and 9.8 µm/hour, respectively. The decrease in cell speed from CIM to CM + 50 µM Zn is statistically significant ($p<0.001$). Also, the decrease from CM + 15 µM to CM + 50 µM Zn is statistically significant ($p<0.05$). Both cell lines show a decrease in cell speed with increasing zinc concentration, with osteosarcoma cells having a greater effect. Osteosarcoma cells are also more mobile than osteoblast cells.

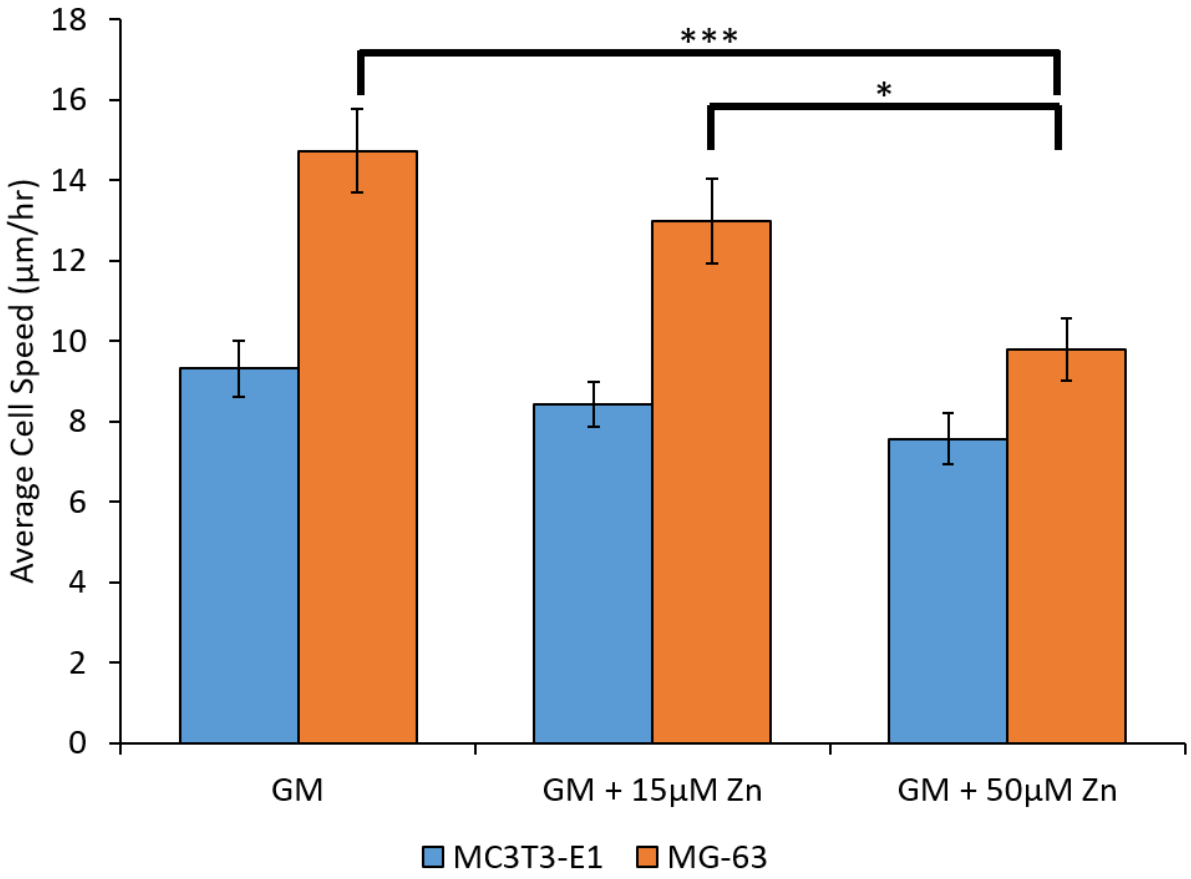

*Figure 2.19. Average cell speed of tracked MC3T3-E1 preosteoblasts and MG-63 osteosarcoma cells on tissue culture polystyrene grown in GM, GM +15 µM Zn, and GM + 50 µM Zn. (*p<0.05, ***p<0.001) Average cell speed calculated from about 20 cells per experiment in three independent experiments.*

2.5 Discussion

The effects of pH, zinc, and copper on FN particle size, and structure, and its subsequent effects of cell morphology, motility, and motility were examined. First, the effects of pH and zinc binding on FN particle size and structure were examined. Particle size measurements of whole FN were examined to determine the effect of pH on protein structure. Since the tumor microenvironment is known to be slightly acidic in pH, the effect of pH was examined to determine any potential differences in FN in cancerous environment compared to healthy tissues. According to the particle size data, it was determined that slightly acidic pH, like that of a tumor microenvironment favor higher FN particle size in solution. Also, interaction with Zn and Cu in solution may be affecting protein conformation, as determined by changes in particle size with addition of excess Zn and Cu.

Next, changes in a FN fragment, FN-III-IC, also known as anastellin, were studied using a fluorescent marker known as ANS, which binds to hydrophobic protein cores. When ANS is exposed to hydrophobic protein cores in solution, it fluoresces greatly compared to unbound ANS. This principle was applied to test the exposure of the gelatin binding domain in anastellin, which is thought to be unexposed in the globular form in solution. Decreasing pH to 6.5 and 5.5 was found to increase fluorescence, indicating increased exposure of hydrophobic protein core, which would agree with the FN particle size data, which shows increase of protein size with increasing acidity. However, addition of Zn had no effect on ANS fluorescence, indicating that Zn does not change exposure of hydrophobic cores in anastellin. Since Zn was previously shown to induce a structural change in the gelatin binding domain (GBD) of fibronectin, it was thought that zinc may affect hydrophobic core of anastellin, a specific fragment which is involved inducing FN aggregation, a process of building the ECM.[63,64] However, addition of Cu was shown to decrease ANS fluorescence at neutral and acidic pHs, indicating Cu and Zn may be differentially regulating anastellin size.

Additionally, coordination distance of Zn and Cu to binding sites on anastellin were attempted to be measured using EXAFS. Protein samples in solution at pH 7.4, pH 6.5, and pH 5.5 were measured with the addition of zinc and compared to protein free samples in buffer only. According to the results of EXAFS, copper binding was unsuccessfully measured in solution, as the coordination distance measured was roughly equivalent for protein-free, and samples

containing anastellin. A measured coordination distance of 1.82 – 1.81 Å was detected for all samples, which most likely indicates a Cu-H_2O interaction. The interaction with Zn resulted in measurable differences in coordination distance at pH 7.4 and pH 6.5. Coordination distance of samples containing Zn are decreased from 1.93 in buffer only to 1.91 and 1.88 Å in pH 6.5, and pH 7.4, respectively. Since proteins are in solution with buffer, it can be assumed that most of the observed interaction Zn-H_2O. However, there are measurable differences at pH 6.5, and pH 7.4, when anastellin is present. This indicates a protein-Zn interaction that is detectable at pH 7.4, and pH 6.5, but not detectable at pH 5.5. The EXAFS results agree with the ANS fluorescence data, in which Cu and Zn have measurable differences with regards to their interaction with anastellin. Cu was shown to decrease ANS fluorescence, indicating less exposure to the hydrophobic core of the protein. EXAFS data shows no measurable interaction of Cu with anastellin, presumable due to decreased exposure to the binding site, or no affinity to the FN fragment. Zn was shown to slightly increase ANS fluorescence, but not significantly more than the addition of no Zn. This means exposure to hydrophobic core, and binding sites are not beneficially favored due to addition of Zn. EXAFS data shows measurable changes at pH 7.4, and pH 6.5 in the Zn-anastellin coordination distance. Zn-anastellin and Zn-buffer at pH5.5 does not show measurable differences in coordination distances. Together, these data suggests an acidic pH is changing the protein structure, an altering binding of Zn. The Zn binding site could be altered due to deformation caused by acidic pH, causing decreased affinity for the binding site, as measured by EXAFS.

The importance of FN, a major non collagenous protein in bone, was investigated through immunofluorescence staining of FN, a specific FN domain known as EDA, and β1 integrin, a known cell surface-receptor protein responsible for FN binding. Using an in vitro osteoblast model containing MC3T3-E1 subclone 4 cells, which strongly mineralize to form bone, and MC3T3-E1 subclone 24 cells which represents mis-differentiated bone, as it weakly mineralizes bone. Immunofluorescence staining of FN, the EDA domain of FN, and β1 integrins have indicated qualitative differences in the ECM of healthy mineralizing cells, and mis-differentiated osteoblast cells. Healthy, mineralizing osteoblasts all showed a more ordered structure of FN, EDA, and β1 integrins, compared to the mis-differentiated osteoblasts. This indicates the importance of ECM structure, specifically FN and its binding sites, to the formation of healthy bone.

The effects of Zn on cell migration were then assessed through calculation of cell morphologies and manually tracked cell speeds. Cell morphologies, such as circularity and roundness, indicate increased exogenous Zn concentration results in lower cell polarity, indicating decrease in motility. In both MC3T3-E1 osteoblasts and MG-63 osteosarcoma cells, cell circularity and roundness are decreased with an increase in Zn concentration. This indicates a decrease in cell polarity, as cells are less round and less circular when moving. Cell motility data agree with cell polarity results calculated. The addition of Zn in both MC3T3-E1 and MG-63 cells results in lower cell motility, as tracked over 2 hours. Cell migration has importance in building ECM and proper bone formation.[54] As related to cancer, for osteosarcoma cells, cell motility is related to metastasis. Proper ECM regulation and Zn levels may also be related to cancer metastasis.

2.6 Conclusion

The addition of zinc into the buffered solvent of fibronectin indicates that the protein is interacting with zinc to change its conformation. Zinc binding could induce the protein to become partially coiled, hiding certain binding domains, while still exposing others. Further tests on the structural interaction of fibronectin are necessary to determine the full effect zinc binding has on structural changes of fibronectin. Structural changes to the ECM and expression of important ECM proteins related to cancer cell metastasis and healthy cell bone remodeling motility should be investigated for their potential effects on cell motility and morphology. Zinc binding proteins such as fibronectin, and its GBD, show potential structural shift related to protein interaction with zinc. Differences in the ECM of mineralizing and non-mineralizing osteoblasts, indicate FN could play an important functional role in healthy bone formation. Addition of excess Zn in vitro shows a decrease in cell motility and morphology. Taken together the conformational changes in FN caused by interaction with Zn may play a role in motility, healthy bone and ECM formation, and cancer metastasis.

Chapter 3 : A Comparison of Zn and Fe Distributions in Healthy and Ovariectomized Rat Femurs Using Synchrotron X-ray Fluorescence

Abstract

The ovariectomized rat model of osteoporosis was used to examine potential changes in trace element zinc and iron distribution and quantity in bone caused by an induced osteoporotic state. The method of x-ray fluorescence was used to compare collected femur bones of rats either ovariectomized (OVX) or healthy age-matched control animals at ages 6 and 12 months. A significant decrease in total calcium is observed, more prominent in the trabecular regions, in OVX bones compared to their age matched healthy groups. The calcium XRF intensity for 12 OVX was 57% and 72% lower than the 12 month control ($p=0.30$), and 6 month control ($p=0.01$), respectively. Overall this shows signs of a bone loss, characteristic of osteoporosis induced by estrogen deficiency. A decrease in total zinc is observed across OVX groups, most observably in the trabecular regions, when compared to age matched control groups. Trabecular zinc for the 12 month OVX group was 31% and 30% lower, compared to the 12 AM group ($p=0.34$), and 6AM group ($p=0.17$), respectively. XRF results for iron, do not show conclusive changes between OVX and age matched control bones unless normalized to calcium content. Once normalized to calcium content, the iron:calcium ratio in 12 OVX is a 149% higher compared to the 12 month age matched control group ($p=0.03$). Overall, a trend of decrease in zinc content and increase in local concentration of iron is observed in bones induced with osteoporosis. The results of this experiment show the potential importance of micronutrients iron and zinc in the homeostasis of bone quality.

3.1 Introduction

Bone is a vital organ which has many functions, providing structure, protecting organs, and assisting movement. Bone is composed of two phases: the organic protein phase, and an inorganic mineral phase. The organic protein phase is composed of type I collagen, which provides the scaffold for bone mineral to be deposited. The mineral phase is composed of hydroxyapatite, which has the chemical formula $Ca_{10}(PO_4)6\ (OH)_2$. Hydroxyapatite is deposited within the crosslinked structures of the collagenous protein matrix.[65] On the macroscopic scale, there are two phases of bone with different morphologies: cortical, and trabecular. Cortical bone is the compact, dense outer layer which accounts for about 80% of the total skeleton. Trabecular bone is the spongy, porous inner region of bone which comprises the remaining 20%

of the skeleton. Cortical and trabecular bone differ in their microstructure and porosity, with trabecular having a less dense, porous structure.[66]

Bone is regulated on the cellular level by osteoblast, osteoclasts, and osteocytes, which serve to remodel bone to maintain a healthy structure. Osteoclasts serve to resorb, or remove old, damaged bone. Osteoblasts then come and rebuild new bone in its place. Osteocytes are the stationary bone cells embedded within the bone structure that send signals to the osteoclasts and osteoblasts to regulate the remodeling cycle. If the remodeling cycle is disrupted, as in the case of osteoporosis, a diseased state of porous, weak bone can occur when an imbalance occurs between the amount of bone resorbed and amount of new bone deposited. Osteoporosis is defined by an increase in bone porosity and decrease in calcium content causing an increased risk of bone fracture.[67,68]

Dietary supplementation of Ca in postmenopausal women is shown to reduce bone loss and help prevent osteoporosis.[69] Although the main constituent of bone is calcium, less frequently studied micronutrients such as iron (Fe) and zinc (Zn) may play crucial roles in bone development. It has been suggested that bone loss in the elderly could be partly attributed to subclinical Zn deficiency.[70]

Osteoporosis has been highly studied in vivo using rat models either through immobilization or ovariectomization.[71] The ovariectomized (OVX) rat model for osteoporosis is the approved preclinical FDA model for studying postmenopausal osteoporosis as affected by the decline in estrogen production.[72] At 9 months of age, the female rat has reached peak bone mass and can be manipulated to induce estrogen deficiency, characteristic of postmenopausal osteoporosis. The OVX model is characterized by rapid loss of trabecular bone mass and strength, and a slow developing cortical bone loss.[71] However, bone loss in this model is not uniform across the skeleton. For example, the amount of time needed to observe significant trabecular bone loss in the femoral neck of OVX rats in the femoral neck and lumbar vertical body are 30 days, and 60 days respectively.[73,74]

Although osteoporosis has been extensively studied using the OVX rat model, there is no agreed upon method for studying the distribution or concentration of trace metals, such as iron or zinc, in the skeleton. Amongst the techniques for analysis of trace elements in biological

samples, atomic absorption spectroscopy (AAS) is the most common technique due to few spectral interferences, good detection limits, small sample volume required, and low costs.[75,76] However, this method is destructive to the sample, requiring the samples to be dissolved in acid, making them useless for further characterization techniques. X-ray fluorescence (XRF) is a non-destructive technique which can be alternatively used trace element quantification in biological samples such as bone. XRF has been extensively used to study lead toxicity by quantifying lead content in human bone.[77] Also, XRF has been widely applied towards measuring strontium levels in bone.[78] Compared to lead or strontium, few publications exist citing the use of XRF in trace metals iron and zinc. XRF has also been applied towards detecting changes in zinc content as an effect of bone development, showing zincs importance in early stage bone ontogenesis.[79] More recently, the study of zinc, iron, and strontium in rat bones and teeth using energy dispersive XRF was performed showing the importance of trace elements in early bone development.[80]

3.2 Objective

The overall objective of this study was to investigate the distribution of trace metals in healthy vs. osteoporotic bone. We hypothesized that Ca, Zn and Fe distributions would be different in the femur bones of ovariectomized rats compared to their age-matched controls. Using Synchrotron Radiation X-Ray Fluorescence (XRF), we performed two-dimensional mapping of the trace elements Zn, and Fe, and examined their intensity and distribution in relation to Ca.

3.3 Materials and Methods

3.3.1 Bone Samples

Ovariectomized (OVX) female Sprague–Dawley rats were used as our model for post-menopausal osteoporosis due to high bone turnover and subsequent bone loss as a result of estrogen deficiency. Femur bone samples from OVX rats and age matched-control (AM) rats were taken at 6 months and 12 months of age, details described by Tommasini et al.[81] Both 6 and 12 month OVX rats were ovariectomized at 5 months yielding 1 and 7 months post-menopausal osteoporotic simulation in each group, respectively. Upon sacrifice at 6 and 12 months, the left femoral diaphysis of each rat was removed, cleaned, and dehydrated in ethanol at -20°C. Bone samples were then individually embedded in a block of polymethyl methacrylate (PMMA) resin with proximal ends exposed. Bone blocks were cut longitudinally and cleaned with polish

treatment on the surface using an abrasive silicon carbon paper and diamond suspension solution. Each rat bone was given a unique number corresponding to its age and experimental condition.

3.3.2 Scanning Electron Microscopy (SEM)

Cross-sections of bone samples embedded in PMMA were coated in roughly 25 nm of carbon (to prevent charging) using a Gatan Model 681 High Resolution Ion Beam Coater (Gatan, Roper Technologies, Sarasota, FL). Additionally, carbon tape was placed along the edges of the blocks to further prevent charging. A JEOL 7600F Schottky Field Emission Scanning Electron Microscope (JEOL, Tokyo, Japan) was used to image each bone block at 5 keV with a 15mm working distance and an LEI detector under low magnification. Multiple magnified images of each bone sample were stitched together using GIMP, an image editing software, to compile the completed images.

3.3.3 Synchrotron X-Ray Fluorescence (XRF) spectroscopy

Synchrotron Radiation X-Ray Fluorescence (XRF) experiments were conducted at Beamline X26A, located at the National Synchrotron Light Source (NSLS), Brookhaven National Laboratory (Upton, NY). The x-ray microprobe was operated in monochromatic mapping mode under 9-11 keV tuned by a Si (111) channel cut monochromator, which is non-destructive to the sample. Samples were mounted on the stage 45° toward the incident photon beam (**Figure 3.1a**).[53] The energy dispersive 9 element Ge detector was at 90° to the beam to eliminate backgrounds from Compton scattering. Energy dispersive spectra and elemental maps were collected using a dwell time of 0.1 s/pixel and a step size of 0.01 mm. The estimated attenuation length of the samples were about 180 m. Attenuation length is defined as the depth into the material where the number of photons has decreased by 37% (1/*e*) from the number of incident photons. An optical microscope was coupled to a digital camera for viewing each sample prior to acquiring spectra. Based on SEM images, it was decided to make the testing area 2 mm below the growth plate. Each testing area was 2 mm in height, and wide enough to cover the entire width of the bone. Each sample tested was between 2mm and 4mm below the growth plate (**Figure 3.1d).** Trabecular and cortical XRF intensity values of Ca, Zn, and Fe were averaged across a 2mm region located 2mm below the femoral growth plate for each sample.

Analysis of raw XRF intensity data was performed in XMap Plotter. A region of interest was drawn around either the trabecular or cortical regions of each bone sample and the average XRF intensity of each element and ratio was recorded. Additionally, XRF intensities were normalized to Ca count by averaging Fe:Ca and Zn:Ca intensity ratio.

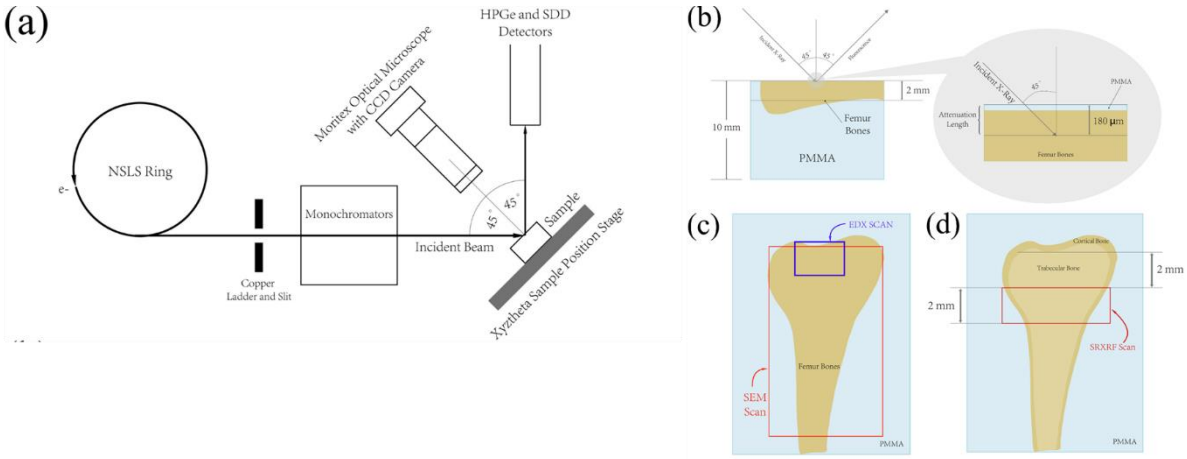

Figure 3.1. (a) XRF instrument setup at NSLS beamline 26A, (b-d) schematic depicting scanned region of each bone sample. (Figure taken from Danhua Yan)[76]

3.4 Results

3.4.1 Scanning Electron Microscopy

Blocks of rat femur bones were separated in four different groups, 6 AM, 6 OVX, 12 AM, and 12 OVX, as shown in **Figure 3.2**. Scanning electron microscopy (SEM) images gave an overall longitudinal view of bone structure and morphology. Qualitatively, it is easy to distinguish between cortical and trabecular bone in all groups. Cortical bone appears as a dense outer dense layer, while the inner porous region is trabecular bone. All SEM images appear to have a lighter (arrows) and darker phases (arrowheads), with the lighter phase corresponding to mineralized bone tissue. It can be observed that there is less trabecular bony tissue within the 12 OVX group compared to all other groups (**Figure 3.2**). It also appears that even after one month of ovariectomization (**Figure 3.2B**), the porosity of the trabecular bone increased when compared to the age-matched control (**Figure 3.2A**). After 7 months ovariectomization, the 12OVX group is observed to have less trabecular bony structures compared to its age matched control (**Figure 3.2C,D**). This is an expected trend inducing an osteoporosis-like condition.[82]

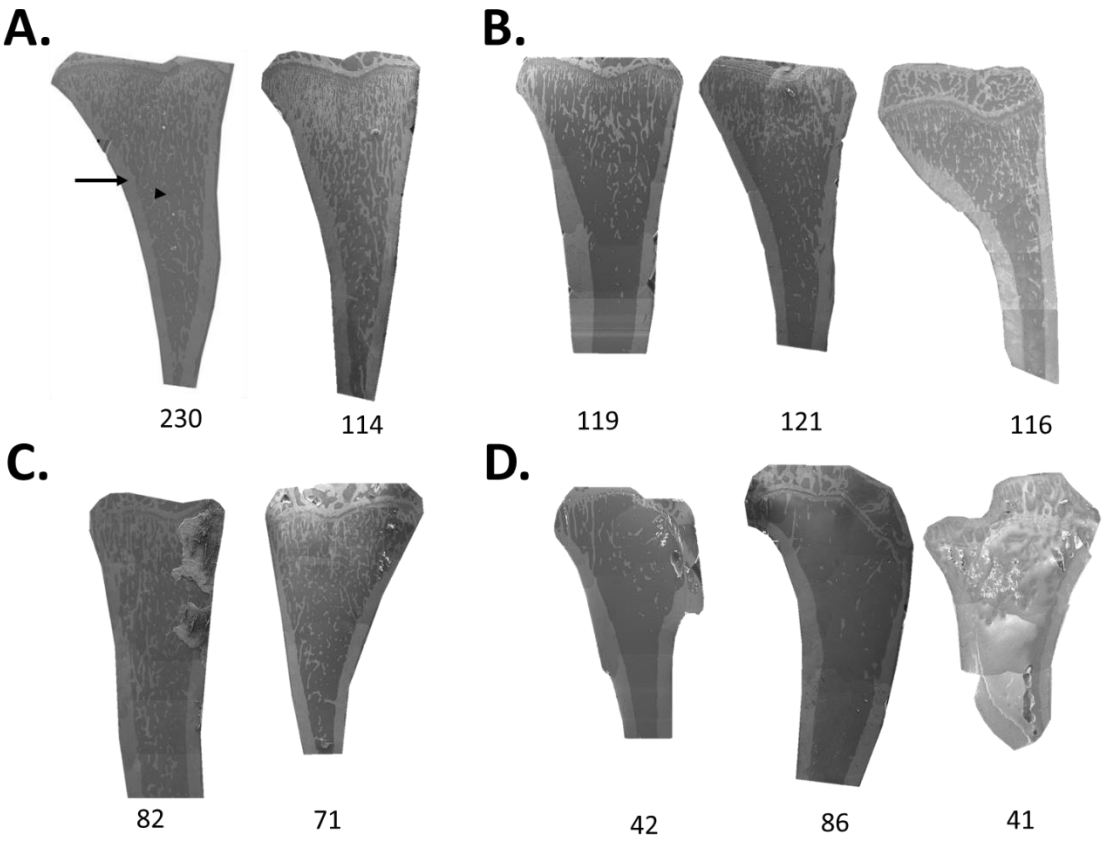

Figure 3.2. SEM images of (A) 6 month AM – 230, 114, (B) 6 month OVX samples – 119, 121, 116, (C) 12 month AM – 82, 71, 70, and (D) 12 month OVX – 42, 86, 40, 41. Cortical regions are shown by the arrow in sample 230. The individual arrow head in 230 represents the trabecular region.

3.4.2 Synchrotron X-ray Fluorescence (XRF) Microscopy (μXRF)

Our study focused in detail on the trace elements Fe and Zn, using Ca as a reference element. Similar regions were chosen for each bone sample, at 2 mm below the growth plate and spanning 2 mm in length, which covered the entire width of the bone section.

Elemental Maps

Maps corresponding to the XRF intensity of Ca, Fe, and Zn were constructed in XMap-Plotter (**Figure 3.3)**. Fe:Ca and Zn:Ca ratio maps were created with the raw XRF intensity value using calcium as the reference element. The intensity of each element was adjusted to give a visual representation of bone with maximum counts for Ca, Fe, and Zn adjusted to 12,000, 625, and 1100, respectively. Individual maps for total Ca, Fe, and Zn counts for each experimental group (**Figure 3.3-3.5**) were generated in XMap-Plotter using the raw XRF intensity data obtained from each pixel. Based on the individual XRF maps, the spatial distribution of each element was evaluated.

Maps of total Ca (**Figure 3.4**) showed that calcium content was very dense in the cortical regions, as expected, and visibly sparser in the porous trabecular regions. Based on the Ca maps, it was observed that the trabecular regions of the 12 OVX group (**Figure 3.4D**) is visually more porous compared to the other groups. Maps of total Fe (**Figure 3.5**) indicated that there was little Fe in the cortical regions, as evident by the low fluorescence signal. Average fluorescent signal in cortical regions averaged between 27 and 40 counts. On the contrary, there was an abundance of Fe in the trabecular regions, with average intensity values ranging from 97 to 133 counts. This is in direct contrast to Ca (**Figure 3.4**), which showed that localization was predominantly in cortical bone. Among the four experimental groups, little difference was visible in the overall intensity of the Fe maps (**Figure 3.5**). Similar to Ca (**Figure 3.4**), Zn was localized in both the cortical and the trabecular regions (**Figure 3.6**). The intensity of Zn was observed to be less in the 12 OVX group (**Figure 3.6D**) compared to the other groups in the trabecular region. The average intensity of Zn in the 12 OVX group was 241 counts, compared to 360, 333, and 350 counts in the 6 AM, 6 OVX, and 12 AM groups, respectively.

Merged maps showing the co-localization of Ca, Fe and Zn (**Figure 3.3)** confirms the relative distributions of each element with respect to each other. Specifically, Ca and Zn are

localized together in both cortical and trabecular regions, whereas Fe is positioned in the porous trabecular regions lacking Ca or Zn. Merged elemental maps (**Figure 3.3**) show Zn is positioned in the cortical regions and porously in the trabecular regions, overlapping Ca.

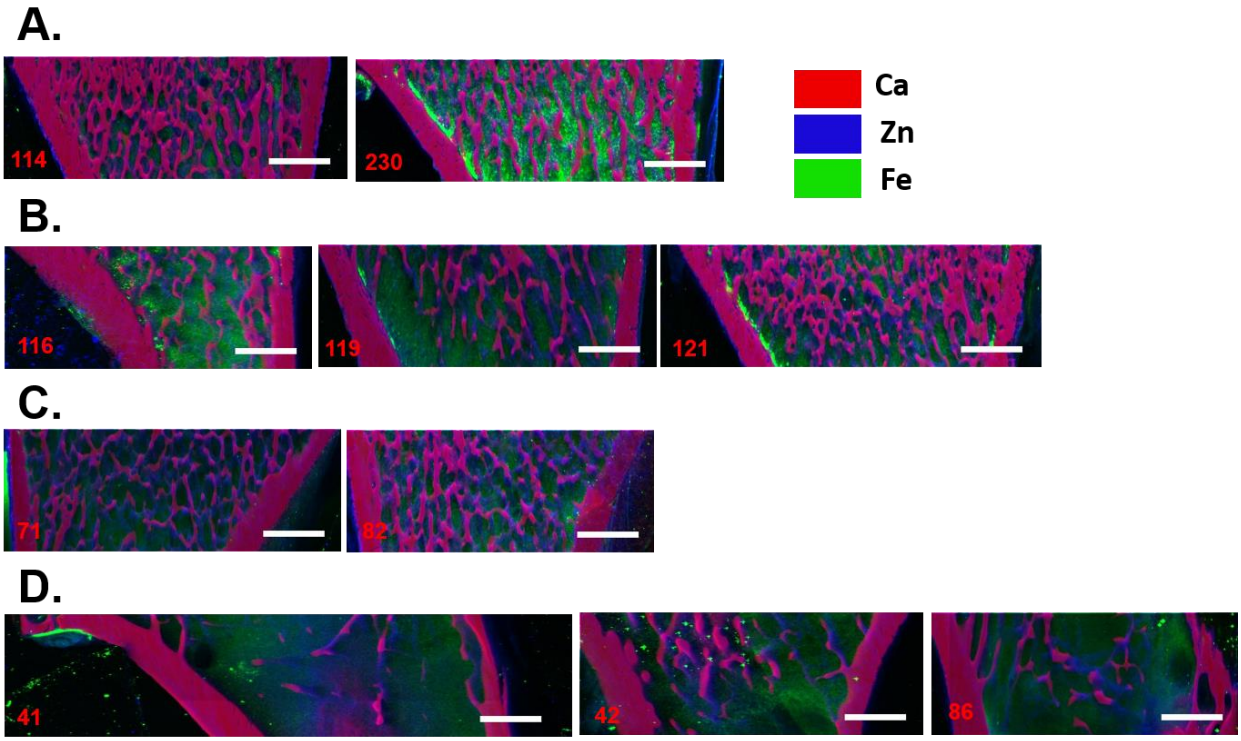

Figure 3.3. XRF tricolor merged images showing elemental distribution of Ca (red), Fe, (green), and Zn (blue) in (A) 6AM, (B) 6 OVX, (C) 12 AM, and (D) 12 OVX bone sections.

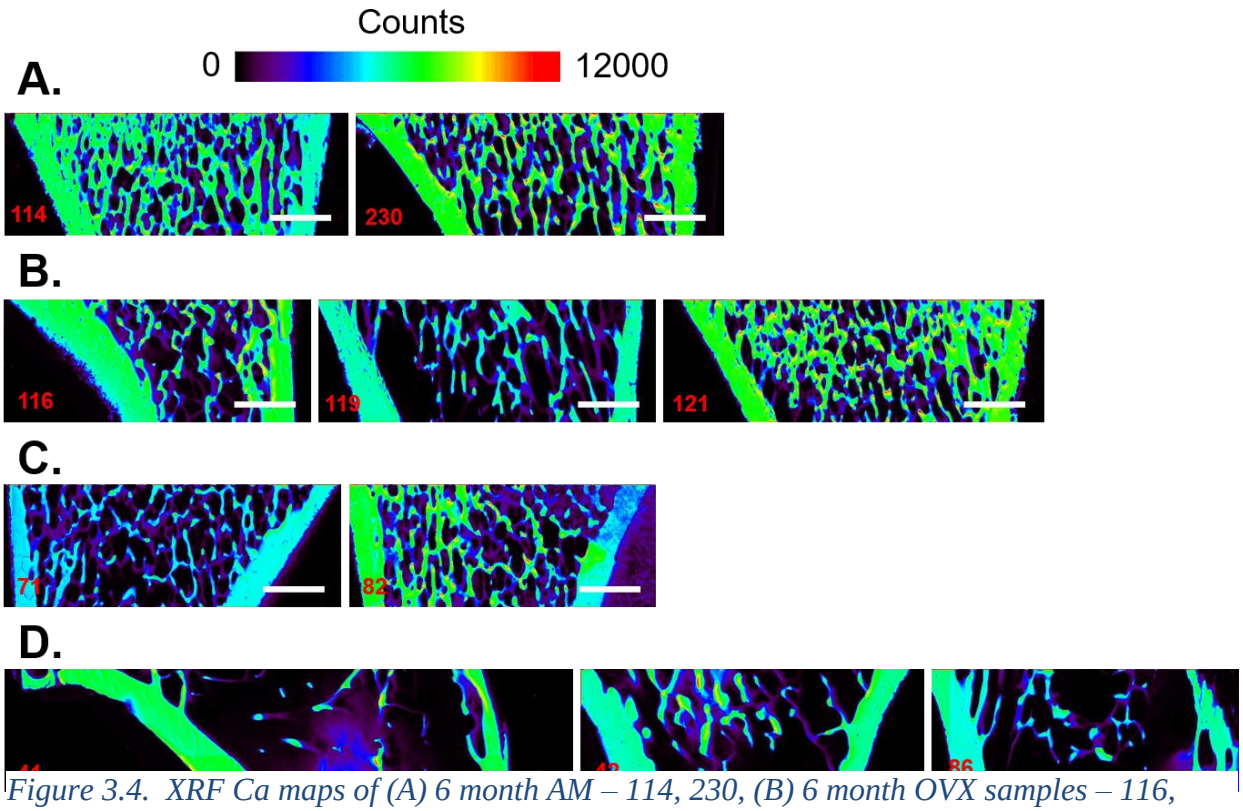

Figure 3.4. XRF Ca maps of (A) 6 month AM – 114, 230, (B) 6 month OVX samples – 116, 121, 119, (C) 12 month AM – 82, 71, and (D) 12 month OVX – 86, 41, 42.

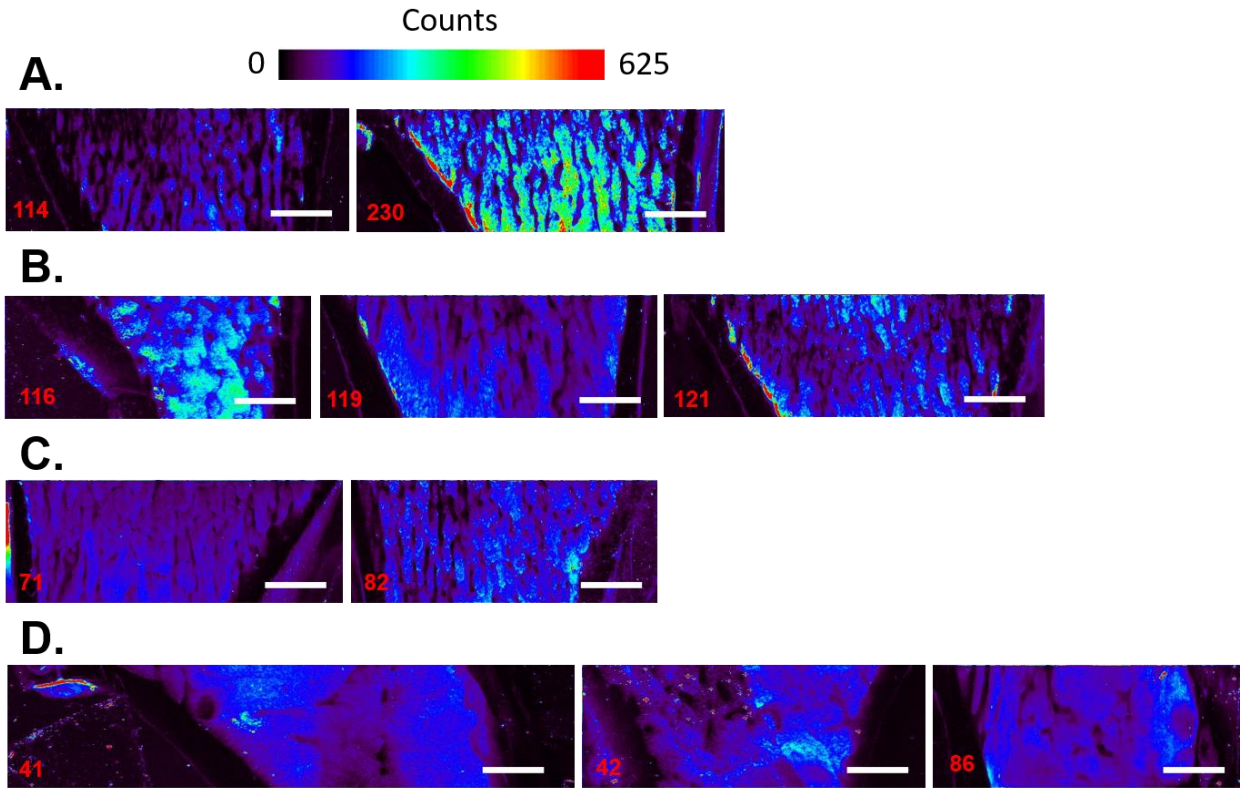

Figure 3.5. XRF Fe maps of (A) 6 month AM – 230, 114, (B) 6 month OVX samples – 119, 121, 116, (C) 12 month AM – 82, 71, 70, and (D) 12 month OVX – 42, 86, 40, 41.

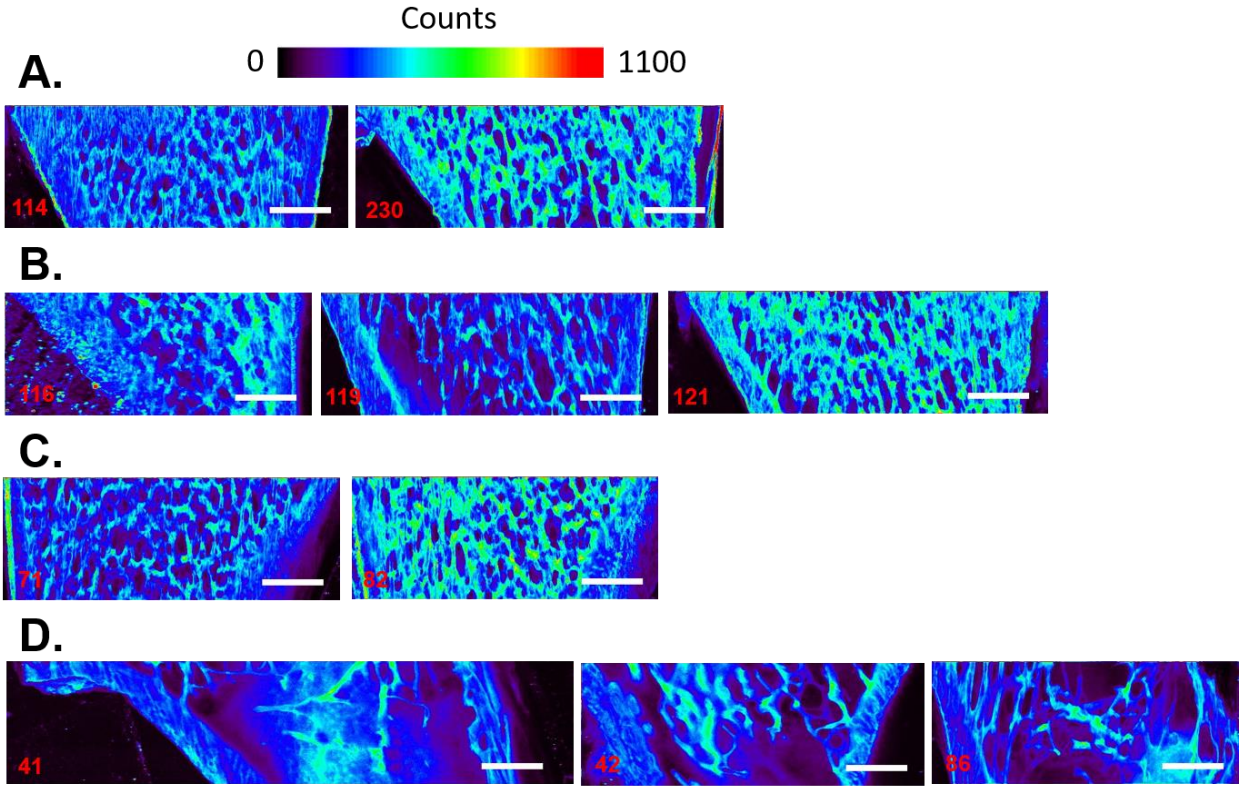

Figure 3.6. XRF Fe maps of (A) 6 month AM – 230, 114, (B) 6 month OVX samples – 119, 121, 116, (C) 12 month AM – 82, 71, 70, and (D) 12 month OVX – 42, 86, 40, 41.

3.4.5 Analysis of Raw XRF Intensity

In order to evaluate the effect of age- and OVX-induced osteoporosis on the spatial distributions of trace metals Fe and Zn in the femur samples, raw XRF intensity of Ca, Fe, and Zn was analyzed in XMAP Plotter by examining raw XRF intensity in both trabecular and cortical regions across all four groups.

Total Calcium

Average Ca XRF intensity (**Figure 3.7**) compared across all four groups show that in trabecular bone (**Figure 3.7A**), there was a 29% decrease in calcium for the 6 OVX group compared to 6 AM controls (p=0.23). The difference was much greater between the 12 month age groups, as the calcium XRF intensity for 12 OVX was 57% lower than 12 AM (p=0.30). Compared to the 6 AM group, a 72% decrease in calcium was observed for the 12 OVX group (p=0.01). Considering the change of age alone, a significant decrease of 35% in trabecular calcium was observed for 12 AM compared to 6 AM (p=0.29).

On the other hand, data analyzed for the cortical regions (**Figure 3.7B**) did not exhibit the same trend. Calcium in the cortical region of 6 OVX and 6 AM groups was very similar, as was calcium in 12 OVX and 12 AM groups. Compared to the healthy 6 AM group, the 12 OVX group showed an 11% decrease in calcium in the cortical regions (p=0.49). Additionally, there was a 13% decrease in cortical calcium content of the 12 AM group compared to the 6 AM group (p=0.43).

Trabecular histograms of total Ca content for each bone sample are shown in **Figure 3.8**. Histograms report XRF voxel intensity and percentage of total voxels in bins that are 1% of the total count. According to the data, it is clear that the 12 OVX group has less voxels presented across the higher intensity bins compared to the other groups. This would agree with data showing the lowest average Ca count in the 12 OVX group.

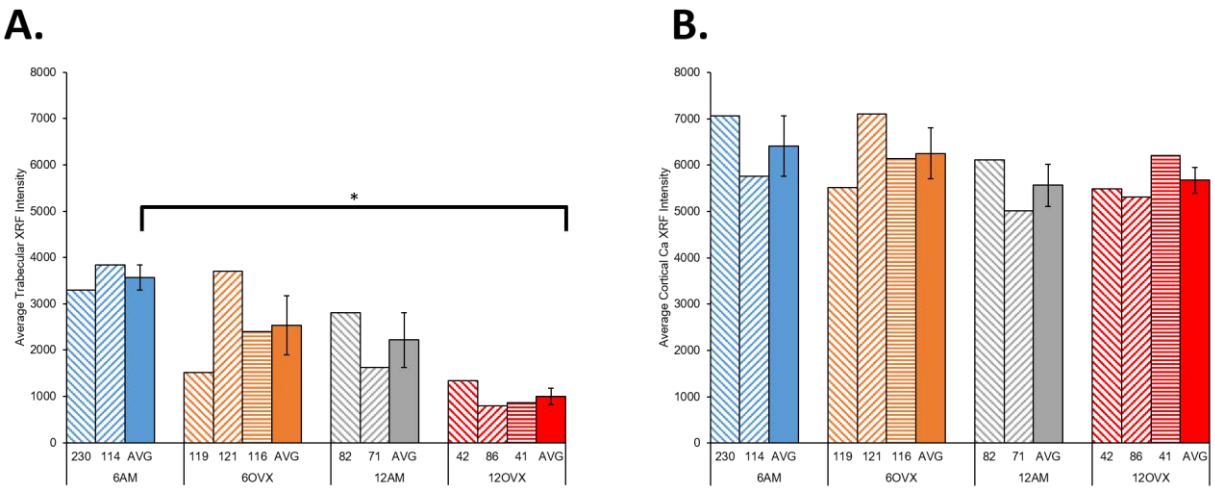

*Figure 3.7. Raw Ca XRF Intensity values in (A) trabecular and (B) cortical bone. Note: individual bone samples in stripes, averages for each group are filled. *p<0.05*

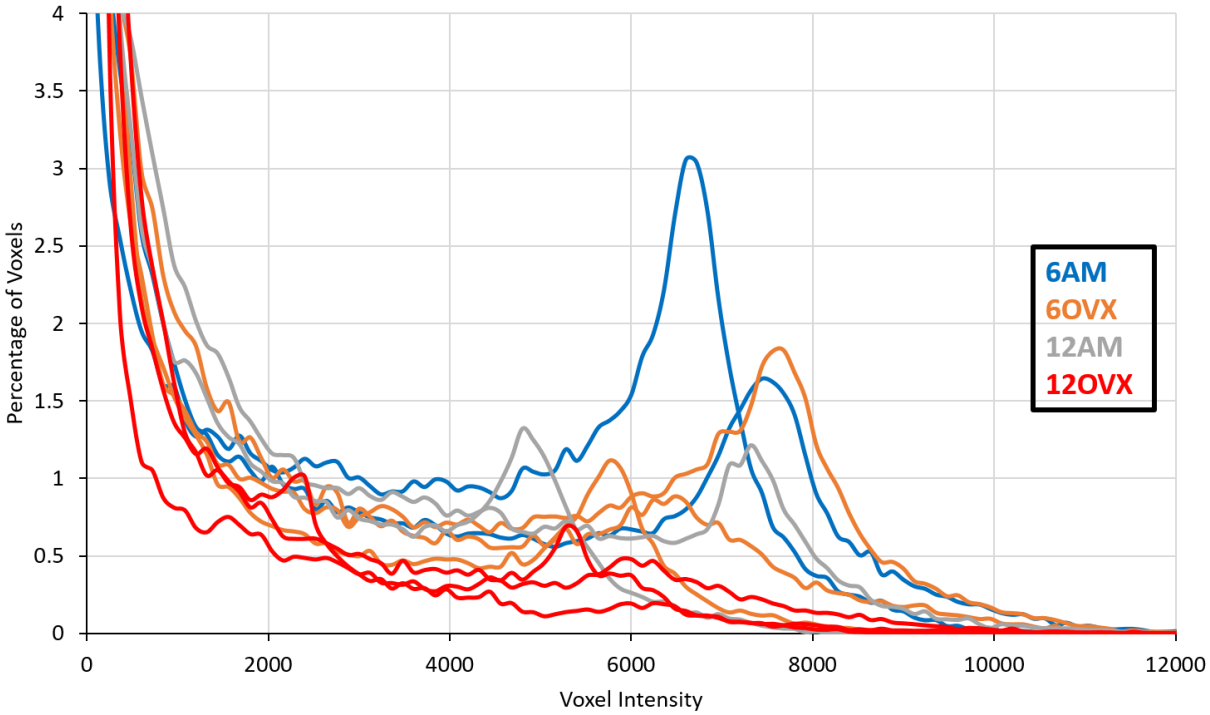

Figure 3.8. Histogram of trabecular Ca content reporting XRF voxel intensity and % of total voxels where every 120 voxels (1% of total) are binned together.

Total Iron

XRF iron intensity values for the trabecular regions (**Figure 3.9A**) showed that there was a 4% decrease in Fe in the 6 OVX group compared to the 6 AM group (p=0.96). Compared to the 12 AM group, there was an 11% increase in Fe in the trabecular region of the 12 OVX group (p=0.57). Moreover, when comparing the 12 OVX group with the healthy 6 AM, there was a 19% decrease in the osteoporotic-like group (p=0.79). However, when considering age alone in the healthy control groups, there was a 27% decrease in trabecular iron for the 12 AM group when compared to the 6 AM (p=0.71).

XRF iron intensity values for the cortical regions (**Figure 3.9B**) showed a 0.3% decrease in the 6 OVX group when compared to the 6 AM control group (p=0.99). Compared to the 12 month AM control group, cortical iron intensity was 31% lower for the 12 month OVX group (p=0.20). When comparing the 12 OVX group to the 6 AM group, there was a 27% decrease in cortical iron for the osteoporotic-like group (p=0.71). Considering the age factor alone, the 12 AM group had an increase of 5% in cortical iron compared to the 6 AM group (p=0.94).

Trabecular histograms of total Fe content for each bone sample are shown in **Figure 3.10**. Histograms report XRF voxel intensity and percentage of total voxels in bins that are 1% of the total count. According to the data, it is unclear as to the effect of Fe age and OVX conditions on trabecular bone. The histograms appear to have a lot of variation from sample to sample which agrees with the large amount of standard error reported in the XRF average intensities.

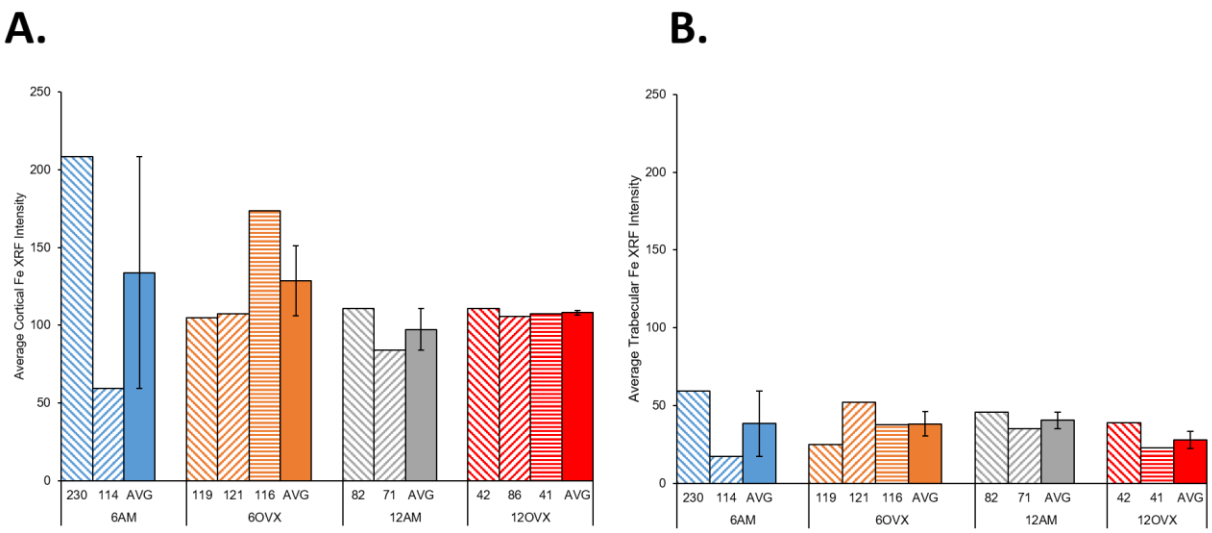

Figure 3.9. Raw Fe XRF Intensity values in (A) trabecular and (B) cortical bone. Note: individual bone samples in stripes, averages for each group are filled.

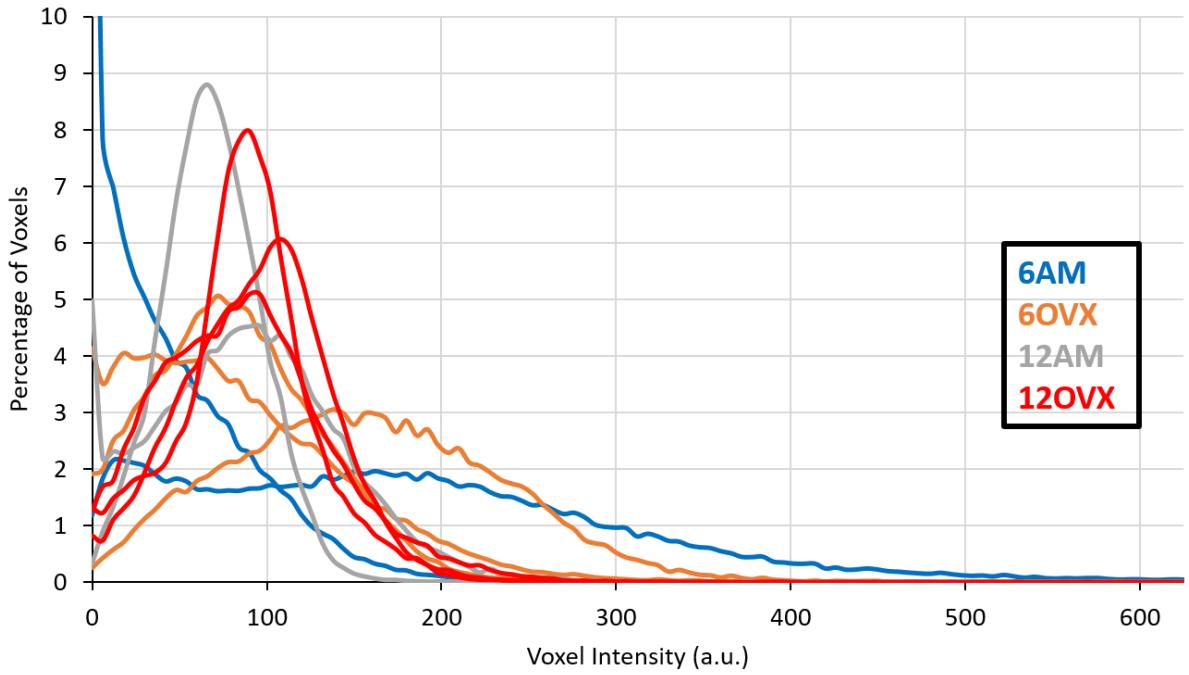

Figure 3.10. Histogram of trabecular Fe content reporting XRF voxel intensity and % of total voxels where every 6 voxels (1% of total) are binned together.

Total Zinc

Data analysis for total zinc intensity (**Figure 3.11**) shows that the 6 OVX group had 7% less zinc in the trabecular region compared to the 6 AM group (p=0.62) (**Figure 3.11A**). Trabecular zinc for the 12 OVX group was significant lower, by 31%, compared to the 12 AM group (p=0.34). Trabecular zinc in the 12 OVX group was also significantly lower, by 30%, compared to the 6 AM group (p=0.17). Considering the age factor alone, we observed a 3% increase in trabecular zinc for the 12 AM group compared to the 6 AM group (p=0.92).

Data analysis for the cortical regions (**Figure 3.11B**) indicate that there was a 6% decrease in zinc for the 6 OVX group compared to the 6 AM group (p=0.68). When comparing the 12 month age groups, a 22% decrease in cortical zinc was observed for the 12 OVX group compared to the age-matched controls (p=0.34). However, compared to the 6 AM group, cortical zinc in the 12 OVX group was only 14% lower (p=0.39). When comparing the two age-matched control groups alone, a 10% increase in cortical zinc was observed for the 12 AM group compared to the 6 AM group (p=0.62).

Trabecular histograms of total Zn content for each bone sample are shown in **Figure 3.12**. Histograms report XRF voxel intensity and percentage of total voxels in bins that are 1% of the total count. The histograms appear to have some variation from sample to sample which agrees with the standard error reported in the XRF average intensities. It does appear that the 12 OVX group has a larger percentage of voxels towards the lower intensity bins, indicating less Zn present in the older osteoporotic samples. This would agree with the trabecular XRF intensity data.

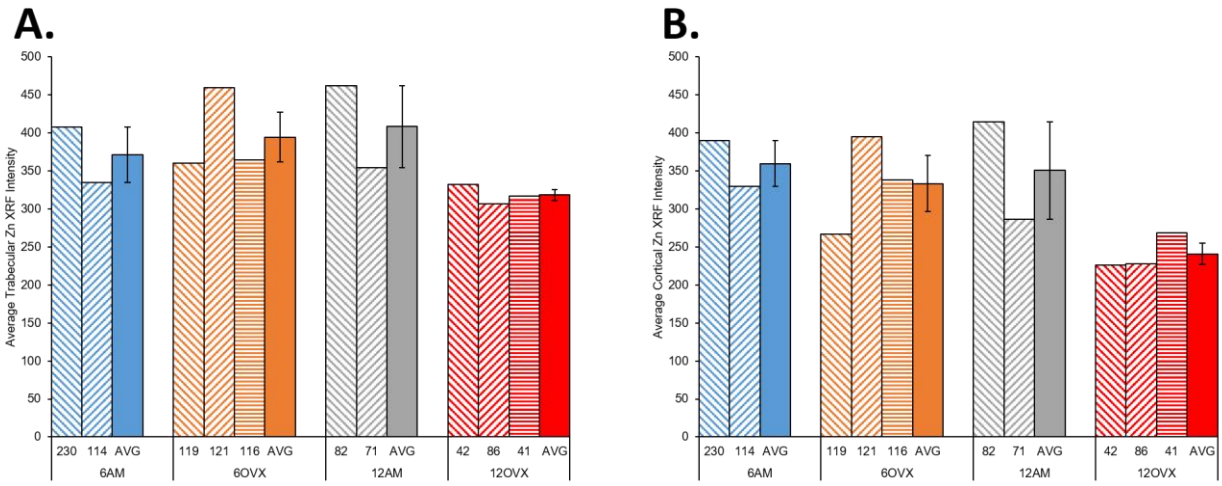

Figure 3.11 Raw Zn XRF Intensity values in (A) trabecular and (B) cortical bone. Note: individual bone samples in stripes, averages for each group are filled.

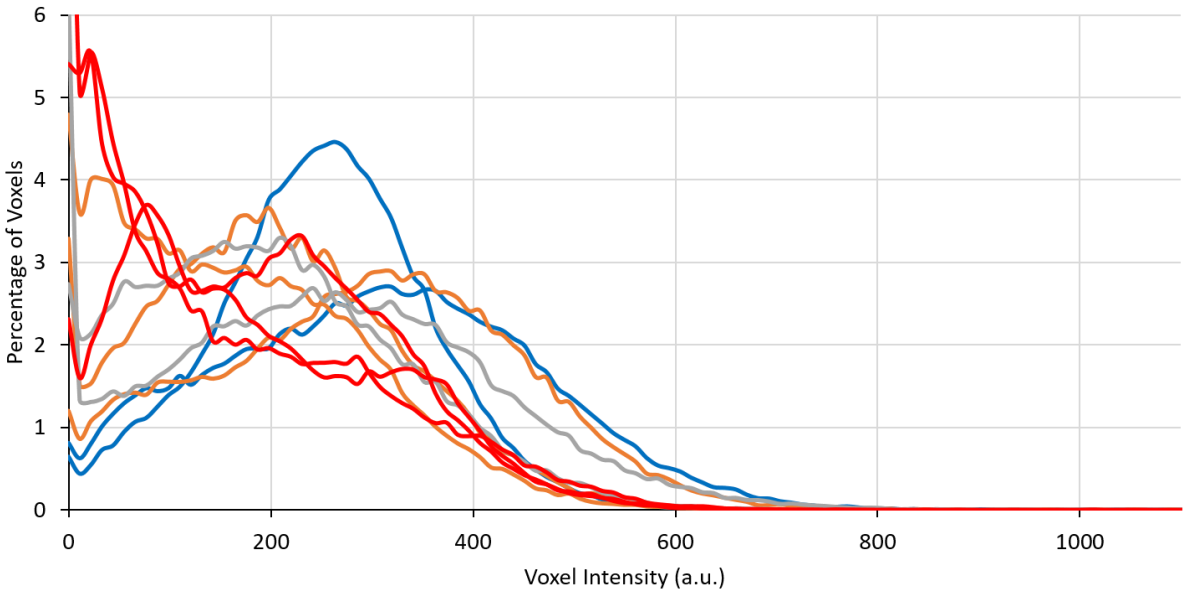

Figure 3.12. Histogram of trabecular Zn content reporting XRF voxel intensity and % of total voxels where every 11 voxels (1% of total) are binned together.

Fe:Ca Ratio

Raw iron XRF intensity was normalized to calcium content by taking average XRF intensity value of iron and dividing by the average intensity of calcium across both trabecular and cortical regions. Because calcium intensity is over two orders of magnitude greater than that of iron, it was used as a reference for data normalization. Average Fe:Ca ratio is reported in trabecular (**Figure 3.13A**) and cortical (**Figure 3.13B**) regions.

Results showed that iron content in the trabecular region (**Figure 3.13A**) was 45% higher for the 6 OVX group compared to the 6 AM group (p=0.59). In the 12 month age groups, 12 OVX is a 149% increase was observed for the 12 OVX group compared to the 12 AM group (p=0.03). Compared to the 6 AM group, the Fe:Ca ratio was 188% higher compared to the 12 OVX group (p=0.12). When considering the age factor alone, Fe:Ca ratio was 15% higher for the 12 AM group compared to the 6AM (p=0.84).

Results for cortical bone (**Figure 3.13B**) showed that overall differences across the groups were not significant. Specifically, Fe:Ca ratio was 5% higher for the 6 OVX group compared to the 6 AM group (p=0.94). In the 12 month age groups, Fe:Ca was 30% lower for the 12 OVX group compared to the 12 AM group (p=0.17). In addition, compared to the 6 AM group, Fe:Ca was 11% lower in the 12 OVX group (p=0.84). Considering the age factor alone, a 27% increase was noted for the 12 AM group compared to the 6 AM group (p=0.67).

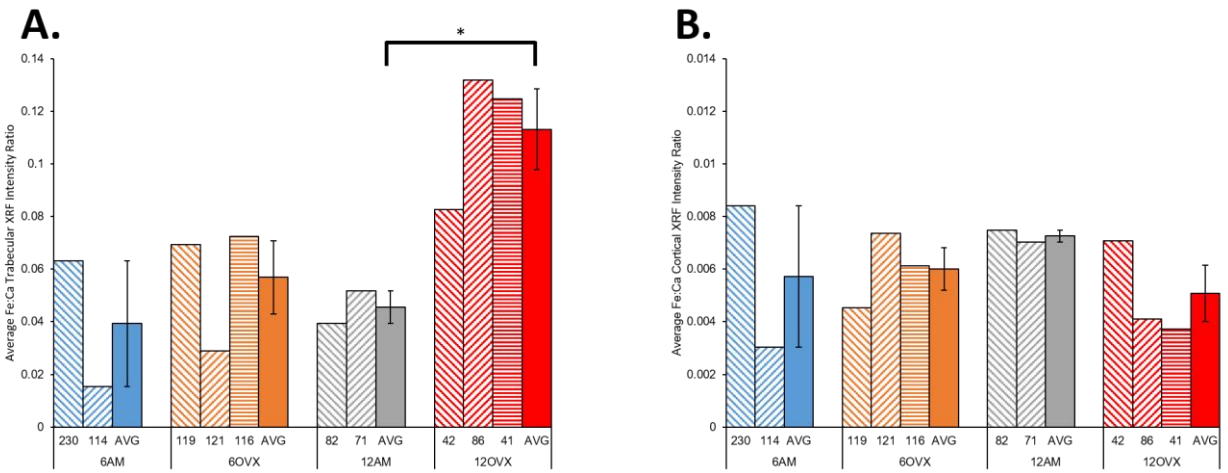

Figure 3.13. Raw XRF Fe:Ca ratio in (A) trabecular and (B) cortical bone. Note: Individual bone samples in stripes, averages for reach group are filled.

Zn:Ca Ratio

Due to its relatively high intensity in the XRF maps, calcium was also used as a reference element normalizing zinc. Average Zn:Ca intensity ratios were calculated for both trabecular (**Figure 3.14A**) and cortical (**Figure 3.14B**) regions. We observed a 38% increase in Zn:Ca ratio for the trabecular bone of the 6 OVX group compared to the 6 AM group (p=0.11). A 57% increase in Zn:Ca ratio was seen in the 12 OVX group compared to the 12 AM group (p=0.18). Compared to the 6 AM group, the 12 OVX group had a 150% increase in Zn:Ca (p=0.08). When considering the age factor alone, a 59% increase in Zn:Ca was observed for the 12 AM group compared to the 6 AM (p=0.11).

Data for cortical bone (**Figure 3.14B**) showed a 9% increase in Zn:Ca for the 6 OVX group compared to the 6 AM group (p=0.11). Compared to the 12 AM group, there was a 30% decrease in Zn:Ca for the 12 OVX group (p=0.02). Moreover, compared to the 6 AM group, a 3% reduction in Zn:Ca was seen for the 12 OVX group (p=0.63). When considering the age factor alone, cortical regions from the 12 AM group had 26% higher Zn:Ca values compared to the 6 AM group (p=0.02).

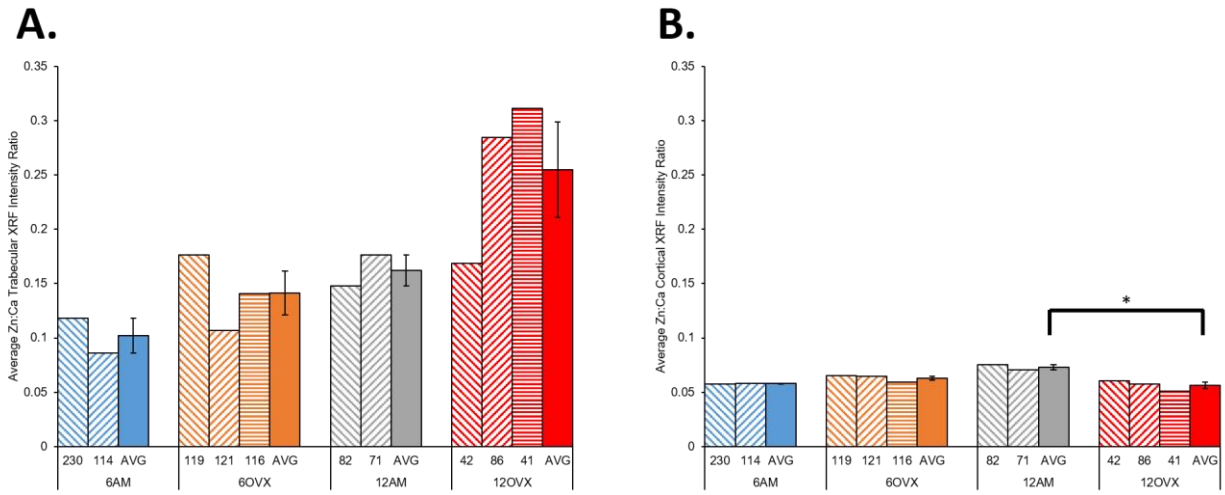

Figure 3.14. Raw XRF Zn:Ca ratio in (A) trabecular and (B) cortical bone. Note: Individual bone samples in stripes, averages for reach group are filled.

3.5 Discussion

Currently, the role of trace elements in the development of osteoporosis is not well understood. Structurally, both Zn and Fe levels have been shown to be lower in osteoporotic patients compared to healthy individuals.[83,84] On the molecular level, the mechanisms support contrasting roles for Zn and Fe in maintaining bone health. Specifically, Zn is involved in stimulating bone growth through promotion of osteoblast proliferation and differentiation.[85–87] Also, Zn inhibits bone resorption though inhibition of osteoclasts formation.[88] Fe shows a contrasting role, promoting osteoclasts formation and inhibiting osteoblastogenesis.[89–91]

Using a murine model, we used synchrotron X-ray fluorescence microscopy (μXRF), a non-destructive technique, to map out the spatial distributions of Fe and Zn in the femurs of 6 and 12 month old ovariectomized (OVX) rats. Trace metal analysis was conducted to confirm the loss of Zn and to clarify the role of Fe in the osteoporotic bone.

3.5.1 Importance of Zinc in maintaining bone health

Human bones only contain about 0.0126-00217 wt. % Zn, however this accounts for 28% of the total amount of Zn in the body.[92–94] Zn plays a structural role in the bone matrix and is involved in the formation of hydroxyapatite crystals, in which Zn complexes with fluoride; and can substitute Ca in the HA crystal.[70,83,95] Zn is also a key component in maintaining bone metabolism, by means of promoting osteoblast cell proliferation and differentiation.[85–87] Specifically, Zn is an essential cofactor for enzymes involved in DNA and RNA synthesis, and enzymes involved in protein synthesis.[70] The synthesis of cellular proteins require Zn to activate aminoacyl-tRNA synthetase. Zn is also a co-factor for alkaline phosphatase (ALP), a key enzyme involved in bone mineralization.[70,96,97] Moreover, Zn inhibits bone resorption by inhibiting osteoclast cell-like formation.[88]

Impaired bone growth is a common finding in both animals and humans with Zn deficiency.[98,99] Indeed, Zn deficiency may lead to significant decreases in the mineral density and volume of both cortical and trabecular bones. For example, Zn deficiency in rats was shown to cause a decrease in Zn concentration in femur bones as well as a reduction in cancellous bone mass and deterioration of trabecular bone architecture.[70,100,101] A clinical research study showed that the Zn content of bones in patients with osteoporosis is significantly lower than that of healthy patients.[83,84] A double-blind study showed that Zn supplements can reduce bone loss in

osteoporotic patients.[70] It has also been suggested that supplements of trace minerals with or without calcium in post-menopausal women have beneficial effects on bone density.[102] Together, these studies highlight the important role of Zn in maintaining bone health.

3.5.2 Importance of iron in maintaining bone health

Similar to Zn, Iron (Fe) is also an important micronutrient involved in many cellular functions, most notably those involving hemoglobin and myoglobin, proteins responsible for transportation of oxygen.[103,104] In contrast to Zn, excessive Fe can be stored in the human body in the form of ferritin, or hemosiderin (the degradation product of ferritin) in the bone marrow, or liver.[105] However, too much excessive Fe can be toxic due to its ability to generate free radicals and the inability of the human body to regulate the excretion of Fe overload.[106–108]

Studies have shown that osteoporosis is a complication of diseases that involve Fe toxicity, such as thalassemia and hemochromatosis.[89,109–113] Experimentally, the thinning of cortical bones and increased bone resorption have been observed in rats experiencing Fe-overload.[114] A clinical research study showed that women age 41 and older with high serum ferritin concentrations were associated with lower bone mineral density and a greater risk of osteoporosis.[115]

Recent studies suggest that iron excess directly controls bone formation and/or remodeling through collagen synthesis.[113,116–120] Iron is a required cofactor for the activity of lysyl oxidase, which catalyzes cross-linking of adjacent collagen fibers. A deficiency in iron may result in decreased cross-linking activity and thus weaker collagen fibers.[121]

Moreover, iron is known to promote bone-resorption by osteoclasts and suppresses osteoblastogenesis.[90,91,111] Studies on the mechanisms of Fe toxicity have showed that increased reactive oxygen species produced by Fe overload may contribute to osteoporosis by increasing bone resorption.[112] Additionally, the inhibition of alkaline phosphatase activity was observed in conjunction with a decline in mineralization caused by Fe overload.[91]

In contrast, some studies have reported the positive effects of Fe supplementation on bone health. For example, one clinical research study reported lower Fe levels in the bones of postmenopausal women with osteoporosis, based on their method of high-resolution inductively

coupled plasma mass spectroscopy.[83] Moreover, an Fe restricted diet was shown to increase the porosity of trabecular bone in rats.[122]

Despite the biological importance of Fe, its role in maintaining bone health is not well understood. This is compounded by a lack of extensive clinical studies in osteoporosis-related phenotypes. With such vast, contrasting evidence, more research is needed to clarify the role of Fe in the development of osteoporosis.

Our work demonstrates the use of a non-invasive technique, Synchrotron Radiation X-Ray Fluorescence (XRF), to analyze the spatial distributions of calcium, iron, and zinc in sectioned rat femurs.

As expected, there was a significant decrease in Ca observed in the bones of ovariectomized (OVX) animals compared with their age matched controls.[71] Moreover, the decrease in Ca was much more apparent in trabecular bone regions compared to the cortical regions. Previous studies have suggested that trabecular bone is more sensitive to biological factors involved in bone remodeling.[123] Raw XRF data also suggest a decrease in overall Zn in the OVX bones that was observed in both trabecular and cortical regions. This decrease was more striking in the trabecular regions. However, when normalized to Ca content, the amount of Zn actually appeared to have increased, when comparing OVX to their age matched controls. These results suggest that, compared to zinc, the loss of calcium as a result of the induced osteoporotic state was more extensive. This may be due to the fact that, proportionally, there is less Ca in OVX bones, thereby contributing to an increased Zn:Ca ratio. In human, vertebral Ca/Zn is inversely related to age, suggesting that skeletal zinc is conserved better than calcium in later life.[124]

No significant changes were observed in the overall amount of Fe in OVX bones compared to the age matched controls. In both trabecular and cortical regions, average Fe XRF intensity were only slightly lower in the OVX samples. However, normalized data showed that Fe:Ca ratio actually increased for OVX samples, suggesting a greater decrease in Ca compared to Fe. This is to say that, proportionally, the relative amount of Fe compared to Ca increased for the OVX samples. More specifically, an increase in Fe:Ca ratio was observed in the trabecular

areas, indicating an increase in relative iron concentration. A small, nonsignificant decrease in Fe:Ca ratio was observed in cortical areas.

Both Zn and Fe contribute greatly to overall bone health, however they have opposite roles in terms of oxidative stress. Zn is an essential component in many of the enzymes that protect cells against reactive oxygen species and help repair damaged DNA.[125] In contrast, free Fe produces reactive oxygen species, leading to oxidative stress.[126] Induced Fe toxicity in rats has been shown to increase oxidative stress, resulting in increased accumulation of Fe in liver, spleen and bone, increased bone resorption, and thinning of trabecular and cortical bone.[114] It has been previously suggested that oxidative stress leads to an imbalance of bone turnover by enhancing bone resorption, the underlying cause of postmenopausal osteoporosis.[127] This will consequently leads to decreased bone strength, and increased bone porosity and fragility. Our results show that estrogen removal and/or the aging process may contribute to a marked decrease and increase in Zn and Fe content of bone, respectively. As a result, there is increased oxidative damage to bone tissue, as well as a reduced ability to protect against these. Together, these factors may be responsible for the increased trabecular porosity observed in osteoporotic bones and the associated fracture risk.

3.6 Conclusion

This work demonstrates the use of X-ray fluorescence (XRF) as a technique to study trace metals in osteoporosis. XRF is non-destructive to the sample and can detect trace amounts of elements, creating elemental maps to study distributions in biological samples. This is one of the first studies to our knowledge using this technique to study the effects of induced osteoporosis on changes in Fe and Zn distributions in bone. This technique has applications across other diseases involving biological tissue. However, for this experiment, XRF helped better define the potential roles of trace metals Fe and Zn in osteoporosis.

Chapter 4 : Investigating the Inhibition of Breast Cancer Microcalcification Formation by Exogenous Zinc

Abstract

A crucial early indicator of breast cancer is the appearance of mammographic mammary microcalcifications, small mineral deposits consisting primarily of hydroxyapatite. The alteration of the physicochemical properties of these microcalcified nodules during breast cancer progression is believed to be linked to malignancy, and as such, better understanding of the functional role of microcalcifications could improve our knowledge of the metastatic behavior of breast cancers. Histological characterization of 4T1 breast cancer calcifications in conjunction with Raman spectroscopy reveal that the 4T1 spheroids contain bone-like microcalcified regions similar to hydroxyapatite in mineralized osteoblasts. Additionally, we observed a reduction of microcalcification formation and a decrease in metastatic behavior in the presence of exogenous zinc. Taken together, our results demonstrate the potential use of zinc as a therapeutic agent for inhibiting breast microcalcifications.

4.1 Introduction

Breast cancer is the most frequently diagnosed cancer and the leading cause of death among the female population. It accounts for 23% of total cancer cases, and 14% of all cancer deaths.[128] Despite the increasing incidence rates, annual mortality rates have decreased by 1.9% per year from 2008 to 2012.[129] This is thought to be contributed by a combination of early detection through better diagnostic methods and enhanced treatment methods. Mammographic detections account for up to 90% of breats cancer detections. Mammographies detect cancers through either a soft tissue mass, which accounts for 40% of detections, or thought clustered microcalcifications, which account for 60% of detections.[130] Breast calcifications are very common in elderly, as they appear in roughly 86% of mammographies in women age 76-79.[131] Breast microcalcifications are small mineral deposits consisting of crystalline calcium or calcium phosphate. Mammographies of mammary microcalcifications are routinely used as an early indicator of breast cancer detection. In fact, up to 50% of nonpalpable breast cancers are detected exclusively through microcalcifications.[130]

However, not all calcifications are cancerous. Only about 20% of biopsied calcifications found in mammograms are cancerous, while 80% are benign calcified breast tissue.[130,132]

Although benign and cancerous calcifications are both forms of calcified tissues, they differ drastically in both physical appearance and chemical composition. Understanding the difference between benign and cancerous calcifications is a crucial step in the diagnostic process.[132]

Physically, benign and cancerous breast calcifications are differentiated by their shape, size, density, number and distribution. Breast calcifications have numerous shapes, most of which are benign. Typically, benign breast calcifications are seen as large, spherical, round, dense structures. However, many other shapes and morphologies have been identified, such as linear, coarse, cylindrical, and punctate small grains of round regular size. Although many different shapes exist for benign calcifications, cancerous, malignant calcifications exist predominantly in small, variable shape clusters with a branching structure.[132] The size of breast calcifications is another important characteristic which will give insight into its classification as benign or cancerous. Typically calcifications under 2mm in size are considered suspicious. Larger calcifications are thought to be associated with benign tissues.[132] While size is an important indicator, it is not enough to decide the classification of malignant cancer or benign tissue. Density is another characteristic important in identifying and classifying breast calcifications in mammographies. It is generally agreed that low density calcifications are suspicious and suggest cancer. High density calcifications are usually accompanied by benign lesions.[132] However, similar to size, density alone cannot conclusively conclude the nature of a calcification. The number of calcifications also plays a role in determining the nature of its classification. Clusters, or numerous calcifications within close proximity, are characteristic of malignant breast cancer.[132] When radiologist analyze mammographies, a cluster is defined as five microcalcifications within one cubic centimeter, or one square centimeter on two projections.[132] Clusters are one of the most important physical characteristics in differentiating benign lesions from metastatic cancers. Distribution is the final physical characteristic used in identifying potentially cancerous calcifications. A diffuse, or disperse patter of calcifications usually indicates benign lesions, whereas clusters tend to indicate cancer.[132] Linear or segmentally patterns tend to indicate more malignant cancer, as these are signs of cancer spreading. Overall, microcalcifications that indicate breast cancer on mammograms tend to have branched structure, with small, low density, clustered calcifications.[132] Benign lesions can have various shapes, but tend to be larger, high density, diffuse calcifications. Physical characteristics

of microcalcifications alone are not sufficient enough to diagnose breast cancer, but they often can be used to predict whether further testing should be done.[132]

Benign and cancerous breast calcifications differ in physical appearance, but also in chemical composition. Chemically, breast calcifications are classified into two types: type I calcium oxalate (CO), or type II hydroxyapatite (HA).[133,134] The chemical composition between type I and type II calcifications differ greatly, as CO has the formula $CaCO_4$ and HA has the formula $Ca_{10}(PO_4)_6(OH)_2$. The characteristics between CO and HA are governed by their chemical composition and lead to different structural and physical appearances. Type I CO calcifications are amber in color and partially transparent. Type II HA calcifications have a greyish white color and are more opaque. The crystal structure between type I and type II are distinctively different. Type I CO calcifications have a pyramidal structure with planar surfaces, whereas type II HA calcifications are egg-like or spindle-like shaped with irregular surfaces.[133,134] More importantly, the chemical composition and classification of breast calcifications are associated with metastatic behavior of cancers. Type I CO calcifications are associated with benign lesions and non-invasive carcinomas. Type II HA calcifications are associated with both benign and metastatic cancer.[133,134]

4.1.1 Carbonate Substitution in Breast Cancer Calcifications

Type II HA calcifications can be found in both benign (non-invasive) and invasive cancers. Since type II HA calcifications can be found in all types of breast cancers, it may be difficult to distinguish between them using calcifications alone. However, there is a measurable difference in the number of impurities within the HA crystal. Type II HA calcifications are chemically impure, containing small amounts of carbonate ions, which displace phosphate ions in their crystal structure. Rogers et al. demonstrated a relationship between pathological grade of breast cancer and the chemical nature associated with microcalcifications.[135] Specifically, they found that carbonate substitution is associated with the pathology of breast cancers. Benign lesions tend to have the highest carbonate substitution, non-invasive cancers have an intermediate amount of carbonate substitution, and invasive cancers have the lowest amount of carbonate substitution. In their study, 236 patient biopsies of breast cancers were studied for both pathological grade and carbonate content in microcalcifications. The degree of carbonate substitution was assessed through Fourier Transform Infrared Spectroscopy (FTIR) using

hydroxyapatite standards of known carbonate concentration. FTIR is a vibrational fingerprinting technique which relies on absorbance of atoms at different frequencies based on their bond lengths. Briefly, chemical bonds will have distinct wavelengths of light that are absorbed due to natural vibration of the molecules. In this case, the carbonate content in each biopsied sample was quantified through comparison of peak intensities between the standards. The intensity of the phosphate peaks and amide peaks in each sample were compared to yield a matrix:mineral ratio (amide:phosphate). Baker et al. was able to demonstrate that the degree of carbonate substitution in microcalcifications of breast cancer biopsies ranged from roughly 1% to 2.5%. Within this range, three pathologies of breast cancer were able to be identified based on degree of carbonate substitution. Benign breast cancers had an average carbonate substitution of about 2.08%. Ductal carcinoma in situ (DCS), a form of non-invasive breast cancer had an average carbonate substitution of about 1.83%. Lastly, invasive breast cancer had an average carbonate substitution of about 1.41%. Furthermore, matrix:mineral ratio decreased with pathological invasiveness of the cancer. Mean values of invasive, DCIS, and benign breast tissue calcifications were: 0.82, 0.37, and 0.11, respectively. Together the data suggest a strong correlation between pathological invasiveness of breast cancer and degree of carbonate substitution in breast tissue calcifications.[133]

Although the correlation between decreasing carbonate substituted hydroxyapatite and increasing malignancy of cancer is generally accepted, the mechanism remains unclear. On the molecular level, increased carbonate content in benign calcifications is thought to be related to its reactivity and solubility. Porter et al. demonstrated an increase in reactivity of carbonated hydroxyapatite due to more carbonate ions in the lattice structure, making it less stable.[136] Increased carbonate content in calcified tissue leads to a more soluble calcium phosphate crystal, which in turn will increase the number of free calcium, phosphate, and hydroxide ions. Increased calcium, phosphate, or hydroxide ions may have an inhibitory effect on cancer progression, through preventing the activation of certain enzymes. For example, MMP-1 and MMP-3 mRNA protein expressions were found to be upregulated by calcium phosphate crystal induction.[137] Choi et al. demonstrated the effects of carbonate substituted hydroxyapatite on breast cancer cell behavior by growing cancer cells on varying carbonate substituted levels of hydroxyapatite.[138] Varying the degree of carbonate substitution lead to changes in both chemical and physical surface properties of the hydroxyapatite crystal. Briefly, increased carbonate

substitution in HA crystal linearly decreased surface roughness while increasing crystallinity. Breast cancer cell adhesion, growth, and interleukin-8 (IL-8) secretion were all studied in this experiment. IL-8 is an inflammatory cytokine overly expressed in cancer cells which promotes metastasis and angiogenesis.[139] On surfaces with low carbonate content, surface topography changes seemed to be the primary driver of differential cell behavior. Conversely, surfaces with high carbonate substitution saw cell behavior regulated by surface chemistry of the coatings. Also, the increase in calcium ions present from the increased solubility of carbonated substituted hydroxyapatite was shown to have no effect on IL-8 secretion or cell growth. Together, the data suggest carbonate substitution is decreases surface roughness while altering surface chemistry. This could have an effect on protein adsorption on the crystal surface, and subsequently integrin binding, affecting various integrin regulated pathways.[138]

Understanding breast cancer microcalcifications and its role in the development and progression of the disease could have numerous important benefits. It is still unknown how microcalcifications are involved in the mechanisms associated with breast cancer progression. Research in potential mechanisms of microcalcification development and progression could lead to discoveries in future diagnostic methods and targeted drug discovery and development treatments.

Until recently, the importance of microcalcifications in breast cancer was overlooked and considered to be a passive process associated with cellular degeneration, lacking biological significance. However, recent studies have suggested mammary mineralization is an active process regulated by similar cellular physiological pathways as those in bone mineralization.[140–142] Furthermore, breast cancers have been shown to overly express several bone matrix proteins, such as osteopontin (OPN) and bone sialoprotein.[143,144] Together these observations suggest mechanisms involved in bone mineralization could be involved in the formation of breast cancer calcifications.

4.1.2 Zinc and Cancer Progression

Zinc is a micronutrient essential for maintaining homeostasis in various anatomical systems. Zinc has functions in the gastrointestinal reproductive, neural, endocrine, ocular, and immune system. On the molecular level, zinc is widely found in numerous enzymes and proteins such as MMPs, lysases, isomerases, and hydrolases. Zinc has two unique properties that make it

unique compared to all other micronutrients. Firstly, zinc is virtually non-toxic, and the mechanisms that regulate its entry, distribution, and excretion from cells and tissues are so efficient that no disorders are known to be associated with excessive accumulation.[145] Secondly, zinc ions generally form stable, and flexible chemical bonds, or coordination with macromolecules, such as proteins. These unique properties are the reason why zinc participates in various biological processes, such as DNA synthesis.[146–149]

Zinc is thought to have important roles in chemoprevention. Serum zinc levels were linked to breast cancer risk in a clinical research study by Kaczmarek et al.[150] This study examined females with and without the BRCA1 mutation, a tumor suppressor gene. Women with this genetic mutation are five times more likely to develop breast cancer than those without the mutation.[151] In this study, females with and without the BRCA1 mutation who had higher serum zinc levels had a significantly lower risk of breast cancer than those with low serum zinc levels. This was true when serum was collected at moment of diagnosis or when serum was collected 1-2 years prior to diagnosis. Lower serum zinc levels, less than 750μg/L were at an increased risk of developing breast cancer regardless of BRCA1 mutation.[150]

Since higher serum zinc levels are correlated to decreased risk in development of breast cancer, it is not surprising that there is a close link between breast tissue zinc levels and breast cancer development. Higher zinc levels in breast tissue has been correlated to increased risk in development of breast cancer.[152,153] Compared to the adjacent tissues, breast tumor tissues have an accumulation of zinc which has been correlated with higher expression of cellular zinc importing proteins and lower levels of zinc transporters which efflux zinc out of the cell. This suggests cancer cells are bringing more zinc into the cell and transporting less out of the cell, leading to an overall intracellular accumulation.[154–156]

Zinc transportation into the cell, within the cell, and out of the cell is a complex process which involves dozens of zinc transporter proteins. Briefly, zinc transporter proteins can be categorized into two groups: ZnT and Zip zinc transporter proteins. ZnT and Zip have opposing roles in the regulation of zinc within the cell. Zip transporters increase intracellular zinc by promoting extracellular zinc to be transported across the cell membrane into the cytosol. ZnT proteins decrease intracellular zinc by transporting cytosolic zinc out of the cell. There are over 86 Zip and over 100 ZnT proteins known and of those 15 Zip, and 9 ZnT proteins are involved in

human cellular functions.[155] In breast cancer, zinc accumulates at the tumor site because there is an imbalance between Zip bringing zinc into the cell, and ZnT removing zinc from the cell. Specifically, high levels of ZIP6, 7, and 10 has been associated with breast cancer growth and metastasis.[153,157–159] Also, a rat tumor model was used by Lee et al. to confirm low level of ZnT1 in breast tumor cells. Compared to normal mammary cells, breast tumor cells saw a 55% reduction in the mRNA level of ZnT-1. This was accompanied by a 3.5 times increase in metallothionein (MT) protein levels. MT is a protein used to store cytosolic zinc or copper in order to prevent oxidative stress, suggesting zinc is being stored in tumor cells and not released through the normal ZnT-1 mechanism.[156] Accumulation of zinc in breast cancer may indicate a potential need for zinc in development and progression of breast cancer.

4.1.3 Zinc and Mineralization

Breast cancer is the most common cancer in women and second most common cancer worldwide, but many of its mechanisms are not fully understood.[160] In particular, the accumulation of zinc within the tumor cells is quite rare. Alterations in total zinc content are tissue specific and not associated with all cancers. Cancerous tissues of the liver, gallbladder, prostate, lung, cervix, and uterus are all associated with decreased zinc tissue concentrations compared to their healthy non-cancerous counterparts.[161–166] Prostate and breast cancers are often compared due to their many similarities. Anatomically, breast and prostate organs both contain ducts and function in similar fashions. Both breast and prostate cancers are known to be highly metastatic, form calcifications, and have abnormal zinc metabolisms.[167] The opposing accumulation of zinc in breast cancer and depletion in prostate cancers is unique, suggesting that altered zinc regulation in cancer is specific to the tissue. Two unique characteristics of breast and prostate cancers are their altered zinc accumulation and depletion, respectively, and their formation of calcified tissues. Whether these two properties are linked has yet to be fully examined.

It is known that zinc biology has importance in regulating healthy calcified tissues of the skeletal system. Zinc is an essential trace element which is needed in bone formation. Additionally, zinc deficiency has been linked to diseases like osteoporosis.[97,168] Zinc has been shown to stimulate alkaline phosphatase (ALP) and collagen synthesis in osteoblast cells in vitro.[169] However, the effects of excess zinc on osteoblasts cells was shown to alter the levels of

activated MMP-2, ALP, and inhibit mineralization in vitro.[55] Recently, Cox et al. investigated the role of ALP in breast cancer mineralization. A 4T1 mammary breast cancer 2D in vitro model was used to show ALP and proper phosphate transport are required for breast cancer mineralization. Also, this demonstrates that mineralization is a cell-mediated process which is actively being regulated, in part by ALP.[170] Although zinc important in regulating calcified tissue has been extensively studied for osteoporosis research, the effects of zinc on microcalcification formation in breast cancer has yet to be examined. This has in part been due to a lack of model system to form breast microcalcifications.

4.2 Objective

The goal of this study was to test the effects of exogenous zinc on in vitro microcalcification formation using a two-dimensional in vitro breast cancer model. Potential mechanisms of microcalcification formation thought to be inhibited by zinc such as ALP activity, and cell migration were investigated using this model. Previous work performed by Dorst et al. showed exogenous zinc inhibiting calcification of osteoblasts, ALP activity, and migration of osteoblasts in vitro. Using the results of this previous study we tested if zinc could inhibit microcalcification formation in an in vitro breast cancer model previous developed by Cox et al.[170] The goal was to determine any potential effects exogenous zinc has on ALP and migration of breast cancer cells to determine their role in microcalcification formation. Since ALP is thought to be necessary in the mineralization process, any potential inhibition by zinc may be caused by dysregulation of ALP. Since Dorst et al. determined zinc as an inhibitor of cell migration in osteoblasts, cell migration of breast cancer cells were tested with exogenous zinc to determine if the behavior is true for breast cancer cells, as well.[54,55]

4.3 Materials and Methods

4.3.1Materials

4T1 cells were cultured using low glucose DMEM obtained from ThermoFisher scientific (11885084), phosphate buffered saline obtained from ThermoFisher scientific (10010072), 0.05% trypsin EDTA obtained from ThermoFisher scientific (25300054). Culture medium supplement FBS was obtained from Atlanta Biologicals (S11050H) and 10,000 U/mL Penicillin-streptomycin solution obtained from ThermoFisher scientific (15140122). The MTS assay was purchased from Promega (G5421), and PicoGreen assay purchased from ThermoFisher scientific (P7589). ALP staining was performed using SIGMAFAST BCIP®/NBT tablets purchased from

Sigma-Aldrich (B5655). ALP quantification was performed using 4-nitrophenyl phosphate disodium salt hexahydrate purchased from Sigma-Aldrich (N4645). Raman spectroscopy was performed at Stony Brook Universities' School of Atmospheric and Marine Sciences with a Renishaw inVia Confocal Raman Microspectrometer. Type I rat tail collagen used in migration studies was purchased from Corning (354236). Gel Zymograms were run using the Criterion™ cell purchased from Bio-Rad (1656001) and 10% Criterion Zymogram Gels with Gelatin, 12 + 2 well 45µL (3450079).

4.3.2 Cell Culture

4T1 murine mammary adenocarcinoma cells were used as a model cell line for studying breast cancer microcalcifications. 4T1 cells closely mimic highly metastatic stage IV human breast cancer. Cox et al. previously showed the ability of the 4T1 cell line to produce microcalcifications in vitro.[170] Cells were grown in complete growth medium containing Dulbecco's Modified Eagle Medium (DMEM) containing low glucose (1g/L), supplemented with 10% fetal bovine serum (FBS) and 1% Penicillin-Streptomycin solution to yield a final concentration of 100 units/mL Penicillin and 100 µg/mL Streptomycin.

4.3.3 Zinc Cytotoxicity

Cytotoxicity of zinc was first assessed through the MTS cell proliferation assay kit. The MTS assay is a colormetric assay consisting of a tetrazolium compound (3-(4,5-dimethylthiazol-2-yl)-5-(3-carboxymethoxyphenyl)-2-(4-sulfophenyl)-2H-tetrazolium (MTS) which is bioreduced by metabolically active cells into a soluble formazan product, which has a maximum absorbance of 490nm. Cell viability of 4T1 cells was investigated in complete growth medium, growth medium +50 µM $ZnCl_2$, and growth medium +100 µM $ZnCl_2$. 4T1 cells were plated at a density of 5,000 cells/cm^2 and allowed overnight to attach before changing culture medium with zinc treatments. Cytotoxicity of zinc was assessed for up to 3 days in two dimensional culture. Culture medium was changed every 24 hours during cell growth. On the day of the assay, culture medium was changed two hours prior to assay. 25 µL of MTS reagent was added to each well of a 25 well plate containing 500 µL of culture medium. After 3.5 hour incubation at 37 °C culture medium was collected and absorbance at 490nm was measured and normalized to day 0 control.

The PicoGreen DNA Quantification assay was performed to verify the results obtained from the MTS assay. PicoGreen is an ultrasensitive fluorescent nucleic acid stain specific to double stranded DNA (dsDNA) in solution. As little as 25 pg/mL dsDNA can be detected in 5 minutes. In short, 4T1 cells were plated at 5,000 cells/cm^2 in 24 well plates for up to 3 days with zinc conditioned medium. On the day prior to the assay, cells were rinsed with PBS twice, and lysed using lysis buffer containing 1mM Tris-EDTA and 0.1% Trition X-100. Cells were lysed overnight at 4 °C. On the day of the assay, 100 μL PicoGreen reagent were added to 100 μL of each sample in a 96 well plate. After 5 minutes of incubation at room temperature, fluorescence was measured in a Tecan M2000 plate reader using excitation and emission wavelengths of 480nm and 520nm, respectively. DNA was quantified by comparing samples to the measured fluorescence of a prepared standard curve.

4.3.4 Alkaline Phosphatase Staining

4T1 cells were plated at 50,000 cell/cm^2 in 24 well plates in complete growth medium. After allowing for attachment overnight, culture medium was changed to OC, OC + 50 μM $ZnCl_2$, and OC + 100 μM $ZnCl_2$. Culture medium was changed every 2 days for up to 10 days. On day 10, cells were rinsed twice with PBS and fixed with 4% formaldehyde solution for 2 minutes. Next, one SIGMAFAST BCIP®/NBT (5-Bromo-4-cholor-3-indolyl phosphate/Nitro blue tetrazolium) tablets was dissolved in 10mL deionized water to yield a ready to use buffered solution of pH 9.5. After removing formaldehyde, cells were rinsed with TBST (tris-buffered saline with Tween 20) buffer. In each well, 0.5mL of BCIP/NBT solution was pipetted. Plates were covered from light and incubated at room temperature for 15 minutes. Each well was rinsed twice with TBST buffer and air dried prior to imaging with an inverted light microscope. BCIP/NBT yields an insoluble purple precipitate when reacted with ALP.

4.3.5 ALP Quantification

ALP activity was quantified in both monolayer and spheroids using the colormetric p-nitrophenyl phosphate (pNPP) assay. When reacted with ALP, pNPP is dephosphorylated to p-nitrophenol, which absorbs light is 405nm in alkaline conditions. 4T1 monolayers were plated at 50,000 cells/cm^2 and grown in OC with zinc conditioned medium for up to 10 days. On day 10, monolayers were lysed using a lysis buffer containing 25mM Tris-HCl and 0.1% Triton X-100. Each sample was incubated at 37 °C for 30 minutes, then cycled through 3 free-thaw cycles. The pNPP solution was prepared with 5mM pNPP, 2mM $MgCl_2$, and 0.1M carbonate buffer at pH

9.8. Equal parts sample lysates and pNPP solution were mixed into a 96 well plate (100 µL each). The samples were then incubated at room temperature for 1 hour and absorbance at 405nm was read in a Tecan M200 plate reader. The absorbance for each sample was normalized to the day 0 control. Finally, absorbance was normalized to quantity of protein in each sample. The bicinchoninic acid (BCA) assay was used to quantify the amount of protein in each sample. Final quantification of ALP activity is normalized to both protein concentration in the sample and day 0 activity.

4.3.6 Microcalcification Formation and Histological Staining

In order to confirm the ability of 4T1 cells to mineralize, in vitro cultures were grown in monolayer in a 24 well plate. The effects of high exogenous zinc concentrations were examined for up to 28 days. The three conditions examined were OC, OC +50µM $ZnCL_2$, and OC +100µM $ZnCl_2$. Two dimensional staining of 4T1 cells grown in OC was performed after 28 days. Qualitatively, mineralization was examined through von Kossa staining protocol. Briefly, after 28 days, cells were gently rinsed twice with PBS and fixed with 4% formaldehyde in PBS for 15 minutes. Cells were then rinsed with water twice and stained with 1% silver nitrate under ultraviolet (UV) light for 1 hour. In the tissue sample, silver is deposited by replacing the calcium in the sample. The silver nitrate is reduced to metallic silver under UV light, which is visualized as a dark brown/black color. Unreacted silver nitrate was removed with 5% sodium thiosulfate for 3 minutes. A final rinse with deionized water was performed prior to drying and imaging. Monolayers in 24 well plates were imaged with an inverted light microscope.

In order to further confirm the presence of calcium, Alizarin Red staining was performed on monolayer samples. After 14, and 21 days, cells were fixed with 70% ethanol for 1 hour at 4°C. Next, cells were stained with 10% Alizarin Red for 10 minutes and rinsed with deionized water 5-10 times. Plates were air dried and imaged with an inverted light microscope.

4.3.7 Raman Spectroscopy

4T1 calcifications grown on tissue culture polystyrene were analyzed with Raman spectroscopy to confirm the presence of hydroxyapatite. After 28 days in culture, 4T1 monolayers were fixed for 30 minutes in methanol and air dried. A Renishaw inVia Confocal Raman Microspectrometer located at Stony Brook University's School of Atmospheric and Marine Sciences (Stony Brook, NY) with a 633nm laser of spot size 0.858 µm was used to

acquire Raman spectra from 200 to 2,000 cm^{-1} of 5 spots containing mineralized matrix on each sample. A total of 150 accumulations for each spot were averaged to yield the final spectrum. WiRE software was used to quantitatively analyze peak position, integration, and ratios.

4.3.8 Manual Tracking Migration Assay

Two dimensional manual tracking was performed on 4T1 cells to test the effects of exogenous zinc concentrations on metastatic behavior of 4T1 breast cancer cells. The link between migration and mineralization was studied by Dorst et al. in investigating osteoblast cells.[54,55] They showed decreased migration and mineralization in MC3T3-E1 osteoblasts with exogenous zinc treatment.[54,55] Migration may be a necessary function of all mineralized biological tissues, including breast cancer calcifications. Zinc was chosen as a potential inhibitor of migration due to its previous effect on osteoblast cells. 4T1 breast cancer cells were cultured in growth medium containing low glucose DMEM (1g/L glucose) supplemented with 10% fetal bovine serum (FBS), and 1% Penicillin-streptomycin solution. On the day of the assay, a confluent plate of 4T1 cells were detached with incubation of 0.05% trypsin-EDTA for 5 minutes, collected in solution, and counted to determine concentration of cells. 4T1 cells were plated at 5,000 cell/cm^2 in 35mm TC polystyrene dishes and allowed 18 hours to attach. Cells were rinsed with fresh DMEM, and culture medium replaced with CO_2 independent culture medium (CIM) containing no additional, +50µM Zn, or +100µM Zn. Using an inverted light microscope in phase contrast mode with a heated chamber set to 37°C, timelapse images of 4T1 cells migrating were captured every 2 minutes for 2 hours. Timelapse images were analyzed using the Manual Tracking plugin in ImageJ to determine an average cell speed for each condition. Three dishes for each experimental condition, and a total of 30-40 cells for each dish were tracked, giving around 100 cells per condition.

4.3.8 Quasi-Three Dimensional Migration Assay

A quasi-three dimensional migration assay was performed to assess the effects of exogenous zinc concentrations on the metastatic behavior of 4T1 breast cancer cells. The purpose of performing a quasi-three dimensional migration assay is to better assess cell migration in an environment more realistic to how cells move in vivo. The manual tracking assay described in *section 4.3.8* was previously performed by Dorst et al. to assess how osteoblast migration was affected by exogenous zinc and its link to mineralization.[54,55] However, cells in vivo do not migrate on a planar polystyrene surface. Therefore, an assay

which places cells in a three dimensional collagen network to study migration was developed for breast cancer cells. Based on the results of Dorst et al. osteoblast migratory behavior and ability to mineralize were influenced by exogenous zinc. The migration experiments were performed to test if breast cancer cells behave in a similar manner as osteoblast cells when exposed to exogenous zinc. Osteoblasts were found to migrate slower in high zinc environments, and have decreased mineralization potential.[54,55]

4T1 breast cancer cells were cultured in growth medium containing low glucose DMEM (1g/L glucose) supplemented with 10% fetal bovine serum (FBS), and 1% Penicillin-streptomycin solution. On the day of the assay, a confluent plate of 4T1 cells were detached with incubation of 0.05% trypsin-EDTA for 5 minutes, collected in solution, and counted to determine concentration of cells. 4T1 cells were resuspended in a microcentrifuge tube to a final concentration of 80,000 cells/µL. In a second microcentrifuge tube, 10 µL of 4T1 cell suspension was mixed with 10 µL of a neutralized 2 mg/mL collagen solution containing 2.5x DMEM. In a non-tissue culture treated 96 well dish, 1.2 µL of the collagen/cell mixture was pipetted into the middle of each well to create a collagen hemisphere of embedded cells. Hemispheres were incubated at 37 °C for 6 minutes to partially harden collagen solution. Next, 100 µL of culture medium was pipetted into each well and plates were incubated for 18 hours. **Figure 4.1** is a diagram of the experimental setup showing the collagen hemisphere. The three zinc treatments tested to determine effects on migration were complete growth medium (no added Zn), 50 µM added Zn, and 100 µM added Zn. After 8 hours of migration, cells were fixed and stained for 15 minutes with a solution containing 8% formaldehyde and 2.5 µg/mL DAPI in PBS. Finally, fluorescence microscopy images were taken on 4 sides of each hemisphere. Images were analyzed using the ImageJ ITCN plugin, counting the total number of cells which have migrated from the collagen hemisphere.

4.3.9 MMP Gel Zymography

4T1 cells in monolayer were plated at 50,000 cells/cm^2 in 24 well plates were grown for up to 10 days in OC, OC +50 µM $ZnCl_2$, or OC + 100 µM $ZnCl_2$. On day 10, culture medium was replaced with serum free DMEM for 24 hours and collected on day 11. Protein concentration in culture medium was quantified using the Tecan Infinite 200 Pro NanoQuant plate reader. Relative MMP-2 and MMP-9 activity in each sample was quantified using gel

zymography. Samples were diluted with water to contain 2.5 mg/mL protein. Next, each sample was mixed 1:1 with sample buffer containing 0.5M Tris-HCl at pH 6.8, 20% glycerol, 10% SDS, 0.1% and Bromophenol Blue and incubated at room temperature for 15 minutes. 40 µL of each sample was pipetted into individual wells of a 10% Criterion™ Zymogram Gel with gelatin. Running buffer was transferred to the Criterion™ cell, and electrophoresis was run at 200V for 1 hour. Next, the gel was removed, rinsed with water, and renatured with 2.5% Triton X-100 for 1 hour under constant shaking. The gel was rinsed several times with deionized water and developed for 48 hours at 37 °C with constant shaking. Developing buffer consisted of 50mM Tris base, 0.2M NaCl, 5mM $CaCl_2$, and 0.02% Brij 35. After developing, the gel was rinsed with deionized water and stained with Coomassie Blue R-250 stain for up to 4 hours with constant shaking. Next, the gel was destained with 50% methanol and 10% acetic acid in water for 15 minutes with constant shaking. Finally, the gel was rinsed with deionized water, sandwiched between two sheets of transparent paper, and scanned to create a grayscale image. Images were analyzed in ImageJ using the Analyze Gels function.

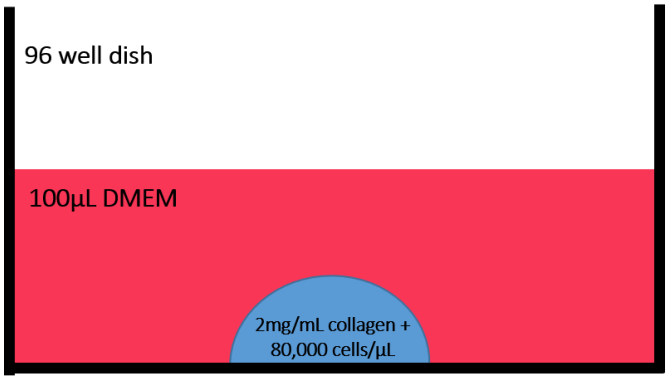

Figure 4.1. Experimental diagram of the quasi-three dimensional migration assay. 4T1 cells are made into a condensed hemisphere containing 2mg/mL collagen. Cells migrate out of the hemisphere and attach to the surface of the 96 well dish.

4.4 Results

4.4.1 Zinc Cytotoxicity

The effects of excess zinc on 4T1 breast cancer cell growth in vitro was tested in order to confirm the inhibitory effects of zinc on calcification formation is not due to cytotoxicity. First, the 2D monolayer model was tested using the MTS assay. Cell viability was tested for up to 3 days with viability on each day presented as a percentage of Day 0. 5,000 cells plated in growth medium (GM) were either treated with GM as a control, GM + 50 μM Zn, or GM + 100 μM Zn. Results of the MTS assay are reported in **Figure 4.2**. After one day of growth, cell viability in GM, GM + 50 μM Zn (moderate zinc), and GM + 100 μM Zn (high zinc) groups were 257%, 249%, and 232% of the day 0 control sample, respectively. After two days, viability for GM, moderate zinc, and high zinc groups were 455%, 461%, and 445% of day 0, respectively. After three days, the viability for GM, moderate zinc, and high zinc groups were 467%, 464%, and 464% of day 0, respectively. According to the results of the MTS assay, there appears to be no cytotoxic effects up to 100 μM Zn for up to 3 days. Cell viability was decreased slightly in the high zinc group, but the result was not significant. Although, cell growth appears to have reached a plateau at day 2, the cells are still growing and are more numerous by day 3. This effect is caused by a saturation of MTS reagent in culture.

Since a suspected saturation effect was occurring in the MTS assay, a second experiment was performed to examine potential cytotoxic effects of zinc in culture. The PicoGreen assy was performed to quantify DNA content in cell culture. Results of DNA quantification are reported in **Figure 4.3**. According to the results, average DNA per well for 4T1 cells grown in GM on days 1, 2, and 3 are 415, 1459, and 2127 ng, respectively. Compared to the moderate zinc group where 4T1 cells grown in GM + 50 M Zn, average DNA per well on days 1, 2, and 3 are 394, 1423, and 2002 ng, respectively. Similarly, the high zinc group where 4T1 cells were grown in GM + 100 M Zn had an average DNA per well on days 1, 2, and 3 of 393. 1445, and 2106 ng, respectively. Overall, DNA content increases on each day, unlike the MTS cell viability assay. This confirms the saturation of the MTS cell viability assay in 2D monolayer, suggesting DNA quantification by PicoGreen assay as a better method for testing cell growth in vitro. According to the results, by day 3 the DNA content for GM, moderate zinc, and high zinc were 2127, 2002, and 2106 ng, respectively. The difference observed between GM and the two zinc groups were not significant, indicating that zinc at up to 100 μM concentration has no effect on 4T1 cell growth in vitro.

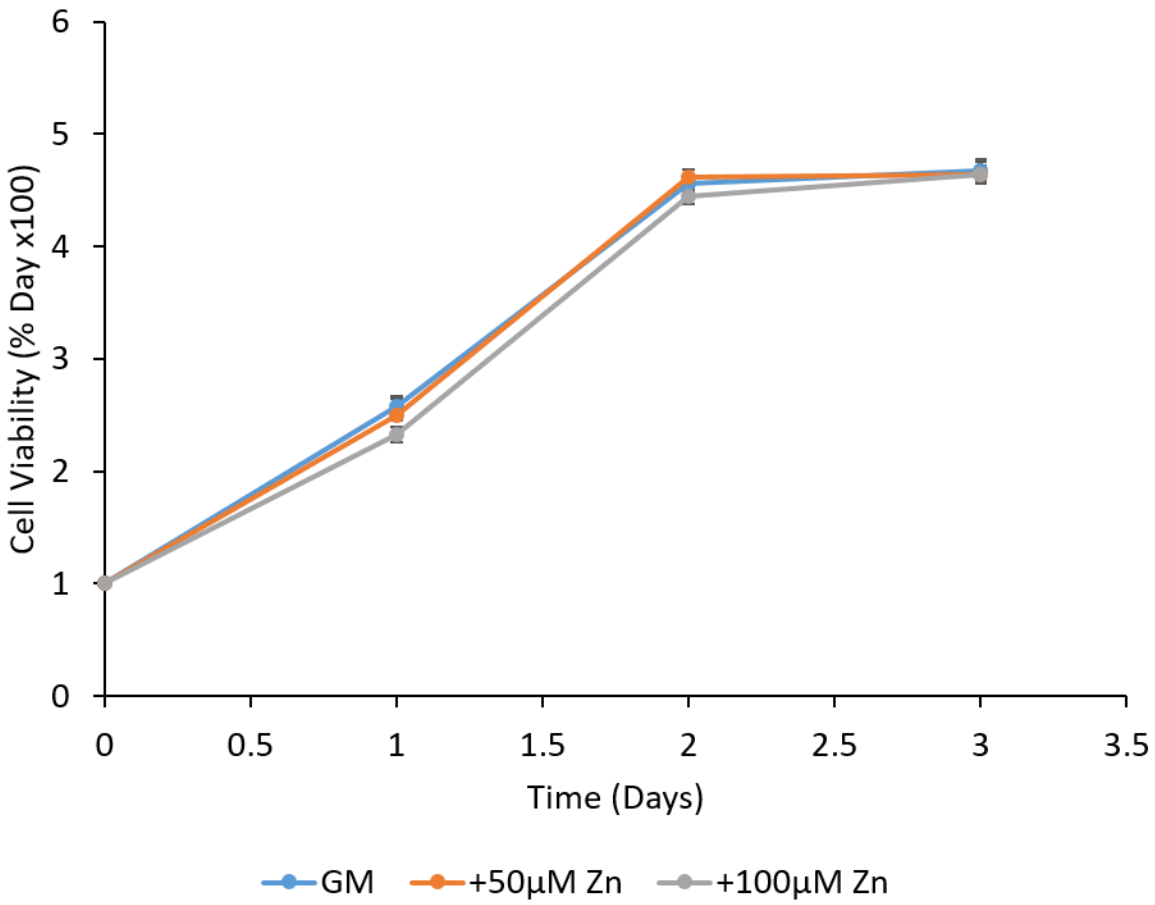

Figure 4.2. MTS cell viability assay performed in 2D monolayer culture of 4T1 cells in GM, GM + 50 µM Zn, and GM + 100 µM Zn. No cytotoxic effects are seen up to 3 days in culture. Averages are calculated based on 3 wells per experiment in 3 independent experiments.

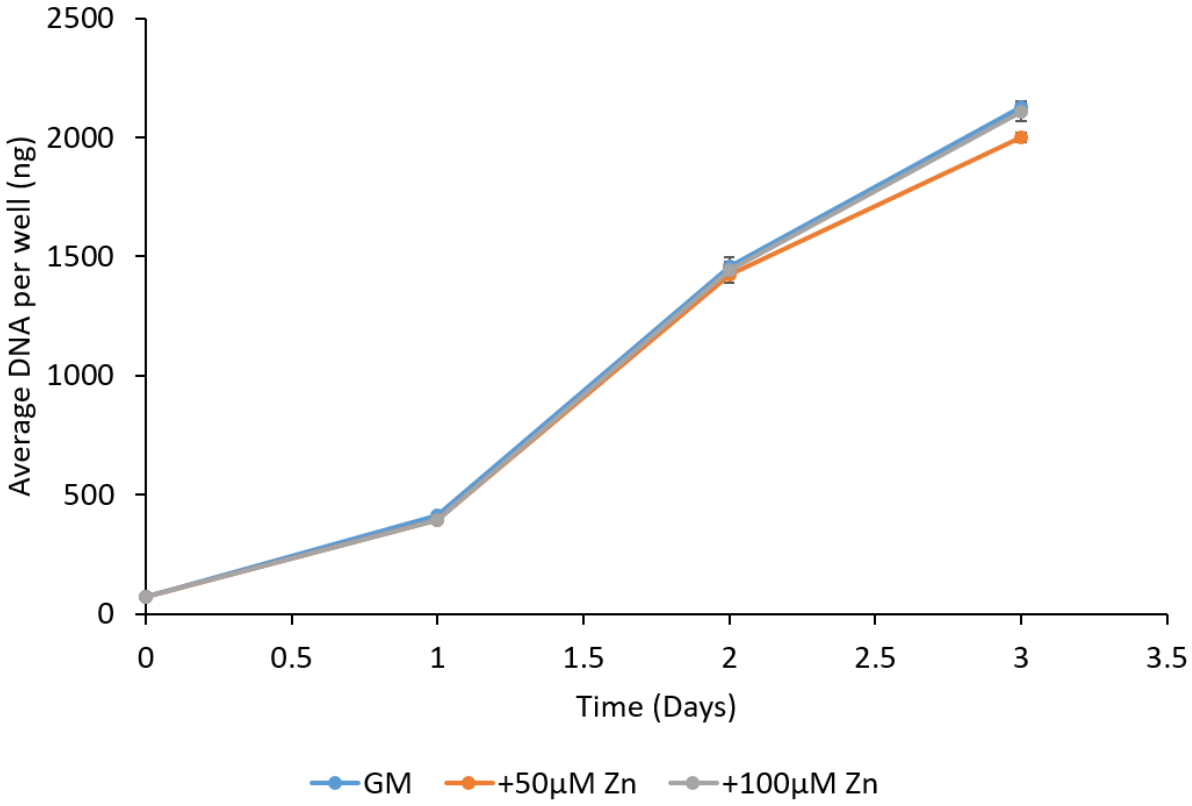

Figure 4.3. DNA quantification of 4T1 monolayers in 24 well plate grown in GM, GM + 50 µM Zn, and GM + µ100 M Zn. Cells were plated at 5,000 cell/cm^2 in 24 well plates and collected after 1, 2, and 3 days of growth in GM, GM + 50 µM Zn, and GM + µ100 M Zn. DNA in cell lysates were quantified using the PicoGreen Assay. Averages are calculated based on 3 wells per experiment in 2 independent experiments.

4.4.2 Alkaline Phosphatase Activity

The effect of exogenous zinc on 4T1 ALP activity was investigated qualitatively through BCIP/NBT staining and quantitatively through the pNPP assay. Qualitative ALP staining of 4T1 monolayers after 10 days is shown in **Figure 4.4**. Areas of unspecific phosphatase activity are shown in dark purple, indicating ALP activity. Qualitatively, as zinc concentration in culture was increased from control OC conditions to 50 μM and 100 μM, ALP activity appears to decrease with increasing zinc concentration. Cultures grown in 50 μM Zn, appear to have slightly less purple stain compared to the OC control. However, this difference is much more apparent at 100 μM Zn, as there is far less positive phosphatase staining in each well.

The results of qualitative staining were confirmed though a colorimetric quantitative pNPP assay, which used cell lysates to directly test phosphatase ability to cleave a phosphate group off of pNPP. Results from the pNPP assay are shown in **Figure 4.5**, which confirms a decrease in ALP activity in vitro with increasing zinc concentration. Results are normalized to protein concentration, then reported as a percentage increase from the day 0 control sample. Average ALP activity in OC, OC + 50 μM Zn, and OC + 100 μM Zn groups on day 10 were 572%, 443%, and 315% of ALP activity on day 0. Differences between all groups were statistically significant ($p<0.001$). Addition of 50 μM Zn to 4T1 cells in vitro resulted in a decrease of 129% ALP activity compared to the OC group. Furthermore, addition of 100 μM Zn to 4T1 cells in vitro resulted in a decrease of 257% decrease in ALP activity compared to the OC group. These results confirm the qualitative staining performed on 4T1 cell monolayers, which showed a decrease in ALP activity with increasing zinc concentration.

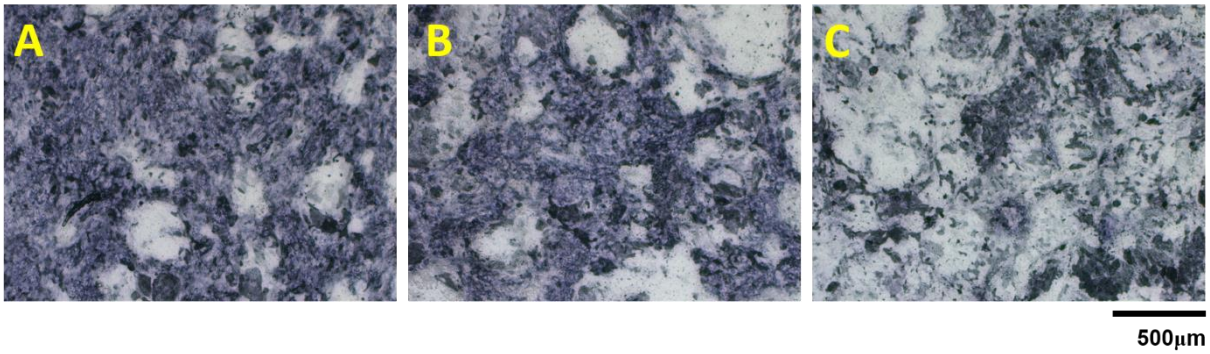

Figure 4.4. ALP staining using BCIP/NBT to qualitatively determine ALP activity in 4T1 monolayers at 10 days grown in (A) OC, (B) OC +50 μM Zn, and (C) OC +100 μM Zn. Images are representative of 3 wells per experiment in two independent experiments.

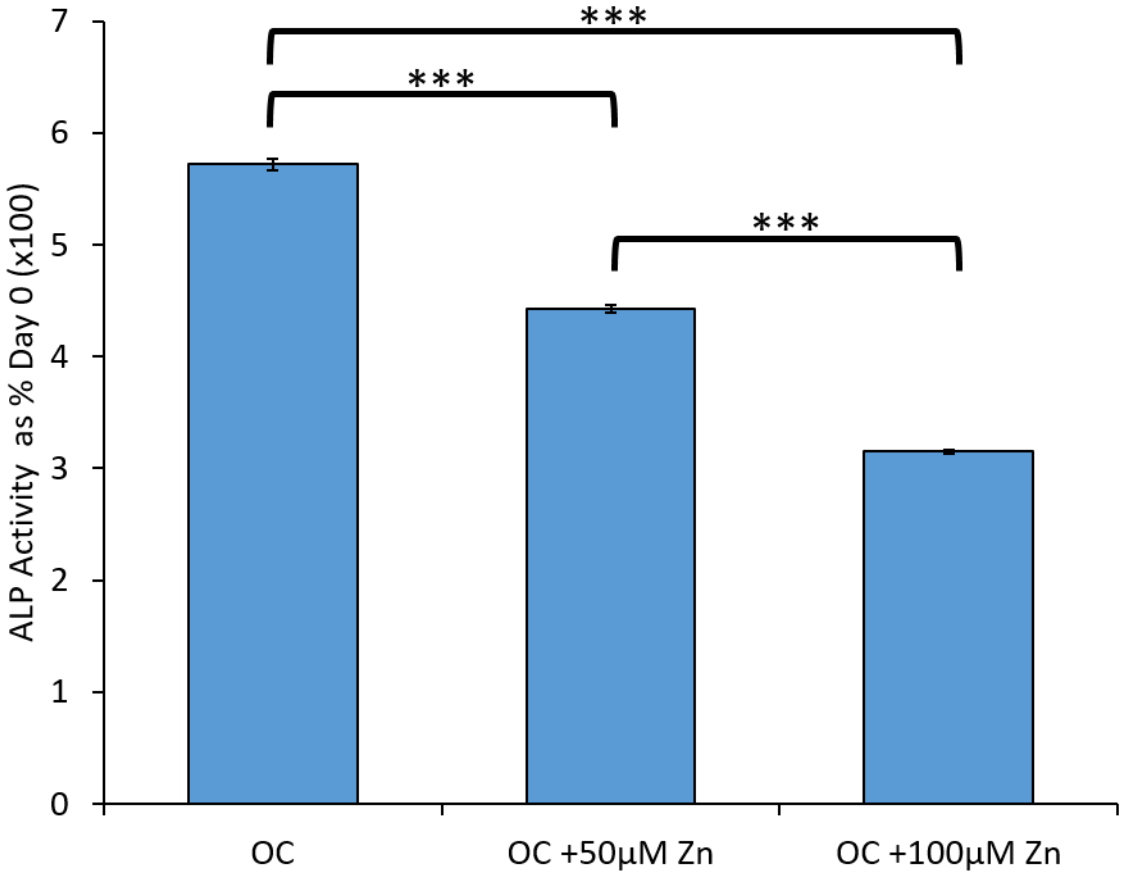

*Figure 4.5. Quantitative analysis of ALP activity in 4T1 monolayers grown in OC, OC + 50 µM Zn, and OC + µ100 M Zn using the pNPP assay. ALP activity is normalized to protein concentration, then reported as a percent of Day 0 control. ALP activity is decreasing with increasing zinc concentration. (***p<0.001) Averages are representative of 3 wells per experiment in 2 independent experiments.*

4.4.3 Mineralization and Histological Staining

Histological staining of 4T1 cells grown in 2D was performed to confirm the ability of 4T1 cells to produce microcalcifications in vitro. At early time points, Alizarin Red was used to stain for calcium at day 14 and day 21, shown in **Figure 4.6**. Von Kossa staining was performed later at day 21 and day 28, shown in **Figure 4.7**. According to the results of the histological staining, microcalcifications can be seen by 21 days of culture, when grown in OC. Both Alizarin Red and von Kossa confirmed the presence of calcium crystals in 2D culture at 21 days.

Next, the use of high exogenous zinc concentrations were used to inhibit microcalcification formation. Cultures grown in OC containing +50 μM $ZnCl_2$ saw mild inhibition of microcalcification formation. The calcifications that formed when grown in OC +50 μM $ZnCl_2$ were both smaller and less numerous compared to those grown in OC on days 21 and 28 when stained for Alizarin Red and von Kossa. When zinc concentration was increased to 100 μM $ZnCl_2$, the result was a complete inhibition of microcalcification formation. The inhibition is more apparent at the later time points, as shown in **Figure 4.7**. By day 28, microcalcifications are large and numerous when grown in OC, but completely inhibited when grown in OC + 100 μM $ZnCl_2$. There is no positive staining for von Kossa, and very weak, non-specific staining for calcium present at when stained with Alizarin Red. Overall, histological staining of 4T1 2D monolayers confirmed the mineralization potential of OC on 4T1 breast cancer cells grown in vitro. Also, the results of high zinc concentration on in vitro culture showed an inhibitory effect towards formation of microcalcifications.

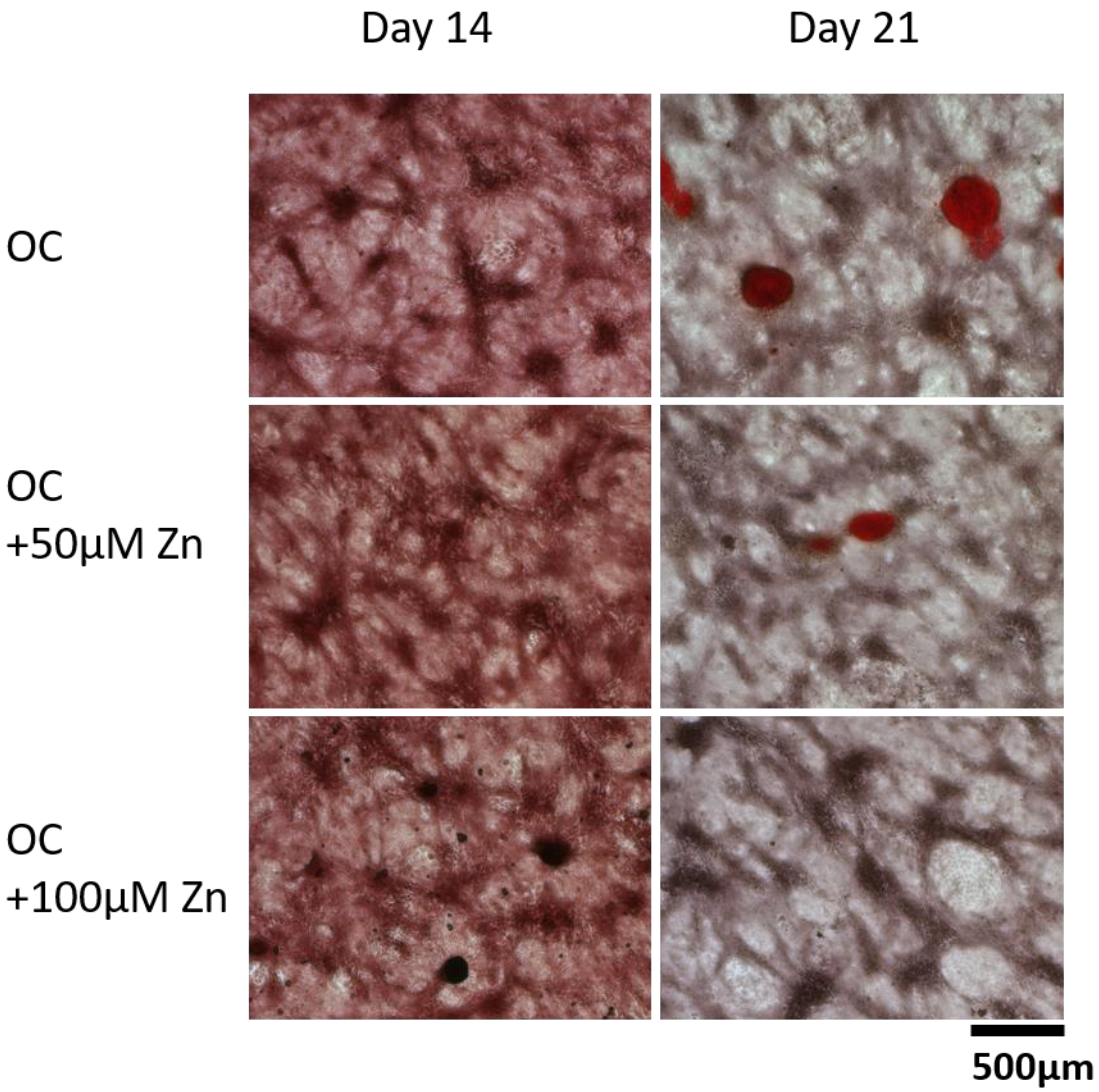

Figure 4.6. Alizarin Red staining of 4T1 monolayers grown in 24 well plates on days 14 and 21. Positive stain for calcium will appear red. Images are representative of 3 independent experiments.

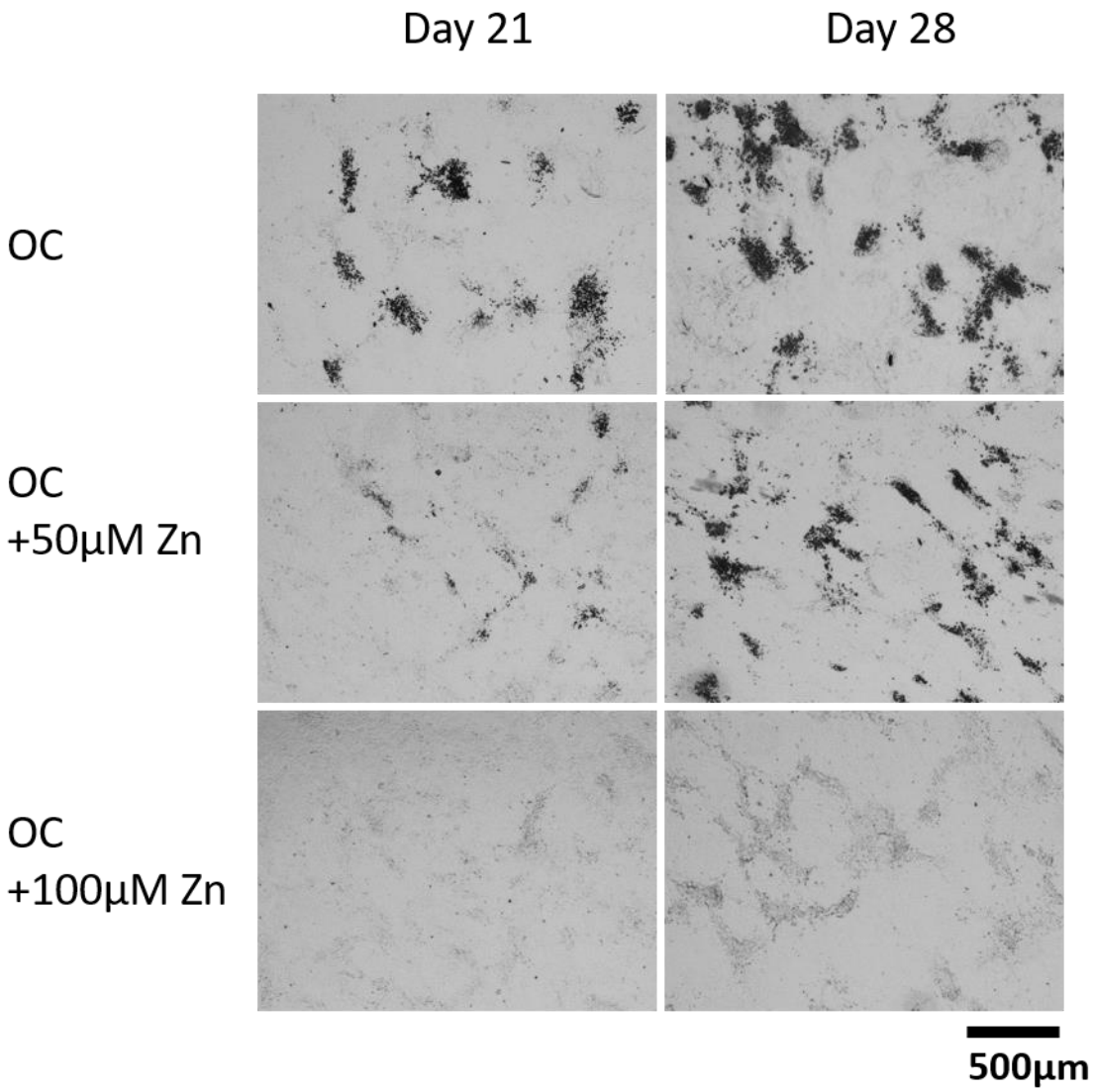

Figure 4.7. Von Kossa staining of 4T1 cells grown in monolayer at days 21 and 28. Dark areas are positively stained for calcium. Images are representative of 3 independent experiments.

4.4.4 Raman Spectroscopy

Raman spectroscopy was first performed on the calcified regions of day 28 4T1 2D monolayers in 35mm tissue culture treated polystyrene dishes. Next, Raman spectroscopy was performed on 8 µm spheroid sections, which were placed on stainless steel slides. Spectra from 5 calcified regions of spot size 0.858µm of each 2D monolayer and in each spheroid were captured and analyzed for mineral:matrix ratio and crystallinity. Mineral:matrix ratio is defined as the ratio of the area of the phosphate peak at 960$cm^{-1}$to the area of the amide I peak at 1660cm^{-1}. Crystallinity is defined as the full width at half maximum (FWHM) height of the phosphate peak at 960cm^{-1}.

Table 2 represents a summary of the most prominent Raman peaks in mineralized biological tissue and their corresponding vibrational assignment. According to the Raman spectra, the most prominent peaks present are the phosphate peak at 960 cm^{-1}, which is caused by the symmetric stretching of the phosphate group, the carbonate peak at 1070 cm^{-1}, which is caused by symmetric stretching of the carbonate group, and the amide I peak at 1660 cm^{-1}, which is caused by the double bond between carbon and oxygen in the amide group.[171]

Raman spectra of a purified hydroxyapatite standard commercially purchased was tested to confirm the presence of phosphate peaks. As shown in **Figure 4.8**, the hydroxyapatite standard contains only the four phosphate peaks corresponding to the four vibrational assignments of the phosphate molecule. No carbonate is present because the hydroxyapatite used is a purified, commercially available standard. Also, no amide peaks are present because there are no proteins or cellular components in the sample. The hydroxyapatite standard has a crystallinity value of 9.8, representing its full-width at half maximum height (FWHM). This means the width of the phosphate peak at 960cm^{-1} at half the height is 9.8. Hydroxyapatite standards with negligible wt% carbonate substitution have been reported to have FWHM values of approximately 7cm^{-1}. Whereas, 3.5 wt% carbonate substitution has yielded between 9-14cm^{-1}.[172] According to Penel et. al, FWHM values of 4.5, 7, and 10 wt% carbonate substituted hydroxyapatites yield FWHM values of 13, 15, and 17cm^{-1} respectively.[173]

Raman Shift (cm^{-1})	Assignment	Notes
430	$\nu 2\ PO_4^{3-}$	symmetric bend
584-590	$\nu 4\ PO_4^{3-}$	antisymmetric bend
960	$\nu 1\ PO_4^{3-}$	symmetric stretch
1003	C-C	phenylalaline
1070	$\nu 1\ CO_3^{2-}$	symmetric stretch – overlap with $\nu 3\ PO_4^{3-}$
1076	$\nu 3\ PO_4^{3-}$	symmetric bend – overlap with $\nu 1\ CO_3^{2-}$
1300	Amide III	Protein α-helix
1446	δCH_2	Protein CH_2 deformation
1660	Amide I	C=O vibration component is strongest

Table 2. A list of the most prominent Raman shifts assigned to calcified biological tissue.[171]

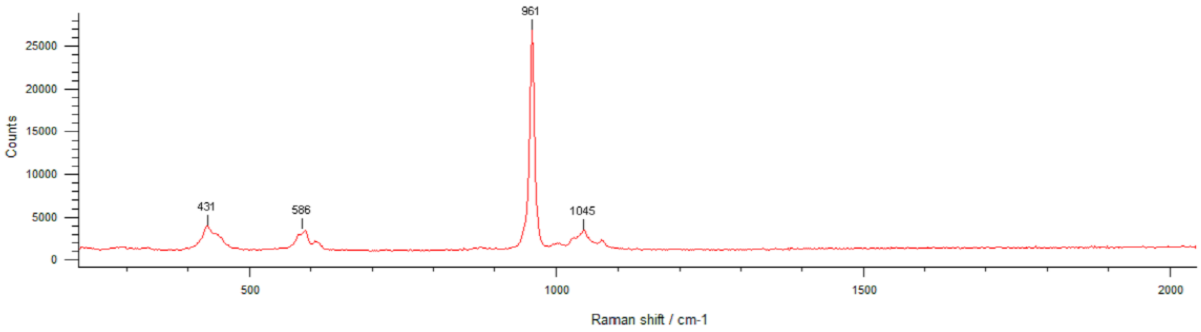

Figure 4.8. Raman spectrum of purified hydroxyapatite standard. Peaks at 431, 586, 961, and 1045cm^{-1} all correspond to phosphate peaks. Lack of carbonate peaks signify minimal carbonate substitution.

Representative Raman spectra from day 28 4T1 monolayers grown in OC, OC +50 μM Zn, and OC + 100 μM Zn are shown in **Figure 4.9**. The most prominent feature in samples from 2D monolayers is the interference from polystyrene at 1001cm^{-1} and 1031cm^{-1}. **Figure 4.10** shows Raman spectra of polystyrene, containing peaks at 621, 795, 1001, 1031, 1155, 1181, 1200, 1449, 1583, and 1602cm^{-1}. Also, the carbonate peak at 1060cm^{-1} overlaps with the polystyrene peak at 1031cm^{-1}, making it impossible to analyze phosphate:carbonate ratio data in monolayer samples. The effects of zinc on carbonate content and crystallinity were analyzed through mineral:matrix ratio and FWHM of phosphate peak at 960cm^{-1}, respectively. As shown in **Figure 4.9**, calcified regions in 2D monolayers contain a large phosphate peak at 960cm^{-1} and organic peaks at 1300, 1446, and 1660cm^{-1} corresponding to amide III, CH, and amide I, respectively. According to the list of Raman shifts in **Table 1**, the spectrum acquired in Figure 24 from day 28 calcifications in 2D monolayers shows the peaks representing carbonated hydroxyapatite.

According to the Raman spectra of 2D monolayers, mineral:matrix ratios and crystallinity were calculated. Mineral:matrix ratio for 4T1 calcifications are reported in **Figure 4.11**, where 4T1 monolayers grown in OC are compared to 4T1 monolayers grown in moderate zinc (OC + 50 M Zn). High zinc conditions (OC +100 M Zn) inhibited microcalcification formation, so Raman data yielded no phosphate peak, as shown in **Figure 4.9C**. Average mineral:matrix ratios for monolayers grown in OC and OC + 50 μM Zn were calculated to be 1.06, and 2.92, respectively. The two groups were calculated to be significant ($p= 0.048$). However, since there is potential interference from the polystyrene, due to the polystyrene peaks at 1001cm^{-1} interfering with the phosphate at 960cm^{-1}, and the polystyrene peak at 1602cm^{-1} interfering with the amide III at 1600cm^{-1}, it could be obstructing the results. Finally, crystallinity was compared between the OC and OC + 50 μM Zn groups, in **Figure 4.12**. Average FWHM values for the OC and OC + 50 μM Zn groups are 21.79 and 21.17, respectively. These results are not considered significant, and are much higher than the FWHM value of the purified hydroxyapatite sample, which is 9.8, indicating more impurities, such has carbonate, within the crystal structure.

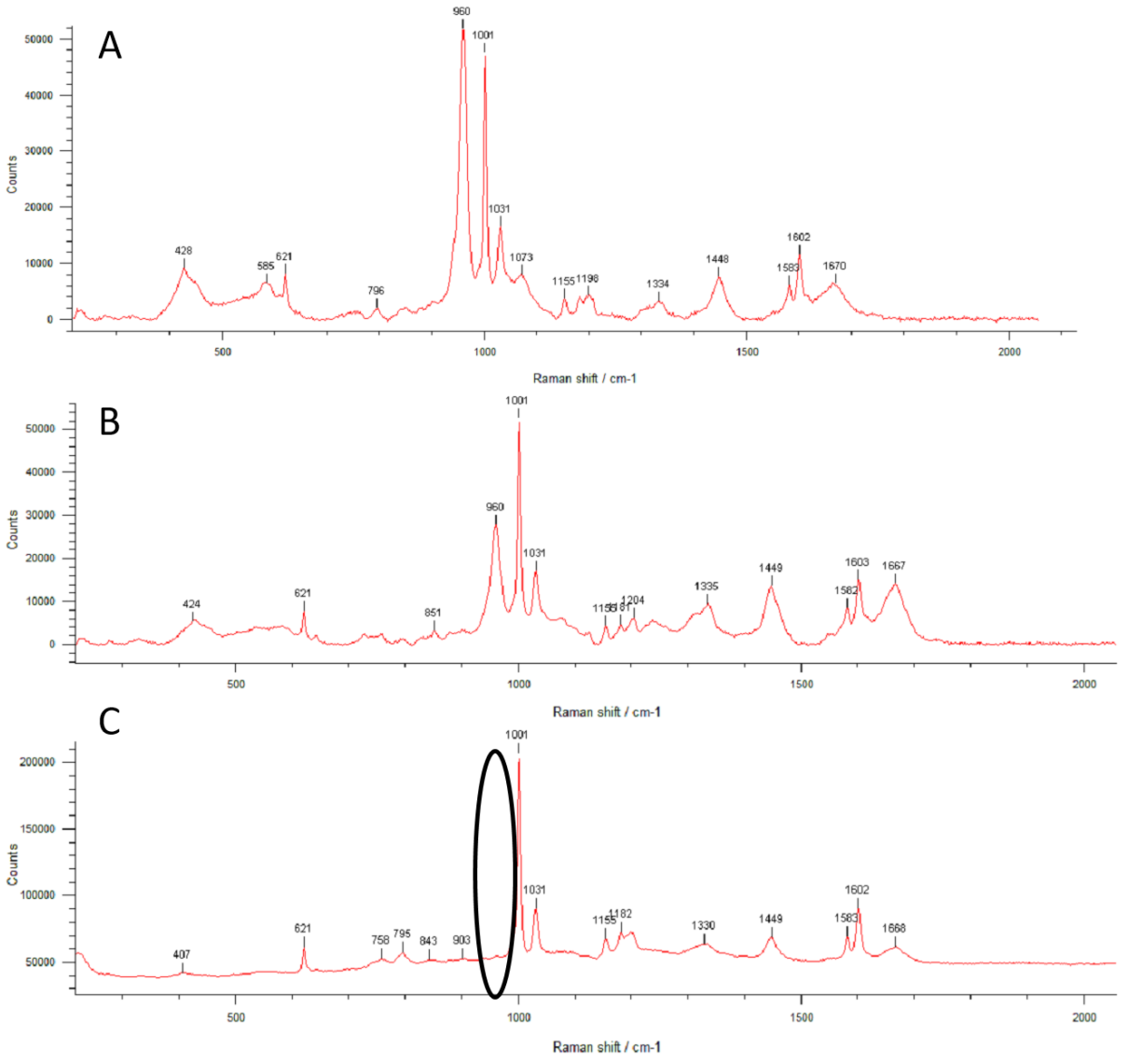

Figure 4.9. Representative Raman spectrums of 4T1 2D monolayers grown in (A) OC, (B) OC + 50 µM Zn, and (C) OC + 100 µM Zn. Absence of phosphate peak at 960cm^{-1} shown by black oval. Representative Raman spectra taken from 5 different regions of spot size 0.858 µm.

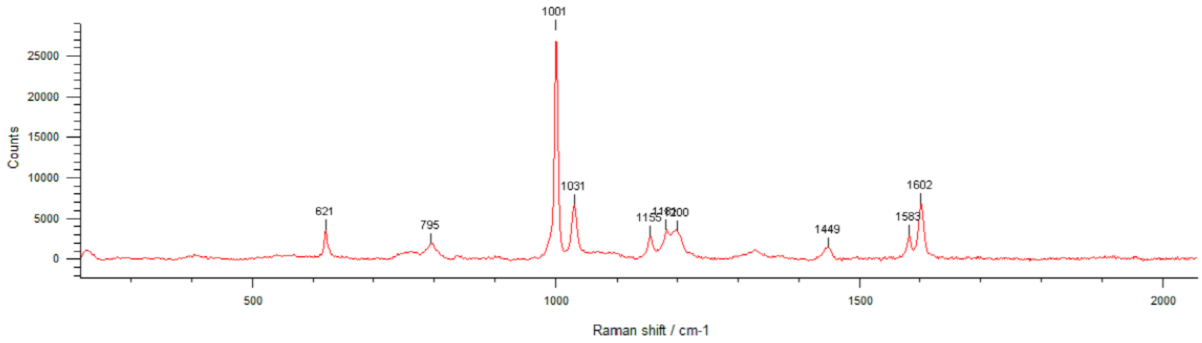

Figure 4.10. Representative Raman spectrum of tissue culture treated polystyrene.

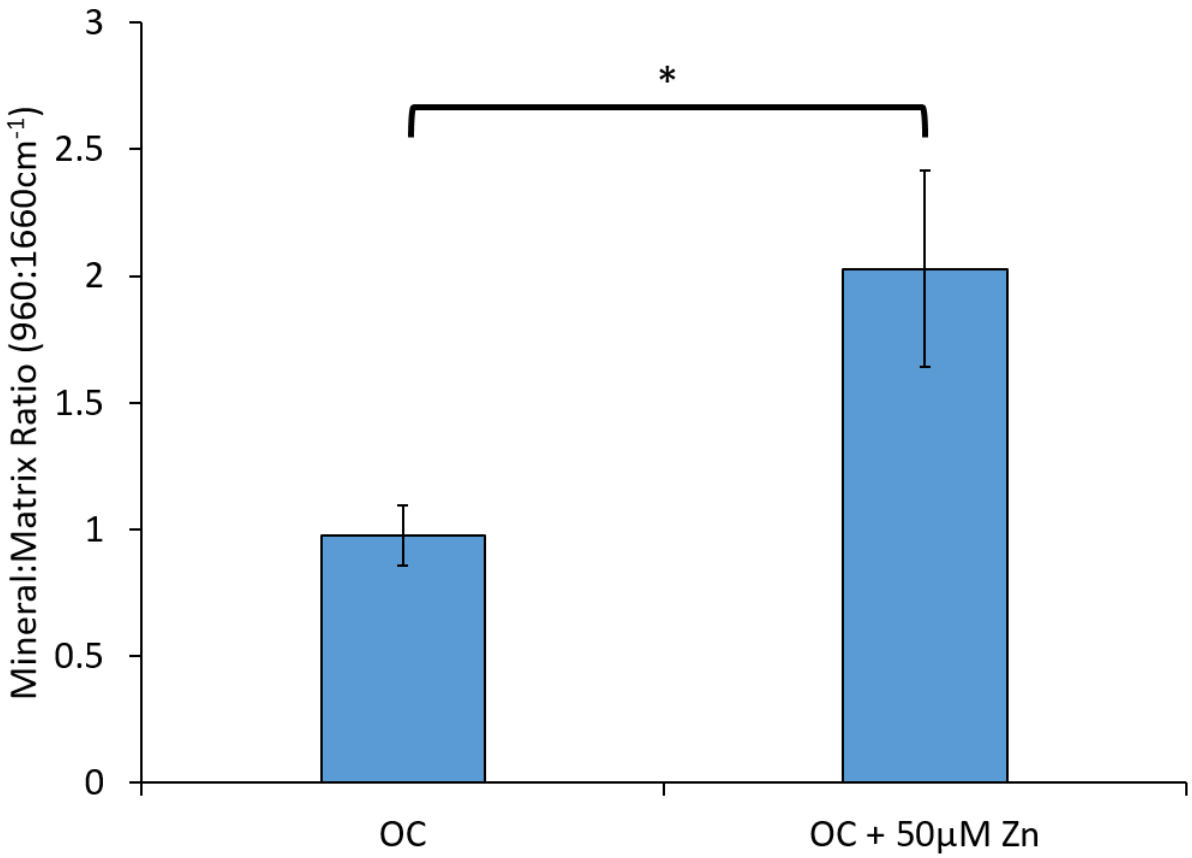

*Figure 4.11. Mineral:Matrix ratio corresponding to integrated peak area of phosphate peak at 960cm^{-1} and amide III peak at 1660cm^{-1} for calcified regions of 4T1 monolayers grown in OC and OC + 50 µM Zn. Average mineral:matrix ratio of OC group is 1.06, compared to 2.92 for OC + 50 µM Zn group. (*p<0.05) Averages are calculated based Raman spectra of 5 different calcified regions of 0.858 µm spot size.*

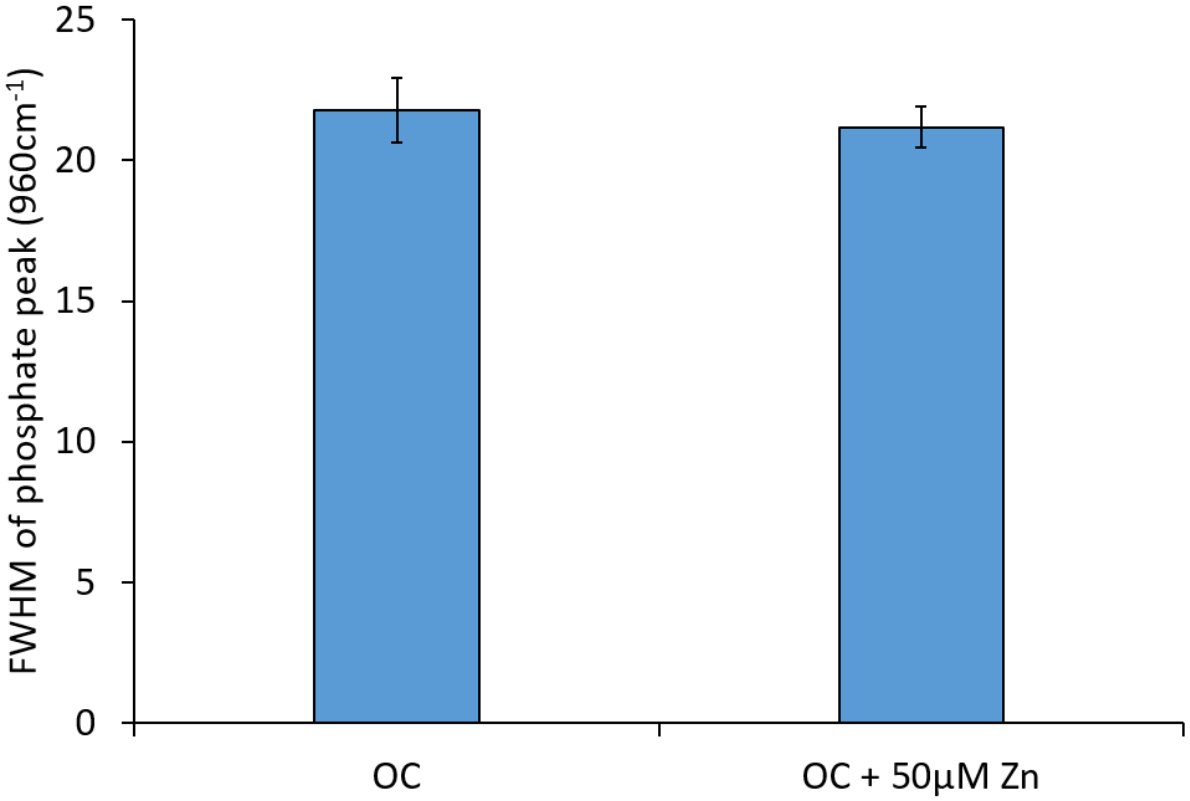

Figure 4.12. Average full-width at half maximum height (FWHM) of phosphate peak at 960cm^{-1} of calcified regions of 4T1 day 28 2D monolayers grown in OC and OC + 50 µM Zn. Averages are calculated based Raman spectra of 5 different calcified regions of 0.858 µm spot size.

4.4.6 Cell Migration – Manual Tracking

Representative phase contrast images of manually tracked of 4T1 cells are shown in **Figure 4.13**. Cells are tracked by tracing nuclei of each successive picture taken 2 minutes apart. Cell speed is determined by calculating number of pixels traveled and converting to a distance over the 2 hour time period. Average cell speed for each zinc condition are reported in **Figure 4.14**. The average speed of 4T1 cells in CO_2 independent medium (CIM), CIM + 50 µM Zn, and CIM + 100 µM Zn are 30.2, 22.2, and 19.4 µm/hour, respectively. Cell speed in both Zn treated groups were significantly slower than cells in CIM ($p<0.001$). Also, cells in CIM + 100 µM Zn were significantly slower than cells in CIM + 50 µM Zn ($p<0.01$). Two dimensional migration shows an effect of zinc on decreasing metastatic potential by slowing migration in 4T1 breast cancer cells.

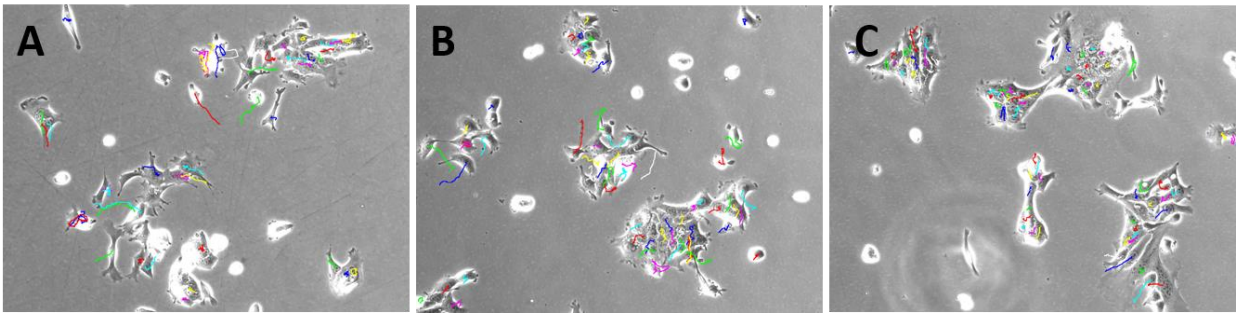

Figure 4.13. Phase contrast images analyzed with the ImageJ Manual Tracking plugin showing 4T1 cell migration in (A) CO_2 independent culture medium (CIM), (B) CIM + 50 µM Zn (moderate zinc), and (C) CIM + 100 µM Zn (high zinc). Images are representative of 3 independent experiments.

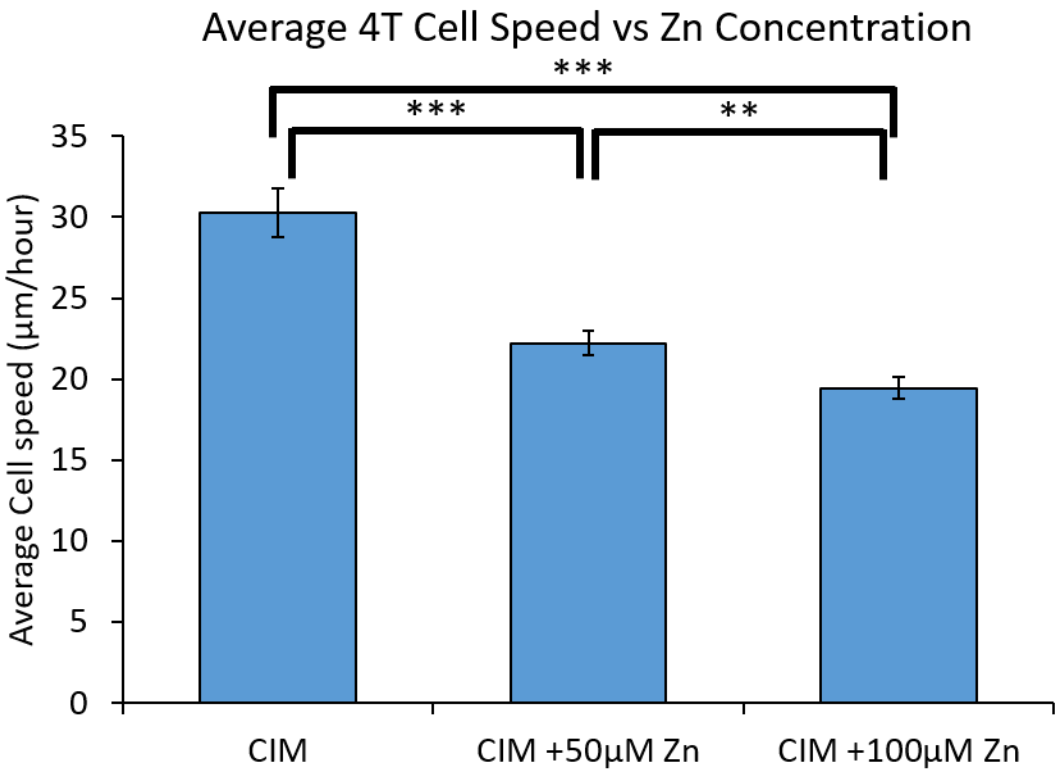

*Figure 4.14. Average cell speed of manually tracked 4T1 cells in 2D on tissue culture polystyrene over a 2 hour period in CIM, CIM + 50 µM Zn, and CIM + 100 µM Zn. Cell speed of 4T1 cells with no added Zn (CIM) is 30.2 µm/hr. Compared to moderate Zn (CIM + 50 µM Zn), cell speed is 22.2 µm/hr and high ZN (CIM + 100 µM Zn), cell speed is 19.4 µm/hr. (**p<0.01 and ***p<0.001) Average cell speeds are calculated from 30-40 cells per experiment in 3 independent experiments.*

4.4.6 Quasi-Three Dimensional Migration Assay

Representative fluorescence images of DAPI stained 4T1 migrated cells are shown in **Figure 4.15**. Qualitatively, it is difficult to see a difference in the number of migrated cells when compared cells plated in GM with moderate or high Zn supplemented groups. Once, quantified using the ICTN plugin of ImageJ, a difference was observed between the high Zn group and the GM and moderate Zn groups. Results of the semi-three dimensional migration assay are reported in **Figure 4.16**, in terms of total number of migrated cells in one field of view. On average, both the GM and moderate Zn (GM + 50 μM Zn) groups have 256 cells migrated from the collagen hemisphere. Both the group grown in GM and moderate Zn are significantly higher than the high Zn group (GM + 100 μM Zn), which averaged 175 cells migrated in one field of view ($p<0.001$). The high Zn group has less cells migrating, showing the potential effect of Zn to partially inhibit, or slow cell migration.

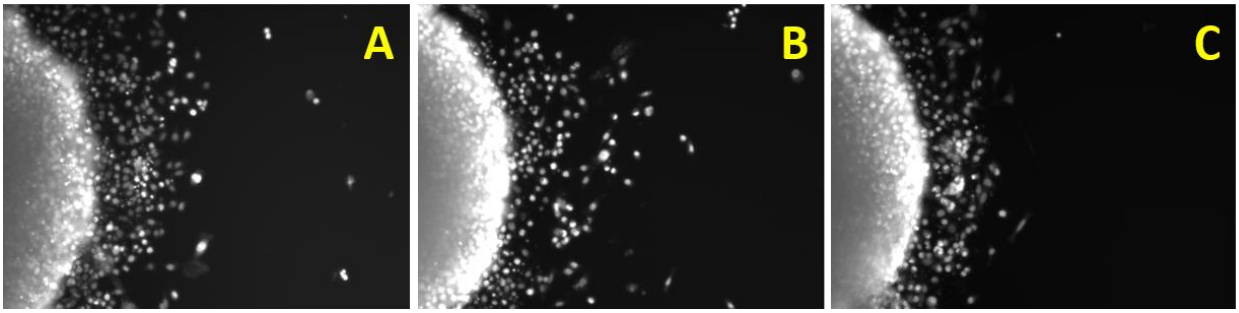

Figure 4.15. Representative fluorescence images of DAPI stained 4T1 cells after 18 hours plated in a semi-three dimensional collagen hemisphere migration assay. Cells were cultured in (A) no added Zn (GM), (B) moderate Zn (GM + 50 µM Zn), and (C) high Zn (GM + 100 µM Zn). Images are representative of 12 images per experiment with 3 independent experiments.

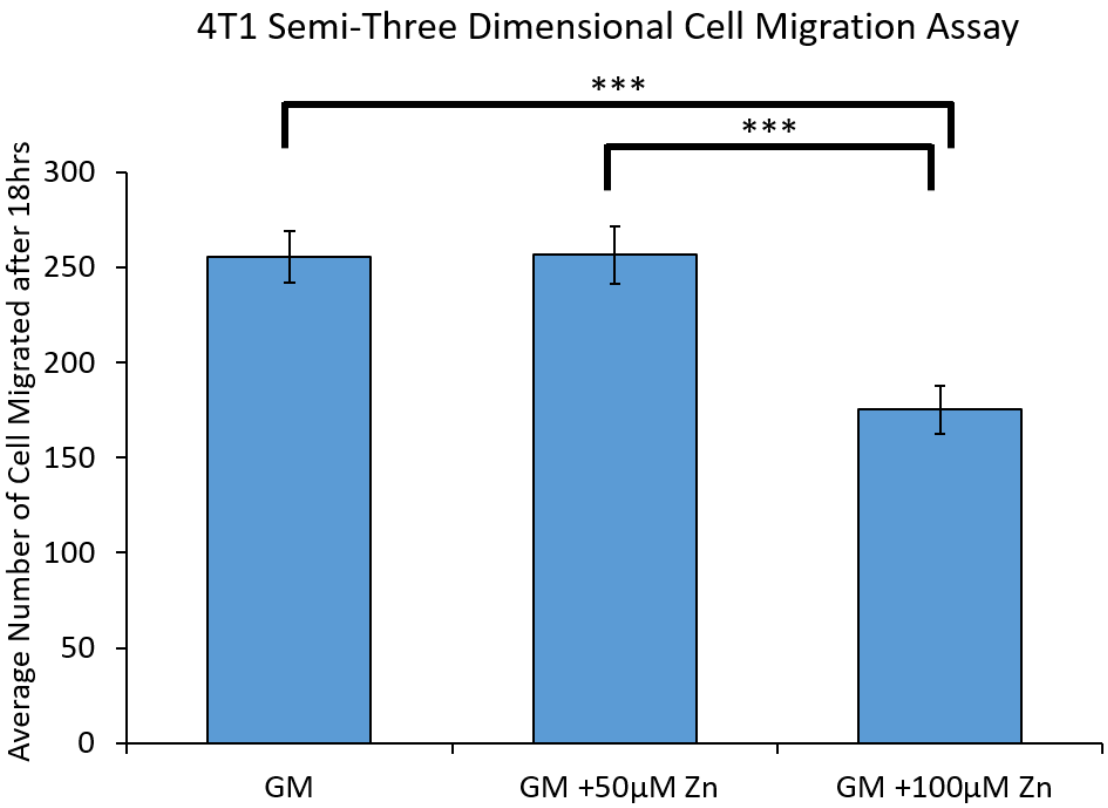

Figure 4.16. Average number of cells counted in one field of view calculated from fluorescence images of DAPI stained collagen hemispheres after 18 hours using the ICTN plugin of ImageJ. Average number of cells migrated in one field of view for no added Zn (GM), moderate Zn (GM +50 µM Zn), and high Zn (GM + 100 µM Zn) are 256, 256, and 175, respectively. The number of cells migrated in high Zn medium is significantly lower than moderate Zn and no added Zn ($p<0.001$). Averages number of cells are calculated from 4 collagen dots per experiment using 4 field of views per collagen dot with 3 independent experiments.

4.4.7 MMP Gel Zymography

The effects of zinc on MMP activity were examined through gel zymography using both a 2D monolayer and 3D spheroid model of 4T1 in vitro cultures. Band density of each lane of the gels were quantified in ImageJ to quantitatively compare MMP-2 and MMP-9 activity. MMP-2 and MMP-9 activity in 2D monolayers are represented by light bands shown in **Figure 4.17**. Compared to day 0, there is little MMP-9 activity in 2D, as represented by the lack of visualized bands in the gel at 92 kDa. At day 0 and day 10, there are minimal visualized bands representing MMP-2 at 72 kDa. Based on the lack of visualized bands in the gel from the supernatants collected in 2D monolayers, it is assumed minimial MMP-2 and MMP-9 are produced in 2D cultures.

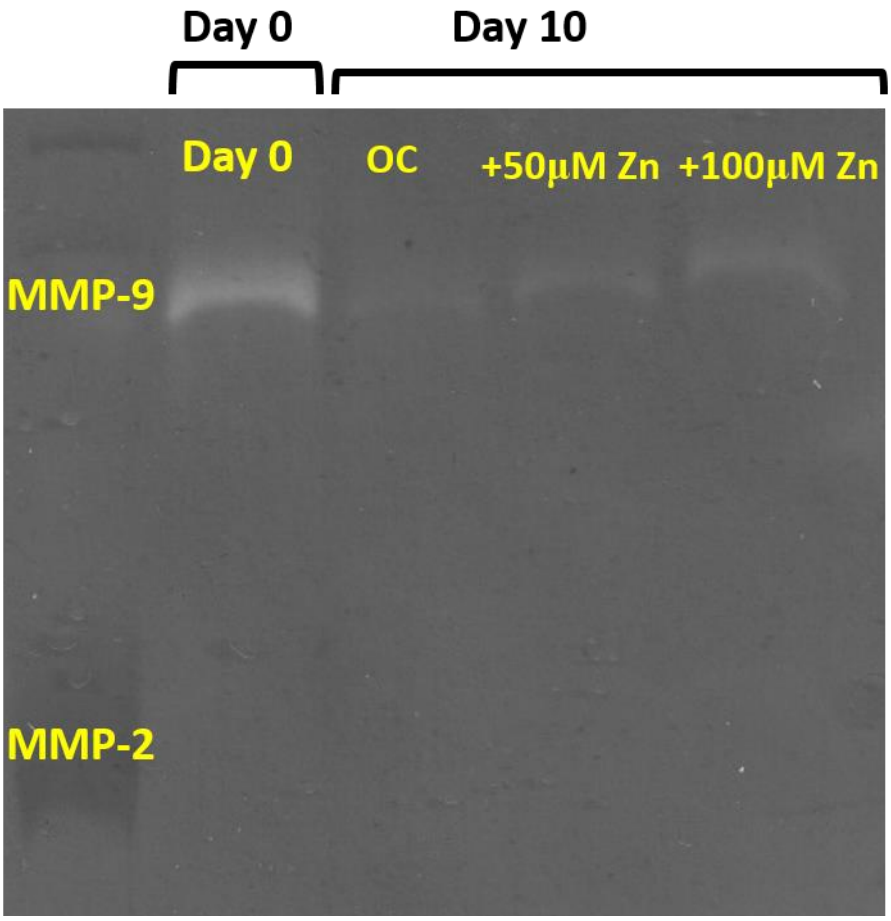

Figure 4.17. Scanned image of gel zymogram representing MMP-9 (92 kDa) and MMP-2 (72 kDa) activity in supernatants of 4T1 2D monolayer in vitro cultures at day 0, and day 10 grown in OC, OC + 50 µM Zn, and OC + 100 µM Zn. Gel zymogram is representative of 3 independent experiments.

4.5 Discussion

The effects of exogenous zinc concentrations on 4T1 microcalcification formation were tested for the ability to inhibit calcification formation in a 2D monolayer and a 3D spheroid model. Histological staining of 2D monolayers grown in OC, OC with moderate zinc, and OC with high zinc in **Figure 4.6** and **Figure 4.7**, show a moderate inhibition of microcalcification formation at 50 μM Zn, and complete inhibition of microcalcification formation at 100 μM Zn. Alizarin Red staining at 14 and 21 days and von Kossa staining at days 21 and 28 in monolayer cultures show partial inhibition of microcalcification formation at 50 μM Zn, and complete inhibition of microcalcification formation at 100 μM Zn.

Raman spectroscopy on calcified 2D monolayers showed interference with several polystyrene peaks, leading to questionable results as to the effects of zinc on calcified crystals. However, the peaks present were able to confirm the presence of a carbonated form of hydroxyapatite based on phosphate and carbonate peaks. A more conclusive approach was then taken to study effects of zinc on calcified sections of 4T1 spheroids, placed on stainless steel slides, which yield no Raman background, eliminating interference.

Raman spectroscopy on calcified regions of spheroid sections showed phosphate and carbonate peaks typical of calcified biological tissue, carbonated hydroxyapatite. The phosphate peak at 960 cm^{-1}, carbonate peak at 1060cm^{-1}, amide III peak at 1300cm^{-1}, and amide I peak at 1660 cm^{-1}confirm the presence of carbonated hydroxyapatite, as all of these peaks are characteristic of carbonated hydroxyapatite, the main component in type II breast cancer microcalcifications.[171] Raman spectra of spheroid sections grown in OC and OC + 50 μM Zn were quantitatively compared for phosphate:carbonate, mineral:matrix ratio, and crystallinity to determine the effects of growth in moderate zinc concentration on the calcified crystal. Both phosphate:carbonate ratio and mineral:matrix ratio are lower in spheroids treated with moderate zinc concentrations. Phosphate:carbonate and mineral:matrix ratios could not be calculated for sections treated with high zinc because no phosphate peak was found due to lack of calcifications. Moderate zinc concentration resulted in lower phosphate:carbonate ratio compared to conditions with no added zinc. This would suggest less carbonate substitution in hydroxyapatite crystals formed from 4T1 spheroids grown in moderate zinc conditions. Also, mineral:matrix ratio was lower in moderate zinc sections, meaning there are more organic components and less mineral components to the crystal. Less phosphate relative to carbonate is

caused by an increased degree of carbonate substitution, which has been associated with less degree of invasiveness or severity of cancer.[133,135] Also, a decrease in mineral:matrix ratio suggests less hydroxyapatite and more organic cellular components. According to the data on crystallinity, using FWHM of the phosphate peak at 960cm^{-1}, crystallinity of hydroxyapatite is not affected by growth in moderate zinc concentrations. However, small changes in carbonate content were not shown to affect hydroxyapatite crystallinity. In fact, in artificially synthesized carbonate substituted hydroxyapatites, samples under 6.5% carbonate substitution can be classified as low carbonate/high crystallinity, all with similar properties. Around 6.5% carbonate substitution, there is a transition to high carbonate/low crystallinity.[174] Therefore, small changes in carbonate substitution will not affect crystallinity of hydroxyapatite unless it passes this transition.[174] Overall, differences in mineral:matrix, and phosphate:carbonate ratio suggest growth in moderate zinc is producing less calcifications with higher carbonate substitution, which would suggest a less invasive cancer.

Cox et al. showed formation of breast cancer microcalcifications is an active cell mediated process reliant on ALP and phosphate transport.[170] Since high zinc concentrations were shown to inhibit microcalcification formation in vitro, the effects of zinc on ALP activity in breast cancer cells were examined. Both qualitative ALP staining using the BCIP/NBT staining in **Figure 4.4**, and quantitative measurement of phosphatase activity in cell lysates from the pNPP assay in **Figure 4.5** show increasing zinc concentration decreases phosphatase activity. Therapeutically, higher serum alkaline phosphatase levels in breast cancer patients has been shown to be associated with increased disease progression and bone metastasis.[175] Therefore, ALP is a potential target to slow or inhibit calcification formation of breast cancers, which is linked to metastatic activity. In this work exogenous zinc has been shown to inhibit phosphatase activity, and inhibit microcalcification formation. This provides further evidence that calcification formation in breast cancer is an active, cell mediated process which may require ALP.

The effect of zinc on MMP formation was examined to see any potential link to MMP activity and breast cancer calcification formation. Since MMP-2 is involved in osteogenesis, and MMP-9 is involved in bone resorption, it is thought that they may play a role in breast cancer microcalcification formation.[176] However, their potential roles in breast cancer calcifications are not well understood. It is known that MMP-2 and MMP-9 are involved in driving metastatic

behavior of breast cancers, but not much is known about potential effects on formation of calcifications.[177,178] High exogenous zinc concentrations in culture has been shown to decrease MMP-2 in MC3T3 osteoblasts, therefore was tested for its potential effect on breast cancer cells.[55] However the representative gel zymogram in **Figure 4.17** shows little MMP-2 or MMP-9 activity when grown in 2D culture.

4.6 Conclusion

This work demonstrates the use of high exogenous zinc concentrations to inhibit microcalcification formation in breast cancer in vitro. Microcalcifications, specifically type II containing hydroxyapatite, are a strong indicator of metastatic breast cancer, but are not fully understood in their relation to the disease. Microcalcification formation is by breast cancer is an active, cell mediated process similar to formation of bone, which may require ALP and cell migration, both of which were partially inhibited by zinc.

Chapter 5 : Development of a Novel in Vitro 3D Tumor Spheroid Model for the Study of Breast Cancer Microcalcifications

Abstract

A crucial early indicator of breast cancer is the appearance of mammographic mammary microcalcifications, small mineral deposits consisting primarily of hydroxyapatite. The alteration of the physicochemical properties of these microcalcified nodules during breast cancer progression is believed to be linked to malignancy, and as such, better understanding of the functional role of microcalcifications could improve our knowledge of the metastatic behavior of breast cancers. Currently, however, there is a lack of model systems for studying breast microcalcifications. To our knowledge, most previous in vitro work on breast cancer microcalcifications has been limited to single-culture monolayer systems. In this work, we present a novel three-dimensional in vitro model composing of murine 4T1 breast carcinoma cells that self-assemble into multi-cellular tumor spheroids (MCTS), which are cultured for up to 28 days. Histological characterization of the MCTS in conjunction with Raman spectroscopy reveal that the 4T1 spheroids contain bone-like microcalcified regions similar to hydroxyapatite in mineralized osteoblasts. Additionally, we observed a reduction of microcalcification formation in the presence of exogenous zinc. Taken together, our results demonstrate the potential use of zinc as a therapeutic agent for inhibiting breast microcalcifications. The system was also demonstrated to be effective in applications involving co-culture with HUVEC or for the study of prostate cancer VCaP cells.

5.1 Introduction

Until recently, the importance of microcalcifications in breast cancer was overlooked and considered to be a passive process associated with cellular degeneration, lacking biological significance. However, recent studies have suggested mammary mineralization is an active process regulated by similar cellular physiological pathways as those in bone mineralization.[140–142] Furthermore, breast cancers have been shown to overly express several bone matrix proteins, such as osteopontin (OPN) and bone sialoprotein.[143,144] Together this evidence suggest mechanisms involved in bone mineralization could be involved in the formation of breast cancer calcifications. However, very few in vitro models for studying breast cancer calcifications exist.

The first in vitro model for studying breast cancer calcifications was developed by Cox et al. in 2012. This model uses 4T1 murine mammary adenocarcinoma cell line in a 2D cell culture. It was the first in vitro cell culture model to successfully develop breast cancer microcalcifications.[170]

Although the model developed by Cox et al. has been effectively used to study microcalcifications in breast cancer, it has many limitations.[170] The main limitation of the model is the fact that it is a two dimensional model, in which cells are grown on tissue culture polystyrene. However, solid tumors grow in three-dimensions. A three dimensional spheroid model represents a more realistic intermediate in between two dimensional in vitro culture and an in vivo animal model. Spheroids are aggregates of cells which grow in suspension. Spheroid cancer models have gained popularity over the past several decades because they mimic several characteristics of in vivo tumors that two dimensional models fail to produce.[179] For example, when solid tumors grow in three dimensions, the results are a heterogeneous exposure to oxygen, nutrients, and physical and chemical stresses. In vivo solid tumors contain non-proliferating but viable hypoxic tumor cells, due to the oxygen gradient across the tumor.[180] The diffusion and distribution of oxygen, nutrients, and signaling molecules is not represented in two dimensional cultures.[181] In addition to chemical gradients across the tumor, three dimensional models are more realistic in their cellular surface interactions. In two dimensions, cells are adherent to tissue culture polystyrene and appear flattened and their morphology is not likened to their in vivo structures. In three dimensions, cell-cell and cell-ECM interactions are crucial factors which influence cell structure, adhesion, mechanotransduction, and signaling responses. Overall, the cellular interactions with the surface regulate overall cell function in ways that differ dramatically from two dimensions to three dimensions.[182]

Spheroid size is an important factor to consider when developing an accurate three dimensional tumor model. The optimal spheroid size which best simulates in vivo tumors is between 200 and 500 μm. Spheroids at this size have the properties of obtaining cell-cell and cell-ECM interactions, while also developing an oxygen and chemical gradient which is similar to that of an in vivo tumor. Small spheroids with a size less than 150 μm obtain the cellular interactions, but fail to develop an oxygen and chemical gradient. Large spheroids, over 500 μm typically develop central secondary necrosis. Due to prolonged hypoxia, cells in the center

eventually die due to apoptosis or necrosis, as their cell cycle becomes disrupted. Although the ideal spheroid size is cell-line dependent, the most important features across spheroid models are the cell-cell or cell-ECM interactions, and the development of a hypoxic core with a diffuse oxygen and chemical gradient. Interestingly, the central cells of the spheroid will metabolically adapt and maintain intracellular homeostasis in response to the microenvironment.[183–188] The most prominent application of spheroid models is the testing of therapeutic drugs, or drug candidates. In contrast to two dimensional testing, factors in spheroid model that need to be considered are: diffusion and penetration barriers.[189] While in vivo models are the gold standard for pharmacology testing, it has been shown that IC50 values can vary greatly from two dimensional to three dimensional spheroid models.[190–192] Replacing two dimensional models with more realistic spheroid models has the benefits of reproducing more realistic chemistry, environments, and toxicology.

It was the goal of this project to engineer a novel multi-cellular tumor spheroid (MCTS) model for study of microcalcifications in breast cancer. Since all previous work in vitro work on breast cancer microcalcificions have been performed in a two dimensional model, the establishment of a three dimensional model will improve our understanding of the relationship between the development of microcalcifications and breast cancer.

5.2 Objective

The aim of this project was to apply the effects of exogenous Zn on the inhibition of breast cancer microcalcifications towards a three dimensional in vitro spheroid model. The goal was to develop a three dimensional spheroid model for studying breast cancer microcalcifications and apply exogenous zinc to inhibit in vitro breast cancer calcifications.

5.3 Materials and Methods

5.3.1 Cell Culture

4T1 murine mammary adenocarcinoma cells were used as a model cell line for studying breast cancer microcalcifications. 4T1 cells closely mimic highly metastatic stage IV human breast cancer. Cox et al. has previously shown the ability of the 4T1 cell line to produce microcalcifications in vitro.[170] Cells were grown in complete growth medium containing Dulbecco's Modified Eagle Medium (DMEM) containing low glucose (1g/L), supplemented

with 10% fetal bovine serum (FBS) and 1% Penicillin-Streptomycin solution to yield a final concentration of 100 units/mL Penicillin and 100 µg/mL Streptomycin.

5.3.2 Self-Assembly of 4T1 MCTS

4T1 cells were grown in complete growth medium attached to 10 cm tissue culture polystyrene dishes until 70-80% confluency was reached. **Figure 5.1** shows the self-assembly of 4T1 MCTS. Briefly, self-assembly of 4T1 spheroids was achieved by coating each well of a 96 well plate with 50 µL of 1.5% agarose in DMEM. The solidified agarose coating is hydrophobic and prevents cell adhesion to the surface. Suspended cells will adhere to each other, forming a spheroid in solution. 1.5% agarose solution in DMEM was autoclaved to sterilize and dissolve the solution. 50 µL of hot agarose solution was pipetted into each well and allowed 20 minutes to cool and solidify. Cells were detached through 5 minute incubation with 0.05% trypsin EDTA solution. Collected cells were resuspended in fresh complete growth medium and counted. 5,000 4T1 cells were plated in 0.2mL in each well of a 96 well plate that had been coated with 1.5% agarose in DMEM. After 72 hours incubation, the spheroid self-assembly is complete. For all experiments, Day 0 is considered 72 hours after plating. Spheroids were grown up to 28 days in an osteogenic cocktail (OC) consisting of complete growth medium supplemented with 4mM β-glycerol phosphate and 50 µg/mL ascorbic acid. Culture medium was replenished every 2 days by removing 100 µL from the 96 well plate and carefully pipetting 100 µL fresh osteogenic cocktail into the well. The effect of excess zinc was investigated on 4T1 spheroid growth and mineralization. Three conditions were tested: OC, OC +50µM $ZnCl_2$, and OC +100µM $ZnCl_2$.

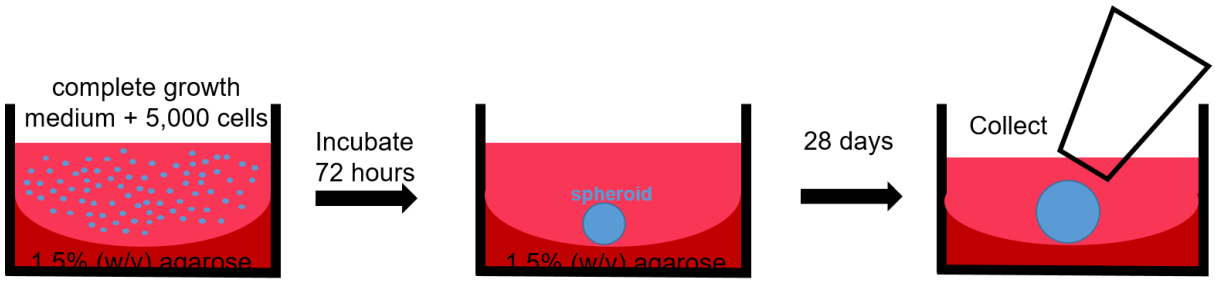

Figure 5.1. Self-assembly of 4T1 MCTS, growth, and collection at 28 days.

5.3.9 Zn Cytotoxicity

4T1 spheroids were plated at 5,000 cells per spheroid. The DNA of spheroids grown for up to 7 days in zinc conditioned medium were quantified. Spheroids were collected the day prior to the assay, rinsed twice with PBS and dispersed with Accumax, a mixture of EDTA and collagenase enzyme. Ten minute incubation in Accumax in a 37 °C water bath followed by pipetting up and down several dozen times completely dispersed the spheroids. Spheroid dispersions were mixed equally with 2x lysis buffer to yield 1x lysis buffer containing 1mM Tris-EDTA and 0.1% Triton X-100. Spheroid dispersions were lysed overnight at 4 °C. Lysates were mixed equally with PicoGreen reagent and fluorescence was measured. DNA was quantified by comparing each sample to a standard curve of prepared concentrations.

5.3.3 Sectioning of 4T1 MCTS

After 28 days of growth, MCTS were collected with a truncated pipette tip and sectioned for histological staining and Raman spectroscopy**. Figure 5.2** shows a flow chart of the steps taken to collect, embed, and section the spheroids. Briefly, a cut pipette tip was used to collect the spheroids and transfer into a microcentrifuge tube. In each microcentrifuge tube, 6-8 spheroids were collected. Once settled to the bottom of the tube, spheroids were rinsed once with 0.5mL phosphate buffered saline (PBS). Next, spheroids were incubated with 4% formaldehyde solution in PBS overnight at 4 °C. Spheroids were then embedded in 0.3mL of a neutralized 2mg/mL collagen solution containing 2.5x DMEM. The collagen-spheroid solution was then transferred to a well in a 24 well plate using a cut pipette tip to form a thin layer. Collagen-spheroid layers were incubated for 10 minutes at 37 °C to partially solidify the collagen into a gel. The collagen layer was removed with a tweezer and placed into a cryomold containing 2mL of 50% OCT and 15% (w/v) sucrose. After allowing 5-10 minutes for the collagen layer to settle to the top, the cryomold was frozen at -80 °C. Once frozen, blocks were removed from the cryomold and sectioned into 8 µm sections using a ThermoFisher Scientific Cryostat Microm HM550. Sections were placed onto glass microscope slides to be stained. Several sections were placed onto cleaned stainless steel slides to be analyzed with Raman spectroscopy.

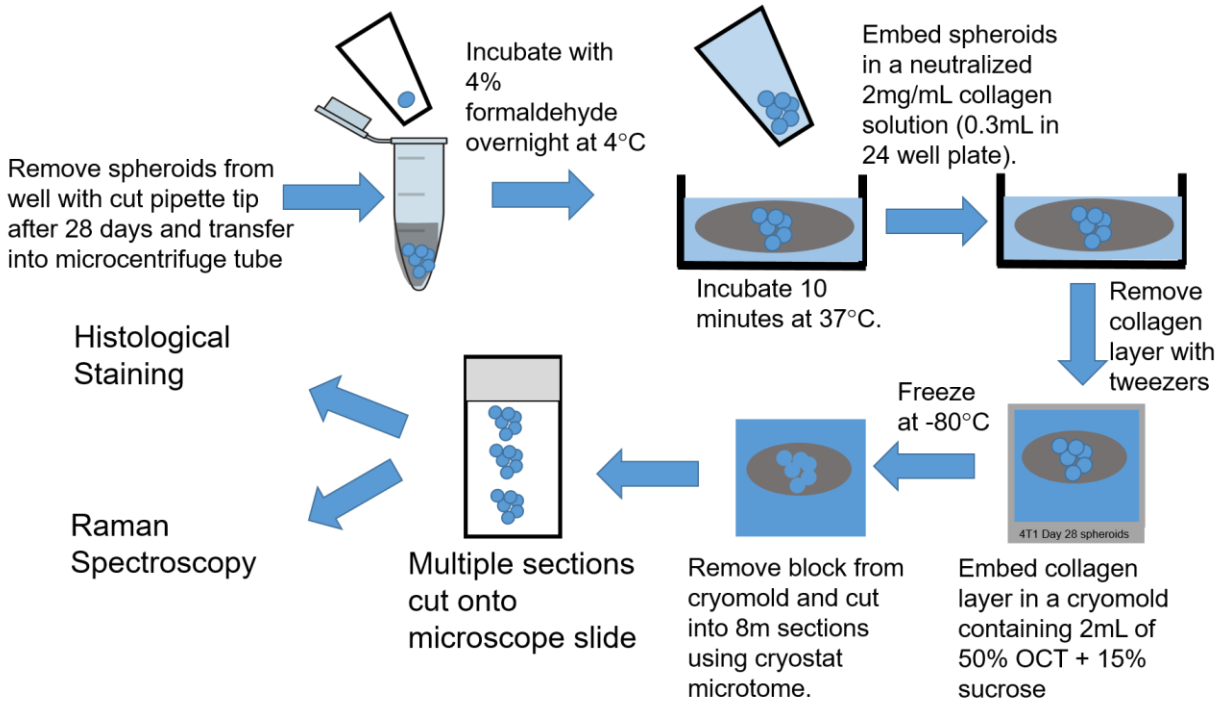

Figure 5.2. Flow chart showing collection and sectioning of 4T1 MCTS.

5.3.4 Spheroid Characterization

Phase contrast images of spheroids were captured every 2-3 days with an inverted light microscope. Images of 12 spheroids per condition were captured for 28 days and the size of each spheroid was analyzed using SpheroidSizer, a high throughput Matlab program developed by Chen et al.[193] SpheroidSizer rapidly estimates spheroid size by measuring changes in contrast in grayscale images. Spheroid volume is estimated using the equation 5.1 shwon below:

$$(5.1)\ Volume = \left(\frac{1}{2}\right)(Major\ \ Axis)x(Minor\ Axis)^2$$

5.3.5 Analysis of Necrotic Core

Qualitative and quantitative analysis of spheroids necrotic core was examined through live/dead fluorescent staining. At days 3 and 7, living spheroids were stained for 15 minutes with 7 g/mL carboxyfluorescein diacetate succinimidyl ester (CFDA-SE) and 25 g/mL propidium iodide (PI). CFDA-SE will stain for living cells, whereas PI will stain for dead cells. CFDA-SE is a cell permeable dye which diffuses into cells and react with intracellular proteins to form a detectable fluorophore. The acetate group on CFDA is cleaved by esterase enzymes to form carboxyfluorescein succinimidyl ester (CFSE), a fluorescent product which covalently binds to sources of amine, such as lysines. CFSE has a maximum fluorescence excitation and emission wavelength at 492 nm and 517 nm, respectively. At low concentrations, CFSE is stable for several days, non-toxic, and detectable fluorescence can be passed to daughter cells up to 8 divisions. Cells that are metabolically active with functioning esterase enzymes will stain positive for CFSE. PI is a cell impermeable dye, and will be excluded from viable cells. PI will only penetrate cells with compromised cell membranes. When PI is bound to nucleic acids in either DNA or RNA, the maximum fluorescence emission and excitation are 535 nm and 617 nm, respectively. Free, unbound PI has very little fluorescence, but once bound to nucleic acids, the fluorescence is enhanced 20 to 30 fold. Once stained with CFDA and PI, spheroids were rinsed 2x with complete growth medium and imaged. An inverted fluorescence light microscope was used to capture phase contrast, green fluorescence from CFDA, and red fluorescence from PI. Images were artificially colored based on greyscale images taken in each channel. Qualitatively, images were used to confirm the presence of a necrotic core, a characteristic of spheroids. Quantitatively, Matlab SpheroidSizer was used to compute the volume of spheroid

stained with PI, and total spheroid volume. Estimated necrotic core volume was calculated using equation 5.2 below:

$$(5.2)\ \%\ Necrotic\ Core = \frac{Volume\ PI}{Total\ Volume}\ x\ 100$$

5.3.6 Flow Cytometry to Quantify Necrotic Core

Necrotic core of 4T1 spheroids were analyzed quantitatively using Flow Cytometry to count the number of cells which have stained positive for PI (dead) compared to the number of cells which have stained positive for CFDA (live). On days 3 and 7 spheroids were stained as described in the live/dead analysis, then disassembled using Accumax for 10 minutes in a water bath at 37 °C. After pipetting up and down several times to break apart the spheroid, the stained cell solutions were counted in a BD Accuri C6 fluorescence activated cell sorter (FACS). Spheroids were grown in three conditions with different zinc concentrations: GM, GM + 50 µM Zn, and GM + 100 µM Zn. Six spheroids from each group were sorted based on fluorescence signal, and 5,000 cells from each spheroid were measured. Average %Live, %Dead, and Live/Dead ratio for each group are reported to quantify the effects of zinc on the necrotic core of 4T1 spheroids in vitro.

5.3.7 Histological Staining

Once sectioned and placed onto microscope slides, 8 µm slides of 4T1 3D MCTS were stained for the presence of calcium using von Kossa staining method. Spheroid sections were also stained with eosin, which will stain all proteins a pink/red color. Spheroid sections were fixed with 70% ethanol for 5 minutes, then 100% ethanol for 5 minutes. Next, sections were rinsed with deionized water and covered with 1% silver nitrate for 1 hour under UV light. Sections were rinsed with 5% sodium thiosulfate for 3 minutes and then rinsed with water, followed by 100% ethanol for 5 minutes each. Finally, sections were stained with Eosin-Y Alcoholic solution for 6 minutes. Microscope slides were rinsed with 100% ethanol and imaged under brightfield microscopy.

5.3.8 Raman Spectroscopy

Spheroid sections placed onto cleaned stainless steel slides were analyzed with Raman spectroscopy to confirm the presence of hydroxyapatite. Sections were first rinsed with deionized to remove any OCT on the slide, and then air dried. A Renishaw inVia Confocal Raman Microspectrometer with a 633nm laser of spot size 0.858 µm was used to acquire Raman

spectra from 200 to 2,000 cm^{-1} of 5 spots containing mineralized matrix on each sample. A total of 150 accumulations for each spot were averaged to yield the final spectrum. WiRE software was used to quantitatively analyze peak position, integration, and ratios. Spheroid sections were additionally analyzed for phosphate:carbonate ratio, which was not performed on 2D monolayers due to interference from polystyrene which overlaps with carbonate peak.

5.3.10 Gel Zymography

4T1 cells in monolayer were plated at 50,000 cells/cm^2 in 24 well plates. 4T1 spheroids were plated at 5,000 cells per spheroid. Both monolayers and spheroids were grown for up to 10 days in OC, OC +50 μM $ZnCl_2$, or OC + 100 μM $ZnCl_2$. On day 10, culture medium was replaced with serum free DMEM for 24 hours and collected on day 11. Protein concentration in culture medium was quantified using the Tecan Infinite 200 Pro NanoQuant plate reader. Relative MMP-2 and MMP-9 activity in each sample was quantified using gel zymography. Samples were diluted with water to contain 2.5 mg/mL protein. Next, each sample was mixed 1:1 with sample buffer containing 0.5M Tris-HCl at pH 6.8, 20% glycerol, 10% SDS, 0.1% and Bromophenol Blue and incubated at room temperature for 15 minutes. 40 L of each sample was pipetted into individual wells of a 10% Criterion™ Zymogram Gel with gelatin. Running buffer was transferred to the Criterion™ cell, and electrophoresis was run at 200V for 1 hour. Next, the gel was removed, rinsed with water, and renatured with 2.5% Triton X-100 for 1 hour under constant shaking. The gel was rinsed several times with deionized water and developed for 48 hours at 37 °C with constant shaking. Developing buffer consisted of 50mM Tris base, 0.2M NaCl, 5mM $CaCl_2$, and 0.02% Brij 35. After developing, the gel was rinsed with deionized water and stained with Coomassie Blue R-250 stain for up to 4 hours with constant shaking. Next, the gel was destained with 50% methanol and 10% acetic acid in water for 15 minutes with constant shaking. Finally, the gel was rinsed with deionized water, sandwiched between two sheets of transparent paper, and scanned to create a grayscale image. Images were analyzed in ImageJ using the Analyze Gels function.

5.3.11 Applications to Co-culture Models

The 4T1 spheroid model used in this study was further investigated for potential applications to co-culture models. Addition of human umbilical cord endothelial cells (HUVEC) were investigated as a potential co-culture system. HUVECs were cultured in Endothelial Cell Medium (ECM) supplemented with 5% FBS and 1% endothelial cell growth supplements

(ECGS). Spheroids were plated via liquid overlay method on agarose coated 96 wells in three different ratios of 4T1:HUVEC cells: 3:1, 1:1, and 1:1. Spheroids were self assembled and culture medium was changed every 2-3 for up to 28 days. The system was characterized for size of spheroids generated and quantification of necrotic core via live/dead staining through fluorescence microscopy and flow cytometry for up to 7 days.

5.4 Results

5.4.1 Zinc Cytotoxicity

DNA quantification using the PicoGreen assay was then applied to the 4T1 3D spheroid model to determine if zinc has cytotoxic effects on 4T1 spheroids. The spheroid model is a more realistic approach to determining potential cytotoxic effects of zinc on breast cancer cells, as a spheroid more closely mimics a tumor in vitro compared to a monolayer. Spheroids collected at days 0, 1, 3, and 7 were collected, lysed, and tested for total DNA content when grown in GM, GM + 50 μM Zn, and GM + 100 μM Zn. Results of spheroid DNA quantification are reported in terms of ng/spheroid in **Figure 5.3**. After 7 days in culture, DNA content in 4T1 spheroids grown in GM, GM + 50 μM Zn, and GM + 100 μM Zn is 312, 331, and 335 ng per spheroid. Spheroid growth is not inhibited by high exogenous zinc concentration, since DNA content in the spheroids grow in moderate and high zinc concentrations were slightly higher compared to spheroids grown in GM. Overall, DNA content of spheroids were not significantly affected by zinc concentration, showing that zinc has little cytotoxic effect in vitro using a 3D spheroid model of breast cancer.

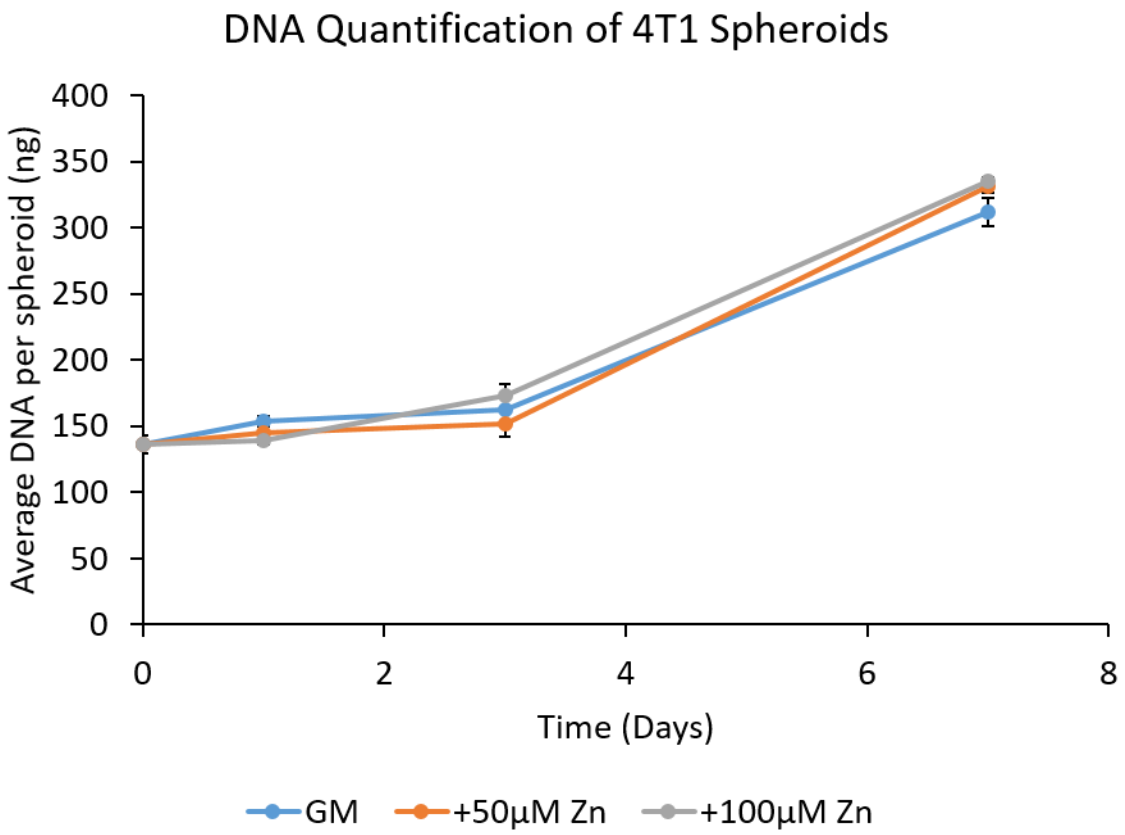

Figure 5.3. DNA content in 4T1 spheroids up to 7 days grown in GM, GM +50 µM Zn, and GM +100 µM Zn. Averages are representative of 2 independent experiments taking 9 spheroids per condition per experiment.

5.4.1 Spheroid Characterization

Figure 5.4 shows representative phase contrast images of 4T1 spheroids grown for up to 28 days in OC, OC + 50 µM $ZnCl_2$, and OC + 100 µM $ZnCl_2$. After 72 hours, spheroids are fully self-assembled at day 0. Between days 3-7 spheroids are roughly 400-500 µm, and grow to about 700-800 µm by day 28. Qualitatively, treatment with 50 and 100 µM Zn does not have any effect of spheroid growth for a 28 day period. In **Figure 5.5**, the average spheroid volume for the 28 day period is calculated using Matlab SpheroidSizer. Little difference is seen between spheroid volumes for up to two weeks. After two weeks, error within the experimental groups increases as spheroids continue to grow. The average volume for 4T1 spheroids grown in OC is smaller at 28 days compared to the two zinc treated groups. However, the differences are not significant as there is a large amount of error due to the size of individual spheroids within experimental groups varying greatly throughout the 4 week period.

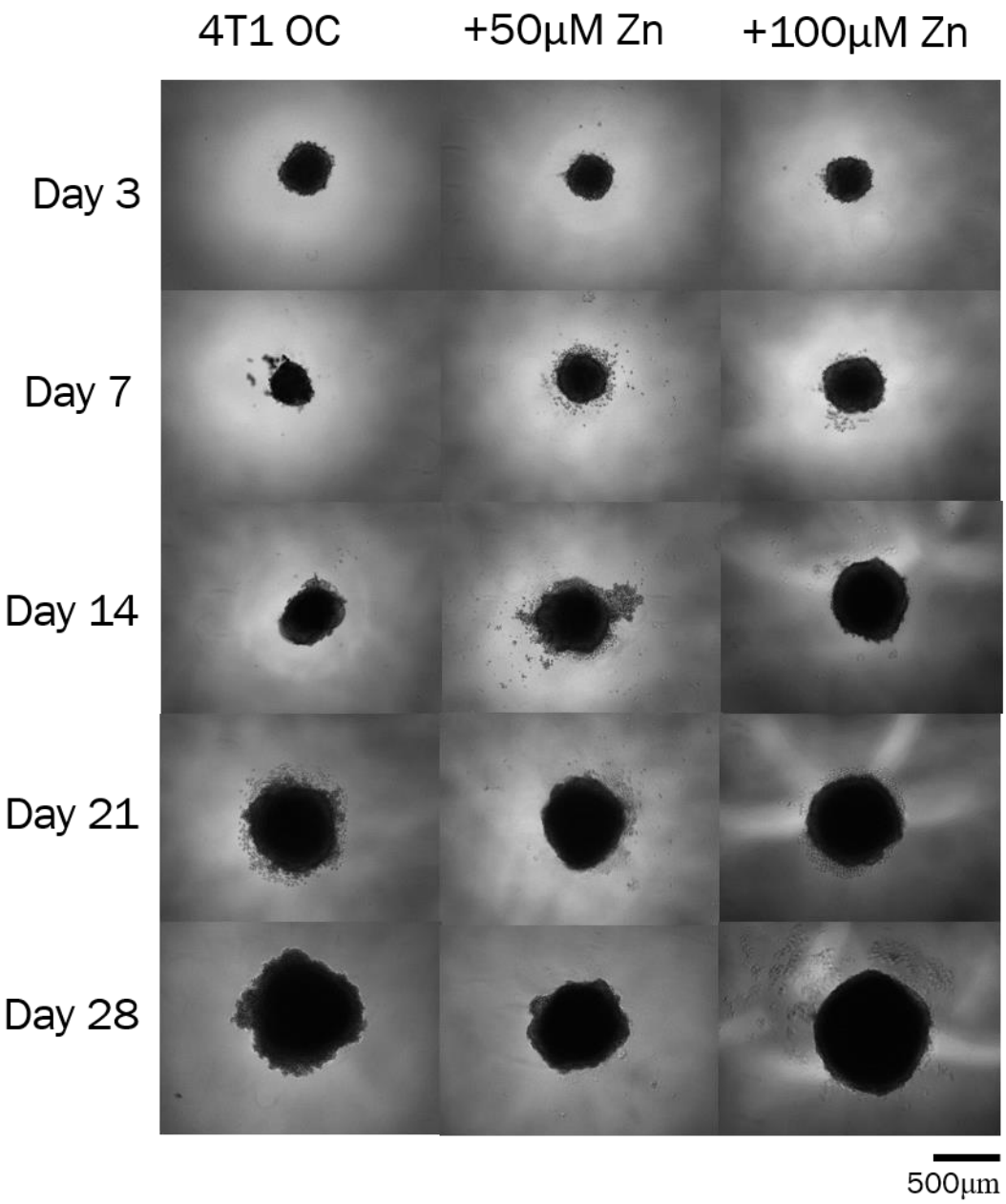

Figure 5.4. Growth of 4T1 spheroids plated at 5,000 cells/cm^2. On Day 3, spheroids are 400-500 µm and grow to 700-800µm by day 28. Qualitatively, zinc has no effect on spheroid growth. Micrographs are representative of 12 spheroids per condition in two different experiments.

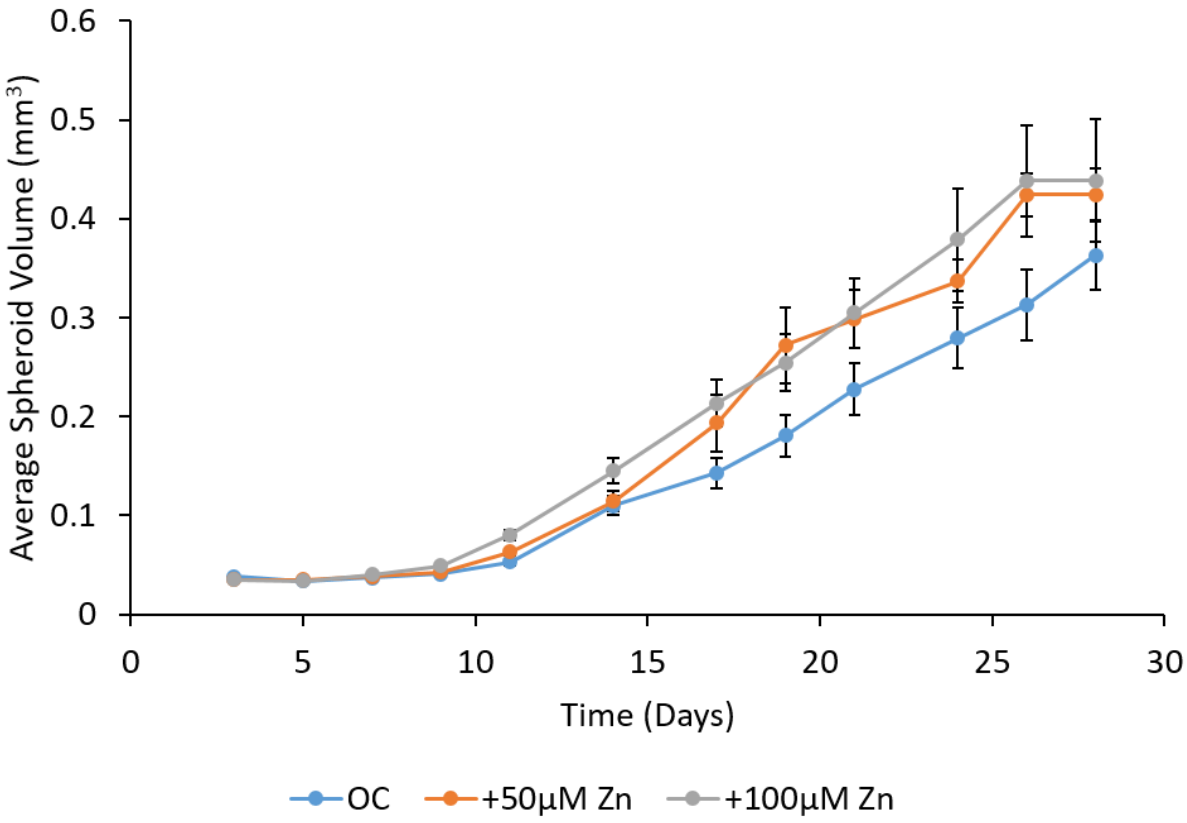

Figure 5.5. Spheroid growth through 28 days. Estimated spheroid volume shows no cytotoxic effects of zinc treatments through 28 days. Plot is representative of 2 independent experiments. Spheroid size is an average between 12 spheroids per experiment.

Live/dead fluorescent staining was performed to investigate the necrotic core of the 4T1 spheroids formed with the liquid overly method on agarose. The presence of a necrotic core is apparent by the red fluorescence staining in the center of the spheroid. A positive red stain indicates PI is penetrating compromised cell membranes in the spheroid core and binding to DNA base pairs. Presence of a necrotic core is an important characteristic of 3D spheroid models, especially in tumor spheroids. The presence of a positively stained PI indicates a necrotic core present, validating the characteristics of the spheroid model.

Figure 5.6 shows a qualitative representation of 4T1 spheroid necrotic cores. According to the live/dead staining, there is little difference at days 3 and 7 between necrotic cores of spheroids treated with zinc. This would indicate that zinc is having no cytotoxic effects on spheroid growth. **Figure 5.7** shows a quantitative analysis of necrotic core volumes, which were estimated using Matlab SpheroidSizer program. The average percent necrotic core volume was calculated by dividing the estimated volume taken from positively stained PI by the total estimated volume derived from the phase contrast images. According to the volume estimates, there is little difference between zinc treated groups and control OC treated group at both days 3 and 7. On day 3, the OC + 100 M Zn group had a necrotic core of 46% compared to the necrotic core of 56% for the OC group, but this difference was not significant. By day 7, as the spheroid grow in size, the average necrotic core volume has decreased in all the groups. The OC group decreased from 56% to 39% necrotic core volume from day 3 to 7.

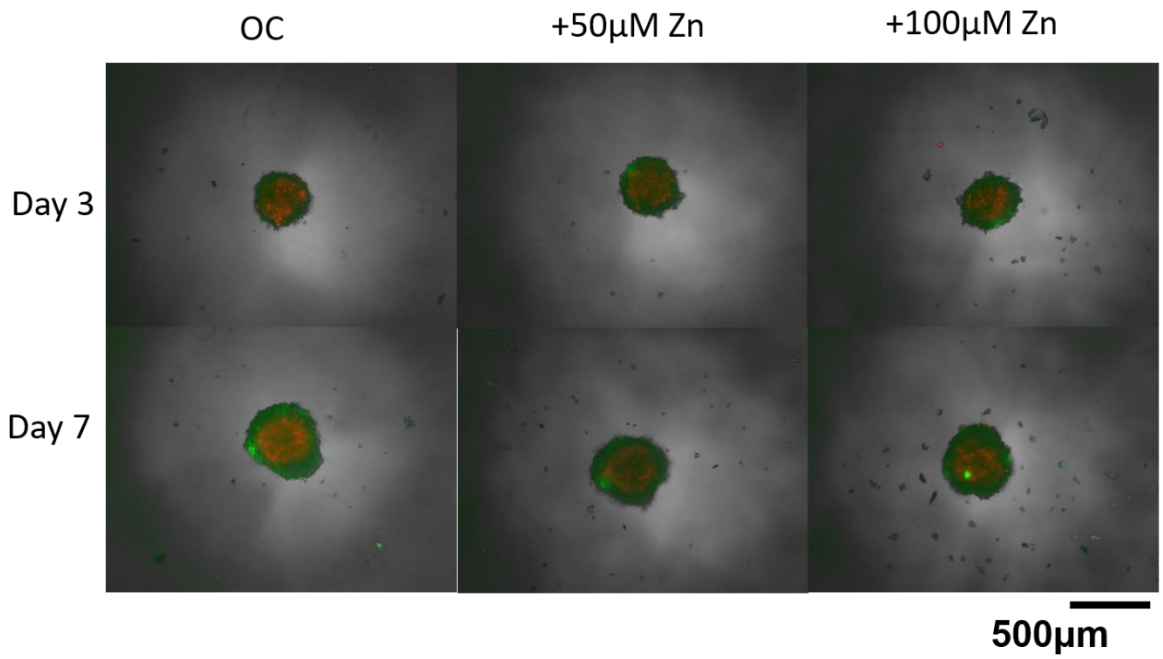

Figure 5.6. Necrotic core of 4T1 spheroids were assessed using a live/dead fluorescence staining.

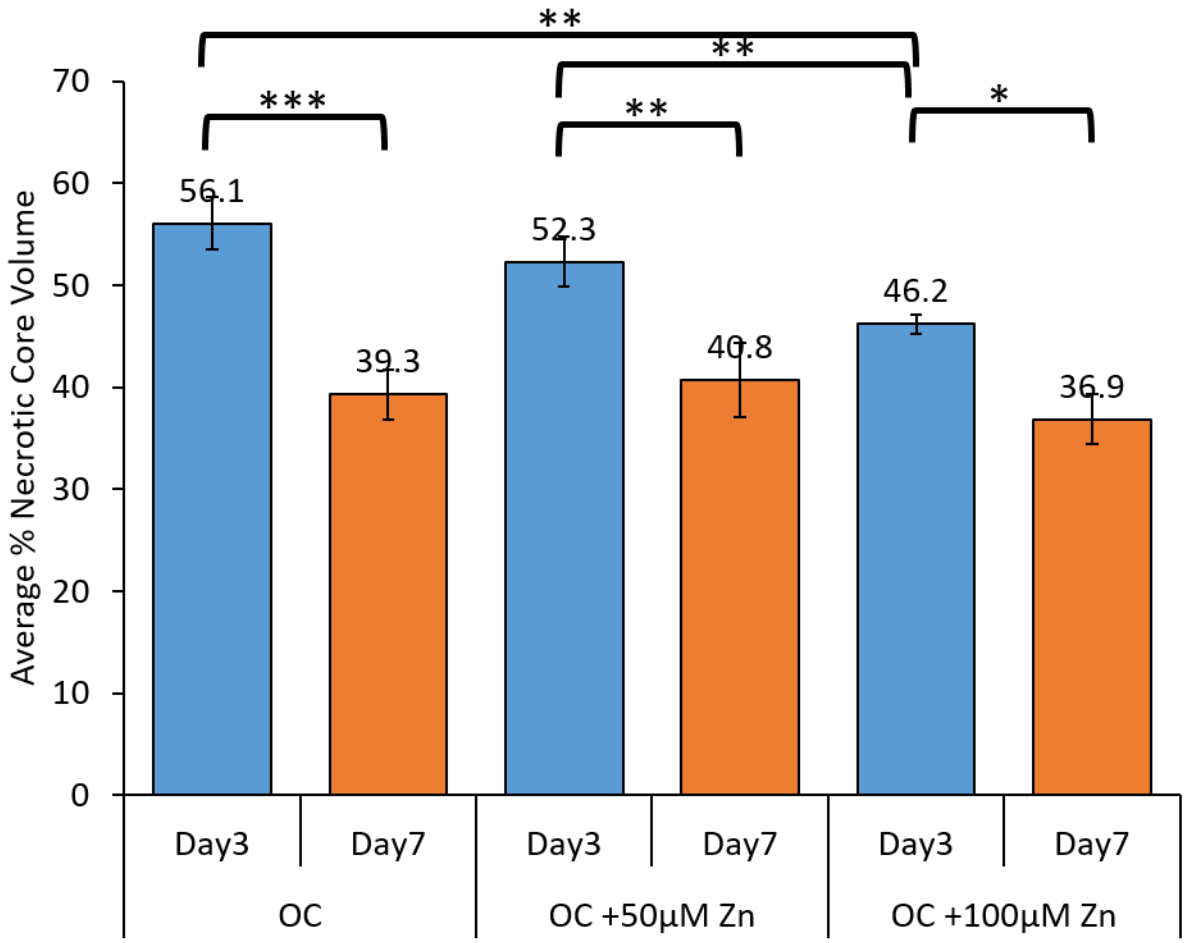

Figure 5.7. Analysis of necrotic core volume performed with Matlab SpheroidSizer program on days 3 and 7 grown in OC, OC + 50 µM Zn, and OC + 100 µM Zn. Averages are representative of 2 independent experiments, each containing 8 spheroids per condition.

5.4.2 Flow Cytometry to Quantify Necrotic Core

Necrotic core of 4T1 spheroids were analyzed quantitatively using Flow Cytometry to count the number of cells which have stained positive for PI (dead) compared to the number of cells which have stained positive for CFDA (live). On days 3 and 7 spheroids were stained as described in the live/dead analysis, then disassembled using Accumax for 10 minutes in a water bath at 37 °C. After pipetting up and down several times to break apart the spheroid, the stained cell solutions were counted in a BD Accuri C6 fluorescence activated cell sorter (FACS). Six spheroids from each group were counted based on fluorescence. Cells stained positive for red are considered necrotic dead cells. Cells stained positive for green are considered living metabolically active. Cells stained positive for red and green are considered viable cells with compromised membranes, possibly hypoxic. Finally, cells not stained are considered quiescent due to their lack of metabolic activity, but intact membranes. The effects of zinc on necrotic core of 4T1 spheroids is summarized in **Figure 5.8**. The percentage of dead cells is not significantly affected by zinc concentration as it remained between 2-3% for all samples. The percentage of living cells is not significantly affected by zinc concentration. The three zinc concentration are all within error and range between 23-25% on day 3 and 15-18% no day 7. The major observed differences between spheroids seem to be affected by time, which would indicate size affects necrotic and hypoxic characteristics. The number of unstained cells decreases as spheroid size grows and the number of stained cells positive for both live and dead stains is increasing. This would indicate an increasing number of viable cells with compromised membranes, possibly affected by hypoxia due to growing spheroid size and decrease availability of oxygen and nutrients within the spheroid core.

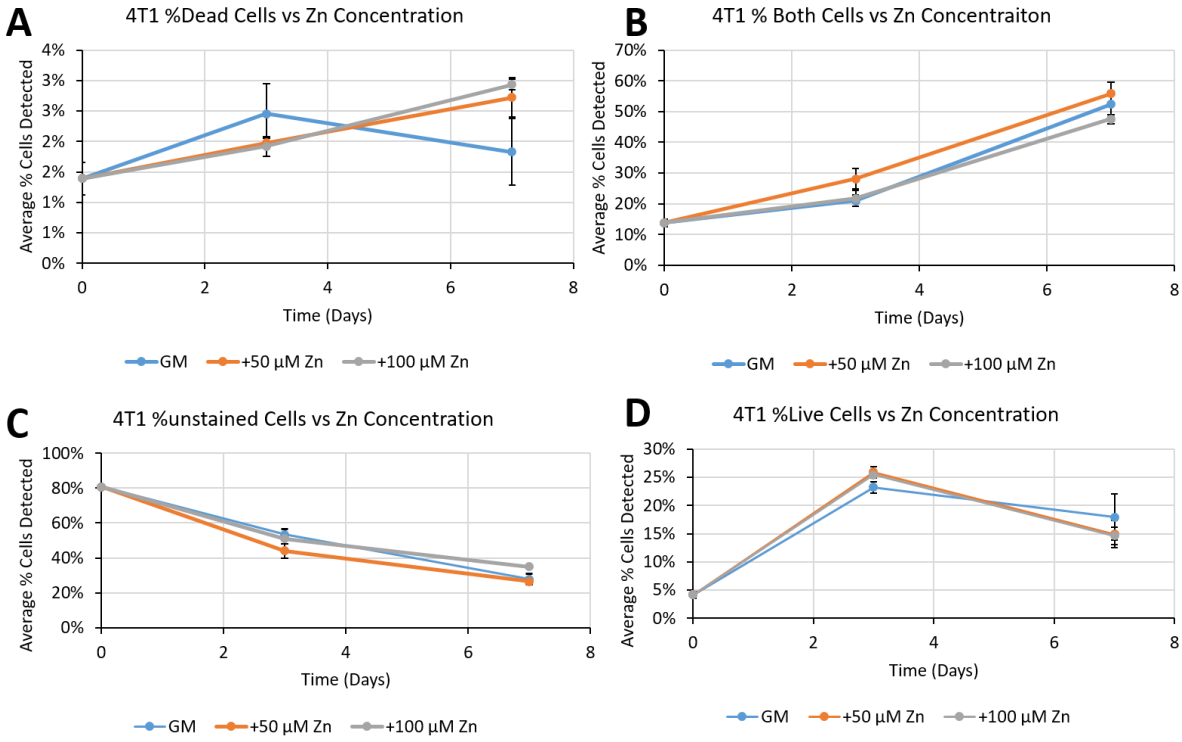

Figure 5.8. Flow cytometry analysis of live/dead stained 4T1 spheroids at days 0, 3, and 7 measuring (A) % dead cells, (B) % both live and dead cells, (C) % unstained cells, and (D) % live cells, in GM,GM + 50 µM Zn, and GM + 100 µM Zn. Each data point represents the average % of cells detected in 3 independent solutions containing 3 spheroids each, 9 spheroids total.

5.4.3 Histological Staining

Results of histological staining in the 2D in vitro model were a promising start towards understanding the role of zinc in breast cancer microcalcifications. The mineralization potential of 4T1 breast cancer cells in vitro was confirmed in monolayer culture. Also, the potential of zinc to inhibit breast cancer microcalcification formation was confirmed at concentrations of up to 100 µM Zn, and partial inhibition at a concentration of 50 µM Zn. Next, the 4T1 in vitro microcalcification system was modified to engineer a novel system for studying microcalcifications in breast cancer using a 3D MCTS model. As shown in **Figure 5.9**, 4T1 spheroids grown after 28 days in OC have a strongly mineralized core, apparent by the dark von Kossa stain in the center. Sections of spheroids grown in OC +50 µM Zn showed slightly less calcium, but similar to the OC treated spheroids, the calcified region was located in the core. Finally, 4T1 spheroids grown in OC +100 µM Zn had no calcium regions stained with von Kossa. This result was similar to 4T1 monolayers grown in 100 µM Zn, confirming the inhibitory effects of high exogenous zinc concentrations on microcalcification formation of a mineralizing breast cancer cell line.

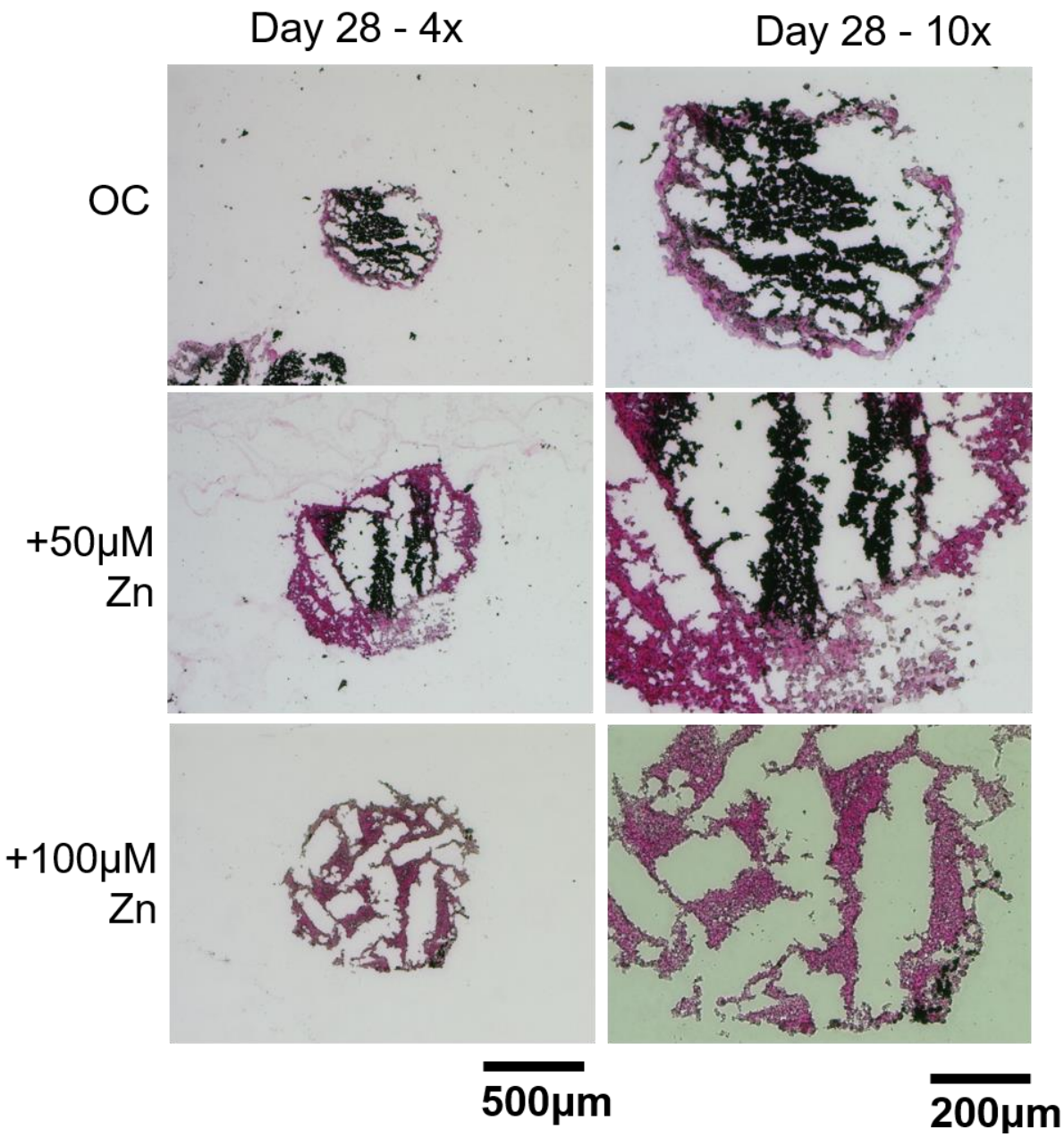

Figure 5.9. Representative 8 µm thick 3D MCTS sections after 28 days in culture grown in OC, OC + 50 µM Zn, and OC + 100 µM Zn. Self-assembled spheroids were grown in 96 well plate via liquid overlay method, with culture medium changed every 2 days. After collection, spheroids were fixed with 8% formaldehyde overnight and embedded into a 2mg/mL collagen layer which was frozen in OCT. Next, spheroids were sectioned and placed onto glass microscope slides, rinsed with deionized water, and stained with Eosin for protein (red), and von Kossa for calcium (black).

5.4.4 Raman Spectroscopy

Raman spectroscopy was performed on 8 μm thick spheroid sections, which were placed on stainless steel slides. Spectra from 5 calcified regions in each spheroid were captured and analyzed for mineral:matrix ratio and crystallinity. Spheroid sections were additionally analyzed for phosphate:carbonate ratio.

Table 3 represents a summary of the most prominent Raman peaks in mineralized biological tissue and their corresponding vibrational assignment. According to the Raman spectra, the most prominent peaks present are the phosphate peak at 960 cm^{-1}, which is caused by the symmetric stretching of the phosphate group, the carbonate peak at 1070 cm^{-1}, which is caused by symmetric stretching of the carbonate group, and the amide I peak at 1660 cm^{-1}, which is caused by the double bond between carbon and oxygen in the amide group.[171]

Raman Shift (cm^{-1})	Assignment	Notes
430	ν2 PO_4^{3-}	symmetric bend
584-590	ν4 PO_4^{3-}	antisymmetric bend
960	ν1 PO_4^{3-}	symmetric stretch
1003	C-C	phenylalaline
1070	ν1 CO_3^{2-}	symmetric stretch – overlap with ν3 PO_4^{3-}
1076	ν3 PO_4^{3-}	symmetric bend – overlap with ν1 CO_3^{2-}
1300	Amide III	Protein α-helix
1446	δCH_2	Protein CH_2 deformation
1660	Amide I	C=O vibration component is strongest

Table 3. A list of the most prominent Raman shifts assigned to calcified biological tissue.[171]

Raman spectra of a purified hydroxyapatite standard commercially purchased was tested to confirm the presence of phosphate peaks. As shown in **Figure 4.4**, the hydroxyapatite standard contains only the four phosphate peaks corresponding to the four vibrational assignments of the phosphate molecule. No carbonate is present because the hydroxyapatite used is a purified, commercially available standard. Also, no amide peaks are present because there are no proteins or cellular components in the sample. The hydroxyapatite standard has a crystallinity value of 9.8, representing its full-width at half maximum height (FWHM). This means the width of the phosphate peak at 960cm^{-1} at half the height is 9.8.

Representative Raman spectra from day 28 4T1 spheroids grown in OC, OC + 50 μM, and OC + 100 μM Zn are shown in **Figure 5.10**. According to the Raman spectra in **Figure 5.10A**, carbonate, amide I, and amide III peaks are all present at or near their assigned Raman shifts. Based on the assigned Raman shifts of the calcified spheroid section, it can be concluded that the calcified tissue section contains an impure, carbonated form of hydroxyapatite. According to the list of Raman shifts in **Table 3**, the spectrum acquired in Figure 24 from day 28 calcifications in 4T1 spheroids shows the peaks representing carbonated hydroxyapatite. The effects of high exogenous zinc concentration on the calcifications are apparent in **Figure 5.10B** and **Figure 5.10C**. Specifically, spheroids grown in OC +50 μM Zn were stained positive for von Kossa staining, indicating calcified regions within the spheroid. A representative Raman spectra from 5 of these regions is shown in **Figure 5.10B**, which shows a much smaller phosphate peak when compared to the calcifications formed by breast cancer cells with no added zinc. Raman spectra was acquired for spheroid sections grown in OC +100 M Zn, which revealed no phosphate peaks, confirming the inhibitory effects of high zinc concentration on development of calcifications in vitro.

In order to quantify the differences between sections of spheroids grown in OC and sections of spheroids grown in OC + 50 μM Zn, average peak area between phosphate peak (960cm^{-1}), carbonate (1070cm^{-1}), and amide I (1660cm^{-1}) were calculated and compared. The phosphate to carbonate ratio and phosphate to amide I (mineral to matrix) was calculated for both groups and compared. Average phosphate to carbonate ratio is reported in **Figure 5.11**, showing a higher phosphate to carbonate ratio in 4T1 spheroids grown in OC compared to 4T1 spheroids grown in OC + 50 μM Zn. The average phosphate to carbonate ratio for the OC group was 3.8, compared to 1.8 for the OC + 50 μM Zn group. This result was statistically significant

(p=0.04). The group containing OC + 100 μM Zn could not be calculated due to the lack of a phosphate peak. The phosphate to amide I ratio (mineral to matrix) was also higher in the OC group compared to the OC + 50 μM Zn group. The results are shown in **Figure 5.12**, where the average mineral to matrix ratio for the OC and OC + 50 μM Zn group are 2.0 and 0.5, respectively. This result was statistically significant (p=0008). Again, the OC + 100 μM Zn group could not be calculated to due to absence of a phosphate peak. Finally, the full width at half maximum height (FWHM) was calculated for the phosphate peaks to determine crystallinity of the calcification. As shown in **Figure 5.13**, there was no difference between FWHM of phosphate peaks between the control and zinc treated group. Sections grown in OC and OC + 50 M Zn had FWHM values of 16.5 and 16.3, respectively.

Overall, analysis of the calcified regions of spheroid sections confirmed the presence of a carbonated hydroxyapatite in spheroid sections grown in OC for 28 days. Also, the inhibitory effects of zinc at high concentration was also confirmed at + 100 μM Zn, as no phosphate peaks were present in sections at this concentration. Interestingly, there was a significant difference in phosphate between the OC and OC + μ50 M Zn group

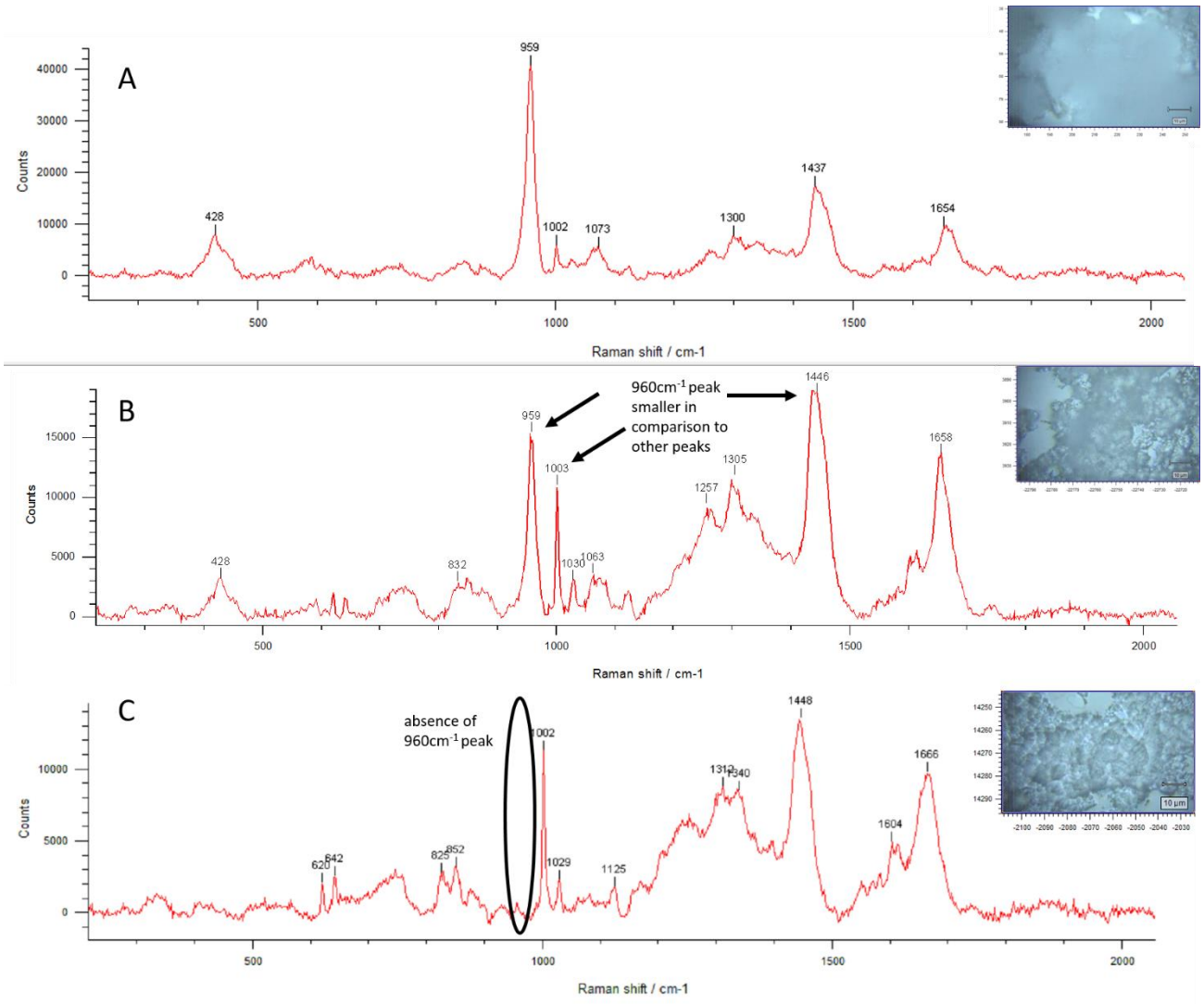

Figure 5.10. Representative Raman spectra of day 28 4T1 spheroids grown in (A) OC, (B) OC + 50 µM Zn, and (C) OC + 100 µM Zn.

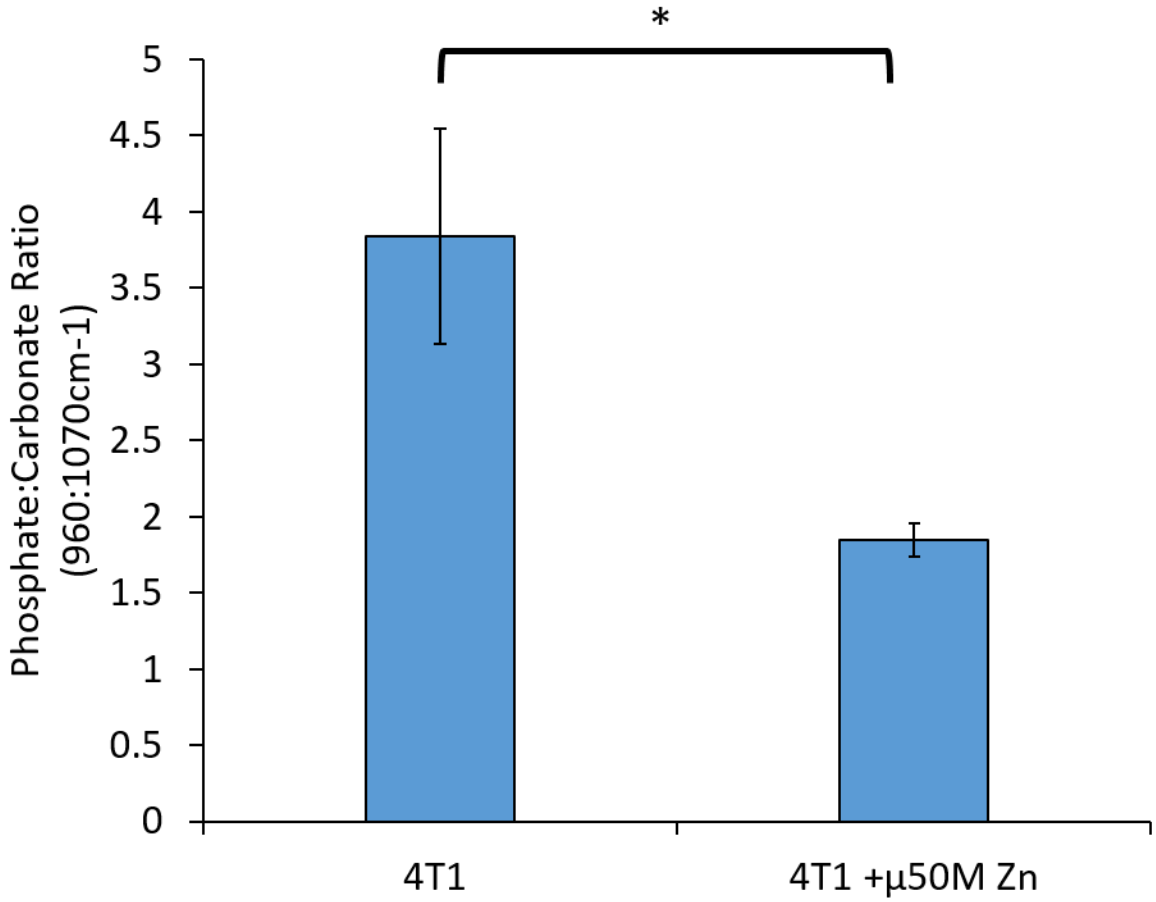

*Figure 5.11. Average phosphate to carbonate ratio in mineralized regions of 4T1 spheroid sections grown in OC and OC + 50 µM Zn. (*p<0.05)*

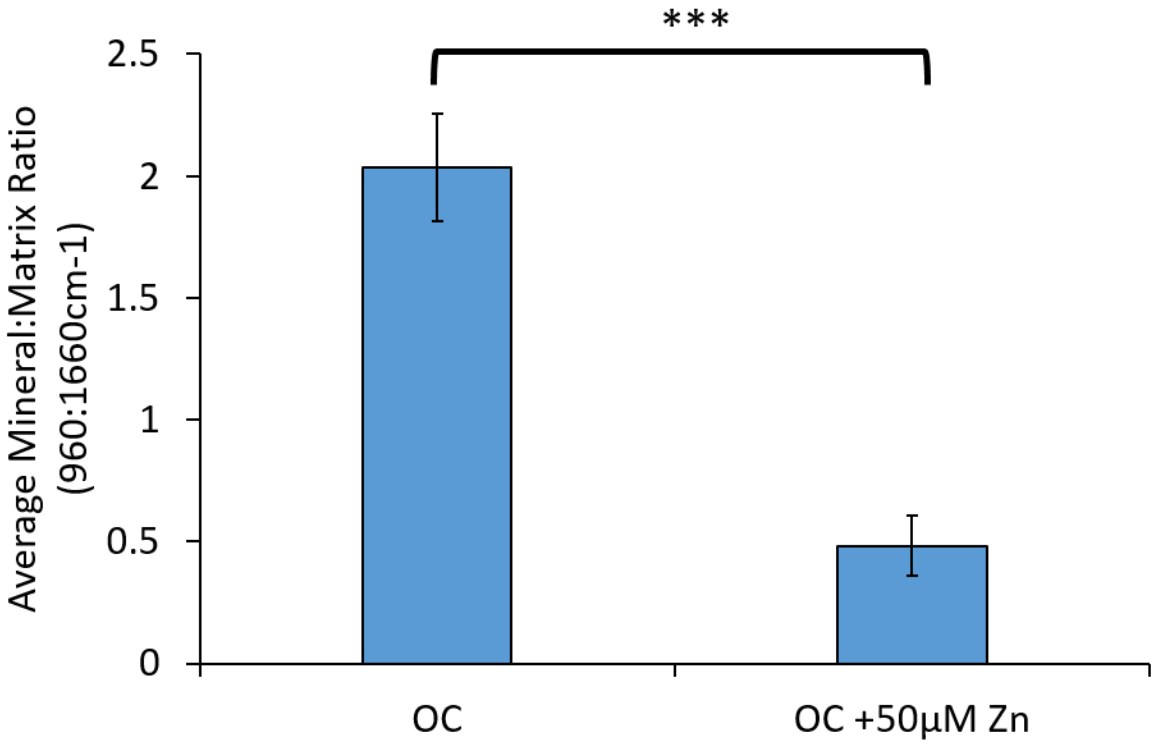

*Figure 5.12. Average mineral to matrix ratio of calcified regions of 4T1 spheroids grown in OC and OC + 50 µM Zn. (***p<0.001)*

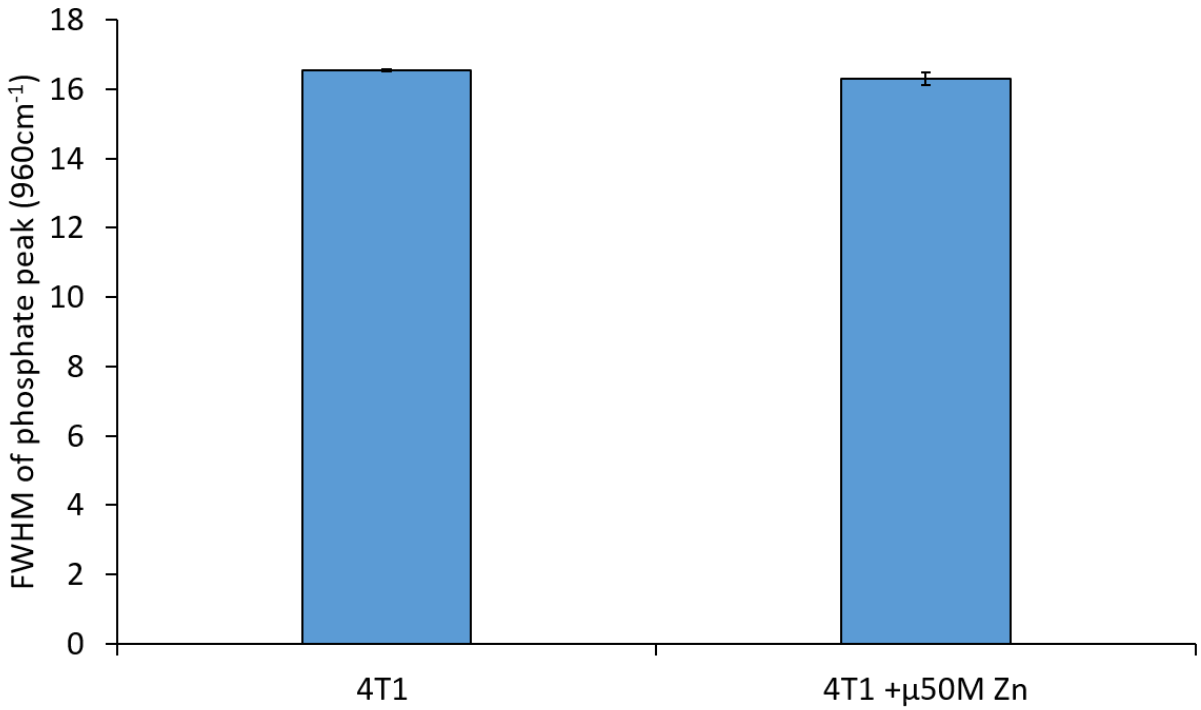

Figure 5.13. Average full width at half maximum (FWHM) of phosphate peak at 960cm^{-1} in calcified regions of 4T1 spheroids grown in OC and OC + 50 µM Zn.

5.4.6 MMP Activity

The effects of zinc on MMP activity were examined through gel zymography using both a 2D monolayer and 3D spheroid model of 4T1 in vitro cultures. Band density of each lane of the gels were quantified in ImageJ to quantitatively compare MMP-2 and MMP-9 activity. MMP-2 and MMP-9 activity in 2D monolayers are represented by light bands shown in **Figure 4.17**. Compared to day 0, there is little MMP-9 activity in 2D, as represented by the lack of visualized bands in the gel at 92 kDa. At day 0 and day 10, there are minimal visualized bands representing MMP-2 at 72 kDa. Based on the lack of visualized bands in the gel from the supernatants collected in 2D monolayers, supernatants of 3D spheroids were tested to examine any potential differences between the models. **Figure 5.14** is a scanned image of the gel zymogram showing the MMP-9 and MMP-2 bands formed from spheroid supernatants. Based on the bands, which represent gelatinase activity, there is a difference in MMP-2 and MMP-9 production using a 3D spheroid model, compared to a conventional 2D monolayer. As shown in the gel zymogram in the spheroid model of **Figure 5.14**, the bands for both MMP-9 and MMP-2 are both brighter on both day 0 and day 10 compared to 2D monolayer model of **Figure 4.17**. The fact that MMP production is increased in a spheroid model shows the importance of using a 3D model, as it more realistic in cell-cell interactions, which could be affecting expression of proteins and enzymes on the molecular level.

The effect of zinc on MMP activity, represented by band density was then quantified using the scanned images in **Figure 4.17** and **Figure 5.14**. Calculated band densities are reported in terms of MMP-9 activity in **Figure 5.15**, and MMP-2 activity in **Figure 5.16**. Overall, MMP-9 and MMP-2 activity is much higher in 3D spheroid models compared to 2D monolayers. The potential effects of zinc on MMP activity are shown in the day 10 band densities. There is an increase of MMP-9 activity with an increase in zinc concentration, based on the calculated band densities. At day 10, 3D spheroid MMP-9 band density for OC, OC + 50 μM Zn, and OC + 100 μM Zn groups are 3166, 4726, and 5369, respectively. At day 10, the spheroid MMP-2 band density for OC, OC + 50 μM Zn, and OC + 100 μM Zn groups are 2273, 2127, and 1174, respectively. Overall, there is a much higher MMP-9 activity compared to MMP-2 activity. Increased zinc concentrations appear to be increasing MMP-9 activity and decreasing MMP-2 activity in the spheroid model.

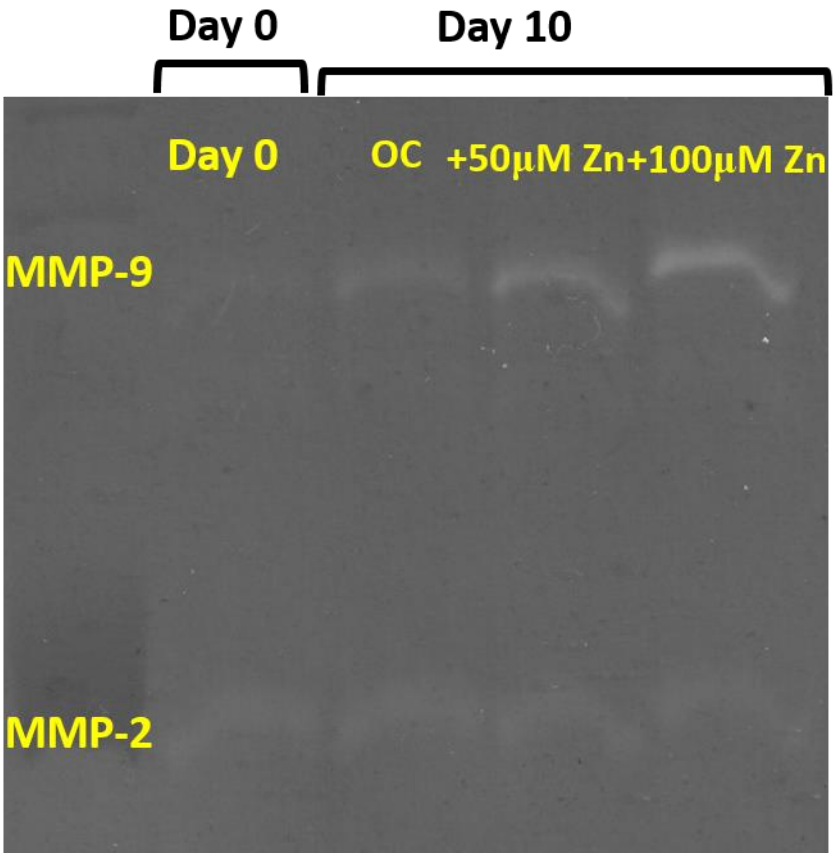

Figure 5.14. Scanned image of gel zymogram representing MMP-9 (92 KDa) and MMP-2 (72 KDa) activity in supernatants of 4T1 spheroids in vitro at day 0 and day 10 grown in OC, OC + 50 μM Zn, and OC + 100 μM Zn. Gel zymogram is representative of 3 independent experiments.

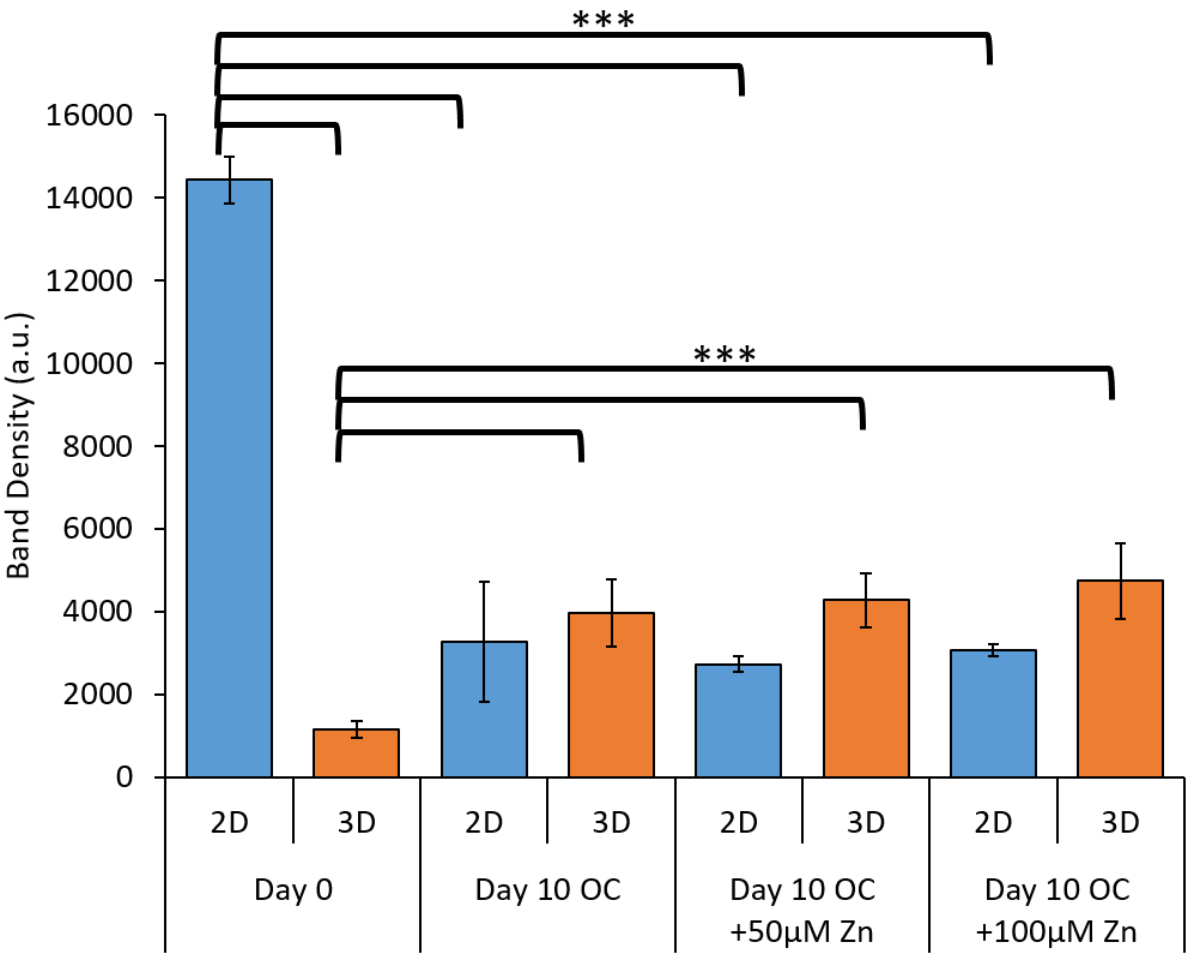

*Figure 5.15. MMP-9 activity calculated by gel zymogram band density of 3D spheroid supernatants at day 0, and day 10 in OC, OC + 50 μM Zn, and OC + 100 μM Zn. MMP-9 activity is increased greatly at day 10 in the spheroid model compared to the 2D monolayer. Also, MMP-9 activity appears to increase with increasing zinc concentration. Band densities are reported as average of three independent experiments. (***p<0.001)*

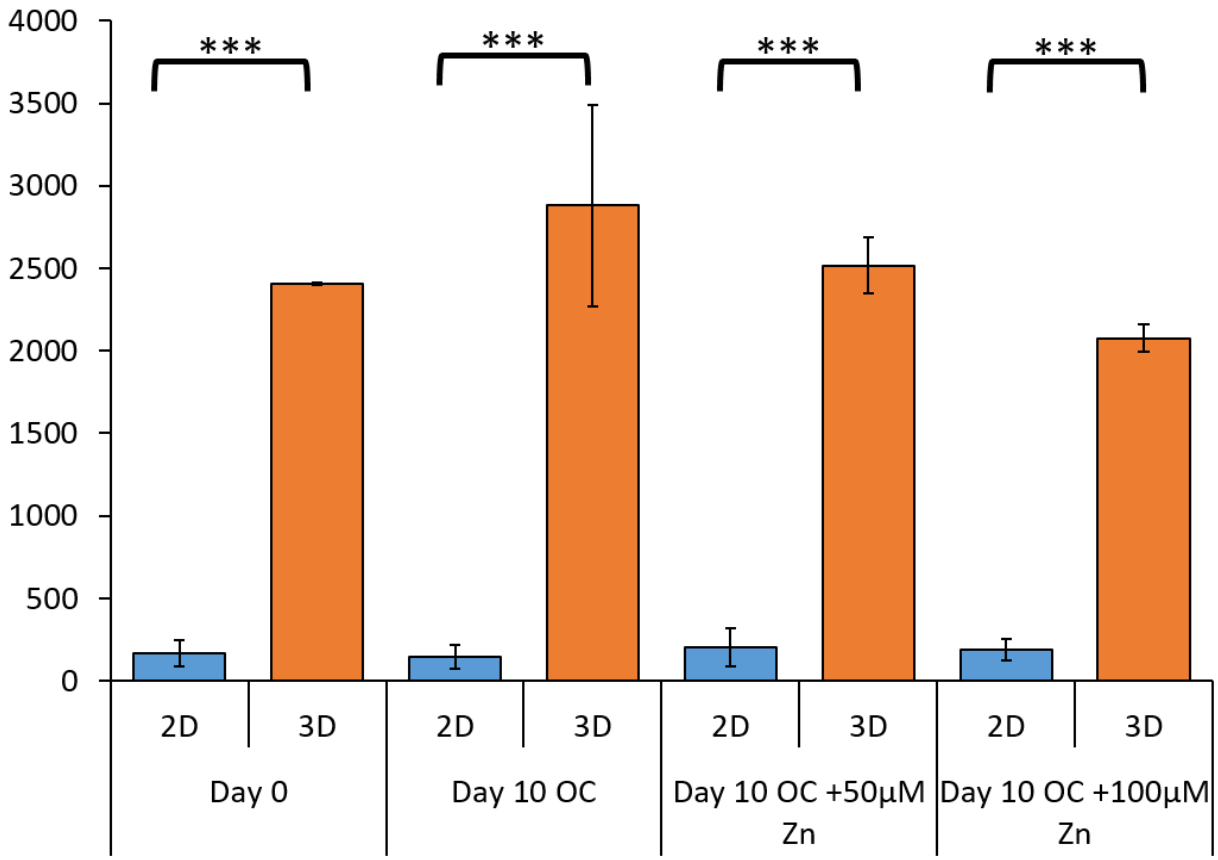

*Figure 5.16. MMP-2 activity calculated by gel zymogram band density of 3D spheroid supernatants at day 0, and day 10 in OC, OC + 50 µM Zn, and OC + 100 µM Zn. MMP-2 activity is increased greatly at day 0 and day 10 in the spheroid model compared to the 2D monolayer. Also, MMP-2 activity appears to decrease with increasing zinc concentration. Band densities are reported as average of three independent experiments. (***p<0.001)*

5.4.7 Applications to Co-culture Models

The 4T1 spheroid model used in this study was further investigated for potential applications to co-culture models. Addition of endothelial cells were tested at a 4T1:HUVEC ratio of 3:1, 1:1, and 1:3. **Figure 5.17** shows representative co-culture spheroids grown for up to 10 days. Average spheroid size is calculated and reported in **Figure 5.18**, which shows a much larger spheroid size with the addition of HUVECs. The spheroids with the largest size are the 3:1 and 1:1 4T1;HUVEC ratio. The 1:3 4T1:HUVEC ratio is much smaller than the other co-culture models, but still much larger than 4T1 cells by themselves.

Live/dead staining on spheroids was performed on co-culture spheroids to assess size of necrotic core with different ratios of HUVECs. **Figure 5.19** shows representative fluorescence images of co-cultured spheroids at days 3 and 7. Necrotic core sizes were calculated in the SpheroidSizer program of Matlab to yield an average necrotic core volume, shown in **Figure 5.20**. Based on the calculated necrotic core volumes, there does not appear to be a trend between necrotic core and HUVEC concentration. However, the 1:3 4T1:HUVEC ratio yielded the lowest necrotic core volume of the co-culture spheroids. Since the 1:3 ratio was the smallest spheroid, it makes sense that spheroid size and necrotic core volume would be correlated. Larger spheroids have a larger oxygen and nutrient gradient, as less oxygen and nutrients get in the center of a larger mass. According to the flow cytometry data in **Figure 5.21**, which analyzed dispersed co-culture spheroids which were stained with live/dead markers, there is little difference in necrotic core between the different ratios. Compared to 4T1 spheroids, co-culture spheroids did have a slightly larger population of cells that stained positive for dead stain and a also a slightly larger population of cells that stained positive for the live stain. Co-culture spheroids are much larger than 4T1 spheroids, so the presence of a larger population of dead cells is expected. However, these differences are not large enough to merit a conclusive statement. The presence of a large population of unstained and cells stained for both live and dead markers could either indicate a problem with the system, meaning the dyes are not as specific towards their respective populations, or it could indicate separate populations of senescent cells. Cells stained positive for both live and dead could be viable cells with partially compromised membranes. Unstained cells could be senescent cells with intact membranes, but not metabolically active. These two populations could be caused by the diffusion gradient presenting a diminished oxygen and nutrients supply.

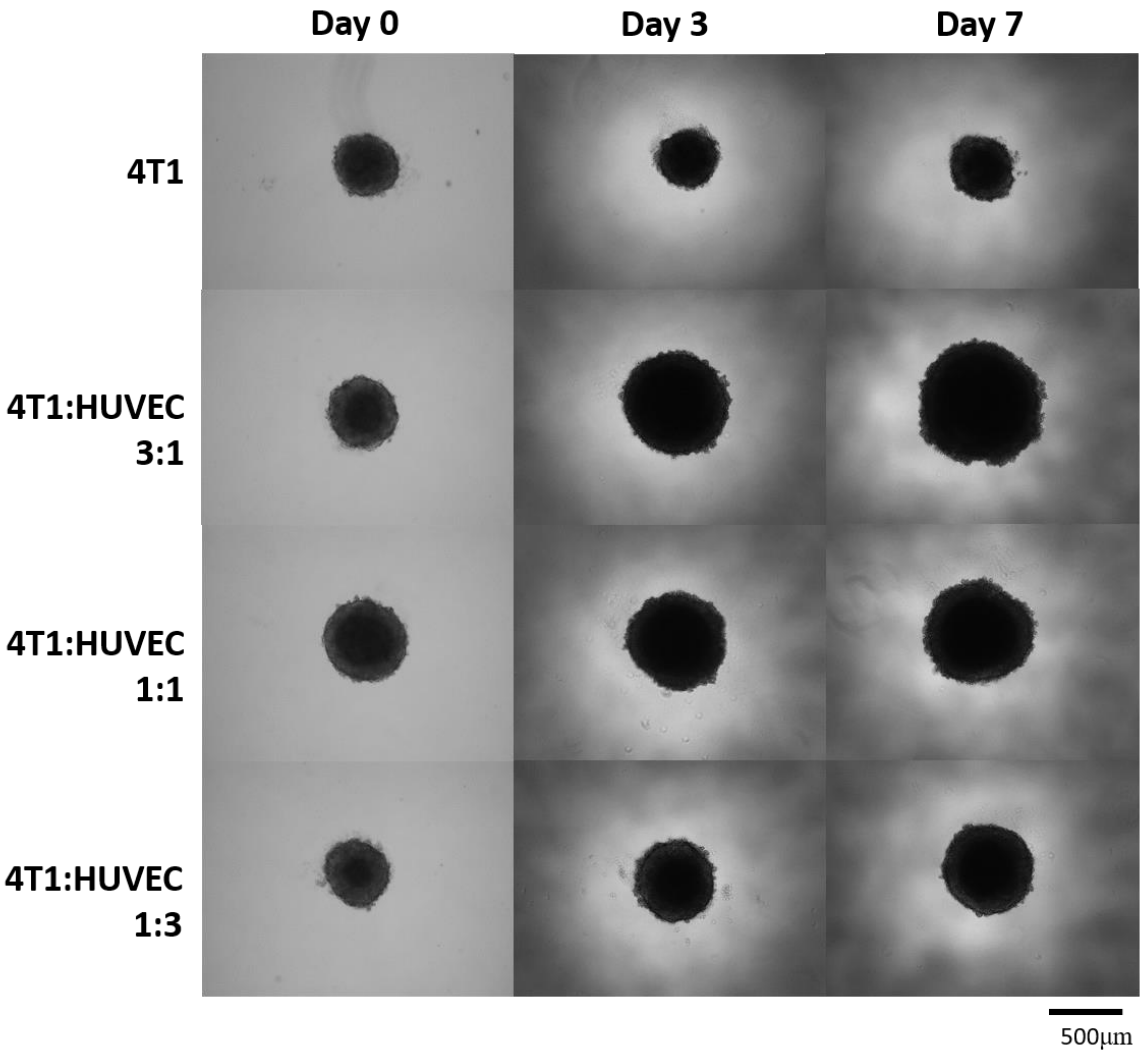

Figure 5.17. Representative images of 4T1:HUVEC co-culture spheroids taken up to 7 days.

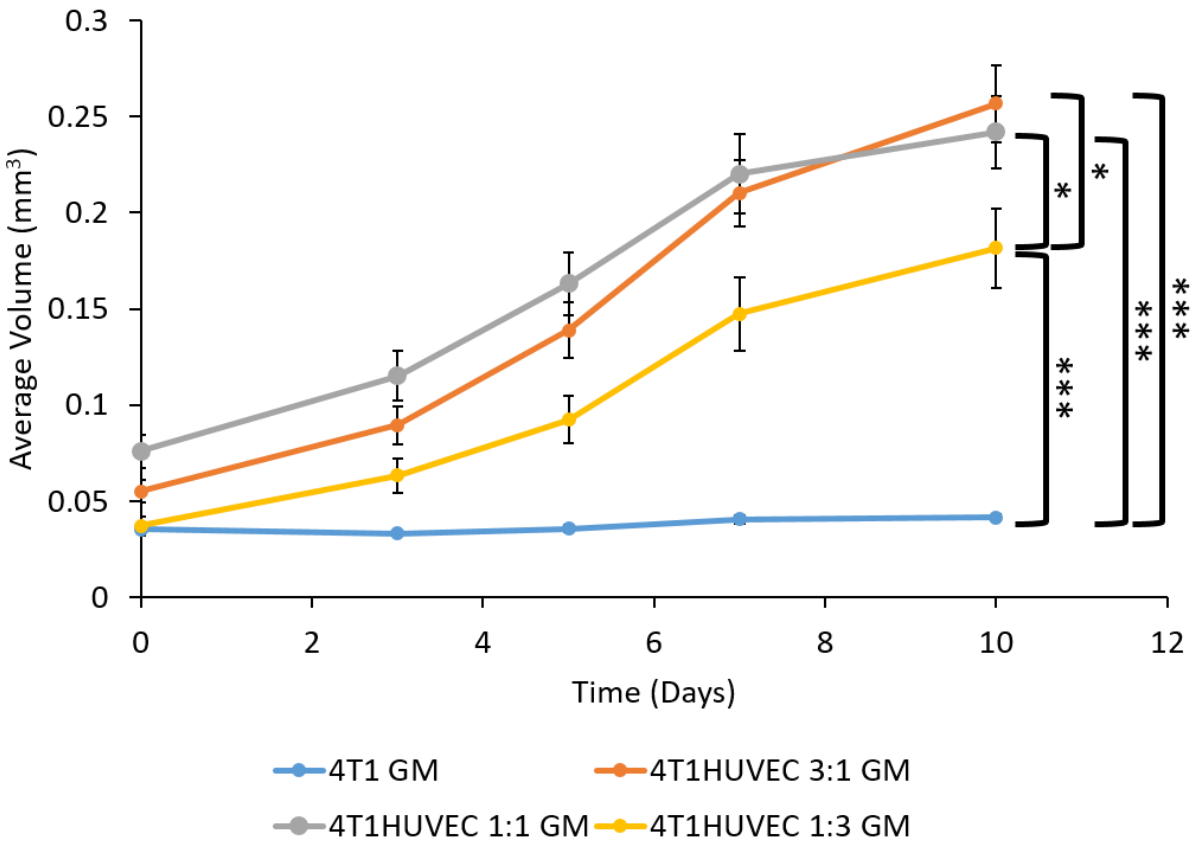

*Figure 5.18. Average size of 4T1:HUVEC co-culture spheroids measured with SpheroidSizer program in Matlab Averages taken between 12 spheroids each experiment in 2 independent experiments.(*p<0.05, ***p<0.001)*

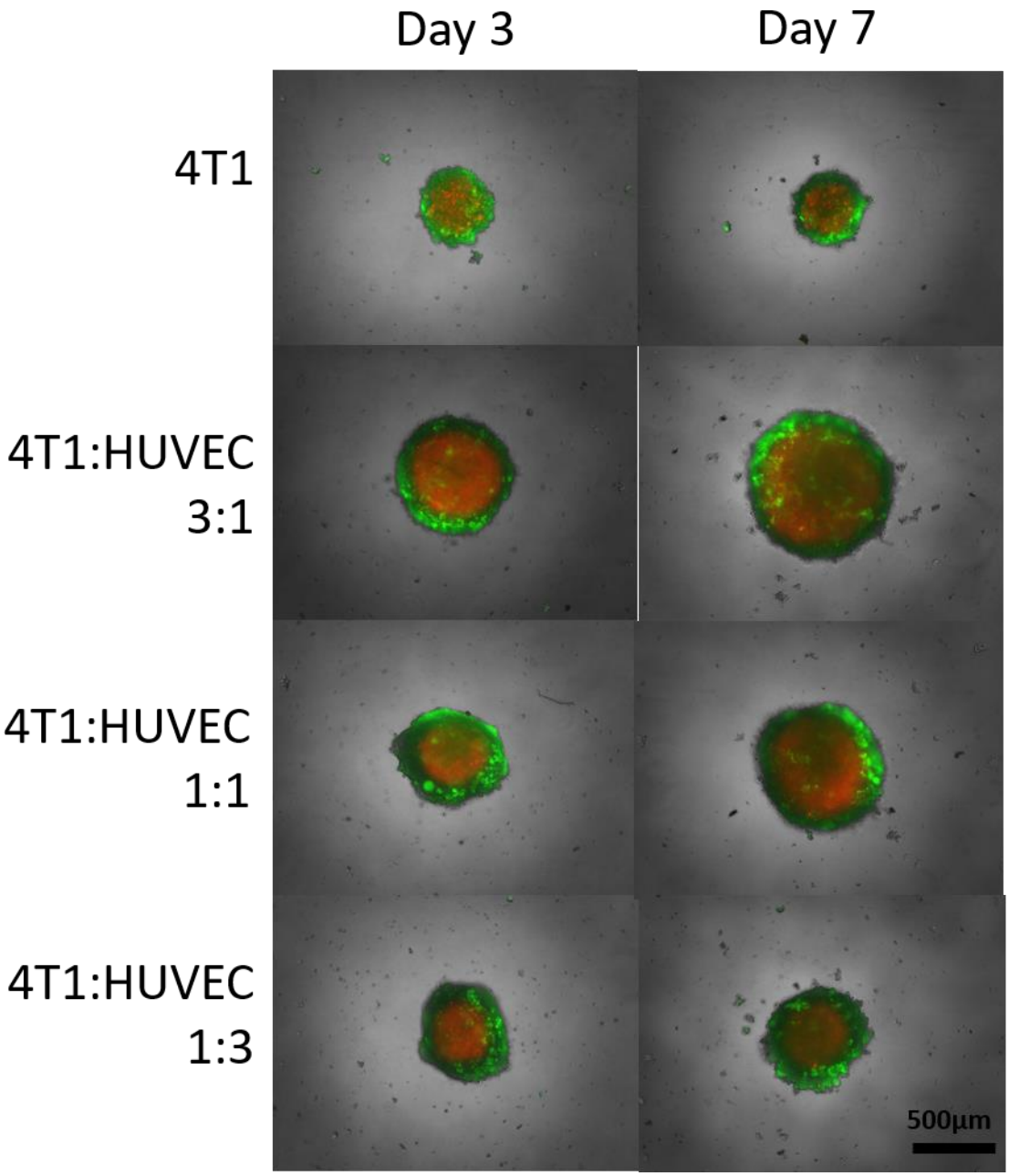

Figure 5.19. Representative fluorescene images of live/dead stained co-culture spheroids at days 3 and 7.

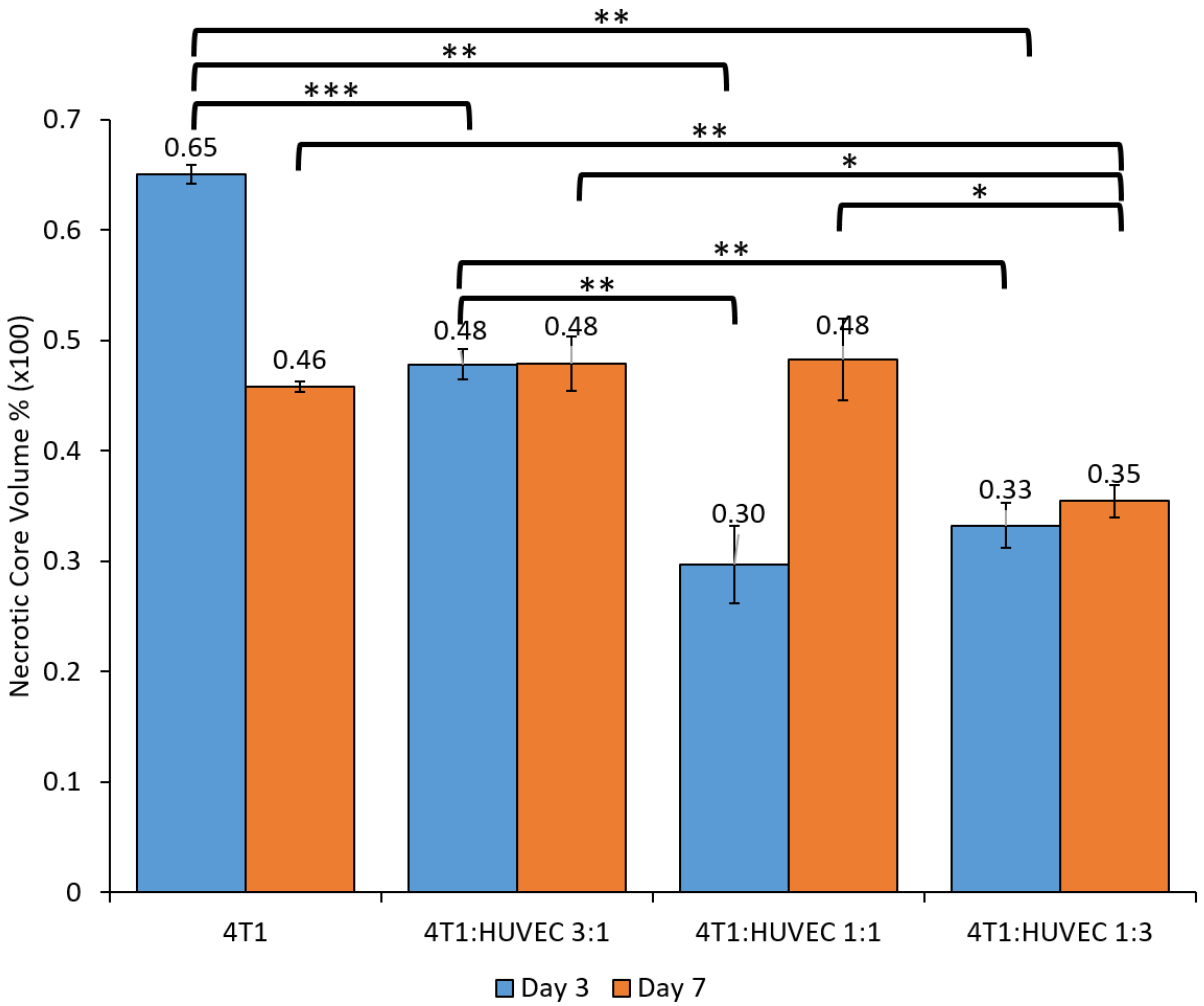

*Figure 5.20. Average calculated necrotic core volume based on fluorescence images taken of live/dead stained co-culture spheroids at days 3 and 7. Averages representative of 8 spheroids per experiment in 2 independent experiments. (*p<0.05, **p<0.01, ***p<0.001)*

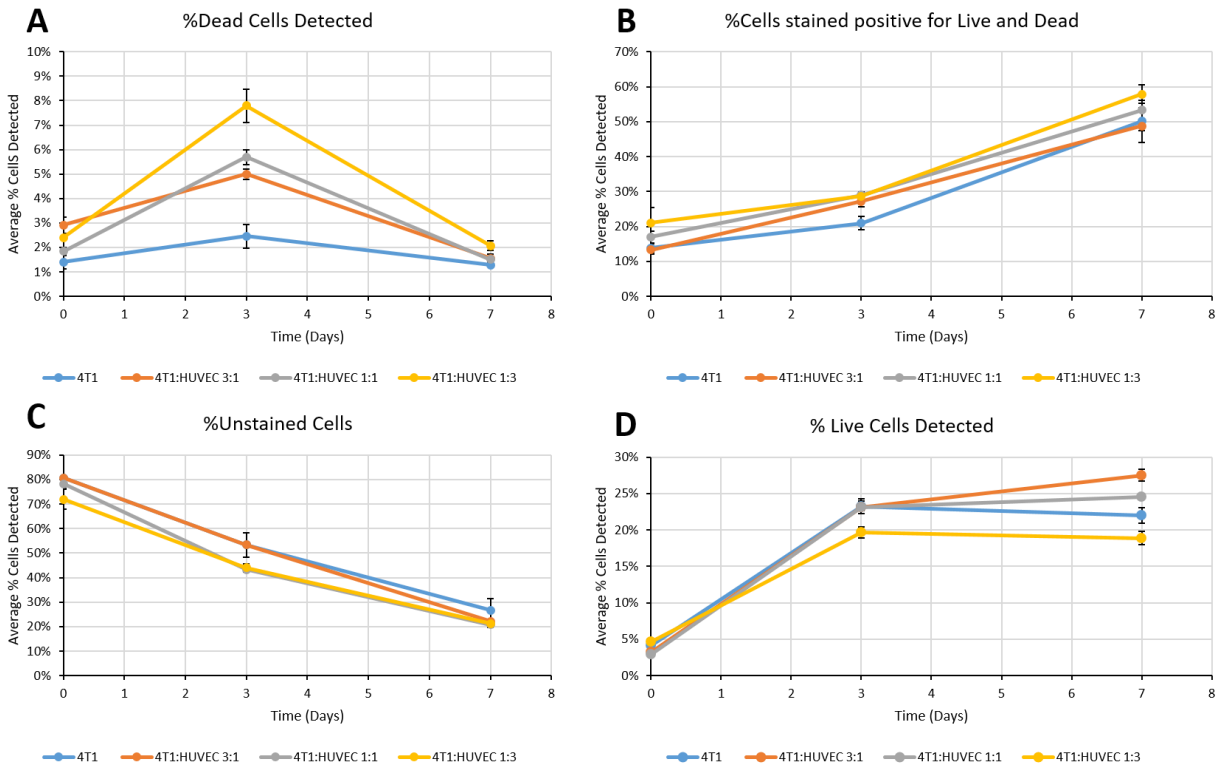

Figure 5.21. Flow cytometry analysis of live/dead stained 4T1:HUVEC co-culture spheroids at days 0, 3, and 7 measuring (A) % dead cells, (B) % both live and dead cells, (C) % unstained cells, and (D) % live cells. 5,000 cells per tube were counted, where 3 spheroids were dispersed in each tube. Averages taken of 3 tubes, totaling 9 spheroids counted.

5.5 Discussion

This work demonstrates the successful engineering of a three dimensional in vitro spheroid model for studying breast cancer microcalcifications in 4T1 murine breast cancer cells. The 3D spheroid model developed was used to investigate the potential effects of high exogenous zinc concentrations on the inhibition of microcalcification formation. Zinc was chosen as a potential anti-cancer target due to its potential role in the development of breast cancer. Specifically, high serum zinc levels have been correlated to a decreased risk in the development of breast cancer.[150] Furthermore, breast cancers have the tendency to accumulate intracellular zinc compared to surrounding tissues. This is caused by the imbalance between membrane bound Zip proteins bringing zinc into the cell and ZnT proteins transferring zinc out of the cell. Some breast cancers have more Zip and less ZnT proteins, resulting in more zinc entering, with less zinc exiting the cell.[154–156] Recently, studies have suggested mammary mineralization is an actively regulated process, with similar cellular pathways as those in bone mineralization.[140–142] Breast cancers have been shown to express several bone matrix proteins, such as OPN, bone sialoprotein, and ALP.[143,144,170] Cox et al. demonstrated mineralization in breast cancer is an active cell-mediated process which is partially regulated by ALP.[170] The effects of excess zinc has been shown to inhibit ALP levels, resulting in altered mineralization of osteoblasts in vitro.[55] We hypothesized that excess zinc concentration would inhibit breast cancer microcalcification formation in a similar manner as excess zinc has been shown to inhibit mineralization in osteoblast cells.

A novel three dimensional spheroid model for studying breast cancer microcalcifications was successfully characterized by monitoring spheroid size and necrotic core. Spheroids plated at 5,000 cells per well, self-assembled into a spheroid of size between 400-500 μm after 72 hours. It has been suggested that optimal size for tumor spheroids in vitro is between 200-500 μm to best simulate the properties of cell-cell and cell-ECM interactions, while developing an oxygen and chemical gradient most similar to that of in vivo tumors.[183–188] As shown in **Figure 5.4**, spheroids are an acceptable size when first assembled, measuring between 400 and 500 μm. **Figure 5.6**, shows the characteristic development of a necrotic core through live/dead fluorescence staining. The 3D spheroids developed using 4T1 breast cancer cells are of an acceptable size and developed a necrotic core, showing it is an ideal model for studying breast cancer in vitro. Specifically, this model was used to study breast cancer microcalcifications. As

shown in **Figure 5.9**, when 4T1 cells are grown in OC for up to 28 days, they are strongly mineralizing in a 2D monolayer. Mineralization potential of the 3D spheroid model was proven in **Figure 5.9**, as shown by dark stained calcium in the core of the spheroid. An engineered 3D spheroid model using 4T1 cells to develop breast cancer microcalcifications in vitro is the first of its kind.

The 4T1 spheroid model was used to investigate the effects of zinc on its ability to inhibit breast cancer microcalcifications in vitro. Two exogenous zinc concentrations were tested: moderate zinc (+50 μM Zn added), and high zinc (+100 μM Zn added), using growth medium conditions as a control. Firstly, cytotoxicity of zinc was tested to ensure zinc was not causing any decrease of cell viability. Cytotoxicity was first assessed in monolayer using the MTS assay for cell viability, and PicoGreen assay for quantification of DNA. Based on these results in **Figure 4.2** and **Figure 4.3**, both the moderate and high zinc concentrations used did not show any cytotoxic effects on 2D in vitro cultures. The 3D spheroid model was also used to show no cytotoxic effects of zinc at moderate and high zinc concentrations, based on the PicoGreen assay results in **Figure 5.3**. No significant differences in DNA per spheroid are observed up to 7 days with moderate and high zinc concentration compared to the control.

Spheroids grown in moderate and high zinc concentrations were characterized to ensure no negative, cytotoxic effects of exogenous zinc occurred. Based on the sizes in **Figure 5.4** and **Figure 5.5**, zinc does not appear to be negatively affecting spheroid growth up to 28 days, further supporting the cytotoxicity and DNA quantification results. Live/dead staining to visualize and calculate necrotic core in 4T1 spheroids was used to further assess any potential effects on spheroid growth. Based on the images in **Figure 5.6** and corresponding calculated necrotic core volumes in **Figure 5.7**, zinc does not appear to affect necrotic core characteristics of spheroids. Overall, spheroid DNA content, size, and necrotic core were not affected negatively by moderate and high zinc concentrations, compared to control conditions with no added zinc. Also, necrotic core of spheroids were examined through flow cytometry after dispersing spheroids into a homogenous cell suspension stained with live/dead fluorescence markers. Overall, zinc showed little effect on the percentage of living, dead, cells stained for live and dead, and unstained cells up to 7 days. As spheroid size from grew from day 0 to 3 to 7, it was observed that the percentage of unstained cells decreased and the percentage of cells stained for both live and dead fluorescent markers increased. This would indicate the effects of hypoxia

on the spheroid are increasing, as there more cells with compromised membranes. As spheroid size increases, more cells are hypoxic as nutrients and oxygen availability become scarcer. Cells stained for both live and dead markers are thought to be viable with compromised membranes, or may be binding non-specifically to the live cell marker. This is because dead population of cells often produce false positives to many other reagents due to non-specific binding.[194] Overall, the flow cytometry data reinforce evidence that exogenous zinc concentrations up to 100 μM Zn are not cytotoxic and do not affect characteristics of 4T1 spheroid populations.

The effects of moderate and high zinc concentrations on 4T1 microcalcification formation were then tested for the ability to inhibit calcification formation in a 2D monolayer and a 3D spheroid model. Histological staining of 2D monolayers grown in OC, OC with moderate zinc, and OC with high zinc in **Figure 4.6** and **Figure 4.7**, show a moderate inhibition of microcalcification formation at 50 μM Zn, and complete inhibition of microcalcification formation at 100 μM Zn. Alizarin Red staining at 14 and 21 days and von Kossa staining at days 21 and 28 in monolayer cultures show partial inhibition of microcalcification formation at 50 μM Zn, and complete inhibition of microcalcification formation at 100 μM Zn. The inhibitory effects of zinc on formation of breast cancer microcalcifications were examined in the 3D spheroid model. Similar results are seen in the spheroid model as in the monolayer. Histological staining of spheroid sections showed in **Figure 5.9** show partial and complete inhibition of calcifications in 4T1 spheroids when grown with 50 μM and 100 μM Zn, respectively.

Raman spectroscopy on calcified 2D monolayers in *section 4.4.2* showed interference with several polystyrene peaks, leading to questionable results as to the effects of zinc on calcified crystals. However, the peaks present were able to confirm the presence of a carbonated form of hydroxyapatite based on phosphate and carbonate peaks. A more conclusive approach was then taken to study effects of zinc on calcified sections of 4T1 spheroids, placed on stainless steel slides, which yield no Raman background, eliminating interference.

Raman spectroscopy on calcified regions of spheroid sections in section 5.4.4 showed phosphate and carbonate peaks typical of calcified biological tissue, carbonated hydroxyapatite. The phosphate peak at 960 cm^{-1}, carbonate peak at 1060cm^{-1}, amide III peak at 1300cm^{-1}, and amide I peak at 1660 cm^{-1}confirm the presence of carbonated hydroxyapatite, as all of these peaks are characteristic of carbonated hydroxyapatite, the main component in type II breast

cancer microcalcifications.[171] Raman spectra of spheroid sections grown in OC and OC + 50 μM Zn were quantitatively compared for phosphate:carbonate, mineral:matrix ratio, and crystallinity to determine the effects of growth in moderate zinc concentration on the calcified crystal. Both phosphate:carbonate ratio and mineral:matrix ratio are lower in spheroids treated with moderate zinc concentrations. Spheroids treated with high zinc concentrations had no calcified regions found in spheroid sections, which agreed with histological staining results. Phosphate:carbonate and mineral:matrix ratios could not be calculated for sections treated with high zinc because no phosphate peak was found due to lack of calcifications. Moderate zinc concentration resulted in lower phosphate:carbonate ratio compared to conditions with no added zinc. This would suggest less carbonate substitution in hydroxyapatite crystals formed from 4T1 spheroids grown in moderate zinc conditions. Also, mineral:matrix ratio was lower in moderate zinc sections, meaning there is more organic components and less mineral components to the crystal. Less phosphate relative to carbonate is caused by an increased degree of carbonate substitution, which has been associated with less degree of invasiveness or severity of cancer.[133,135] Also, a decrease in mineral:matrix ratio suggests less hydroxyapatite and more organic cellular components. According to the data on crystallinity, using FWHM of the phosphate peak at 960cm^{-1}, crystallinity of hydroxyapatite is not affected by growth in moderate zinc concentrations. However, small changes in carbonate content was not shown to affect hydroxyapatite crystallinity. In fact, in artificially synthesized carbonate substituted hydroxyapatites, samples under 6.5% carbonate substitution can be classified as low carbonate/high crystallinity, all with similar properties. Around 6.5% carbonate substitution, there is a transition to high carbonate/low crystallinity. Therefore, small changes in carbonate substitution will not affect crystallinity of hydroxyapatite unless it passes this transition.[174] Overall, differences in mineral:matrix, and phosphate:carbonate ratio suggest growth in moderate zinc is producing less calcifications with higher carbonate substitution, which would suggest a less invasive cancer.

Cox et al. showed formation of breast cancer microcalcifications is an active cell mediated process reliant on ALP and phosphate transport.[170] Since high zinc concentrations were shown to inhibit microcalcification formation in vitro, the effects of zinc on ALP activity in breast cancer cells were examined. Both qualitative ALP staining using the BCIP/NBT staining in **Figure 4.4**, and quantitative measurement of phosphatase activity in cell lysates from the pNPP assay in **Figure 4.4** show increasing zinc concentration decreases phosphatase activity.

Therapeutically, higher serum alkaline phosphatase levels in breast cancer patients has been shown to be associated with increased disease progression and bone metastasis.[175] Therefore, ALP is a potential target to slow or inhibit the growth of breast cancers. Growth of 4T1 cells in high zinc environments has been shown to inhibit phosphatase activity, and inhibit microcalcification formation. Growth in a high zinc environment is affecting phosphatase activity of breast cancer cells, which is most likely contributing to the inhibitory effects of microcalcification formation.

The effect of zinc on MMP formation was examined to see any potential link to MMP activity and breast cancer calcification formation. Since MMP-2 is involved in osteogenesis, and MMP-9 is involved in bone resorption, it is thought that they may play a role in breast cancer microcalcification formation.[176] However, their potential roles in breast cancer calcifications are not well understood. It is known that MMP-2 and MMP-9 are involved in driving metastatic behavior of breast cancers, but not much is known about potential effects on formation of calcifications.[177,178] High exogenous zinc concentrations in culture has been shown to decrease MMP-2 in MC3T3 osteoblasts, therefore was tested for its potential effect on breast cancer cells.[55] Gel zymograms in **Figure 4.17** and **Figure 5.14** show differences between MMP production when cells are grown in 2D vs a 3D spheroid environment with a necrotic core. The most obvious difference is an increased production of MMP-2 and MMP-9 in the spheroid model, which were almost non-detectable when grown in 2D environment. These results further confirm and validate the importance of using a simulated tumor spheroid model for in vitro culture studies. According to the corresponding band densities of MMP-9 and MMP-2 zinc is having the effect of increasing MMP-9 activity, while decreasing MMP-2 activity. This would mean more gelatinases associated with hydroxyapatite resorption, and less gelatinases associated with hydroxyapatite formation. The gel zymography data agrees with the overall theme of zinc inhibiting breast cancer calcification formation, as relatively more MMPs associated with bone resorption are produced in a high zinc environment, and relatively more MMPs associated with bone formation are produced in a low zinc environment.

The 3D MCTS model developed in this study was further investigated for its ability to be used in co-culture systems and applications in VCaP prostate cancer cells. Analysis of co-culture spheroids assembled with 4T1 and HUVEC cells reveals similarities between 4T1:HUVEC 3:1 and 1:1 ratios. Both had larger sizes compared to the 4T1:HUVEC 1:3 ratio.

Necrotic core sizes of co-culture spheroids reveal necrotic core could be more related to actual spheroid size, and not cell-type populations. Co-culture applications, specifically with endothelial cells, have applications in studying angiogenesis in relation towards cancer and tumor development.

5.6 Conclusions

This work demonstrates the use of a novel system for growing 4T1 breast cancer spheroids in vitro for the study of breast cancer microcalcifications. The MCTS model developed in this study is multi-functional, as it has applications towards co-culture systems as well as prostate cancer. Formation of breast cancer calcifications was shown to be partially inhibited by moderate zinc concentrations up to 50 μM Zn, and completely inhibited by high zinc concentrations up to 100 μM Zn. Growth in high zinc concentrations was shown to partially inhibit phosphatase activity, increase MMP-9 activity, and decrease MMP-2 activity, showing that many of the mechanisms involved in osteogenesis may be responsible for formation of microcalcifications in breast cancer. A better understanding on the formation and mechanism of breast cancer microcalcification development may lead to new targeted approaches for slowing cancer progression.

Chapter 6 : Summary and Contributions

Overall, this work has made progress towards understanding the development of mineralized biological tissue as it relates to both the development of healthy bone tissue, compared to the diseased state of osteoporosis and towards microcalcifications which develop in breast cancers. The work involved applications of many techniques to new disciplines not previously examined. Specifically, synchrotron x-ray fluorescence (XRF) was used to study trace elements in osteoporotic rat femurs and an in vitro spheroid model was developed for the study of microcalcifications in breast cancer.

XRF has been widely used across many applications to determine elemental composition, but has rarely been used in mineralized biological tissues. In *Chapter 2,* we examined the composition of Ca, Fe, and Zn in healthy rat femurs compared to osteoporotic rat femurs. Although osteoporosis has been studied extensively, the use of XRF to study the effects of micronutrients in bones affected by osteoporosis has yet to be accomplished until this study. The generation of elemental maps to compare trace metal distribution in trabecular and cortical regions is a technique that had not previously been applied to bone samples. Although time consuming, we demonstrated that XRF can feasibly be used to distinguish and compare relative elemental composition within biological tissues. XRF is shown to be a very sensitive technique, as it can detect trace elemental quantities without destroying the sample. Due to time constraints of beamline availability, we were not able to acquire data from many samples, which left our data on Fe and Zn inconclusive. However, our limited evidence suggests possible different effects of Fe and Zn on osteoporotic bone compared to healthy bone. Knowledge of these differences is an important aspect of basic research, which can develop therapeutic targets in the form of drugs or dietary supplementation. Further evidence is needed to be conclusive, but this study may provide evidence for the roles of Fe and Zn in osteoporosis. XRF as a technique may also be applied to other micronutrients in bone to study their effects on osteoporosis and better our understanding on the differences between healthy and diseased bone.

In the introductory *Chapter 1,* Zn was studied in its interaction with fibronectin, an ECM protein which helps in cell adhesion. This work provided evidence of the interaction of Zn with fibronectin (FN), which could be altering the conformation of the protein. Since Zn was also

shown to decrease migration, there may be a link between conformational state of FN and an attached cell's ability to migrate, which has effects in both bone formation and cancer metastasis.

The study of micronutrient zinc was examined in *Chapter 4* and *Chapter 5* as a potential target towards inhibiting metastatic potential of breast cancers. Microcalcifications have been linked to malignancy of breast cancers, but the process of microcalcification formation has yet to be well understood. Malignant microcalcifications, which are composed of a bone-like mineral, are a pathological indicator of metastatic, aggressive breast cancers. Diagnostically, these calcifications are becoming easier to distinguish, but little is known about their genesis. In this work, we used exogenous zinc to inhibit microcalcification formation and, potentially, metastatic potential in both a 2D and 3D spheroid environment. Zinc is known to have anti-cancer properties and also plays a role in regulating many of the bone-morphogenic proteins which are highly expressed in metastatic breast cancer. An abundance of exogenous Zn was targeted to the cells, which was shown to decrease ALP activity. This work demonstrates zinc, and potentially zinc transporter proteins, and ALP as potential targets for breast microcalcifications. Zinc as an anti-breast calcification target is a stepping stone towards understanding how and why metastatic breast cancers form calcifications. This research has demonstrated that zinc can play a functional role in the inhibition of calcifications, suggesting its anti-cancer properties can slow the pathological progression of metastatic breast cancer.

The development of an in vitro self-assembled three dimensional multicellular tumor spheroid (MCTS) model for the study of breast cancer microcalcifications was highlighted in *Chapter 5*. To our knowledge, there has yet to be an in vitro model developed specifically for studying breast cancer microcalcifications. A three dimensional model presents a more realistic approach as it better mimics the *in vivo* microenvironment. In addition, nutrient and oxygen gradients are needed to represent *in vivo* conditions. Due to its affordability and ethicality, the spheroid model is being used as precursors to *in vivo* testing. The *in vitro* MCTS model for studying breast cancer microcalcifications thus has potential for accelerating drug discovery and enhancing basic research on mechanisms of microcalcification formation, which is still not fully understood. This work successfully engineered a three dimensional MCTS model which was fully characterized to study breast cancer microcalcifications. After 3-4 weeks of growth, this model can reproduce aspects of *in vivo* conditions of breast cancer microcalcifications using a

murine cell model. Clearly, any *in vitro* model would not completely represent *in vivo* conditions, however the MCTS model developed is an improvement upon traditional 2D monolayers. More importantly, the breast cancer calcifications grown in the MCTS model were shown be inhibited by Zn concentrations, similar to the 2D monolayer. This shows that Zn is a potential anti-cancer therapeutic that can inhibit the development of breast cancer calcifications, a pathological indicator of highly metastatic cancer. Such three dimensional spheroid models would greatly aid further *in vitro* studies on breast cancer microcalcifications.

Additionally, the versatility of the self-assembled model was examined in its applications towards prostate cancers. Specifically, the ability of human prostate cancer cells to develop into spheroidal systems was examined across multiple cell lines. Similar to breast cancers, prostate cancers often form calcifications, which are not well understood. In this study, VCaP spheroids were plated at three different densities and fluorescently labeled with live/dead staining. Phase contrast and fluorescence images of VCaP spheroids shown in **Figure 6.1** demonstrate that VCaP cells successfully self-assemble into spheroids using the liquid overlay method. Additionally, spheroids plated at 5,000 cells appear to be close to 500 µm, meaning they would be ideal candidates for studying prostate cancer using a 3D spheroid model. This work demonstrates the applicability of a 3D tumor spheroid model for the study of human prostate cancer cells.

Although breast cancer was the primary focus of this dissertation, the spheroid model system can be applied towards many other cell lines and can be used for *in vitro* applications as a more economical, early stage alternative to *in vivo* testing.

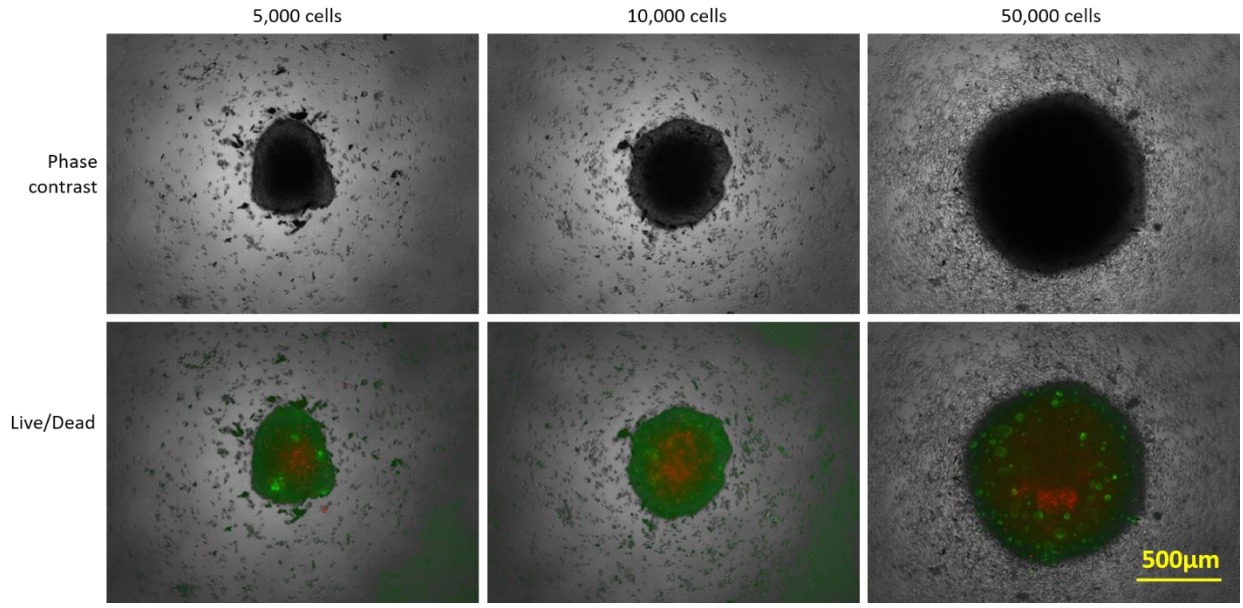

Figure 6.1. Live/dead staining of VCaP spheroids at day 7 after

Chapter 7 : References

1. Beniash, E. Biominerals- hierarchical nanocomposites: the example of bone. *Wiley Interdiscip. Rev. Nanomed. Nanobiotechnol.* **3,** 47–69 (2011).
2. Weiner, S. & Wagner, H. D. THE MATERIAL BONE: Structure-Mechanical Function Relations. *Annu. Rev. Mater. Sci.* **28,** 271–298 (1998).
3. Swartz, J. D. & Loevner, L. A. *Imaging of the Temporal Bone*. (Thieme, 2009).
4. BBML Research: General Introduction to Bone. Available at: http://www.iupui.edu/~bbml/boneintro.shtml. (Accessed: 11th August 2013)
5. bone remodeling. *Encyclopedia Britannica* Available at: http://www.britannica.com/EBchecked/media/138385/Bone-remodeling. (Accessed: 11th August 2013)
6. Raisz, L. G. Physiology and pathophysiology of bone remodeling. *Clin. Chem.* **45,** 1353–1358 (1999).
7. Hadjidakis, D. J. & Androulakis, I. I. Bone remodeling. *Ann. N. Y. Acad. Sci.* **1092,** 385–396 (2006).
8. Schor, S. L., Ellis, I., Banyard, J. & Schor, A. M. Motogenic activity of IGD-containing synthetic peptides. *J. Cell Sci.* **112 (Pt 22),** 3879–3888 (1999).
9. Graille, M., Pagano, M., Rose, T., Ravaux, M. R. & Tilbeurgh, H. van. Zinc Induces Structural Reorganization of Gelatin Binding Domain from Human Fibronectin and Affects Collagen Binding. *Structure* **18,** 710–718 (2010).
10. Askari, J. A., Thornton, D. J., Humphries, J. D., Buckley, P. A. & Humphries, M. J. The alternatively spliced type III connecting segment of fibronectin is a zinc-binding module. *Matrix Biol. J. Int. Soc. Matrix Biol.* **26,** 485–493 (2007).
11. Bassil, J. *et al.* Expression of MMP-2, 9 and 13 in newly formed bone after sinus augmentation using inorganic bovine bone in human. *J. Periodontal Res.* **46,** 756–762 (2011).
12. Liu, L., He, F., Li, L. & Hu, J. [The expression of MMP-9, MMP-2 in the remodeling bone tissue around implant during unloaded period]. *Hua Xi Kou Qiang Yi Xue Za Zhi Huaxi Kouqiang Yixue Zazhi West China J. Stomatol.* **22,** 325–327 (2004).

13. Das, S., Banerji, A., Frei, E. & Chatterjee, A. Rapid expression and activation of MMP-2 and MMP-9 upon exposure of human breast cancer cells (MCF-7) to fibronectin in serum free medium. *Life Sci.* **82,** 467–476 (2008).
14. Chow, A. K., Cena, J. & Schulz, R. Acute actions and novel targets of matrix metalloproteinases in the heart and vasculature. *Br. J. Pharmacol.* **152,** 189–205 (2007).
15. Nagase, H. & Woessner, J. F. J. Matrix metalloproteinases. *J. Biol. Chem.* **274,** 21491–21494 (1999).
16. Díaz, N. & Suarez, D. Molecular dynamics simulations of matrix metalloproteinase 2: role of the structural metal ions. *Biochemistry (Mosc.)* **46,** 8943–8952 (2007).
17. Houard, X. *et al.* Migration-stimulating factor displays HEXXH-dependent catalytic activity important for promoting tumor cell migration. *Int. J. Cancer J. Int. Cancer* **116,** 378–384 (2005).
18. Humphries, M. J., Akiyama, S. K., Komoriya, A., Olden, K. & Yamada, K. M. Neurite extension of chicken peripheral nervous system neurons on fibronectin: relative importance of specific adhesion sites in the central cell-binding domain and the alternatively spliced type III connecting segment. *J. Cell Biol.* **106,** 1289–1297 (1988).
19. McDonald, J. A., Kelley, D. G. & Broekelmann, T. J. Role of fibronectin in collagen deposition: Fab' to the gelatin-binding domain of fibronectin inhibits both fibronectin and collagen organization in fibroblast extracellular matrix. *J. Cell Biol.* **92,** 485–492 (1982).
20. Schor, S. L. *et al.* Migration-stimulating factor: a genetically truncated onco-fetal fibronectin isoform expressed by carcinoma and tumor-associated stromal cells. *Cancer Res.* **63,** 8827–8836 (2003).
21. Kozlowski, H. *et al.* Copper, iron, and zinc ions homeostasis and their role in neurodegenerative disorders (metal uptake, transport, distribution and regulation). *Coord. Chem. Rev.* **253,** 2665–2685 (2009).
22. *Metallothioneins and Related Chelators*.
23. Alexandrova, A., Bandžuchová, E., Kebis, A., Kukan, M. & Kuba, D. Copper decreases gene expression of TNF-α, IL-10, and of matrix metalloproteinases MMP-2 and MMP-9 in isolated perfused rat livers. *Biologia (Bratisl.)* **62,** 365–369 (2007).
24. Lönnerdal, B. Intestinal regulation of copper homeostasis: a developmental perspective. *Am. J. Clin. Nutr.* **88,** 846S–850S (2008).

25. Goodman, V. L., Brewer, G. J. & Merajver, S. D. Copper deficiency as an anti-cancer strategy. *Endocr. Relat. Cancer* **11,** 255–263 (2004).
26. Kaplan, J. H. & Lutsenko, S. Copper transport in mammalian cells: special care for a metal with special needs. *J. Biol. Chem.* **284,** 25461–25465 (2009).
27. Fogelgren, B. *et al.* Cellular Fibronectin Binds to Lysyl Oxidase with High Affinity and Is Critical for Its Proteolytic Activation. *J. Biol. Chem.* **280,** 24690–24697 (2005).
28. Wilgus, M.-L. *et al.* Lysyl oxidase: a lung adenocarcinoma biomarker of invasion and survival. *Cancer* **117,** 2186–2191 (2011).
29. Reeves, P. G., Briske-Anderson, M. & Newman, S. M. High Zinc Concentrations in Culture Media Affect Copper Uptake and Transport in Differentiated Human Colon Adenocarcinoma Cells. *J. Nutr.* **126,** 1701–1712 (1996).
30. Gupta, S. K., Shukla, V. K., Vaidya, M. P., Roy, S. K. & Gupta, S. Serum trace elements and Cu/Zn ratio in breast cancer patients. *J. Surg. Oncol.* **46,** 178–181 (1991).
31. Lowndes, S. A. & Harris, A. L. The role of copper in tumour angiogenesis. *J. Mammary Gland Biol. Neoplasia* **10,** 299–310 (2005).
32. Rink, L. & Gabriel, P. Zinc and the immune system. *Proc. Nutr. Soc.* **59,** 541–552 (2000).
33. Hambidge, M. Human Zinc Deficiency. *J. Nutr.* **130,** 1344S–1349S (2000).
34. Hadley, K. B., Newman, S. M. & Hunt, J. R. Dietary zinc reduces osteoclast resorption activities and increases markers of osteoblast differentiation, matrix maturation, and mineralization in the long bones of growing rats. *J. Nutr. Biochem.* **21,** 297–303 (2010).
35. Kwun, I.-S. *et al.* Zinc deficiency suppresses matrix mineralization and retards osteogenesis transiently with catch-up possibly through Runx 2 modulation. *Bone* **46,** 732–741 (2010).
36. Roth, H. P. & Kirchgessner, M. Influence of zinc and calcium deficiency on the concentrations of calcitonin, parathyroid hormone, and 25-hydroxy-vitamin D3 in rat serum. *J. Trace Elem. Electrolytes Health Dis.* **3,** 225–230 (1989).
37. Scrimgeour, A. G., Stahl, C. H., McClung, J. P., Marchitelli, L. J. & Young, A. J. Moderate zinc deficiency negatively affects biomechanical properties of rat tibiae independently of body composition. *J. Nutr. Biochem.* **18,** 813–819 (2007).
38. Osorio, R. *et al.* Zinc reduces collagen degradation in demineralized human dentin explants. *J. Dent.* **39,** 148–153 (2011).

39. Franceschi, R. T., Ge, C., Xiao, G., Roca, H. & Jiang, D. Transcriptional regulation of osteoblasts. *Ann. N. Y. Acad. Sci.* **1116,** 196–207 (2007).
40. Humphries, M. J., Komoriya, A., Akiyama, S. K., Olden, K. & Yamada, K. M. Identification of two distinct regions of the type III connecting segment of human plasma fibronectin that promote cell type-specific adhesion. *J. Biol. Chem.* **262,** 6886–6892 (1987).
41. Arnold, F. H. & Haymore, B. L. Engineered metal-binding proteins: purification to protein folding. *Science* **252,** 1796–1797 (1991).
42. Thomas, D. M. *et al.* Terminal osteoblast differentiation, mediated by runx2 and p27KIP1, is disrupted in osteosarcoma. *J. Cell Biol.* **167,** 925–934 (2004).
43. Pino, A. M., Rosen, C. J. & Rodríguez, J. P. In osteoporosis, differentiation of mesenchymal stem cells (MSCs) improves bone marrow adipogenesis. *Biol. Res.* **45,** 279–287 (2012).
44. Jones, S. J. *et al.* Co-expression by keratinocytes of migration stimulating factor (MSF) and a functional inhibitor of its bioactivity (MSFI). *Exp. Cell Res.* **313,** 4145–4157 (2007).
45. Huang, S.-T., Yang, R.-C., Wu, H.-T., Wang, C.-N. & Pang, J.-H. S. Zinc-chelation contributes to the anti-angiogenic effect of ellagic acid on inhibiting MMP-2 activity, cell migration and tube formation. *PloS One* **6,** e18986 (2011).
46. Liu, Y., El-Naggar, S., Darling, D. S., Higashi, Y. & Dean, D. C. ZEB1 Links Epithelial-Mesenchymal Transition and Cellular Senescence. *Dev. Camb. Engl.* **135,** 579–588 (2008).
47. Boskey, A. L. & Coleman, R. Aging and bone. *J. Dent. Res.* **89,** 1333–1348 (2010).
48. Schor, S. L., Ellis, I. R., Jones, S. J., Woolston, A.-M. & Schor, A. M. Bistable switch in migration stimulating factor expression: regulation by the concerted signalling of transforming growth factor-β1 and the extracellular matrix. *Int. J. Cancer J. Int. Cancer* **130,** 2024–2032 (2012).
49. Alcantara, E. H. *et al.* Zinc deprivation inhibits extracellular matrix calcification through decreased synthesis of matrix proteins in osteoblasts. *Mol. Nutr. Food Res.* **55,** 1552–1560 (2011).
50. Chu, B. *Laser Light Scattering: Basic Principles and Practice*. (Acad. Press, 1991).
51. Koningsberger, D. C. & Prins, R. *X-ray absorption: principles, applications, techniques of EXAFS, SEXAFS, and XANES*. (John Wiley & Sons, 1988).
52. Jones, K. W., Gordon, B. M., Hanson, A. L., Kwiatek, W. M. & Pounds, J. G. X-ray fluorescence with synchrotron radiation. *Ultramicroscopy* **24,** 313–328 (1988).

53. Yan, D. Effects of Zinc and Iron on Bone Health in a Rat Model of Osteoporosis. (Stony Brook University, 2014).
54. Dorst, K., Rammelkamp, D., Hadjiargyrou, M., Gersappe, D. & Meng, Y. The Effect of Exogenous Zinc Concentration on the Responsiveness of MC3T3-E1 Pre-Osteoblasts to Surface Microtopography: Part I (Migration). *Materials* **6,** 5517–5532 (2013).
55. Dorst, K., Rammelkamp, D., Hadjiargyrou, M. & Meng, Y. The Effect of Exogenous Zinc Concentration on the Responsiveness of MC3T3-E1 Pre-Osteoblasts to Surface Microtopography: Part II (Differentiation). *Materials* **7,** 1097–1112 (2014).
56. Kashima, T. *et al.* Overexpression of cadherins suppresses pulmonary metastasis of osteosarcoma in vivo. *Int. J. Cancer J. Int. Cancer* **104,** 147–154 (2003).
57. Daw, N. C. *et al.* Metastatic osteosarcoma. *Cancer* **106,** 403–412 (2006).
58. Briknarová, K., Akerman, M. E., Hoyt, D. W., Ruoslahti, E. & Ely, K. R. Anastellin, an FN3 fragment with fibronectin polymerization activity, resembles amyloid fibril precursors. *J. Mol. Biol.* **332,** 205–215 (2003).
59. Gee, E. P. S., Yuksel, D., Stultz, C. M. & Ingber, D. E. SLLISWD Sequence in the 10FNIII Domain Initiates Fibronectin Fibrillogenesis. *J. Biol. Chem.* **288,** 21329–21340 (2013).
60. EDA-containing cellular fibronectin induces fibroblast differentiation through binding to alpha4beta7 integrin receptor and MAPK/Erk 1/2-dependent ... - PubMed - NCBI. Available at: https://www.ncbi.nlm.nih.gov/pubmed/20643910. (Accessed: 19th December 2016)
61. Manabe, R., Oh-e, N. & Sekiguchi, K. Alternatively Spliced EDA Segment Regulates Fibronectin-dependent Cell Cycle Progression and Mitogenic Signal Transduction. *J. Biol. Chem.* **274,** 5919–5924 (1999).
62. Qadeer, A. *et al.* 1-Anilino-8-Naphthalene Sulfonate (ANS) Is Not a Desirable Probe for Determining the Molten Globule State of Chymopapain. *PLoS ONE* **7,** e50633 (2012).
63. Graille, M., Pagano, M., Rose, T., Ravaux, M. R. & van Tilbeurgh, H. Zinc induces structural reorganization of gelatin binding domain from human fibronectin and affects collagen binding. *Struct. Lond. Engl. 1993* **18,** 710–718 (2010).
64. Singh, P., Carraher, C. & Schwarzbauer, J. E. Assembly of Fibronectin Extracellular Matrix. *Annu. Rev. Cell Dev. Biol.* **26,** 397–419 (2010).
65. Guyton, A. C. *Textbook of Medical Physiology*. **2,** (The American Journal of Medical Sciences, 1961).

66. Weiner, S. & Wagner, and H. D. THE MATERIAL BONE: Structure-Mechanical Function Relations. *Annu. Rev. Mater. Sci.* **28,** 271–298 (1998).
67. Hadjidakis, D. J. & Androulakis, I. I. Bone Remodeling. *Ann. N. Y. Acad. Sci.* **1092,** 385–396 (2006).
68. Raisz, L. G. Physiology and Pathophysiology of Bone Remodeling. *Clin. Chem.* **45,** 1353–1358 (1999).
69. Dawson-Hughes, B. *et al.* A Controlled Trial of the Effect of Calcium Supplementation on Bone Density in Postmenopausal Women. *N. Engl. J. Med.* **323,** 878–883 (1990).
70. Lowe, N. M., Lowe, N. M., Fraser, W. D. & Jackson, M. J. Is there a potential therapeutic value of copper and zinc for osteoporosis? *Proc. Nutr. Soc.* **61,** 181–185 (2002).
71. Jee, W. S. & Yao, W. Overview: animal models of osteopenia and osteoporosis. *J. Musculoskelet. Neuronal Interact.* **1,** 193–207 (2001).
72. Thompson, D. D., Simmons, H. A., Pirie, C. M. & Ke, H. Z. FDA Guidelines and animal models for osteoporosis. *Bone* **17,** 125S–133S (1995).
73. Wronski, T. J., Cintrón, M. & Dann, L. M. Temporal relationship between bone loss and increased bone turnover in ovariectomized rats. *Calcif. Tissue Int.* **43,** 179–183 (1988).
74. Wronski, T. J., Dann, L. M., Scott, K. S. & Cintrón, M. Long-term effects of ovariectomy and aging on the rat skeleton. *Calcif. Tissue Int.* **45,** 360–366 (1989).
75. Olmedo, P. *et al.* Validation of a method to quantify chromium, cadmium, manganese, nickel and lead in human whole blood, urine, saliva and hair samples by electrothermal atomic absorption spectrometry. *Anal. Chim. Acta* **659,** 60–67 (2010).
76. Kubaszewski, Ł. *et al.* Comparison of trace element concentration in bone and intervertebral disc tissue by atomic absorption spectrometry techniques. *J. Orthop. Surg.* **9,** 99 (2014).
77. Todd, A. C. & Chettle, D. R. In vivo X-ray fluorescence of lead in bone: review and current issues. *Environ. Health Perspect.* **102,** 172–177 (1994).
78. Cabrera, W. E., Schrooten, I., De Broe, M. E. & D'Haese, P. C. Strontium and Bone. *J. Bone Miner. Res.* **14,** 661–668 (1999).
79. Drzazga, Z., Michalik, K., Maciejewska, K., Trzeciak, H. & Kaszuba, M. Role of endogenous zinc in bones of newborn rats. *BioFactors Oxf. Engl.* **30,** 243–248 (2007).

80. Maciejewska, K., Drzazga, Z. & Kaszuba, M. Role of trace elements (Zn, Sr, Fe) in bone development: energy dispersive X-ray fluorescence study of rat bone and tooth tissue. *BioFactors Oxf. Engl.* **40,** 425–435 (2014).
81. Tommasini, S. M. *et al.* Changes in intracortical microporosities induced by pharmaceutical treatment of osteoporosis as detected by high resolution micro-CT. *Bone* **50,** 596–604 (2012).
82. Kanis, J. A., Melton, L. J., Christiansen, C., Johnston, C. C. & Khaltaev, N. The diagnosis of osteoporosis. *J. Bone Miner. Res.* **9,** 1137–1141 (1994).
83. Noor, Z. *et al.* Atomic mineral characteristics of Indonesian osteoporosis by high-resolution inductively coupled plasma mass spectrometry. *ScientificWorldJournal* **2012,** 372972 (2012).
84. Reginster, J.-Y., Strause, L. G., Saltman, P. & Franchimont, P. Trace elements and postmenopausal osteoporosis: a preliminary report of decreased serum manganese. *Med. Sci. Res.* **16,** (1988).
85. Baron, R., Vignery & Horowitz. in *Bone and Mineral Research* 175–243 (Elsevier Science Publishing Co., 1984).
86. Canalis, E., McCarthy, T. & Centrella, M. Growth factors and the regulation of bone remodeling. *J. Clin. Invest.* **81,** 277–281 (1988).
87. Mohan, S. & Baylink, D. J. Autocrine and paracrine aspects of bone metabolism. *Growth Genet. Horm.* **6,** 1–6 (1990).
88. Kishi, S. & Yamaguchi, M. Inhibitory effect of zinc compounds on osteoclast-like cell formation in mouse marrow cultures. *Biochem. Pharmacol.* **48,** 1225–1230 (1994).
89. Guggenbuhl, P. *et al.* Bone status in a mouse model of genetic hemochromatosis. *Osteoporos. Int. J. Establ. Result Coop. Eur. Found. Osteoporos. Natl. Osteoporos. Found. USA* **22,** 2313–2319 (2011).
90. Vogiatzi, M. G. *et al.* Bone disease in thalassemia: a frequent and still unresolved problem. *J. Bone Miner. Res. Off. J. Am. Soc. Bone Miner. Res.* **24,** 543–557 (2009).
91. He, Y.-F. *et al.* Iron overload inhibits osteoblast biological activity through oxidative stress. *Biol. Trace Elem. Res.* **152,** 292–296 (2013).
92. Underwood, E. J. *Trace Elements in Human and Animal Nutrition*. (Academic Press).

93. Hamilton, E. I., Minski, M. J. & Cleary, J. J. The concentration and distribution of some stable elements in healthy human tissues from the United Kingdom An environmental study. *Sci. Total Environ.* **1,** 341–374 (1973).
94. Trace elements in human nutrition. Report of a WHO expert committee. *World Health Organ. Tech. Rep. Ser.* **532,** 1–65 (1973).
95. Lappalainen, R., Knuuttila, M., Lammi, S. & Alhava, E. M. Fluoride content related to the elemental composition, mineral density and strength of bone in healthy and chronically diseased persons. *J. Chronic Dis.* **36,** 707–713 (1983).
96. Li, X. *et al.* The optimum zinc content in set calcium phosphate cement for promoting bone formation in vivo. *Mater. Sci. Eng. C Mater. Biol. Appl.* **29,** 969–975 (2009).
97. Yamaguchi, M. Role of zinc in bone formation and bone resorption. *J. Trace Elem. Exp. Med.* **11,** 119–135 (1998).
98. Giugliano, R. & Millward, D. J. Growth and zinc homeostasis in the severely Zn-deficient rat. *Br. J. Nutr.* **52,** 545–560 (1984).
99. Hurley, L. S. Teratogenic aspects of manganese, zinc, and copper nutrition. *Physiol. Rev.* **61,** 249–295 (1981).
100. Eberle, J., Schmidmayer, S., Erben, R. G., Stangassinger, M. & Roth, H. P. Skeletal effects of zinc deficiency in growing rats. *J. Trace Elem. Med. Biol. Organ Soc. Miner. Trace Elem. GMS* **13,** 21–26 (1999).
101. Lowe, N. M., Bremner, I. & Jackson, M. J. Plasma 65Zn kinetics in the rat. *Br. J. Nutr.* **65,** 445–455 (1991).
102. Saltman, P. & Strause, L. Trace elements in bone metabolism. *J. Inorg. Biochem.* **43,** 284 (1991).
103. Shils, M. E. & Shike, M. *Modern Nutrition in Health and Disease*. (1999).
104. Ganz, T. Iron in innate immunity: starve the invaders. *Curr. Opin. Immunol.* **21,** 63–67 (2009).
105. Li, G. F., Pan, Y. Z., Sirois, P., Li, K. & Xu, Y. J. Iron homeostasis in osteoporosis and its clinical implications. *Osteoporos. Int. J. Establ. Result Coop. Eur. Found. Osteoporos. Natl. Osteoporos. Found. USA* **23,** 2403–2408 (2012).
106. Crisponi, G. *et al.* Different approaches to the study of chelating agents for iron and aluminium overload pathologies. *Anal. Bioanal. Chem.* **405,** 585–601 (2013).

107. McCord, J. M. Effects of positive iron status at a cellular level. *Nutr. Rev.* **54,** 85–88 (1996).

108. Andrews, N. C. Disorders of Iron Metabolism. *N. Engl. J. Med.* **341,** 1986–1995 (1999).

109. Guggenbuhl, P., Brissot, P. & Loréal, O. Haemochromatosis: The bone and the joint. *Best Pract. Res. Clin. Rheumatol.* **25,** 649–664 (2011).

110. Matsushima, S., Hoshimoto, M., Torii, M., Ozaki, K. & Narama, I. Iron lactate-induced osteopenia in male Sprague-Dawley rats. *Toxicol. Pathol.* **29,** 623–629 (2001).

111. Guggenbuhl, P. *et al.* Bone mineral density in men with genetic hemochromatosis and HFE gene mutation. *Osteoporos. Int. J. Establ. Result Coop. Eur. Found. Osteoporos. Natl. Osteoporos. Found. USA* **16,** 1809–1814 (2005).

112. Mahachoklertwattana, P. *et al.* Bone histomorphometry in children and adolescents with beta-thalassemia disease: iron-associated focal osteomalacia. *J. Clin. Endocrinol. Metab.* **88,** 3966–3972 (2003).

113. Isomura, H. *et al.* Bone metabolism and oxidative stress in postmenopausal rats with iron overload. *Toxicology* **197,** 93–100 (2004).

114. Tsay, J. *et al.* Bone loss caused by iron overload in a murine model: importance of oxidative stress. *Blood* **116,** 2582–2589 (2010).

115. Kim, B.-J., Lee, S. H., Koh, J.-M. & Kim, G. S. The association between higher serum ferritin level and lower bone mineral density is prominent in women ≥45 years of age (KNHANES 2008-2010). *Osteoporos. Int. J. Establ. Result Coop. Eur. Found. Osteoporos. Natl. Osteoporos. Found. USA* **24,** 2627–2637 (2013).

116. Kudo, H. *et al.* Effects of colloidal iron overload on renal and hepatic siderosis and the femur in male rats. *Toxicology* **246,** 143–147 (2008).

117. Zarjou, A. *et al.* Ferritin ferroxidase activity: a potent inhibitor of osteogenesis. *J. Bone Miner. Res. Off. J. Am. Soc. Bone Miner. Res.* **25,** 164–172 (2010).

118. Medeiros, D. M., Stoecker, B., Plattner, A., Jennings, D. & Haub, M. Iron deficiency negatively affects vertebrae and femurs of rats independently of energy intake and body weight. *J. Nutr.* **134,** 3061–3067 (2004).

119. Medeiros, D. M., Plattner, A., Jennings, D. & Stoecker, B. Bone morphology, strength and density are compromised in iron-deficient rats and exacerbated by calcium restriction. *J. Nutr.* **132,** 3135–3141 (2002).

120. Medeiros, D. M. *et al.* Femurs from rats fed diets deficient in copper or iron have decreased mechanical strength and altered mineral composition. *J. Trace Elem. Exp. Med.* **10,** 197–203 (1997).

121. Tuderman, L., Myllylä, R. & Kivirikko, K. I. Mechanism of the Prolyl Hydroxylase Reaction. *Eur. J. Biochem.* **80,** 341–348 (1977).

122. Parelman, M., Stoecker, B., Baker, A. & Medeiros, D. Iron restriction negatively affects bone in female rats and mineralization of hFOB osteoblast cells. *Exp. Biol. Med. Maywood NJ* **231,** 378–386 (2006).

123. Shen, Y., Zhang, Z.-M., Jiang, S.-D., Jiang, L.-S. & Dai, L.-Y. Postmenopausal women with osteoarthritis and osteoporosis show different ultrastructural characteristics of trabecular bone of the femoral head. *BMC Musculoskelet. Disord.* **10,** 35 (2009).

124. Aitken, J. M. Factors affecting the distribution of zinc in the human skeleton. *Calcif. Tissue Res.* **20,** 23–30 (1976).

125. Song, Y., Leonard, S. W., Traber, M. G. & Ho, E. Zinc deficiency affects DNA damage, oxidative stress, antioxidant defenses, and DNA repair in rats. *J. Nutr.* **139,** 1626–1631 (2009).

126. Galaris, D. & Pantopoulos, K. Oxidative stress and iron homeostasis: mechanistic and health aspects. *Crit. Rev. Clin. Lab. Sci.* **45,** 1–23 (2008).

127. Cervellati, C. *et al.* Oxidative stress and bone resorption interplay as a possible trigger for postmenopausal osteoporosis. *BioMed Res. Int.* **2014,** 569563 (2014).

128. Jemal, A. *et al.* Global cancer statistics. *CA. Cancer J. Clin.* **61,** 69–90 (2011).

129. Kohler, B. A. *et al.* Annual Report to the Nation on the Status of Cancer, 1975-2011, Featuring Incidence of Breast Cancer Subtypes by Race/Ethnicity, Poverty, and State. *J. Natl. Cancer Inst.* **107,** djv048 (2015).

130. Gülsün, M., Demirkazik, F. B. & Ariyürek, M. Evaluation of breast microcalcifications according to Breast Imaging Reporting and Data System criteria and Le Gal's classification. *Eur. J. Radiol.* **47,** 227–231 (2003).

131. Bennett, R. L., Blanks, R. G., Patnick, J. & Moss, S. M. Results from the UK NHS Breast Screening Programme 2000-05. *J. Med. Screen.* **14,** 200–204 (2007).

132. Illie, C. Case 420 Breast Calcifications - Part 1 of 2. (2002).

133. Baker, R., Rogers, K. D., Shepherd, N. & Stone, N. New relationships between breast microcalcifications and cancer. *Br. J. Cancer* **103,** 1034–1039 (2010).

134. Kerssens, M. M., Matousek, P., Rogers, K. & Stone, N. Towards a safe non-invasive method for evaluating the carbonate substitution levels of hydroxyapatite (HAP) in micro-calcifications found in breast tissue. *The Analyst* **135,** 3156–3161 (2010).

135. Rogers, K., Baker, R. & Stone, N. Breast calcification: the 'Cinderella' breast element? *Breast Cancer Res.* **12,** 1–2 (2010).

136. Porter, A. *et al.* Effect of carbonate substitution on the ultrastructural characteristics of hydroxyapatite implants. *J. Mater. Sci. Mater. Med.* **16,** 899–907 (2005).

137. Reuben, P. M., Brogley, M. A., Sun, Y. & Cheung, H. S. Molecular mechanism of the induction of metalloproteinases 1 and 3 in human fibroblasts by basic calcium phosphate crystals. Role of calcium-dependent protein kinase C alpha. *J. Biol. Chem.* **277,** 15190–15198 (2002).

138. Choi, S., Coonrod, S., Estroff, L. & Fischbach, C. Chemical and physical properties of carbonated hydroxyapatite affect breast cancer cell behavior. *Acta Biomater.* **24,** 333–342 (2015).

139. Waugh, D. J. J. & Wilson, C. The interleukin-8 pathway in cancer. *Clin. Cancer Res. Off. J. Am. Assoc. Cancer Res.* **14,** 6735–6741 (2008).

140. Giachelli, C. M. Vascular calcification mechanisms. *J. Am. Soc. Nephrol. JASN* **15,** 2959–2964 (2004).

141. Kirsch, T. Determinants of pathological mineralization. *Curr. Opin. Rheumatol.* **18,** 174–180 (2006).

142. Shroff, R. C. & Shanahan, C. M. The vascular biology of calcification. *Semin. Dial.* **20,** 103–109 (2007).

143. Bellahcène, A. & Castronovo, V. Increased expression of osteonectin and osteopontin, two bone matrix proteins, in human breast cancer. *Am. J. Pathol.* **146,** 95–100 (1995).

144. Bellahcène, A., Merville, M. P. & Castronovo, V. Expression of bone sialoprotein, a bone matrix protein, in human breast cancer. *Cancer Res.* **54,** 2823–2826 (1994).

145. Seiler, H. G., Sigel, H. & Sigel, A. Handbook on toxicity of inorganic compounds. (1988).

146. Vallee, B. L. & Falchuk, K. H. The biochemical basis of zinc physiology. *Physiol. Rev.* **73,** 79–118 (1993).

147. Vallee, B. L. & Auld, D. S. Zinc coordination, function, and structure of zinc enzymes and other proteins. *Biochemistry (Mosc.)* **29,** 5647–5659 (1990).

148. Vallee, B. L. & Auld, D. S. Short and long spacer sequences and other structural features of zinc binding sites in zinc enzymes. *FEBS Lett.* **257,** 138–140 (1989).

149. Vallee, B. L. & Auld, D. S. Active-site zinc ligands and activated H2O of zinc enzymes. *Proc. Natl. Acad. Sci. U. S. A.* **87,** 220–224 (1990).

150. Kaczmarek, K. *et al.* Zinc and breast cancer risk. *Hered. Cancer Clin. Pract.* **10,** A6 (2012).

151. BRCA1 & BRCA2: Cancer Risk & Genetic Testing. *National Cancer Institute* Available at: https://www.cancer.gov/about-cancer/causes-prevention/genetics/brca-fact-sheet. (Accessed: 20th October 2016)

152. Cui, Y., Vogt, S., Olson, N., Glass, A. G. & Rohan, T. E. Levels of Zinc, Selenium, Calcium, and Iron in Benign Breast Tissue and Risk of Subsequent Breast Cancer. *Cancer Epidemiol. Prev. Biomark.* **16,** 1682–1685 (2007).

153. Grattan, B. J. & Freake, H. C. Zinc and cancer: implications for LIV-1 in breast cancer. *Nutrients* **4,** 648–675 (2012).

154. Chasapis, C. T., Loutsidou, A. C., Spiliopoulou, C. A. & Stefanidou, M. E. Zinc and human health: an update. *Arch. Toxicol.* **86,** 521–534 (2012).

155. Liuzzi, J. P. & Cousins, R. J. Mammalian zinc transporters. *Annu. Rev. Nutr.* **24,** 151–172 (2004).

156. Lee, R. *et al.* Zinc accumulation in N-methyl-N-nitrosourea-induced rat mammary tumors is accompanied by an altered expression of ZnT-1 and metallothionein. *Exp. Biol. Med. Maywood NJ* **228,** 689–696 (2003).

157. Taylor, K. M., Morgan, H. E., Johnson, A., Hadley, L. J. & Nicholson, R. I. Structure-function analysis of LIV-1, the breast cancer-associated protein that belongs to a new subfamily of zinc transporters. *Biochem. J.* **375,** 51–59 (2003).

158. Kagara, N., Tanaka, N., Noguchi, S. & Hirano, T. Zinc and its transporter ZIP10 are involved in invasive behavior of breast cancer cells. *Cancer Sci.* **98,** 692–697 (2007).

159. Taylor, K. M. *et al.* ZIP7-mediated intracellular zinc transport contributes to aberrant growth factor signaling in antihormone-resistant breast cancer Cells. *Endocrinology* **149,** 4912–4920 (2008).

160. Worldwide data | World Cancer Research Fund International. Available at: http://www.wcrf.org/int/cancer-facts-figures/worldwide-data. (Accessed: 10th January 2017)

161. Gurusamy, K. & Davidson, B. R. Trace element concentration in metastatic liver disease: a systematic review. *J. Trace Elem. Med. Biol. Organ Soc. Miner. Trace Elem. GMS* **21,** 169–177 (2007).

162. Gupta, S. K., Singh, S. P. & Shukla, V. K. Copper, zinc, and Cu/Zn ratio in carcinoma of the gallbladder. *J. Surg. Oncol.* **91,** 204–208 (2005).

163. Zaichick VYe, null, Sviridova, T. V. & Zaichick, S. V. Zinc in the human prostate gland: normal, hyperplastic and cancerous. *Int. Urol. Nephrol.* **29,** 565–574 (1997).

164. Henshall, S. M. *et al.* Expression of the zinc transporter ZnT4 is decreased in the progression from early prostate disease to invasive prostate cancer. *Oncogene* **22,** 6005–6012 (2003).

165. Díez, M. *et al.* Serum and tissue trace metal levels in lung cancer. *Oncology* **46,** 230–234 (1989).

166. Cunzhi, H. *et al.* Serum and tissue levels of six trace elements and copper/zinc ratio in patients with cervical cancer and uterine myoma. *Biol. Trace Elem. Res.* **94,** 113–122 (2003).

167. Tabár, L. *et al.* A Proposal to Unify the Classification of Breast and Prostate Cancers Based on the Anatomic Site of Cancer Origin and on Long-term Patient Outcome. *Breast Cancer Basic Clin. Res.* **8,** 15–38 (2014).

168. Yamaguchi, M. Role of nutritional zinc in the prevention of osteoporosis. *Mol. Cell. Biochem.* **338,** 241–254 (2010).

169. Seo, H.-J., Cho, Y.-E., Kim, T., Shin, H.-I. & Kwun, I.-S. Zinc may increase bone formation through stimulating cell proliferation, alkaline phosphatase activity and collagen synthesis in osteoblastic MC3T3-E1 cells. *Nutr. Res. Pract.* **4,** 356–361 (2010).

170. Cox, R. F. *et al.* Microcalcifications in breast cancer: novel insights into the molecular mechanism and functional consequence of mammary mineralisation. *Br. J. Cancer* **106,** 525–537 (2012).

171. Mandair, G. S. & Morris, M. D. Contributions of Raman spectroscopy to the understanding of bone strength. *BoneKEy Rep.* **4,** 620 (2015).

172. Awonusi, A., Morris, M. D. & Tecklenburg, M. M. J. Carbonate assignment and calibration in the Raman spectrum of apatite. *Calcif. Tissue Int.* **81,** 46–52 (2007).

173. Penel, G., Leroy, G., Rey, C. & Bres, E. MicroRaman spectral study of the PO4 and CO3 vibrational modes in synthetic and biological apatites. *Calcif. Tissue Int.* **63,** 475–481 (1998).

174. McElderry, J.-D. P. *et al.* Crystallinity and compositional changes in carbonated apatites: Evidence from 31P solid-state NMR, Raman, and AFM analysis. *J. Solid State Chem.* **206,** (2013).

175. Singh, A. K. *et al.* Advanced stage of breast cancer hoist alkaline phosphatase activity: risk factor for females in India. *3 Biotech* **3,** 517–520 (2013).

176. Ortega, N., Behonick, D. J. & Werb, Z. Matrix remodeling during endochondral ossification. *Trends Cell Biol.* **14,** 86–93 (2004).

177. Mehner, C. *et al.* Tumor cell-produced matrix metalloproteinase 9 (MMP-9) drives malignant progression and metastasis of basal-like triple negative breast cancer. *Oncotarget* **5,** 2736–2749 (2014).

178. Jezierska, A. & Motyl, T. Matrix metalloproteinase-2 involvement in breast cancer progression: a mini-review. *Med. Sci. Monit. Int. Med. J. Exp. Clin. Res.* **15,** RA32-40 (2009).

179. Weiswald, L.-B., Bellet, D. & Dangles-Marie, V. Spherical Cancer Models in Tumor Biology. *Neoplasia N. Y. N* **17,** 1–15 (2015).

180. Durand, R. E. & Raleigh, J. A. Identification of nonproliferating but viable hypoxic tumor cells in vivo. *Cancer Res.* **58,** 3547–3550 (1998).

181. Pampaloni, F., Reynaud, E. G. & Stelzer, E. H. K. The third dimension bridges the gap between cell culture and live tissue. *Nat. Rev. Mol. Cell Biol.* **8,** 839–845 (2007).

182. Baker, B. M. & Chen, C. S. Deconstructing the third dimension: how 3D culture microenvironments alter cellular cues. *J. Cell Sci.* **125,** 3015–3024 (2012).

183. Friedrich, J., Ebner, R. & Kunz-Schughart, L. A. Experimental anti-tumor therapy in 3-D: spheroids--old hat or new challenge? *Int. J. Radiat. Biol.* **83,** 849–871 (2007).

184. Kunz-Schughart, L. A. & Freyer, J. P. Adaptation of an automated selective dissociation procedure to two novel spheroid types. *In Vitro Cell. Dev. Biol. Anim.* **33,** 73–76 (1997).

185. Mueller-Klieser, W. Three-dimensional cell cultures: from molecular mechanisms to clinical applications. *Am. J. Physiol.* **273,** C1109-1123 (1997).

186. Mueller-Klieser, W. Multicellular spheroids. A review on cellular aggregates in cancer research. *J. Cancer Res. Clin. Oncol.* **113,** 101–122 (1987).

187. Mueller-Klieser, W. Tumor biology and experimental therapeutics. *Crit. Rev. Oncol. Hematol.* **36,** 123–139 (2000).

188. Sutherland, R. M. Cell and environment interactions in tumor microregions: the multicell spheroid model. *Science* **240,** 177–184 (1988).

189. Hirschhaeuser, F. *et al.* Multicellular tumor spheroids: an underestimated tool is catching up again. *J. Biotechnol.* **148,** 3–15 (2010).

190. Hartung, T. Toxicology for the twenty-first century. *Nature* **460,** 208–212 (2009).

191. Tung, Y.-C. *et al.* High-throughput 3D spheroid culture and drug testing using a 384 hanging drop array. *The Analyst* **136,** 473–478 (2011).

192. Vinci, M. *et al.* Advances in establishment and analysis of three-dimensional tumor spheroid-based functional assays for target validation and drug evaluation. *BMC Biol.* **10,** 29 (2012).

193. Chen, W. *et al.* High-throughput Image Analysis of Tumor Spheroids: A User-friendly Software Application to Measure the Size of Spheroids Automatically and Accurately. *J. Vis. Exp.* (2014). doi:10.3791/51639

194. Cell Viability Assays for Flow Cytometry. Available at: https://www.thermofisher.com/us/en/home/life-science/cell-analysis/flow-cytometry/cell-health-and-viability-assays-for-flow-cytometry/cell-viability-assays-for-flow-cytometry.html. (Accessed: 8th December 2016)